A Novel Compact Pyroelectric X-Ray and Neutron Source

DOE NEER Grant DE-FG07-04ID14596

Y. Danon
Department of Mechanical Aerospace and Nuclear Engineering, Rensselaer Polytechnic Institute, Troy, NY 12180, USA

Final Technical Report

August 2007
Rensselaer Polytechnic Institute

1. INTRODUCTION

This research was focused on the utilization of pyroelectric crystals for generation of radiation. When in constant temperature pyroelectric crystals are spontaneously polarized. The polarization causes internal charges to accumulate near the crystal faces and masking charges from the environment are attracted to the crystal faces and neutralize the charge. When a pyroelectric crystal is heated or cooled it becomes depolarized and the surface charges become available. If the heating or cooling is done on a crystal in vacuum where no masking charges are available, the crystal becomes a charged capacitor and because of its small capacitance large potential develops across the faces of the crystal. This large potential that can exceed 100,000 volts can be utilized to accelerate electrons and ions. By combining two crystals we were able to increase the acceleration potential to over 200 keV. This technology is very attractive because of the ability to build accelerators that can be operated by low voltage (9V battery) that is required to heat the crystals. We have demonstrated an x-ray accelerator with energy of over 200 keV the highest energy produced using this technology. These x-rays were used for x-ray florescent of lead and thorium and for imaging of small objects.
By placing the crystals in a deuterium gas environment, deuterium ions are created and accelerated towards a deutreated plastic target and D-D fusion is created. Our group is one of two groups that pioneered this fusion technology. This discovery has applications in production of small portable neutron generators. Such neutron source for homeland security applications is currently under development by our group.
This report summarizes the work that was done under the NEER DE-FG07-04ID14596 grant funding to develop this unique accelerator technology.

2. REPORT OUTLINE

The main body of the report is a PhD thesis produced by Jeffrey Geuther. The thesis contains a detailed description of the work done and the results accomplished.
A list of publications generated in the course of this work is also included.

3. REFERENCES

[1] Jeffrey Geuther, Yaron Danon, Frank Saglime, and Bryndol Sones, "Electron Acceleration for X-ray Production Using Paired Pyroelectric Crystals," Abstracts of the Sixth International Meeting on Nuclear Applications of Accelerator Technology, AccApp'03, p. 124, San Diego, CA, June 1-5, 2003.

[2] Jeffrey Geuther and Yaron Danon, "Increasing X-Ray Energy By Paring Pyroelectric Crystals, (Invited)", 18th International Conference on the Application of Accelerators in Research and Industry (CAARI 2004), Ft Worth TX, October 10-15, 2004.

[3] Jeffrey A. Geuther, Yaron Danon, "Pyroelectric Electron Acceleration: Improvements and Future Applications", Transactions of the ANS Winter Meeting, Washington, D.C, November 14 – 18, 2004.

[4] Jeffrey A. Geuther, Yaron Danon, "Magnetic Deflection of Electrons and Ions Produced by Pyroelectric Crystals", Transactions of the ANS National Meeting, San Diego CA, June 5 - 9, (2005).
[5] Jeffrey A. Geuther, Yaron Danon, "Development of a Pyroelectric Neutron Source," ANS Winter Meeting, Transactions Vol. 93, Nov. 13-17, 2005, Washington DC.
[6] Jeffrey A. Geuther, Yaron Danon, "High Energy X-ray Production with Pyroelectric Crystals," *J. Appl. Phys.*, **97**, 104916 (2005).
[7] Jeffrey A. Geuther, Yaron Danon, "Electron and Positive Ion Acceleration with Pyroelectric Crystals, " *J. Appl. Phys.*, **97**, 074109 (2005).
[8] Jeffrey Geuther, Yaron Danon, and Frank Saglime, "Nuclear Reactions Induced by a Pyroelectric Accelerator," *Phys. Rev. Lett.* **96**, 054803 (2006).
[10] Jeffrey A. Geuther and Yaron Danon, "Applications of Pyroelectric Particle Accelerators", Proceedings of the Nineteenth International Conference on The Application of Accelerators in Research and Industry, Fort Worth, Texas USA, August 20 - 25, 2006, Nuclear Instruments and Methods in Physics Research Section B, Volume 261, Issues 1-2, , Pages 110-113, 2007.
[11] Jeffrey Geuther, Yaron Danon, Kamron Fazel, "Recent Advances in Pyroelectric Radiation Generation", Winter Meeting of the American Nuclear Society, *ANS transactions* vol. 95, November 12-16, Albuquerque, NM 2006
[12] Jeffrey A. Geuther and Yaron Danon, "Enhanced neutron production from pyroelectric fusion", Appl. Phys. Lett. 90, 174103 (2007).

Radiation Generation with Pyroelectric Crystals

by

Jeffrey A. Geuther

A Thesis Submitted to the Graduate

Faculty of Rensselaer Polytechnic Institute

in Partial Fulfillment of the

Requirements for the degree of

DOCTOR OF PHILOSOPHY

Major Subject: Nuclear Engineering and Science

Approved by the
Examining Committee:

_____
Dr. Yaron Danon, Thesis Adviser

_____
Dr. Don Steiner, Member

_____
Dr. X. George Xu, Member

_____
Mr. James Brownridge, Member

_____
Dr. Robert Block, Member

_____
Dr. Toh-Ming Lu, Member

_____
Dr. Michael Podowski, Member

Rensselaer Polytechnic Institute
Troy, New York

April 13, 2007
(For Graduation May, 2007)

CONTENTS

LIST OF TABLES

LIST OF FIGURES

ACKNOWLEDGMENT

I owe thanks to many people who have helped to make my Ph.D. possible. First, I'd like to thank my family, who have always set high standards for me, and have encouraged me to excel. When I was in high school, I was always encouraged to concentrate on school instead of getting after-school jobs. I suppose one could draw parallels between such encouragement and my decision to go to grad school instead of getting a real job.

My thesis advisor, Yaron Danon, has always provided valuable insight on my project. He has also shown himself to be an excellent advocate for myself and other students. Several students, including Don Gillich, Kamron Fazel, Bryndol Sones, and Frank Saglime, also directly contributed to my research.

Finally, my wife Christine deserves gratitude for marrying me when I was earning the paltry keep of a grad student, which means that any gainfully employed person would have been a better provider. However, she stuck with me through the lean years. Now that we will no longer be living on the edge, I hope she doesn't get bored.

ABSTRACT

Pyroelectric crystals heated or cooled in vacuum have been used to produce low-energy x-ray devices since 1992. In the course of this thesis, experiments with lithium tantalate ($LiTaO_3$) and lithium niobate ($LiNbO_3$) were performed to extend the usefulness of pyroelectric radiation sources. Paired-crystal x-ray generators were shown to double the x-ray energy and yield, and allow the k-shell fluorescence of any metal up to thorium (Z = 90). It was demonstrated that the electron emission from a single pyroelectric crystal could be transmitted through a beryllium window to allow the electron beam to be extracted from the vacuum chamber. The electron emission current and energy were measured, and a mathematical model was developed to predict emission current and energy. Magnetic deflection experiments were used to verify that the electric field produced by the pyroelectric effect in lithium tantalate was sufficient to ionize gas. Finally, a paired-crystal system was used to ionize a deuterium fill gas near a metallic tip mounted to a pyroelectric crystal, and accelerate these ions into a deuterated target mounted to the opposing crystal. This technique was used to produce a compact, low-power fusion neutron source driven by pyroelectric crystals.

1 Introduction

1.1 Historical Review

In order to understand the rate of progress in the study of pyroelectric crystals as radiation sources, one must consider the history of the science of pyroelectricity.

1.1.1 Rochelle Salt: The First Rigorously-Studied Ferroelectric Crystal

The first mention of pyroelectric properties exhibited by any material was in ancient Greece, where Theophrastus observed that a stone called lyngourion (tourmaline) attracted pieces of straw and wood when heated.[1] However, the early study of tourmaline focused on its origin and its possible medicinal uses. No rigorous investigation of the physical properties of pyroelectric crystals was conducted until post-Rennaissance Europe, when tourmaline was studied by numerous scientists, including Carl von Linné, who finally identified electricity as the cause of the interesting properties of tourmaline[1].

A great breakthrough in the scientific study of pyroelectric crystals came in the late 17th century, when Pierre Seignette of La Rochelle, France became the first person to manufacture crystals of sodium tartrate[2] [KNa $(C_4H_4O_6)\cdot 4H_2O$]. This crystal is often called Seignette salt, and more commonly called Rochelle salt, in honor of this discovery.

Rochelle salt was known to be pyroelectric by David Brewster in 1824, and in 1920 Joseph Valasek discovered that Rochelle salt was also ferroelectric.[1] For hundreds of years it was the only ferroelectric crystal known to man.[2] For this reason, Rochelle salt was studied by many scientists who wanted to understand its peculiar properties. In 1921, Valasek discovered that Rochelle salt lost its ferroelectric property when cooled to below 18°C, and when heated to above 24°C[2]. He coined the term "Curie point" to describe the temperatures at which the Rochelle salt lost its ferroelectric properties. He also noticed that the polarization of Rochelle salt could be reversed by applying an electric field, and that the field-polarization curve for Rochelle salt was subject to a hysteresis effect[3]. He noted that the electrical properties of Rochelle salt were remarkably similar to the magnetic properties of iron, and described the unique electrical

properties exhibited by Rochelle salt as "ferroelectricity," an analogy to "ferromagnetism," the term describing the magnetic properties of iron.

The importance of the ferroelectric property of Rochelle salt was not widely recognized until the twentieth century. There are several reasons for the lack of recognition: Rochelle salt contains 112 atoms per until cell, making it hard to manufacture properly and very difficult to study; and Rochelle salt remained the only known ferroelectric crystal until 1935[3]. The discovery of a second ferroelectric ceramic would have certainly helped create interest in ferroelectricity, but from 1935 to 1938 Busch and Scherrer discovered a whole new series of ferroelectric crystals (the potassium dihydrogen phosphate, or KDP family)[2], proving that the phenomenon existed as more than an anomalous property in a few unique ceramics.

1.1.2 Pyroelectric Electron Emission and its Applications

In 1974, Rosenblum *et al*. published the first study of electron emission[*] due to the heating of pyroelectric crystals[4]. Rosenblum found that a $LiNbO_3$ crystal exhibited current densities of $10^{-10} – 10^{-9}$ A / cm^2 when heated slowly from room temperature to 100°C in a vacuum. He observed that the emission from the crystal was still significant when a 5 kV retarding potential was applied. It is probable, therefore, that the electrons created in Rosenblum's experiment created x-rays via interaction with his current measurement apparatus, but pyroelectric x-ray generation would have to wait for more than a decade to be discovered.

In 1992, Brownridge published an article detailing the first results from a pyroelectric x-ray generator[5]. He recognized that the energy of the electrons reported by researchers[4,6,7,8,9,10,11] studying ferroelectric electron emission [FEE] was high enough to fluoresce a metallic target. He used the electrons emitted by pyroelectric $CsNO_3$ to fluoresce the L-shell electrons in gold, thereby beginning the study of x-ray generation via pyroelectric electron emission. Amptek, Inc., inspired by Brownridge's results, has

[*] In this work, *electron emission* refers to the field emission of electrons from pyroelectric crystals. This is in disagreement with J. Brownridge, who believes that the primary source of electrons from pyroelectric crystals is field ionization, not field emission.

since developed a battery-powered, pocket-sized, pyroelectric x-ray device[12], thus showing the commercial applicability of pyroelectric x-ray technology.

Brownridge continued his research of pyroelectric x-ray generation. He has published results indicating that the electron emission from a cylindrical $LiNbO_3$ or $LiTaO_3$ crystal is self-focusing, nearly monoenergetic, and can be up to 170 keV in energy[13]. Brownridge later observed the production of 100 keV positive ion beams were also produced by the heating or cooling of a pyroelectric crystal[14].

1.1.3 Neutron Production

The usefulness of pyroelectric electron and x-ray sources was thus demonstrated by Rosenblum and Brownridge. Researchers then sought to extend pyroelectric radiation generation to the production of neutrons. In 2004, Geuther and Danon proposed that the ion emission from pyroelectric crystals could be used to fabricate a low-power fusion neutron source[15], and presented an outline for how such a device could be built. Later, they experimentally verified the ability of pyroelectric crystals to ionize gas using a magnetic deflection experiment[16].

Naranjo, Gimzewski, and Putterman[17] published a paper in 2005 showing the production of neutrons using a pyroelectric crystal. They mounted a copper disc and ionizing tip to the surface of a 30 mm diameter x 10 mm thick lithium tantalate crystal, and cooled the crystal to 77 °K with liquid nitrogen. They then heated the crystal using a resistor, while maintaining a dilute deuterium gas environment. During heating, the crystal became positively charged, and accelerated deuterium ions into an erbium deuteride (ErD_3) target. Fusion was observed during these experiments, showing for the first time that pyroelectric crystals could be used to make a neutron source.

The following year, Geuther and Danon demonstrated pyroelectric fusion with a paired-crystal source in which one crystal ionized deuterium gas with a 70 nm tip, while a second crystal in reverse polarity and coated with a deuterated polystyrene ($-(C_8D_8)_n-$) target doubled the acceleration potential and acted as the fusion target. This source did not immediately provide a benefit in terms of the neutron yield. However, due to engineering improvements such as the use of thermoelectric heating and cooling instead of cryogenic cooling, this work demonstrated that portable pyroelectric neutron sources

could were feasible. Later work by Geuther and Danon showed that after minor modifications, the paired-crystal source was competitive with the source developed by Naranjo in terms of neutron yield.

1.1.4 Summary

It seems, therefore, that the study of pyroelectric crystals has progressed at an accelerating rate. The first physical effects of pyroelectricity were observed millennia ago, the properties were identified as electrical in nature centuries ago, the first series of pyroelectric and ferroelectric materials were discovered in the last century. The same accelerating rate of progress can be seen in their use as radiation sources: Rosenblum's paper on electron emission from lithium niobate was published twenty-nine years ago; Brownridge's paper on x-ray emission from cesium nitrate, fifteen years ago; Naranjo's paper on neutron production was published only two years ago.

At RPI, contributions to the growth of this science have been made in many ways to be discussed in detail later in this thesis. Paired-crystal sources were demonstrated as a means of creating high-energy x-rays. It was shown that external electron beams can be extracted from a pyroelectric source. Finally, the first paired-crystal pyroelectric neutron source was developed at RPI. This is also the only working pyroelectric source that can easily be made into a portable source.

2 Physics of Pyroelectric Crystals

2.1 Spontaneous Polarization and the Pyroelectric Effect

Pyroelectric crystals are anisotropic dielectric materials that are polarized at equilibrium conditions. That is, with no external applied field, the net integrated dipole moment per unit volume in the crystal is not zero. If the crystal is cut such that its surfaces are perpendicular to the axis of polarization, then one surface will exhibit a positive surface charge and the other will exhibit a negative surface charge. At equilibrium, the polarization is screened, and is not readily observed. The magnitude of the crystal's polarization with no applied electric field (or temperature gradient) is known as the spontaneous polarization[2], P_s.

The change in the spontaneous polarization due to a change in the temperature of the crystal is known as the pyroelectric effect. It is this effect that can be exploited to create the large electric fields necessary for the emission of electrons and production of useful radiation. Consider a cylindrical crystal cut such that its polarization axis (which shall be referred to as the z-axis) is perpendicular to its flat faces. This crystal is spontaneously polarized at a value of P_s, but screening and charge relaxation prevents the observation of any electrical properties. However, when the crystal is heated, the polarization changes by a value ΔP_s, which causes a surface charge to appear at the z+ and z- crystal surfaces. The amount of surface charge produced per unit area is equal to:

$$\sigma = \gamma \cdot \Delta T \qquad (1)$$

where γ is the pyroelectric coefficient of the crystal and ΔT is the change in temperature. It is important to stay below the Curie temperature of the crystal (if the crystal is intended to be re-used), above which most crystals become non-polar and the pyroelectric properties will be lost.

Table I - Pyroelectric properties of selected crystals[18].

Crystal Type (Common Name)	**Pyroelectric Coefficient[18], μC / m² °K**	**Curie Temperature, °K[2,19,20,21,22,23]**
$BaTiO_3$	100	393
$CsNO_3$	4.3	427

$LiNbO_3$	40	1480
$LiTaO_3$	190	813 - 973
$Pb(Ti_{.48}Zr_{.52})O_3$ (PZT)	550	693 (for $Pb(Ti_{.58}Zr_{.42})O_3$)
$NaK\ C_4H_4O_6 \cdot H_2O$ (Rochelle salt)	20	lower = 255 upper = 297
$(NH_2CH_2COOH)_3 \cdot H_2SO_4$ (Triglycine sulfate, TGS)	250	322
$(ND_2CH_2COOD)_3 \cdot D_2SO_4$ (Deuterated TGS, DTGS)	270	336

The formation and change of the polarization of the crystal is best described by a ferroelectric hysteresis loop, such as the one shown in Figure 2.1. The loop is plotted on a Cartesian plane with the polarization of the crystal on the y-axis, and the applied electric field on the x-axis. A virgin crystal begins at the origin, with no polarization. As the applied electric field is increased, the polarization increases along a curve from point *a* to point *b*. Once all of the dipoles in the crystal are aligned, the polarization saturates, at point *c*. The spontaneous polarization results from the fact that once the external field is removed, the crystal's polarization does not return to zero. Instead, it is reduced only slightly from the saturation polarization, to a value known as the remnant polarization (point *d*). The spontaneous polarization is given by the line extrapolated from the linear part of the hysteresis loop (segment *bc*) back to the y-axis, at point e^2. The ferroelectric hysteresis loop can be seen to be quite similar to a ferromagnetic hysteresis loop. Indeed, ferroelectric materials are so called due to their analogous behavior to ferromagnetic materials. In a ferromagnetic hysteresis loop, the y-axis would represent the flux density, *B*, while the x-axis would represent the applied field strength, *H*. It is observed that ferromagnetic materials would retain a residual magnetization after the removal of the external magnetic field, just as ferroelectric materials retain a residual polarization after the removal of the external electric field.

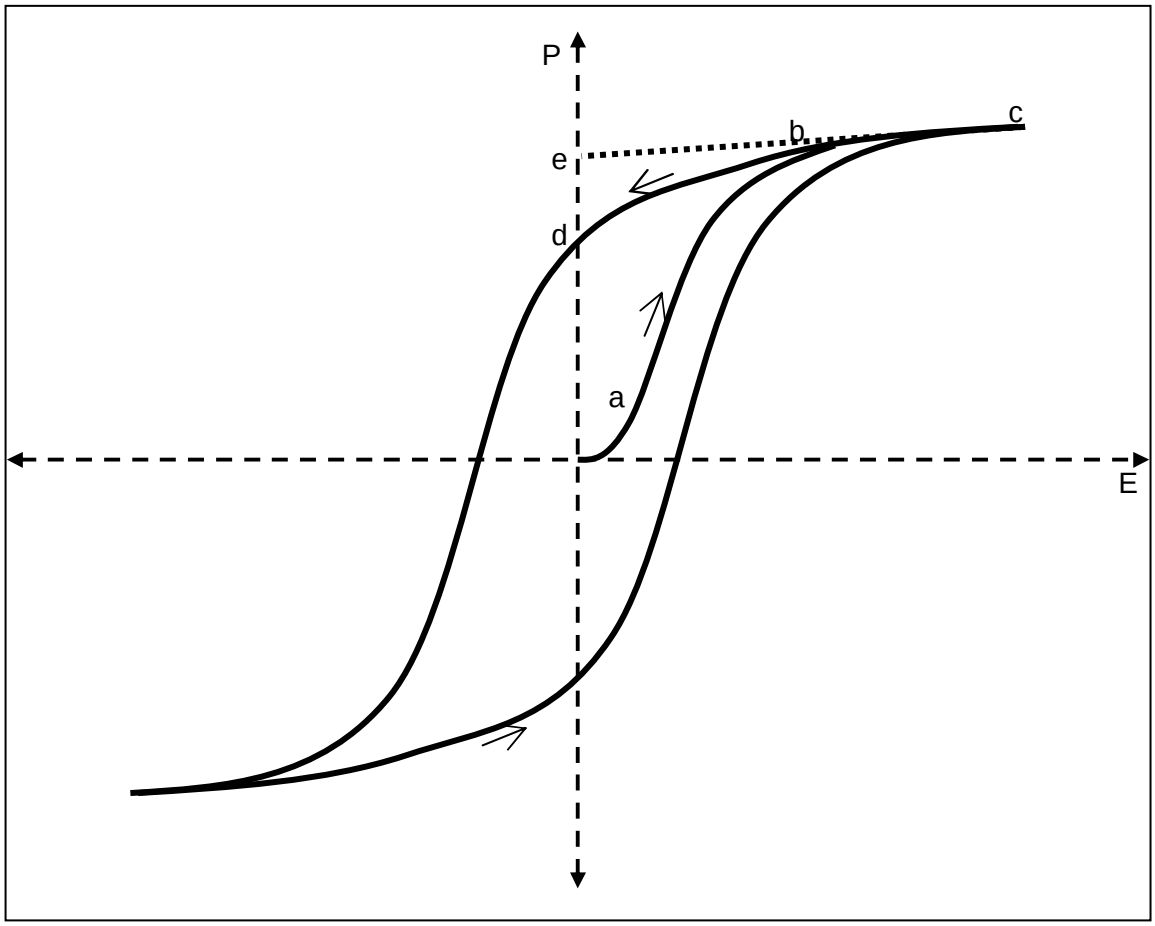

Figure 2.1 - Ferroelectric hysteresis loop showing the change in polarization with an applied electric field. Refer to Section 2.1 for a description of points (a) - (e).

2.1.1 Properties of Lithium Tantalate and Lithium Niobate

The two most common pyroelectric crystals for use in radiation generation experiments are lithium tantalate [$LiTaO_3$] and lithium niobate [$LiNbO_3$]. The unit cells of these crystals consist of lithium and tantalum (or niobium) ions located in the center of rings of oxygen ions, as depicted in Figure 2.2. The dipole moment of these unit cells is non-zero, such that when the crystal is poled using an electric field, the dipoles align and create a structured, polarized crystal in which the spontaneous polarization corresponds to the average dipole moment over the crystal volume[18]. During heating or cooling, the positive (Li and Ta or Nb) ions move relative to the oxygen ions, causing a change in the dipole, ergo a change in the spontaneous polarization.

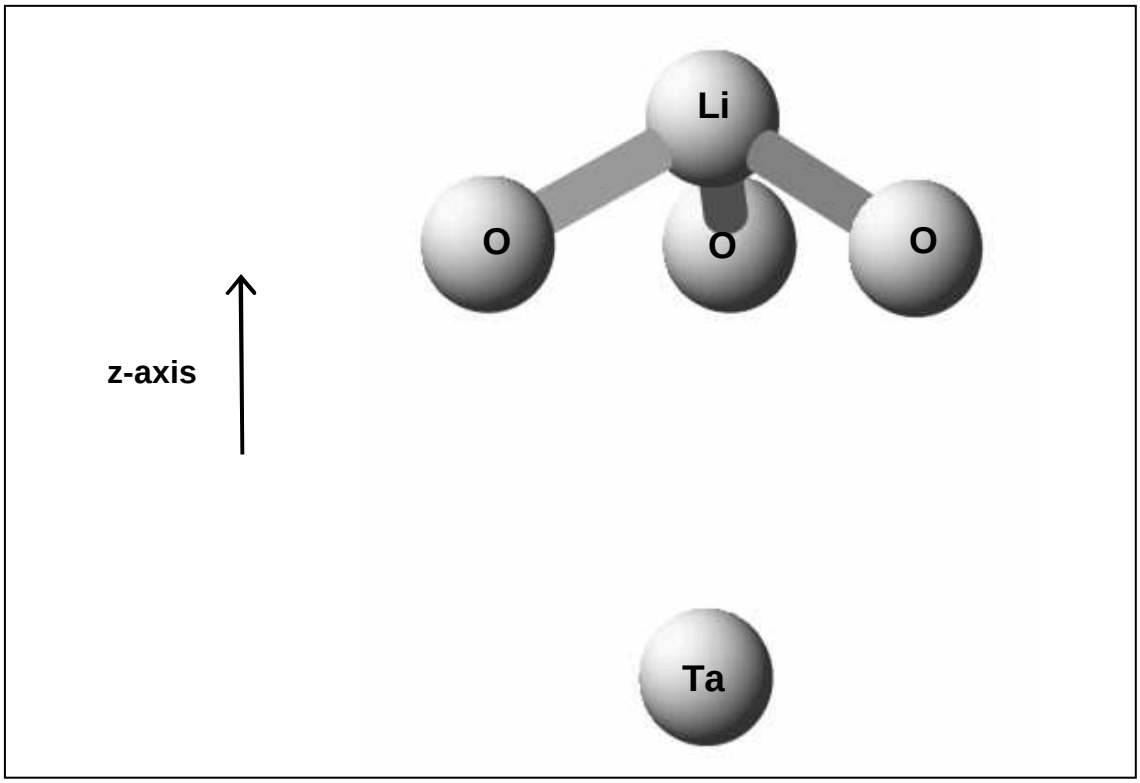

Figure 2.2 - Sketch of a lithium niobate unit cell in the ferroelectric phase, drawn in RASMOL[24] 2.7 using exact ion coordinates[25].

Lithium niobate has a higher spontaneous polarization than lithium tantalate, at 0.7 C / m^2 ($LiNbO_3$) versus 0.5 C / m^2 ($LiTaO_3$)[3]. Both crystals exhibit a single phase transition, in which they go from a ferroelectric phase to a paraelectric phase at their respective Curie temperatures. While their high Curie temperatures are seen as an obstacle by scientists exploring the material properties of these crystals, high Curie temperatures are favorable when producing pyroelectric radiation sources. Due to the extraordinarily high T_C of $LiTaO_3$ [620°C] and $LiNbO_3$ [~1200°C], the engineer can safely ignore the danger of transitioning to the paraelectric phase when designing a lithium tantalate- or niobate-driven radiation source.

The lithium tantalate unit cell is 515.2 pm wide and 1377.8 pm long (z-axis). Lithium tantalate is almost identical, at 514.8 pm wide and 1386.7 pm long. As lithium tantalate is heated from room temperature to its Curie point at 620°C, the oxygen ions are displaced 17 pm in the +z direction, the lithium ion is displaced 43 pm in the –z direction, and the tantalum ion is displaced 3 pm in the –z direction. Similarly, as

lithium niobate is heated to its Curie point of ~1200°C, the oxygen ions are displaced 20 pm in the +z direction, the lithium ion is displaced 51 pm in the –z direction, and the niobium ion is displaced 6 pm in the –z direction[3]. Therefore, the average change in distance between the positive and negative ions per unit temperature is greater for lithium tantalate than lithium niobate, which is manifest in the higher pyroelectric coefficient (change in polarization per unit change in temperature) of lithium tantalate.

The effect of the ion movement is that lithium tantalate and lithium niobate become de-polarized during heating. Therefore, the z- (ie., *c*-, *-z*) surface of the crystal exhibits a net positively charge on heating and a net negative charge on cooling. The z+ surface exhibits a net negative charge on heating and a net positive charge on cooling. This is in agreement with Brownridge and Shafroth, who report "crystal x-ray emission on heating and target x-ray emission on cooling when the -z base is exposed."[26] In other words, as the lithium tantalate or lithium niobate crystal is heated, its z- surface becomes less negative (due to depolarization), causing a net positive charge. This results in the acceleration of electrons from the surrounding environment to the z- surface of the crystal, causing x-rays characteristic of the crystal to be observed. During cooling, the crystal becomes re-polarized. The z- surface then gains negative charge, causing it to emit electrons toward a grounded or positively-charged target.

2.2 Formation and Decay of the Electret State

The charge formed on the surface of the crystal due to the pyroelectric effect can be neutralized over time due to the relaxation of charge through the crystal bulk. However, most pyroelectric crystals are excellent insulators, and the time constant of charge relaxation,

$$\tau = \varepsilon / \sigma \qquad (2)$$

is quite large. This results in the formation of a semi-permanent dipole state, known as an *electret* state. When designing a pyroelectric radiation source, it is important to choose a pyroelectric crystal with a long-lasting electret state. Lithium tantalate, for example, has an electrical conductivity of[27] $\sigma = 2.2 \times 10^{-15}$ ($\Omega^{-1}\ cm^{-1}$) and a dielectric constant of[28] $\varepsilon_{33} = 46\ \varepsilon_0$, where ε_0, the permittivity of free space, has a value[28] of $8.854 \times 10^{-14}\ F\ cm^{-1}$. This gives a relaxation time constant of 1850 seconds, meaning that it

takes roughly half an hour for the surface charge to be reduced by a factor of *e* due to relaxation. Electron emission experiments with lithium tantalate suggest that the relaxation time may actually be much larger, in accord with Rosenman's[29] calculated time constant[†] of $\tau = 10^5 - 10^7$ s for $LiNbO_3$, which is structurally very similar to $LiTaO_3$. Therefore, lithium tantalate and lithium niobate both have very stable electret states, which allow their consideration as crystals for use in pyroelectric radiation sources.

2.3 Thermodynamic Properties of Lithium Tantalate

Lithium tantalate has a thermal conductivity of[30] 45 mJ / (cm second) and a heat capacity of approximately[20] 26 cal / (mol ^oK), or ~470 J / (kg ^oK). While the heat capacity is low, (and similar to that of molybdenum), the thermal conductivity is extremely low, and is approximately equal to that of fiberglass building insulation[32].

To test the ability of a heat source located at the back of a crystal to heat the entire crystal to a useful ΔT, a simple experiment was performed in which a thermocouple was mounted to each end of a 20 mm diameter x 10 mm thick cylindrical crystal. The crystal was heated with a heating resistor for 10 minutes in a vacuum of $\sim 10^{-4}$ Torr. It was found that the exposed surface (front) of the crystal reached the same temperature as the back of the crystal, but was out of phase by one minute. (See Figure 2.3). During cooling, the time rate of change of the temperature at the front of the crystal was slower than the rate of change in temperature at the back of the crystal. Since the front would have been the emitting surface in an experiment, it is important to bear this difference in cooling rate in mind when mathematically modeling the rate of charge emission (as in Section 3.3.3), especially since temperature measurement is conducted at the back surface of the crystal during radiation-generation experiments.

Figure 2.4 shows a similar experiment in which a 5 mm x 5 mm x 10 mm rectangular crystal was substituted for the 10 mm x 20 mm (dia.) cylindrical crystal. The

---

[†] Rosenman calculated this value using the same formula as is presented here, $\tau = \varepsilon/\sigma$, where ε is the product of the dielectric constant of the crystal times the permittivity of free space, and σ is the crystal conductivity.

difference in temperature across the crystal is greater than with the larger crystal. However, the temperature difference between the front and back was still only 7°C.

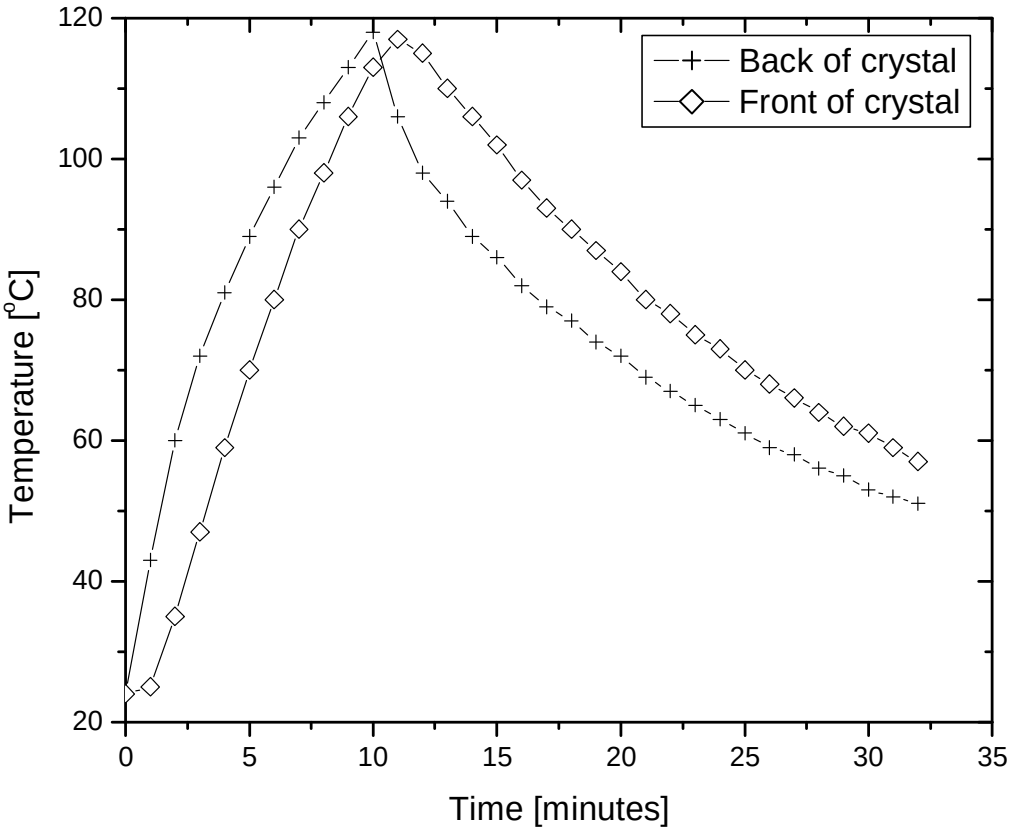

Figure 2.3 - Measured temperature at the front and back surface of a 10 mm thick x 20 mm diameter cylindrical $LiTaO_3$ crystal. The back of the crystal was epoxied to a heating resistor, which supplied 4.5 W of power to heat the crystal over 10 minutes.

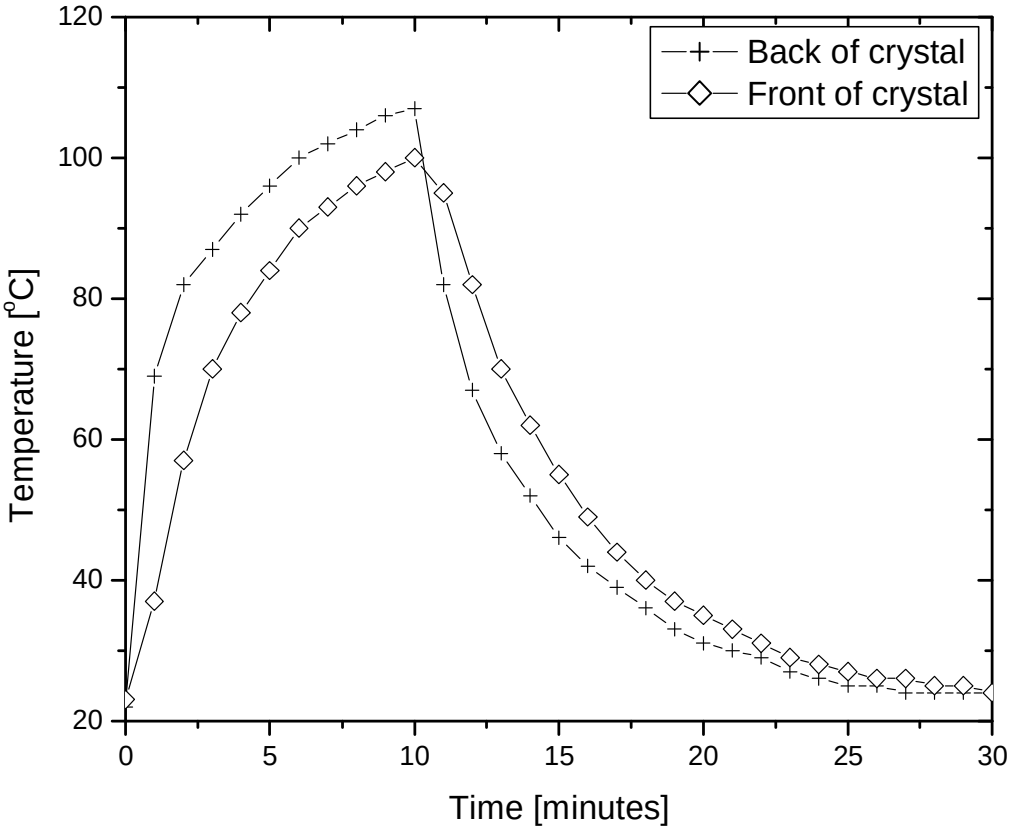

Figure 2.4 - Measured temperature at the front and back of a 10 mm thick x 5 mm x 5 mm $LiTaO_3$ crystal. The crystal was heated for 10 minutes and then allowed to cool. The back of the crystal was epoxied to a heating resistor.

The difference in the heating profile between the thin (5 mm diameter) 1 cm-thick crystal and the thick (20 mm diameter) crystal is explained by considering the crystals to be fins. The effectiveness ε_{fin} of a cylindrical pin fin is given by[32]:

$$\varepsilon_{\text{pin fin}} = \sqrt{\frac{4k}{hD}} \qquad (3)$$

In this equation, D is the crystal diameter, h is the heat transfer coefficient, and k is the thermal conductivity. Therefore, the fin effectiveness is proportional to the inverse square root of the diameter, and the effectiveness of a 20 mm diameter crystal at enhancing the heat transfer via radiation is one half the effectiveness of the 5 mm diameter crystal. This difference in heat loss from the sides of the crystal explains why the difference in temperature between the front and back of the crystal was greater for the narrow crystal (Figure 2.4) than for the wide crystal (Figure 2.3).

Figure 2.5 shows the temperature profile measured at the front and back of a 5 mm x 5 mm x 20 mm thick $LiTaO_3$ crystal heated by a resistor mounted to the back. As the figure shows, for a 20 mm crystal, it is difficult to heat the entire crystal to the temperature measured by the rear thermocouple. The temperature difference after 10 minutes of heating was 47°C. This helps to explain the difficulty observed in scaling the acceleration potential of a pyroelectric radiation source by using thicker crystals (to be discussed in Section 4.3).

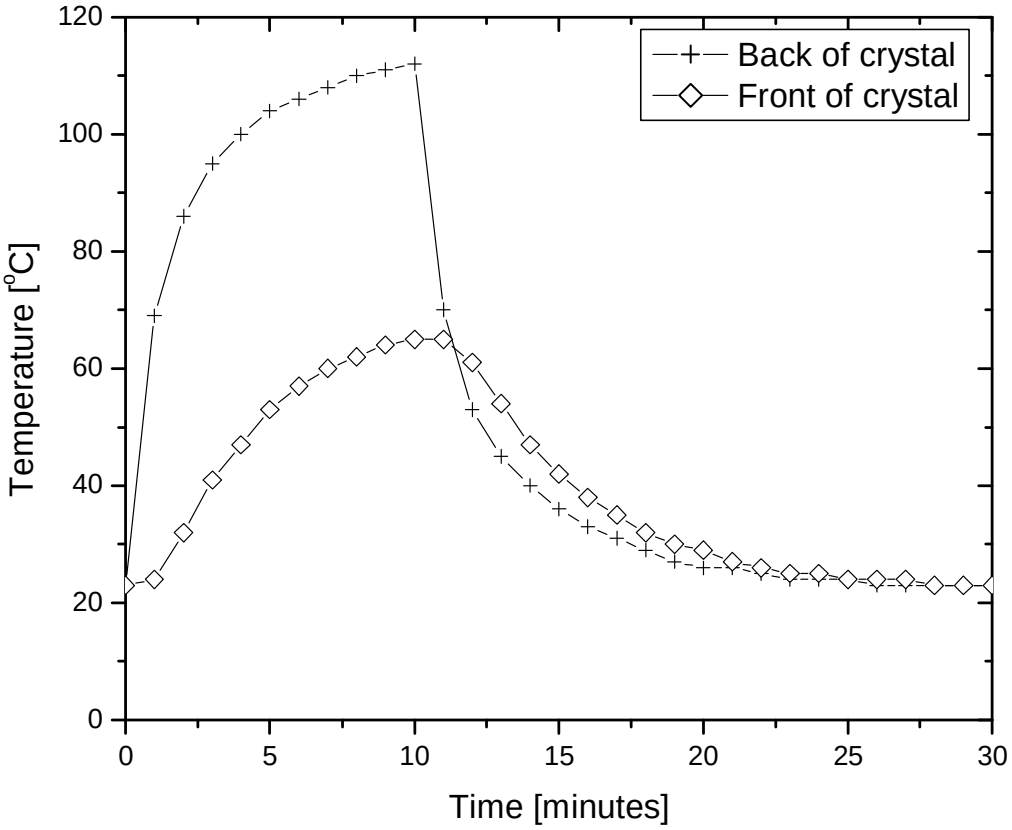

Figure 2.5 - Measured temperature profile of a 5 mm x 5 mm x 20 mm $LiTaO_3$ crystal, showing the difficulty in heating the emitting surface (front) of the crystal to the temperature measured at the heated surface (back) of the crystal.

2.3.1 Applying the One-Term Transient Conduction Model to $LiTaO_3$ Crystals

When the crystals are heated or cooled in vacuum, the heat transport is governed by radiation between the crystals and the surrounding walls and the conduction of heat through the crystal. Heat loss from the crystal can occur either by radiation to the

vacuum chamber walls or conduction to the heat sink through the heating resistor or thermoelectric cooler.

It is of interest to consider the magnitude of a temperature difference which can exist between the crystal surface and edge, since this radial temperature profile has been used to explain[31] the charge focusing phenomenon discussed in Chapter 5. The charge profile of a cylindrical crystal can be determined by considering an isolated crystal heated to 150°C and then placed in a vacuum at room temperature. The heat equation is separable, such that the solution to the radial component of the equation is not affected by the solution to the axial component. The time-dependent radial component of the solution for a cylinder[32] is:

$$\Theta(r,t) = \frac{T(r,t) - T_\infty}{T_{\text{int}} - T_\infty} = \sum_{i=1}^{\infty} A_i \exp\left(-\lambda_i^2 \tau(t)\right) J_0\left(\frac{\lambda_i r}{a}\right) \tag{4}$$

where r is the radial dimension, T_{int} is the temperature at the interface between the cylinder and the surrounding medium, T_∞ is the temperature of the surrounding medium, A_i is a constant, λ_i is the *ith* eigenvalue, τ is the non-dimensional time (Fourier number), and a is the radius of the crystal. The Fourier number is given by:

$$\tau(t) = \frac{\alpha \cdot t}{L^2} \tag{5}$$

Here, L is the half-length of the crystal[‡], and α is the thermal diffusivity:

$$\alpha = \frac{k}{\rho \cdot C_p} \tag{6}$$

where k is the thermal conductivity, ρ is the density, and C_p is the heat capacity. If the Fourier number is greater than 0.2, then the high order terms of the solution can be assumed to have died out, and the solution can be approximated to within 2% error[32] using the first term only:

$$\Theta(r,t) = A_1 \exp\left(-\lambda_1^2 \tau(t)\right) J_0\left(\frac{\lambda_1 r}{a}\right) \tag{7}$$

For the crystals typically used in this thesis (<10 cm in radius), this requirement is equivalent to demanding that several seconds have elapsed, which is a reasonable

[‡] The half-length is the axial (z) distance from the center of the crystal to the edge.

assumption due to the long time scale of most pyroelectric radiation generation experiments. (For a 1 cm thick, 2 cm diameter crystal, this condition is met when t > 2 seconds). The eigenvalues can be found in tables[33] or calculated using the transcendental

$$\cot \lambda = \frac{Bi}{\lambda} \tag{8}$$

The Biot number *Bi* is calculated using the equation:

$$Bi = \frac{h \cdot L}{k} \tag{9}$$

Typically, the value for *h* used in calculating the Biot number is the convection heat transfer coefficient. However, since pyroelectric radiation generation experiments are conducted in vacuum, the radiation heat transfer coefficient is employed instead. This is found using[32]:

$$h_{rad} = \varepsilon \cdot \sigma \left(T_{\text{int}}^2 + T_\infty^2\right)\left(T_{\text{int}} + T_\infty\right) \tag{10}$$

where ε is the surface emissivity, and σ is the Stefan-Boltzmann constant. Table II lists the Biot number, first eigenvalue, and edge temperature to centerline temperature ratio for $LiTaO_3$ crystals of various sizes.

Table II - Calculated Biot number, first eigenvalue, and ratio of edge temperature to center temperature for lithium tantalate crystals of various dimensions.

Half-length, L [cm]	Crystal radius, a [cm]	$T_{int} - T_\infty$ [°C]	Bi	λ_1	T(r = a) / T(r = 0)
0.5	0.25	130	0.012	0.109	0.997
0.5	1	130	0.012	0.109	0.997
0.5	1.5	130	0.012	0.109	0.997
1	0.25	130	0.023	0.151	0.994
1	1	130	0.023	0.151	0.994
1	1.5	130	0.023	0.151	0.994

Depending on the size of the crystal, the temperature at the interface with the vacuum is 99.4 - 99.7% of the centerline temperature. Figure 2.6 shows the temperature profile of a crystal equal in size to those used in many of the pyroelectric electron emission ex-

periments presented in Chapter 5, and suggests that the difference in temperature across the surface of the crystal is insufficient to create a great enough pyroelectric charge difference to result in focusing.

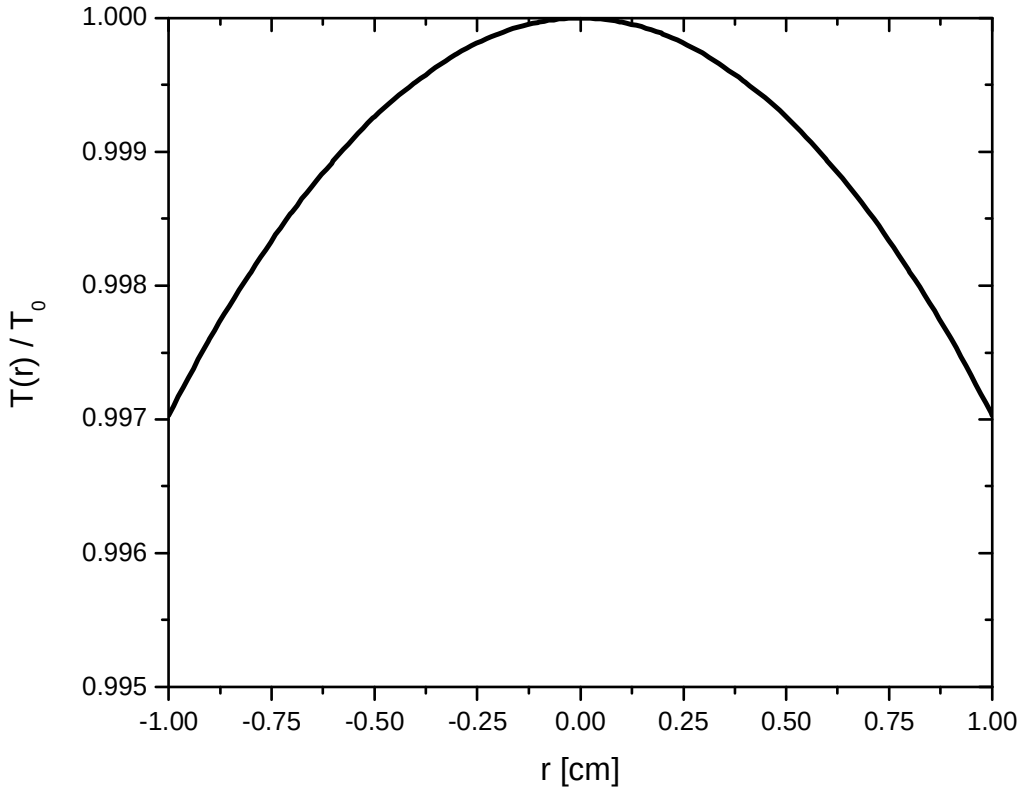

Figure 2.6 - Calculated temperature profile of a 1 cm-thick, 1 cm-radius $LiTaO_3$ crystal using the one-term approximation. Solution valid to within 2% after t = 2 seconds.

The exponential decay term in the one-term approximation gives the rate at which a crystal at a uniform temperature responds to a step change in temperature. The solution of this equation for a 1 cm thick by 2 cm diameter cylindrical crystal at 150°C suddenly immersed in an environment at 20°C shows that the crystal temperature would change with a "half-life" of 174 seconds. That is, if the exponential term stayed constant as the crystal temperature changed from 150°C to some new value, then the crystal temperature would change half-way to its final value in 174 seconds. A 20 mm thick x 20 mm diameter crystal would half a temperature "half-life" of 351 seconds under the same conditions.

This approximation cannot be used to estimate the temperature of the crystals as they cool, because it does not include heat loss due to conduction. Also, the constant in the

exponential depends on the crystal temperature, since it is based partially on the radiation heat transfer coefficient. However, it shows that the thermal response of crystals becomes slow as the crystal thickness increases, and therefore this example helps to illustrate the inherent difficulty in rapidly heating and cooling large (i.e., thick) crystals.

3 Electron Production with Pyroelectric Crystals

The first investigation of pyroelectric crystals as sources of useful radiation was published in 1974 by Rosenblum, Bräunlich, and Carrico.[4] They found that a $LiNbO_3$ crystal, when heated from room temperature to 100°C at a rate of 20°C per minute, emitted electrons at a current in the range of 10^{-10}- 10^{-9} amperes.

Pyroelectric electron emission is an important phenomenon, since the electrons can be used for materials testing, x-ray fluorescence, and may be used for medical applications. Just as important, however, is that the understanding of the electron emission mechanisms from pyroelectric crystals leads to better understanding of the capabilities of pyroelectric radiation generators in general. This is because electron emission is the major mechanism for the re-establishment of equilibrium after a pyroelectric crystal is heated or cooled in a vacuum. Therefore, if the electron emission properties can be characterized, so can the time dependence of the electric field, which is of crucial importance for the use of pyroelectric crystals as x-ray and neutron generators.

In this chapter, experiments performed to measure the electron emission from lithium tantalate crystals will be presented. Evidence of "packeted" electron emission[34] will be shown, and a mechanism for this phenomenon will be suggested. A mathematical model for the time-dependence of the crystal's charge and electric field will then be developed, and will be shown to correspond to the experimentally-observed current.

3.1 Electron Measurements with a PIPS Detector

In early experiments, it was hypothesized that the observed x-ray spectra, which consisted of counts over a broad energy range, were in fact the result of a monoenergetic electron beam hitting the target. The reason for suspecting this was that a monoenergetic electron source produces a bremsstrahlung continuum with a maximum x-ray energy equivalent to the electron energy. Since it was believed that the electrons all came from the same location (the crystal surface) and were accelerated by the same field (the acceleration field between the crystal and the target), it made sense that they would be monoenergetic. In fact, a MCNP simulation showed that the observed x-ray spectra were similar to those expected from a monoenergetic source.

In order to verify that the pyroelectric electron source was monoenergetic, a direct measurement of the electron emission was conducted using a collimated PIPS surface barrier detector.

3.1.1 Experimental Setup

A 5 mm diameter x 10 mm cylindrical $LiTaO_3$ crystal was aimed at a collimated detector, such that the crystal would emit electrons toward the detector during the cooling phase. The detector was a Canberra PIPS[§] A-300-19-AM detector, collimated by a 12 mm-thick aluminum block with a 0.1 mm^2 cylindrical aperture. [See Figure 3.1]. The vacuum pressure during these experiments was typically 4 - 20 mTorr. The crystals were heated for 600 - 1000 seconds with 4 W of power and were then allowed to cool naturally. The electron detector output was sent to an Ortec 142 IH preamplifier. The signal from the preamplifier was sent to an amplifier with a discriminator setting corresponding to 15 keV electrons. Electronic noise prevented the measurement of electrons below this energy.

[§] PIPS = Passively Implanted Planar Silicon

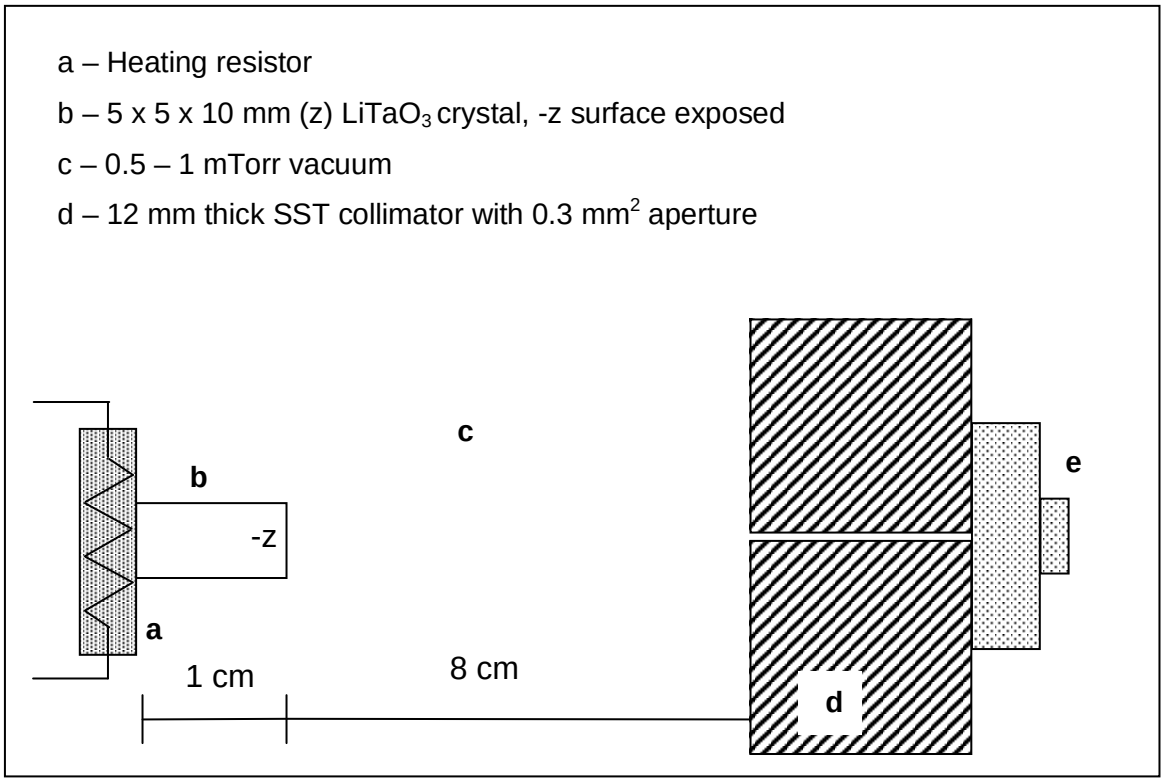

Figure 3.1 - Experimental setup for the measurement of electron emission using a PIPS detector.

3.1.2 Results

It was observed that the electron emission was nearly monoenergetic, with an energy that changed as the crystal cooled. As the cooling phase begins, no emission is observed. After several minutes, a low-energy electron peak begins to be seen above the discriminator level of the detector. For the next few minutes, both the energy and the count rate increase, until the electron energy reaches its maximum value (for example, 143 keV at t = 451 seconds after the beginning of the cooling phase, as in Figure 3.2). After this point, the count rate and electron energy decrease slowly until charge equilibrium is re-established.

These experimental observations can be explained by the build-up of charge due to the pyroelectric effect, and its reduction due to electron emission: At the beginning of the cooling phase, the crystal is at electrical equilibrium. As it cools, the pyroelectric effect results in the formation of a surface charge, which in turn causes an electric field to develop. When the field becomes large enough, field electron emission at the crystal surface can occur. As the charge increases during cooling, the field strength and rate of

field emission also increase, until the charge buildup due to the pyroelectric coefficient is too slow to overcome the loss of charge due to field emission, and can no longer increase the field.

The peak shape observed in Figure 3.2 is that of a large peak followed by a low tail of fairly constant height. This shows that most of the electrons are emitted from the same location (the surface of the crystal), since they must be accelerated by the same potential to be observed as a monoenergetic peak by the PIPS detector. The low tail may represent electrons created by ionization in the gas. This could be tested by performing this experiment at different gas pressures to see if the size of the tail was pressure dependent, but such a test was not performed for this thesis.

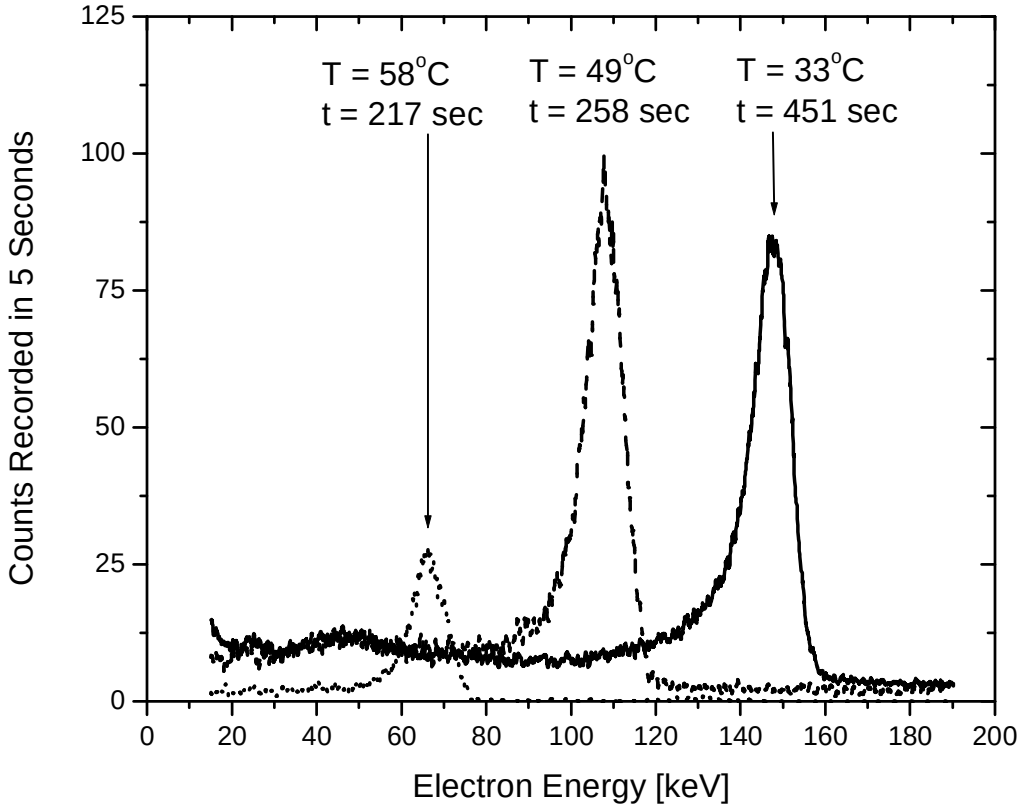

Figure 3.2 - Time-varying monoenergetic electron emission from a pyroelectric crystal during a cooling phase.

3.1.3 Multiple Electron Peaks

The narrow (0.3 mm^2) collimator aperture used in electron detection experiments was used to reduce the pulse pileup that occurred with a wider aperture. When wider apertures were used, it was observed that multiple electron peaks could be observed during the electron emission phase. These peaks correspond to the simultaneous interaction of multiple electrons with the PIPS detector. Remarkably, the magnitude of the pileup peaks greatly exceeds the magnitude expected for random electron emission. Instead, it appears that the electrons can be emitted in "packets." This behavior was also observed by Brownridge[35].

Figure 3.3 shows a spectrum taken during the cooling of a 20 mm x 5 mm x 5 mm $LiTaO_3$ crystal heated for ten minutes to a maximum temperature of 165°C, and then cooled to room temperature in a 0.74 mTorr vacuum. The detector was collimated by a 12 cm aluminum block with a 1 mm^2 aperture. Specifically, Figure 3.3 shows the electron emission near the end of the cooling phase, as the crystal cooled from 32°C to 28°C. The first peak in the spectrum shows that the electron energy was 100 keV. As the figure shows, peaks corresponding to the simultaneous measurement of up to 7 electrons could be seen, with the first six peaks being very clear.

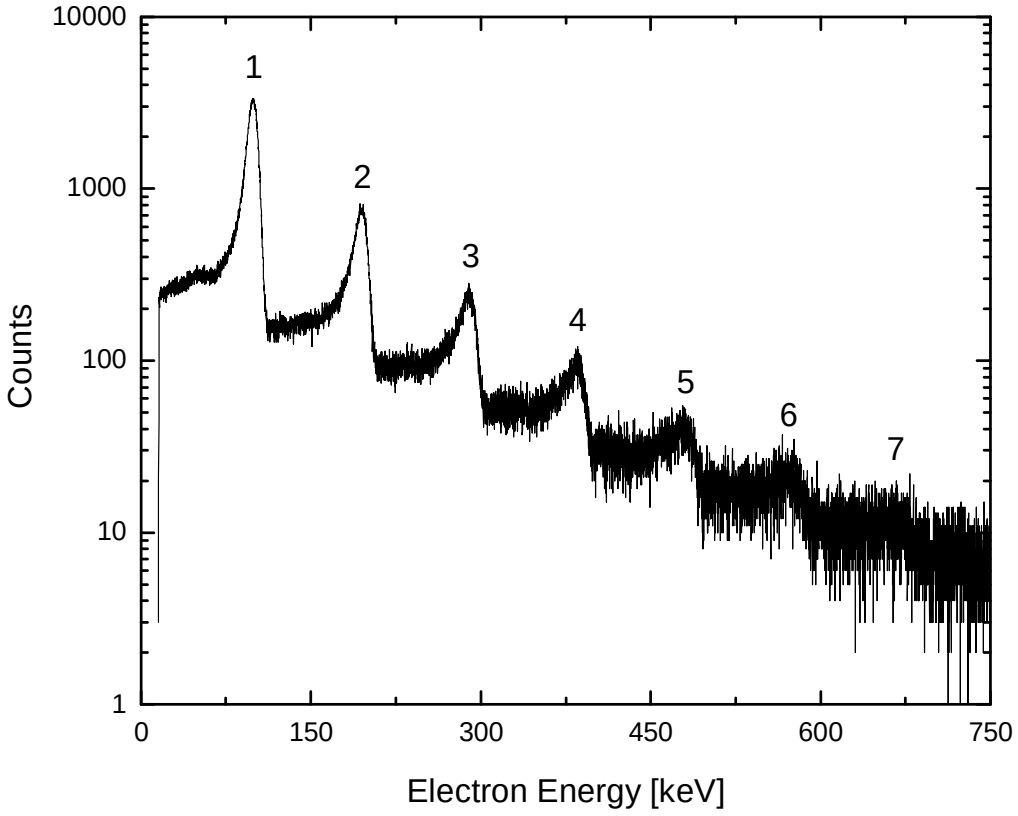

Figure 3.3 - Multiple electron peaks observed during the cooling of a 20 mm thick $LiTaO_3$ crystal.

The detector used in this experiment can be assumed to be paralyzable. The probability of an electron being measured in the *rth* pileup peak of a paralyzable detector is given by[66]:

$$P(r) = e^{-n\tau}(1-e^{-n\tau})^n \qquad (11)$$

where n is the true count rate and τ is the effective pulse width. In Figure 3.4, the counts per peak for the spectrum shown in Figure 3.3 are plotted against the expected counts per peak for the detector, modeled as a paralyzable detector with a 40 μs effective pulse width. (An oscilloscope was used to measure electron pulse widths from the detector, after the preamp and amplifier. The pulse width was measured at 50 μs. It was assumed that two pulses could be discerned from each other after 40 μs.) As Figure 3.2 shows, each peak has a tail corresponding to the electrons from impact ionization in the fill gas. To account for the tails (which comprise the continuum region beneath the well-defined peaks in Figure 3.3), the area of peak *n* was estimated as the area beneath the peak and tail up to the maximum energy of the peak, minus the area below a horizontal line

extrapolated from the tail of peak *n+1* to the y-axis. In this way, the tail area of each peak of a higher index was not included in the area estimate for the preceding peaks. Figure 3.4 shows that a comparison of the measured peak area versus the calculated peak area suggests that the electron emission is not completely random. If it was, then there would only be three clearly discernable pileup peaks, not six.

This phenomenon may be due to ions from impact ionization events impacting the crystal surface and simultaneously freeing multiple electrons from the crystal. These electrons would be accelerated by the same field, and would therefore have a high probability of reaching the detector simultaneously. (The only reason for the probability of the simultaneous measurement of such electrons not being unity is the distribution of their initial direction and kinetic energy).

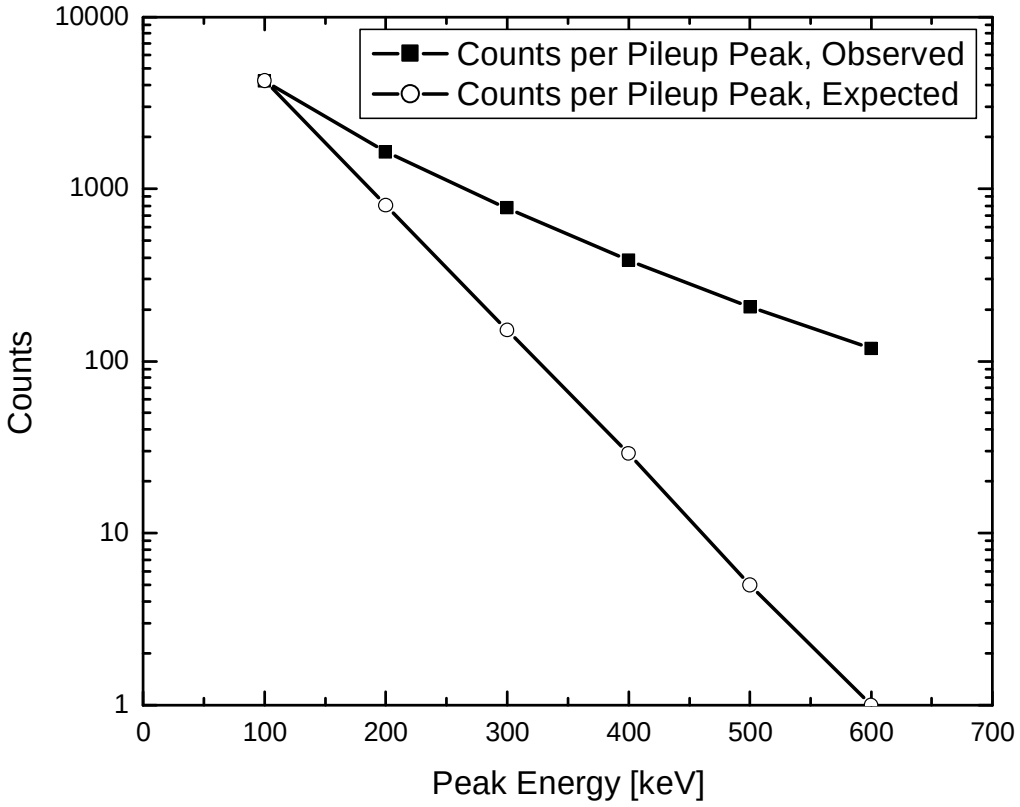

Figure 3.4 - Counts per pileup peak from an electron emission spectrum compared with the counts per peak exptected from a paralyzable detector model with a 40 microsecond pulse width.

3.2 Direct Measurement of Electron Current

In order to better understand the electron emission from pyroelectric crystals, several experiments were conducted in which the electron current was measured directly using a conducting plate and a current meter. The most advanced of these experiments is discussed in later in this chapter. However, an earlier, simpler experiment also led to some important conclusions.

Figure 3.5 shows the geometry for this experiment. A 10 mm thick, 20 mm diameter cylindrical $LiTaO_3$ crystal was mounted to a thermoelectric cooler such that electron emission from the crystal would strike a copper plate. A wire connected to the copper plate would then carry a current signal to a HP3458A digital multimeter. The multimeter was set to integrate over 1000 power line cycles (16.67 seconds) and return an average current value. The pressure for the experiments was typically 30 mTorr, and the temperature range was from room temperature (20°C) to a maximum of 70°C over 450 seconds.

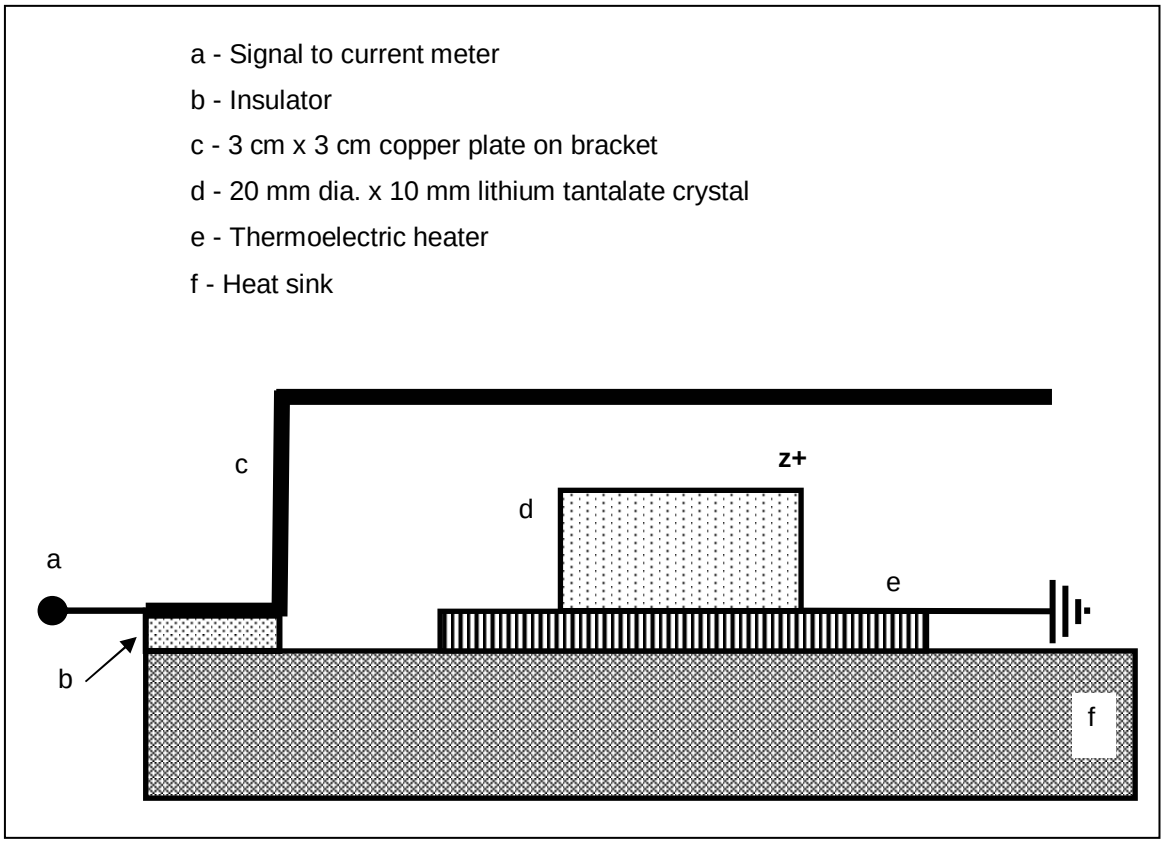

Figure 3.5 - Experimental setup for direct current measurement from a pyroelectric crystal. The distance from the crystal to the copper plate was 7 mm.

Figure 3.6 shows the result from one of these measurements. The electron emission during the heating of the crystal is seen to increase sharply during the early part of the heating phase, when the temperature rate of change is the greatest, and then decrease gradually during the latter stages of the heating phase, when the temperature changes slowly. Integrating the curve, it is found that the total charge emitted in the form of electrons was -368 nC. The charge generated by the pyroelectric effect over $\Delta T = 50°C$ for a lithium tantalate crystal with a 20 mm diameter is 2980 nC. Therefore, it is apparent that only about a tenth of the available charge was emitted in a useful form. These results may be deceptive, however, since discharge events occurring during a period of strong emission may be averaged into the current, and would therefore be difficult to observe. Furthermore, one can see that the emission current was still non-zero at the last measurement point, and was converging to zero very slowly. Therefore, the total measured charge would have increased somewhat if the observation time were longer.

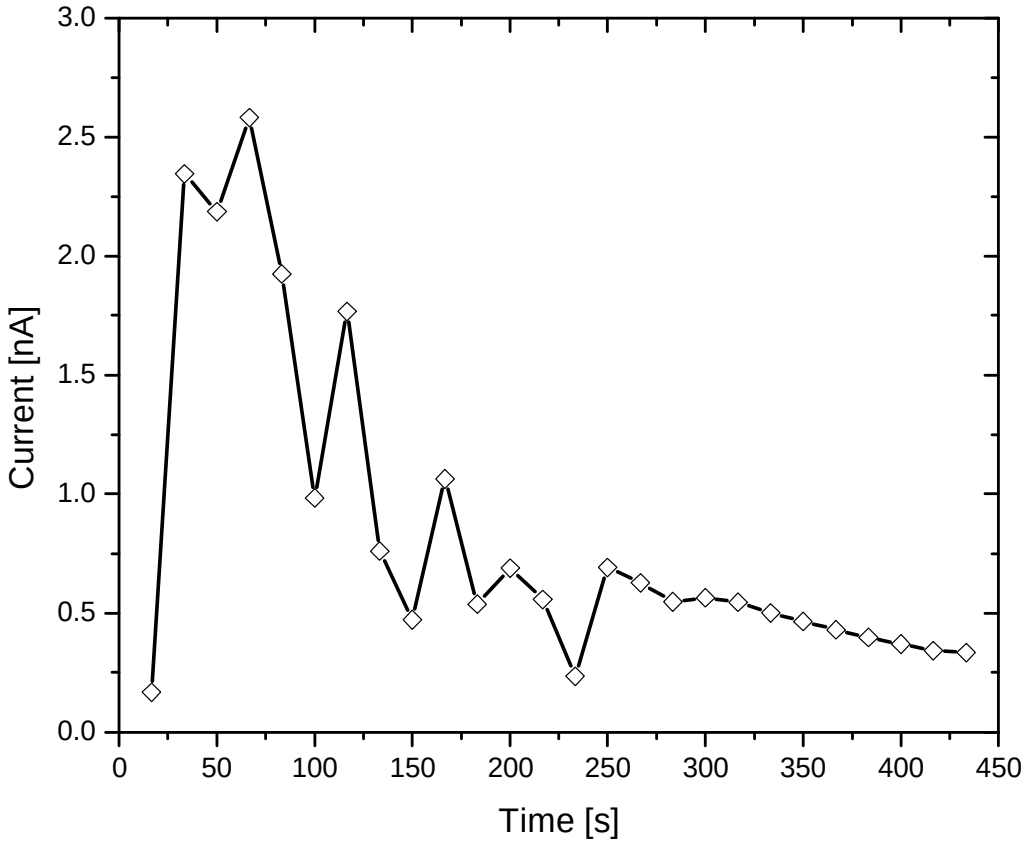

Figure 3.6 - Emitted electron current measured during the heating of a 20 mm diameter x 10 mm thick $LiTaO_3$ crystal.

In a subsequent experiment, the same apparatus was used, but with a 5 mm x 5 mm x 4 mm (z) lithium tantalate crystal in place of the larger crystal depicted in Figure 3.5. The temperature of the crystal was automatically cycled from 20°C to 90°C using a temperature controller. Each heating cycle lasted 190 seconds. The integration time on the digital multimeter was set to 300 power line cycles (5 seconds). The pressure was 16.5 mTorr. The results are shown in Figure 3.7.

The average charge emitted per heating or cooling phase was 1.12 nC. The expected charge per cooling phase, based on $\Delta T = 70°C$, is 332 nC. Therefore, there was an even more pronounced difference between the emitted charge and the charge expected from the pyroelectric effect when using the smaller crystal. There are two reasons for this discrepancy. First, the heating cycle was more rapid, such that the emitting face of the crystal did not get cycled by the full 70°C temperature gradient. Second, the use of a the

thinner crystal meant that the distance to the target was increased, while the distance to the heat sink was decreased, so the electrons had a higher probability of following field lines which would hit the base instead of the target than in the experiment with the large crystal. Figure 3.7 shows that the magnitude of the charge emission during the heating phase is roughly equal to the charge emitted during the cooling phase. This is to be expected, since the pyroelectric coefficient is the same during heating and cooling, and the thermal cycle of the crystals was such that the magnitude of the temperature gradient was the same during heating as it was during cooling.

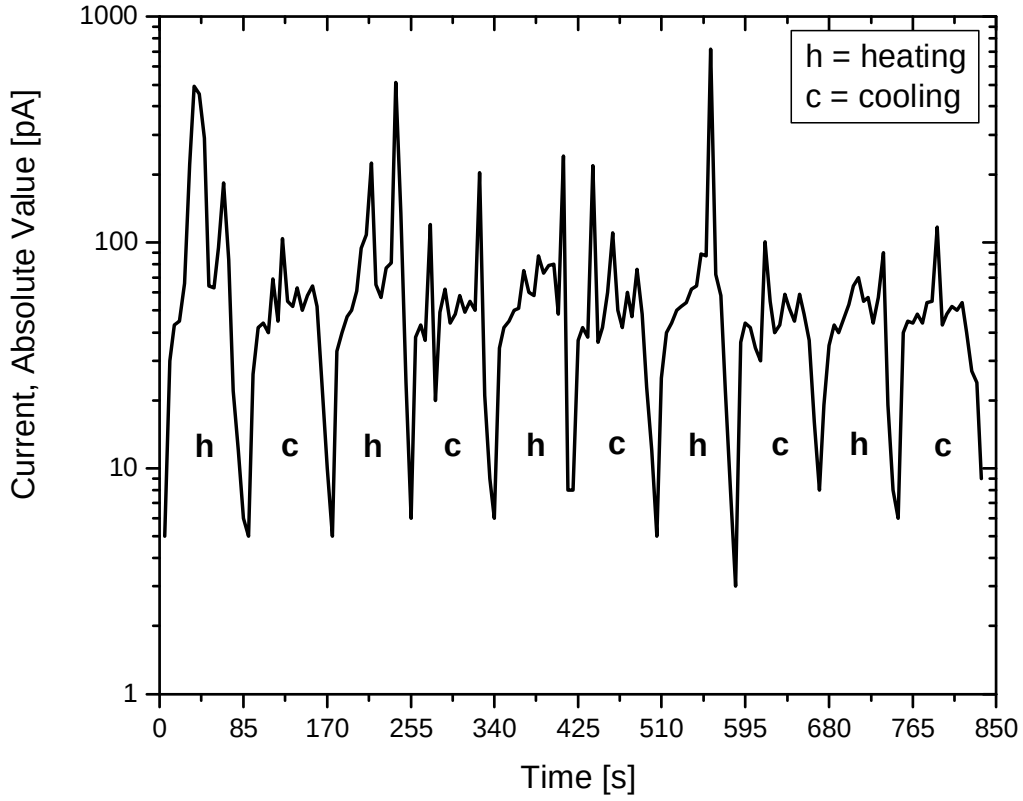

Figure 3.7 - Magnitude of current between a 4 mm thick x 5 mm x 5 mm lithium tantalate crystal and a copper plate.

3.3 Production of an External Electron Beam

3.3.1 Introduction

Due to the proven ability to produce compact, portable radiation sources with pyroelectric crystals, experiments were conducted to determine whether pyroelectric crystals could be used to produce electron beams external to the vacuum chamber. Such

sources may be useful in various medical, industrial, and research applications. This series of experiments resulted in data useful for the mathematical modeling of the charge emission.

3.3.2 Experimental Apparatus

For these experiments, 10 mm thick $LiTaO_3$ crystals were mounted to heating resistors. Both 5 mm x 5 mm rectangular crystals and 20 mm diameter cylindrical crystals were used in this experiment. The crystals were aimed at a 1 mil beryllium window mounted over an opening in a flange on the vacuum chamber. A shielded Faraday cup was mounted outside of the window, and provided a current signal to an HP3458A digital multimeter. A thermocouple connected to the heating resistor provided temperature indication via connection to an HP3457A digital multimeter. Figure 3.8 shows an illustration of the experiment geometry.

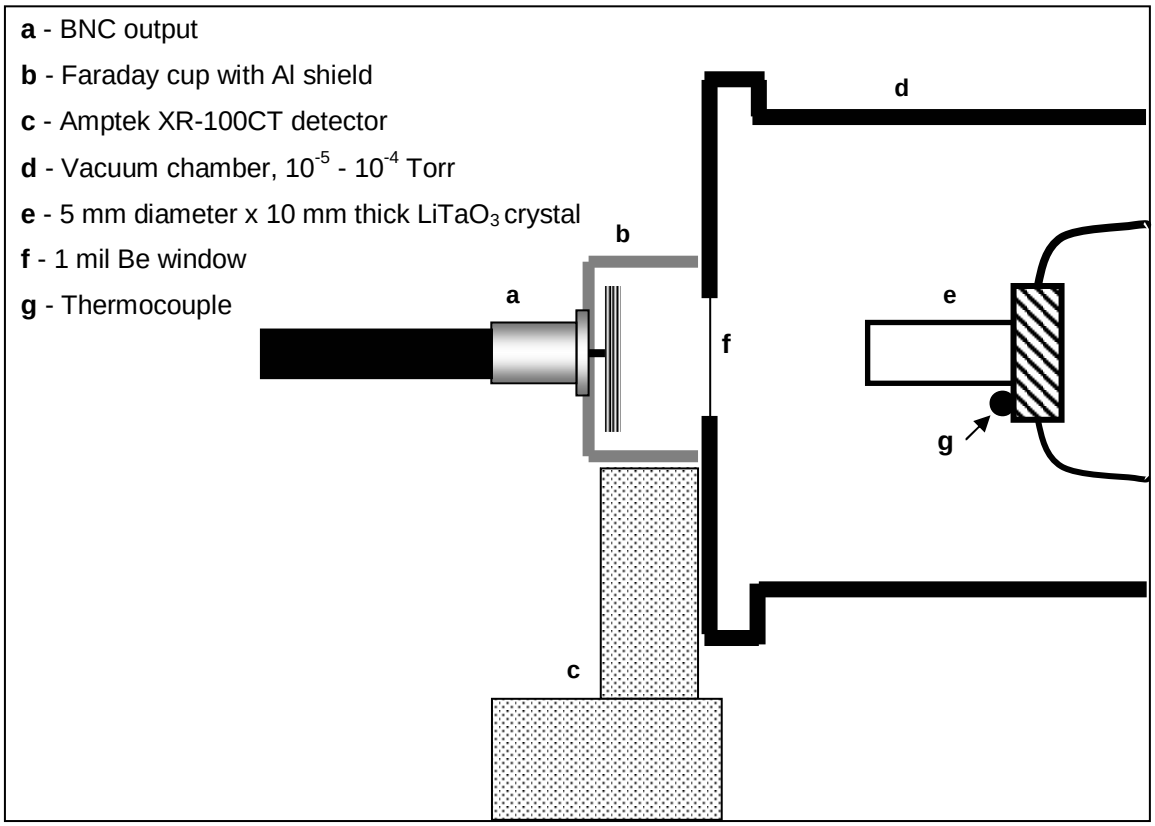

Figure 3.8 - Illustration of the experimental geometry for the measurement of electron emission current from a pyroelectric crystal.

Both of the multimeters were controlled by a LabView program, which stored the temperature and current curves to an output file. The Labview program read the current from the HP3458A every 200 ms, and averaged five consecutive readings to give the current at each second. After five consecutive measurements, the program took 1.5 seconds to compute the average, plot the current and temperature, and store the data. Therefore, every second of time as measured in the LabView program corresponded to 2.5 seconds of real time. A block diagram of this LabView program is shown in Appendix III.

The beryllium window was 16 mm in diameter and 25 μm (1 mil) thick. To find the fraction of electrons expected to be transmitted through the window as a function of energy, a simple MCNP program was used. In this program, 10^6 electrons in a pencil beam were incident on a 25 μm Be window. A *F1* (surface current) tally plane was placed on the other side of the window. The transmission fraction of electrons incident on the window versus energy found in MNCP is shown in Figure 3.9.

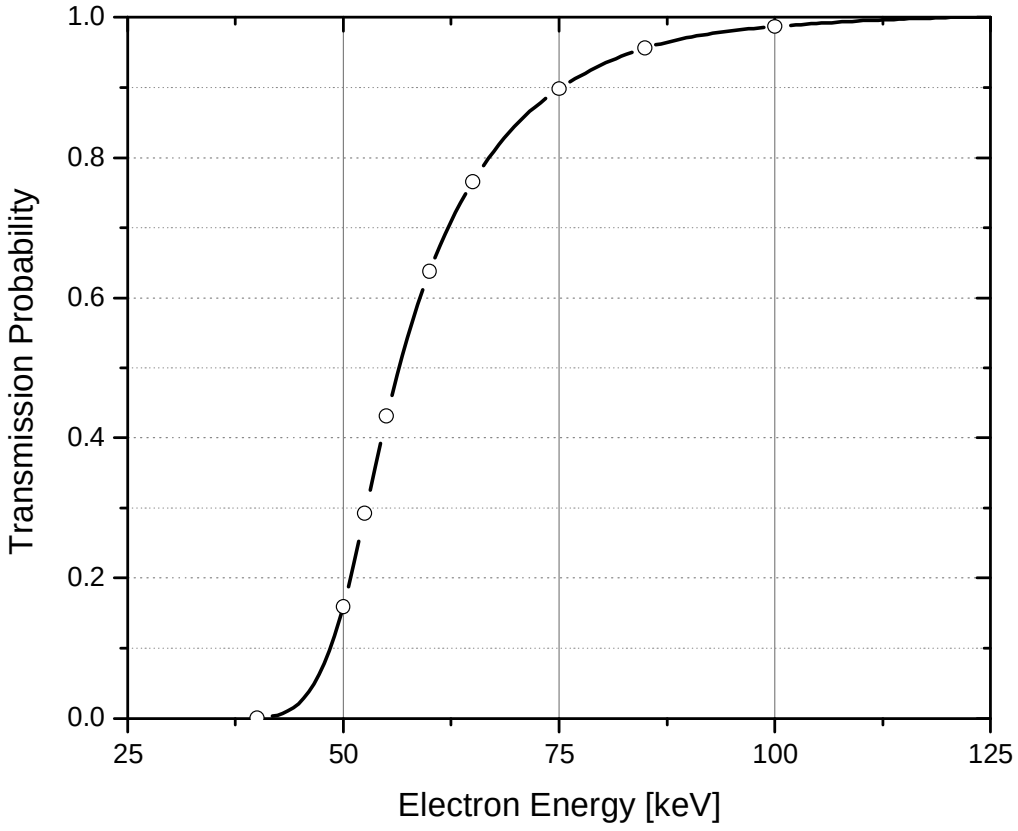

Figure 3.9 - Transmission of electrons through a 1-mil Be window, as calculated in MCNP4C2. Error bars are not shown because statistical error at all points was less than 0.25%.

The current measured by the Faraday cup was divided by the transmission fraction plotted in Figure 3.9 to find the total emission. The incident electron energy as a function of time was found using the endpoint energy of x-ray spectra taken every 300 seconds of experiment time, as shown in Figure 3.12. The electron beam was assumed to be at the same energy after transmission through the Be window as it was when it entered the window. In reality, the electron energy peak is broadened and shifted toward somewhat lower energy, as can be seen in Figure 3.10. The data in Figure 3.10 was obtained using the same MCNP model as Figure 3.9, but with 10^7 incident particles. The relative area of the peaks in Figure 3.10 corresponds to the transmission fraction plotted in Figure 3.9.

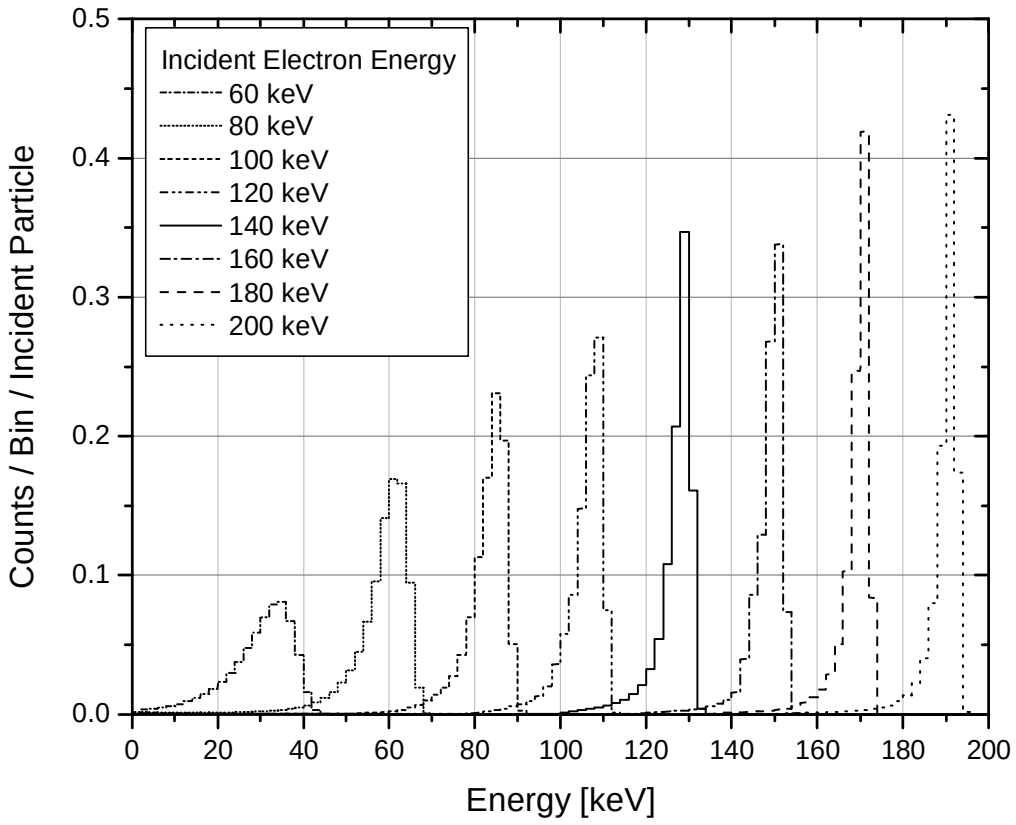

Figure 3.10 - Electron spectra after transmission through a 1-mil Be window for monoenergetic incident electron beams at different energies. Spectra were calculated in MCNP5 with 10^7 incident particles.

3.3.3 Charge Dynamics and the Fowler-Nordheim Equation

Since data had been obtained showing both the temperature rate of change, $\frac{dT}{dt}$, and the electron emission current, $\frac{dQ}{dt}$, it was possible to develop a method for mathematically modeling the electron emission current and the charge on the crystal.

Crystal surface charge is gained through the pyroelectric effect, which causes a rate of change in charge of:

$$\frac{dQ}{dt} = \gamma \cdot A \cdot \frac{dT}{dt} \tag{12}$$

where Q is the crystal charge, γ is the pyroelectric coefficient, T is the temperature, and A is the area of the crystal. This gain in charge is offset by losses due to charge screening, charge relaxation, and charge emission:

$$\frac{dQ}{dt} = \gamma \cdot A \cdot \frac{dT}{dt} - i_{emission} - i_{screening} - i_{relaxation} \tag{13}$$

The screening current is negligible in vacuum, and will be neglected in this model. The relaxation current will also be neglected, due to relaxation of charge through the crystal bulk being a process which takes place over a much longer time scale than the typical electron emission experiment. As for the emission current, it cannot be thermionic emission, since electron emission is only observed during half of the heating cycle, regardless of temperature. Electrons may be produced by gas ionization, but this effect can be ignored, since measurements have shown that the rate of ionization is much lower than the observed electron current. Figure 3.2 shows that, in some experiments, the current from ionization in the fill gas can be of comparable magnitude to the current from field electron emission. In the figure, this is shown by the comparable magnitude of the electron counts in the peaks to the count in the tails of the peaks. (Since electrons from the surface of the crystal are all accelerated by the same potential, they appear in the same energy peak. Electrons produced via gas ionization between the crystal and target can then be accelerated by any fraction of the available potential, resulting in a tail). However, the electron emission experiments discussed in this section were conducted at much lower pressure (~10^{-5} Torr versus ~10^{-2} Torr) than the experiments which led to Figure 3.2. Therefore, the effect of ionization events on the measured current is expected to be negligible.

These simplifications field electron emission as the only loss term to consider in the charge balance equation:

$$\frac{dQ}{dt} = \gamma \cdot A \cdot \frac{dT}{dt} - i_{emission} \tag{14}$$

Field electron emission from conductors has been studied extensively[36,37,38,39,40,41,42,43]. Classically, it is modeled with the Fowler-Nordheim equation[43]:

$$i_{FE} = 6.2 \times 10^{-6} \frac{(\mu + \phi)^{1/2}}{\mu + \phi} E^2 \exp\left[-6.8 \times 10^{7} \frac{\phi^{3/2}}{E} \right] \tag{15}$$

where i_{FE} is the field emission current density in amps / cm^2, μ is the Fermi energy in eV, ϕ is the electronic work function in eV, and E is the electric field strength in V / cm. The field emission current represented by this equation is due to the deformation of the potential barrier of electrons in the conductor. With no external electric field, the potential well is infinitely thick, and no charge emission can occur. However, a uniform electric field will cause a linear deformation in the potential well, which will become triangular. Image charge effects cause a rounding of the top of the barrier, as well.

The result is that the electrons now have some probability of tunneling through the barrier. As the Fowler-Nordheim equation shows, and as intuition would suggest, this probability is increased with a decrease in the work function (which lowers the barrier height and thickness), an increase in the applied electric field strength (which lowers the barrier thickness), or an increase in the Fermi energy of the conductor (which increases the maximum internal electron energy, thereby decreasing the effective barrier height and thickness).

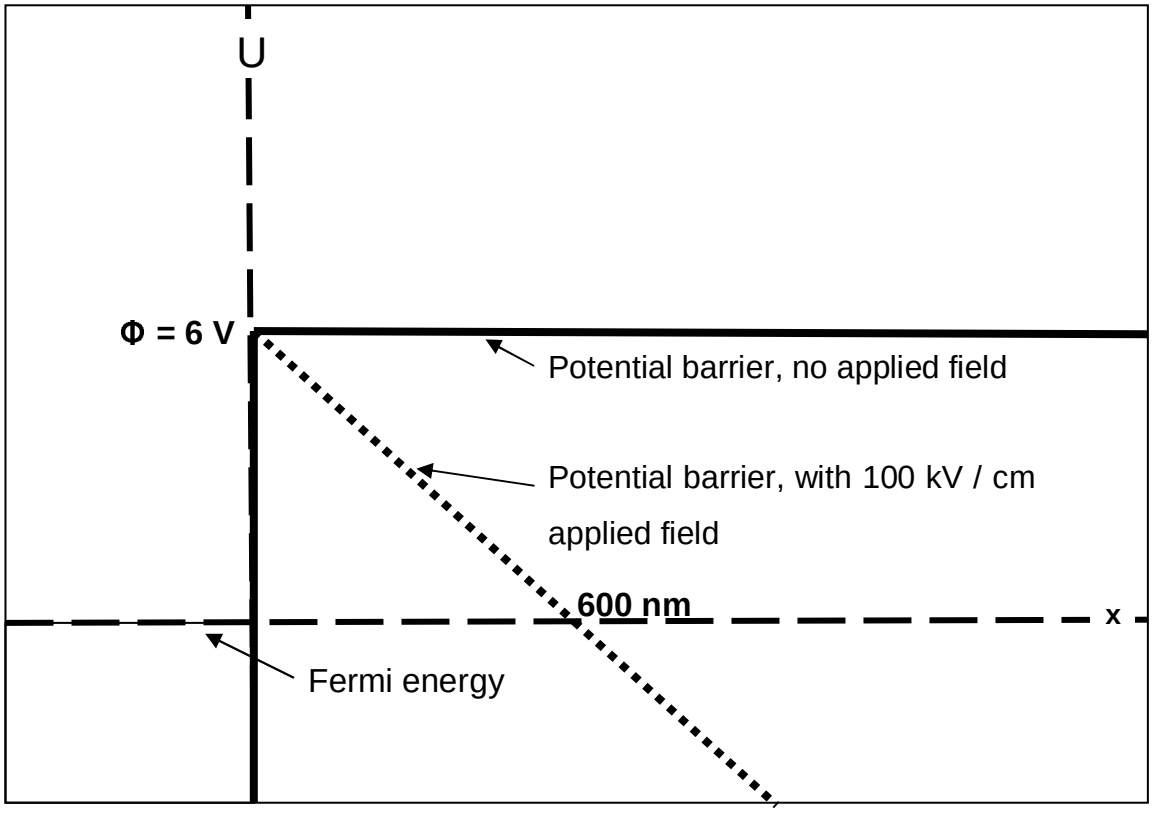

Figure 3.11 - The potential well deformation of a conductor with a work function of 6 eV, due to a uniform 100 kV / cm external electric field. Image charge effects are not shown.

Since this model was developed for conductors, it cannot be directly applied to a pyroelectric crystal, which is a dielectric material. Dielectric materials are more complicated because the population of the internal electron energy states does not obey a Fermi distribution, and there is an internal electric field due to the polarization of the material. Furthermore, Rosenman[29] states that the surface layer of a ferroelectric material is a semiconductor. For semiconductors, effects such as band-bending due to field penetration and the potential of surface impurities must be considered in a rigorous model[36]. Additional problems arise due to the non-uniformity of the electric field. The linear deformation in the potential well used in the Fowler-Nordheim equation does not accurately represent the barrier deformation due to a non-uniform field caused by the edge effects, ring charge effects (see Section 5), and the deviation from the parallel-plate model of the electric field due to a crystal which is small compared to its target. These effects cause the electric field near the crystal surface to be greater than would be predicted by a semi-infinite parallel plate model.

However, this problem is still one of with charges bound in a potential well, which is being deformed by the application of an external field. It is therefore useful to keep the form of the Fowler-Nordheim equation in a field emission current term, and fit it to experimental data. The field emission current term then becomes:

$$i_{FE} = a \cdot E^2 \exp\left[-\frac{b}{E}\right] \tag{16}$$

where *a* and *b* are fitting constants.

In order to obtain experimental data to use with this charge dynamics model, the data collected from the Faraday cup was corrected by dividing by the transmission coefficient plotted in Figure 3.9. In order to choose the correct energy for the transmission correction, 180 second x-ray spectra were taken consecutively during the cooling phase of the crystal. The extrapolated endpoint energy of the x-ray spectrum was taken as the acceleration potential. Figure 3.12 shows four of the x-ray spectra used for this purpose.

Figure 3.13 shows the extrapolated endpoint energy from all of the x-ray spectra taken during one cooling cycle versus time. Also shown is the calculated crystal charge, found by using measured temperature data to find the charge formation due to the pyroelectric coefficient, and then subtracting charge loss due to electron emission. The

difference in the slope of the charge and measured endpoint energy plots at large values of time may be due to the omission of relaxation current from our model.

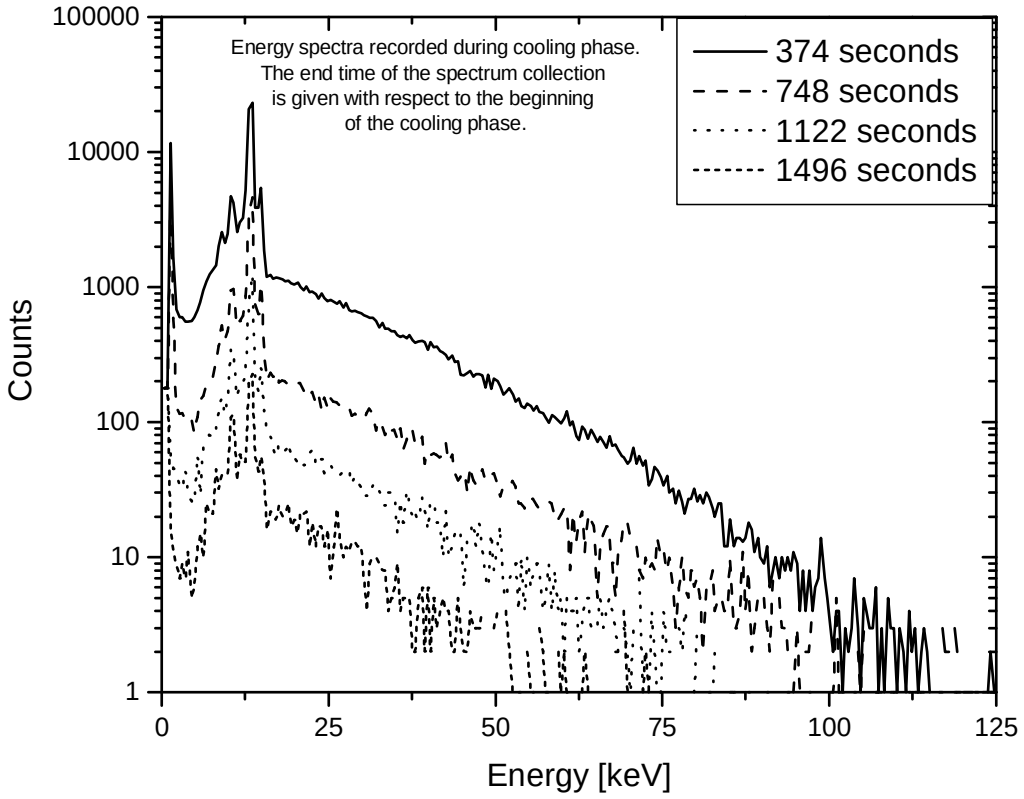

Figure 3.12 - Four of the 180 second x-ray spectra taken to estimate the acceleration potential of the electrons incident on the Be window.

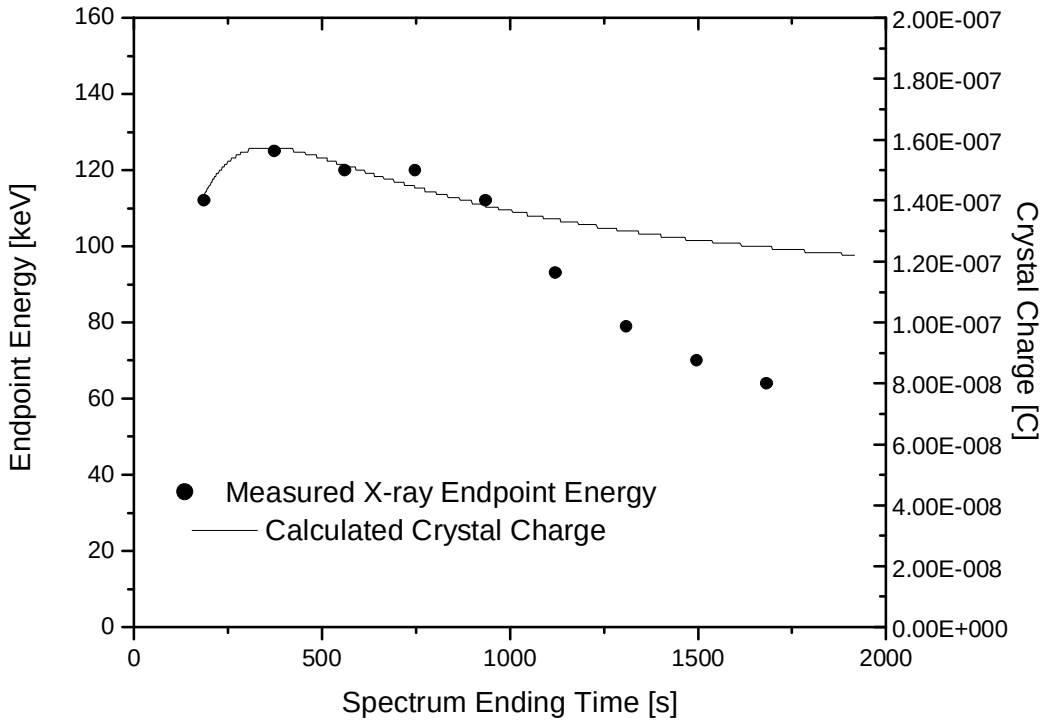

Figure 3.13 - Endpoint energy of all of the x-ray spectra used to estimate the energy of the electrons incident on the Be window. The left axis shows crystal charge, as calculated with the charge emission model.

The transmission-corrected current data was input into a spreadsheet. The electric field strength was estimated based on a finite element model of the experiment given the estimated potential from the endpoint energy data shown in Figure 3.13. This model was used to account for edge effects and the deviation from the ideal point source or semi-infinite plane geometry, but did not include ring charge effects. Equation 16 was then calculated numerically for every 2.5 seconds for assumed values of the Fowler-Nordheim fitting parameters *a* and *b*. These parameters were adjusted to fit the calculated data to the experimental data, with *a* providing an amplitude adjustment and *b* providing an adjustment for the decay of the current curve versus time. It was found that, for $a = 2.5 \times 10^{-19}$ and $b = 7.05 \times 10^{6}$, Equation 14 fit very well against the corrected experimental data. This result suggests that, for a known geometry, an electron emission experiment can be used to obtain fitting constants for a Fowler-Nordheim type field emission current term, which allows the construction of an accurate charge balance

equation. This equation can then be used to find the surface charge and emission current of a pyroelectric crystal versus time.

The constant *b* can be equated to the exponent in the Fowler-Nordheim equation to provide an estimate for the work function:

$$7.05\times10^{6} = 6.8\times10^{7}\cdot\phi^{3/2} \tag{17}$$

This calculation yields a value of $\phi = 0.23$ eV. This value seems low, but it is close to the electron affinity of 0.25 eV for the z^- surface of $LiNbO_3$ calculated by Rosenman[10]. (Rosenman's calculation included changes in internal electron energy due to band bending). An effective Fermi energy can be determined by setting the constant *a* to be equal to the first term in the Fowler-Nordheim equation and entering the calculated value of ϕ:

$$2.5\times10^{-19} = 6.8\times10^{-6}\,\frac{\sqrt{\mu + 0.23\,\mathrm{eV}}}{\mu + 0.23\,\mathrm{eV}} \tag{18}$$

The is equation is solved for $\mu = 1.2$ eV.

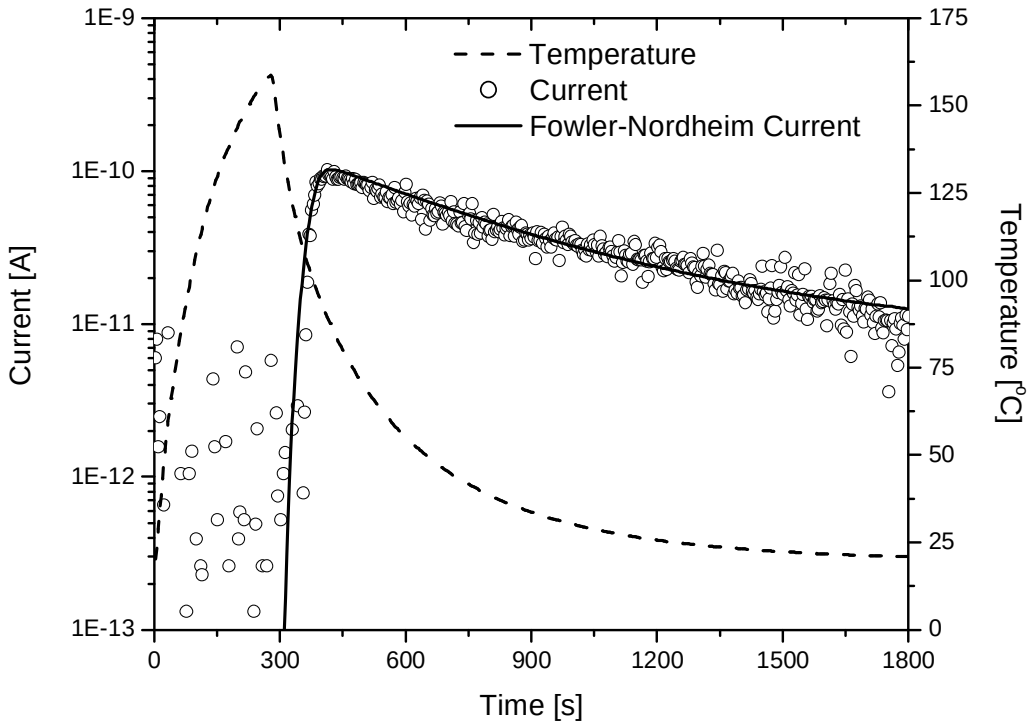

Figure 3.14 - Plot of current calculated using a charge balance equation including a fitted Fowler-Nordheim term versus the current and temperature measured experimentally.

4 X-Ray Generation with Pyroelectric Crystals

The initial thrust of this research was to replicate the x-ray generation results observed by James Brownridge of SUNY-Binghamton. Brownridge discovered that the pyroelectric electron emission observed by Rosenblum *et al*[4]. could be used to generate x-rays. Brownridge's first publication[5] showed that emission from a $CsNO_3$ crystal could cause characteristic L-shell x-ray emission from gold (9.71 and 11.44 keV) if the crystal was slowly heated from 77°K to 150°K. He later improved his technique by using $LiNbO_3$ and $LiTaO_3$ crystals, with which he was able to fluoresce the k-shell of lead[44] (74.96 and 84.92 keV).

This work represented the first independent confirmation of Brownridge's results. Improvements were later made to his design by utilizing a paired-crystal geometry in which the superposition of two pyroelectric fields allowed the doubling of the acceleration potential, x-ray energy, and x-ray yield[50].

4.1 Motivation

The uses of x-ray radiation sources in industry and research are manifold. Analytical techniques like x-ray fluorescence can be used to determine the elemental composition of metals. Crystal structure can be determined using x-ray diffraction. X-rays can be used to image biological specimens, or to sterilize medical equipment. All of these applications require the same tool: a safe source of x-rays.

Typically, the following methods are used to obtain x-rays:

- Radioisotopes - Radioactive isotopes can be manufactured with a variety of half-lives and x-ray (or gamma ray) emission energies. The limited number of useful radioisotopes limits the available energy range. Radioisotopes are typically inexpensive, and therefore offer a cost advantage over most other x-ray and gamma sources. However, they cannot be turned off, and therefore must be shielded when not in use to minimize danger to workers. Also, they decay with a characteristic half-life. Sources with a long half life are difficult to discard safely, and those with a very short half life change in yield greatly during use, and frequently need to be replaced.

- X-ray tubes - X-ray tubes use a hot cathode to emit copious amounts of electrons, with an acceleration potential provided by a biased anode. Advantages of x-ray tubes include moderate cost and tunable bias voltage. Disadvantages include the limitation of maximum x-ray energy to the bias voltage limit on the power supply, the large size of the machine, and the bremsstrahlung-dominated (i.e., "white") x-ray spectrum. The lower limit of the price range is around $8000.
- Linear accelerators - Linear electron accelerators produce x-rays by colliding an energetic electron beam with a high-Z target. These machines can be used to produce intense x-rays at much higher energy than x-ray tubes. However, linacs are large and comparatively expensive, which limits their use in small research facilities and in the field.

In this chapter, it is shown that pyroelectric crystals offer an alternative means of producing x-rays. Like other methods, there are several advantages and disadvantages to pyroelectric x-ray generators. The advantages include:

- Cost - A lithium tantalate crystal capable of producing 100 keV x-rays can be manufactured for about $300. The major cost-determining factor in the manufacture of pyroelectric x-ray sources is the vacuum chamber which houses the crystal. The only pyroelectric x-ray source currently on the market, the Amptek Cool-X[12] costs $2500. Amptek estimates the maximum life of this source to be ~1000 hours of active use, with a reduction in lifespan if the source is used continuously. (The limited lifespan of the source is attributed to the deterioration of the vacuum over time).
- Size - The pyroelectric crystals used in published research have ranged from 1/40 cm^3 to 7 cm^3. The experiments performed at RPI were all able to fit onto a single laboratory bench, including the instrumentation and vacuum pump. The Cool-X is pocket-sized, with the much of the volume dedicated to its 9V battery. Therefore, due to the small size of the crystals and lack of shielding, pyroelectric sources are the premier x-ray sources in terms of portability.
- Safety - Unlike radioisotopes, pyroelectric sources can be turned on and off, which means that shielding is unnecessary when transporting the source. This

feature also recommends pyroelectric sources to educational use, since students can learn about the uses of x-ray radiation without great risk.

Like the other methods of x-ray generation, pyroelectric x-ray generators also have several disadvantages:

- Time-dependent yield - The x-ray yield from a pyroelectric source depends on the charge on the crystal or crystals, which provides the electron acceleration potential. Since the charge is replenished by heating and cooling the crystal and depleted by the electron emission, the yield goes from zero to its maximum value each time the crystal is heated or cooled (usually over several dozen to several hundred seconds). The maximum x-ray energy is also time-dependent.
- Energy limitations - The maximum energy of a pyroelectric source is determined by intrinsic properties of the crystals used in the source (pyroelectric coefficient, resistivity, and dielectric constant). While it is possible that new crystals with excellent properties for x-ray production will be discovered in the future, the maximum x-ray energy achievable with the best crystals currently available on the market ($LiTaO_3$ and $LiNbO_3$) is slightly more than 200 keV.

4.2 Early Experiments

4.2.1 Single Crystal Experiments

4.2.1.1 Experimental Setup

To prevent a masking charge from the atmosphere from masking the change in polarization of a pyroelectric crystal during a temperature change, it is necessary to perform all experiments under vacuum. These experiments were performed in a cylindrical vacuum chamber, 40 cm long and with an inner diameter of 7 cm. The chamber was made of stainless steel. The chamber was equipped with quick-flange (ISO LF and KF) flanges, which were used to mate the chamber to the instrument feed-throughs, vacuum pump, vacuum gauges, and so on.

Two pumps were used to achieve vacuum. The high-vacuum pump was a Key High Vacuum Products DFP-3000 high vacuum diffusion pump, with a nominal maximum pumping capacity of 285 L / s at high vacuum. The backing pump for the DFP-3000

was a Welch Duo-Seal rotary vane mechanical pump. This pump was also used as the sole pump for some low-vacuum experiments, and was capable of pumping the vacuum chamber down to 29 mTorr without the assistance of the diffusion pump. With both pumps in operation, the minimum system pressure was 0.3 mTorr.

Two pressure gauges were used. The low pressure gauge was a Pirani gauge, which measured pressure from 1 mTorr to atmospheric pressure. The high pressure gauge was a glass-tubulated Bayard-Alpert gauge, and was used for monitoring pressure below 1 mTorr. Both gauges were operated with a Stanford Research Systems model IGC100 ion gauge controller. A detailed description of the vacuum system, along with photographs of the vacuum chamber and pumps, is given in Appendix II.

An Amptek XR-100T-CZT cadmium zinc telluride (CZT) semiconductor diode detector was placed inside the vacuum chamber. An electrical feed-through was used to power the detector and carry its signals to the amplifier on the outside of the chamber. Spectra were collected using an Aptec EAGLE / Classic MCA.

In the first generation of x-ray production experiments[45] presented in Chapter 4, a lithium tantalate crystal was mounted to a thermoelectric heater, with the z^+ surface of the crystal facing a copper target at a 45^o angle. The x-rays from the target would then be reflected toward the detector, which was also at a 45^o angle relative to the target. Figure 4.1 shows an illustration of this geometry. In some experiments, thermally-conductive vacuum (high vapor pressure) grease was used in an attempt to enhance thermal conductivity between the crystal and the heater. However, in addition to being messy, the grease can become polarized due to the electric field of the crystal, and can then crawl up the side of the crystal, thereby neutralizing the charge. Therefore, it is favorable to operate without grease, and either use (dry) silver paint or epoxy as a thermal interface, or to simply operate without an interface material.

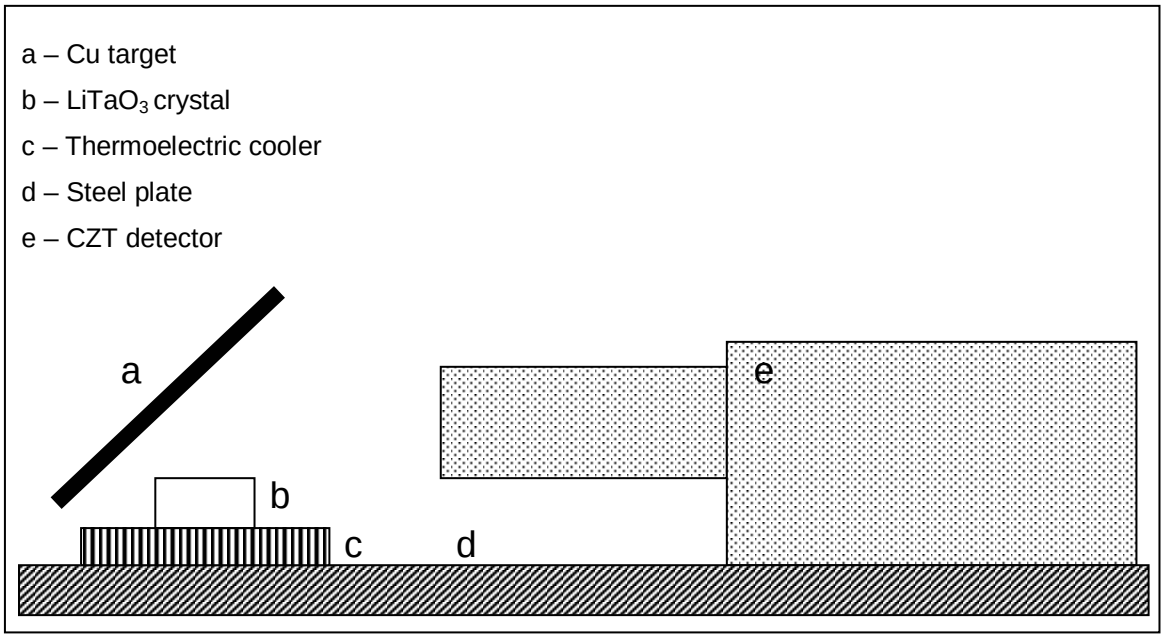

Figure 4.1 - Typical experimental geometry for a pyroelectric x-ray emission experiment.

Early experiments were conducted using rectangular crystals of the following sizes: 1 cm^2 area x 0.05 cm thick; 0.25 cm^2 area by 0.1 cm thick, 0.25 cm^2 area [0.5 cm x 0.5 cm] x 0.2 cm thick; 0.25 cm^2 area x 0.4 cm thick; 0.25 cm^2 area x 1.0 cm; and 0.25 cm^2 area x 2.0 cm thick.

X-rays were successfully generated using the electrons emitted by the pyroelectric crystals. The maximum x-ray energy achievable with the single-crystal system shown in Figure 4.1 was approximately 30 keV, which allowed fluorescence of the k-shell of Cu [8.05 keV, 8.90 keV] and the L-shell of Ta [8.15 keV, 9.34 keV].

4.2.1.2 Cyclical X-ray Emission

Since the acceleration potential changes as the crystal heats and cools, the x-ray emission is cyclical. For example: When the z+ surface of the crystal is facing the target, emission is observed from the target during heating. As the heating cycle progresses, the pyroelectric effect will cause an increase in the acceleration potential until the charge emitted as electrons balances with the charge generated due to the change in polarization. After this point, the acceleration potential will decrease as the excess charge is emitted more rapidly than it can be replenished. In the cooling phase, this process will occur again, with the crystal acting as the target. X-ray emission from the

crystal will increase in the beginning of the cooling phase, as the increase in internal polarization results in a growth in the acceleration potential. As the cooling slows down, and the charge is emitted faster than it is replenished, the x-ray yield will decrease. Therefore, the x-ray emission from the crystals follows the temperature cycle, as shown in Figure 4.2.

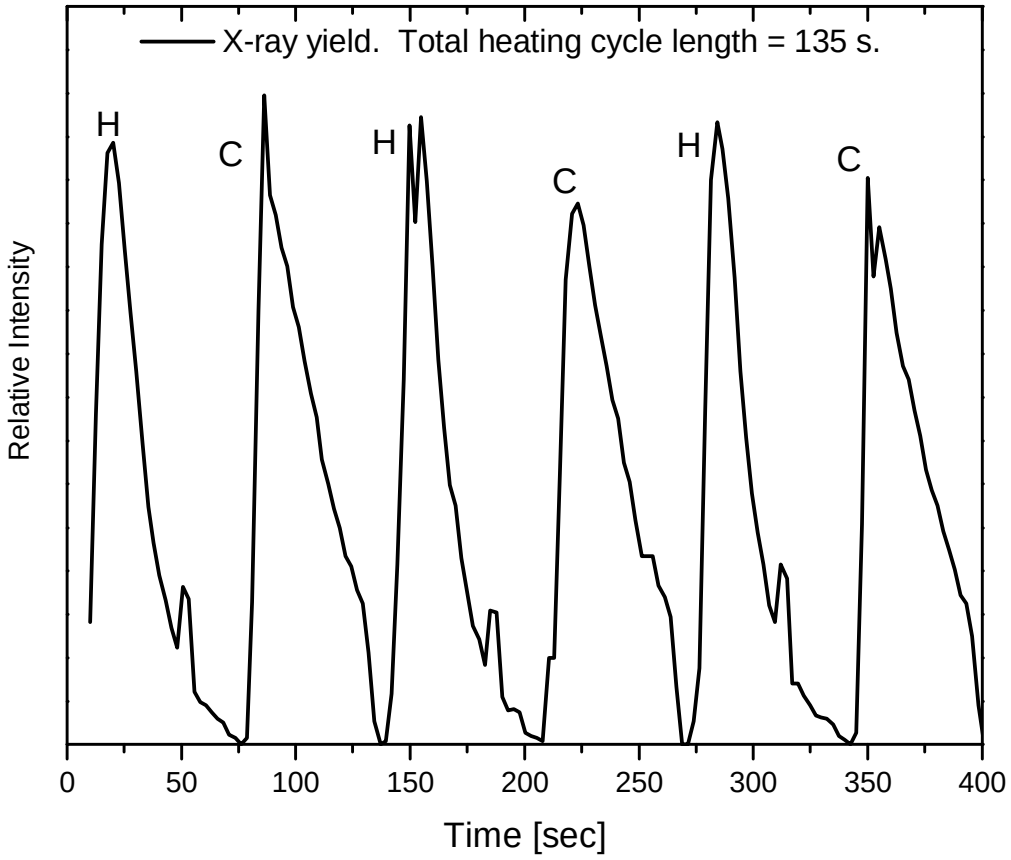

Figure 4.2 - The x-ray yield from a pyroelectric source is cyclical, as shown by this plot of the relative x-ray intensity detected from a 2 mm crystal heated and cooled at a 2 minute repetition rate. "H" designates a heating phase, and "C" designates a cooling phase.

There were several problems with the geometry used in Figure 4.1. The placement of the target at an angle to the crystal was ideal for x-ray detection, but it decreased the distance between the crystal and target (ground) due to the tight spatial limitations inside the vacuum chamber. Therefore, this geometry causes an increased rate of discharge versus a system in which the target is parallel to the crystal. Also, in early experiments, the rear face of the crystal was not typically grounded. This can also cause an increased probability of discharge, since the potential across and un-grounded crystal is much

greater than the potential across a grounded crystal. Since it is only the potential between the crystal and the x-ray target that matters for the maximum electron energy, there is no reason to float the rear face of the crystal. It was also discovered that, in a paired-crystal system, the crystals had to be fixed in place, otherwise they would stick together when charged. These, and other, problems were remedied as they were discovered.

4.2.1.3 X-ray Counts Versus Heating Cycle Length

It was observed that the total x-ray counts during heating remained roughly the same regardless of the heating rate, while the count rate scaled inverse to the heating rate. The reason for this effect is that the total charge produced by a pyroelectric crystal is given by:

$$Q = \gamma \cdot A \cdot \int \frac{dT}{dt} dt = \gamma \cdot A \cdot \Delta T \qquad (19)$$

and is therefore independent of the length of the heating or cooling phase. This is true as long as the crystal temperature change takes place over a long enough time for conduction of heat through the crystal to allow the heating or cooling of the exposed crystal surface. The temperature cycle must also be fast enough such that relaxation current and screening effects remain negligible.

4.2.2 Paired Crystal Experiments

One disadvantage of pyroelectric particle accelerators is that the maximum energy is governed by the physical properties of the crystal and the temperature gradient. However, the acceleration potential for the charged particles emitted by a pyroelectric accelerator can be doubled using a paired-crystal source, as shall be discussed below.

Pyroelectric crystals cannot simply be stacked like DC batteries to gain an increase in the available charge. If two identical crystals of with length *d* and a surface charge of ± *x* Coulombs are stacked end-to-end, the positive end of one crystal and the negative end of the other crystal will neutralize each other, resulting in the equivalent of a single crystal with length *2d* and a surface charge of ± *x* Coulombs. Therefore, there will be an advantage gained by lowering the system capacitance, and this will give some advantage

over a single crystal of length *d*, but not over a single crystal of length *2d*. If, in a different geometry, electrons emitted by one crystal are accelerated toward a grid mounted to the positive side of a second crystal, they will gain energy corresponding to the potential of the grid, but once through the grid, they will decelerate, negating the advantage of the grid.

However, the most effective means of increasing the energy of the emitted radiation in a paired-crystal system is also among the simplest. By using the negative surface of one crystal as the cathode, and the positive side of a second crystal as the target, the electron, ion, and x-ray energy can be doubled. Since lithium tantalate contains tantalum, which is a very efficient x-ray target, this technique causes the production of copious quantities of x-rays. As Figure 4.4 shows, the incident electrons mostly interact with the tantalum, with little loss due to interaction with the oxygen and lithium in the crystals. Therefore, lithium tantalate crystals compare favorably even to tantalum metal targets in terms of x-ray production. (Figure 4.5 shows that the tantalum is also responsible for almost all of the photon absorption in lithium tantalate crystals).

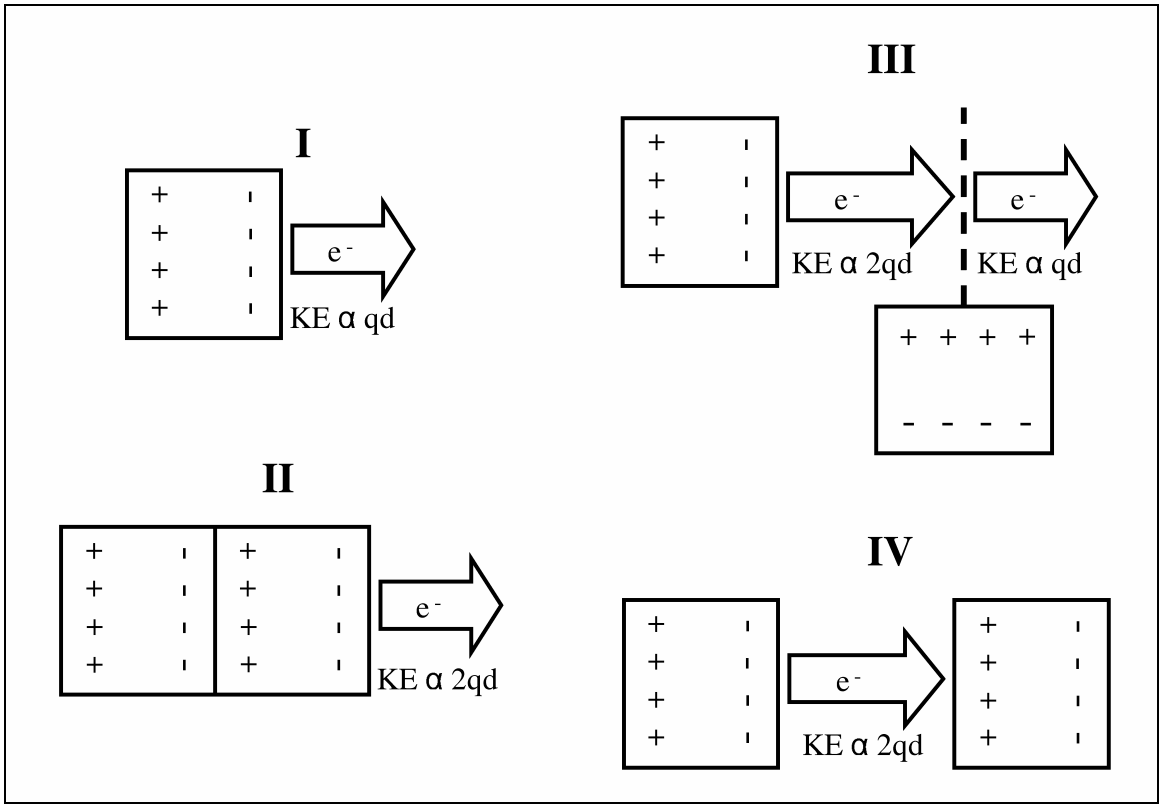

Figure 4.3 - Illustration of electron emission from: I - Single crystal; II - Two crystals stacked end-to-end; III - Two crystals, with grid mounted to second crystal; IV - Two crystals, with second crystal acting as a target for emission from the first crystal. The kinetic energy of the emitted electrons *KE* is proportional to the thickness of a single crystal *d* and the charge on the crystal surface *q*. In geometry II, the energy is doubled by decreasing the capacitance. In geometry IV, it is doubled by superimposing the electric field from two crystals.

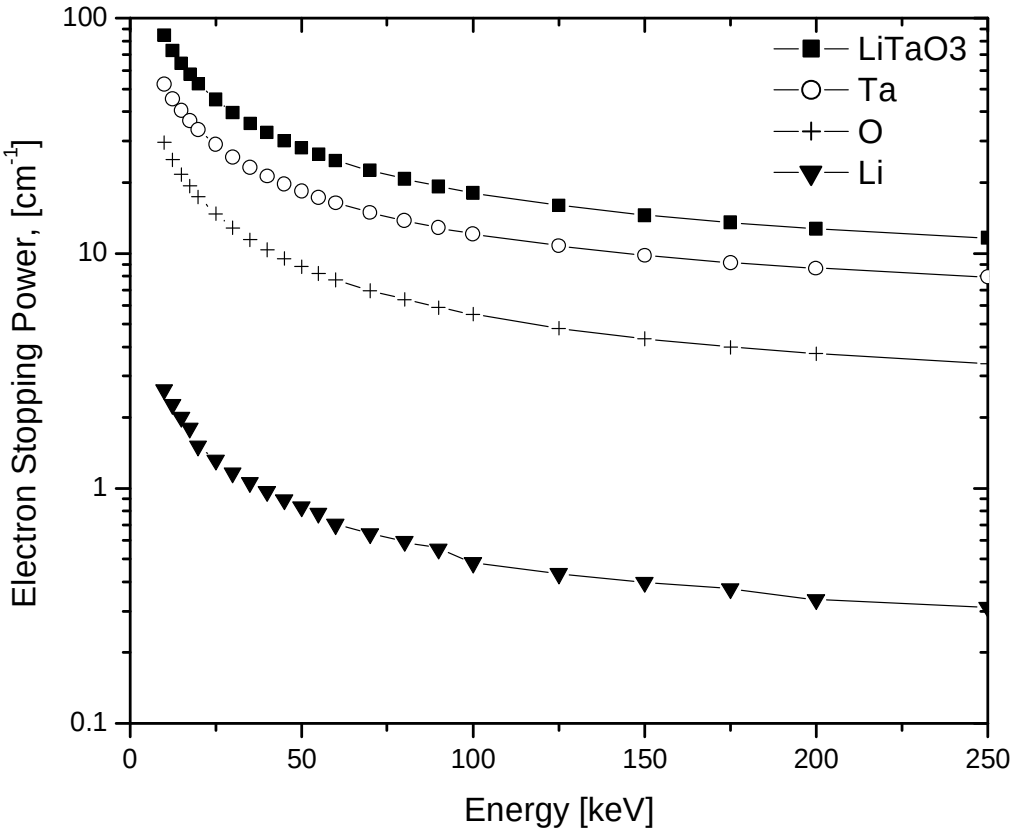

Figure 4.4 - Electron stopping power of lithium tantalate plotted against the contribution of each of the constituent atoms. Data taken from the NIST E-Star database[46].

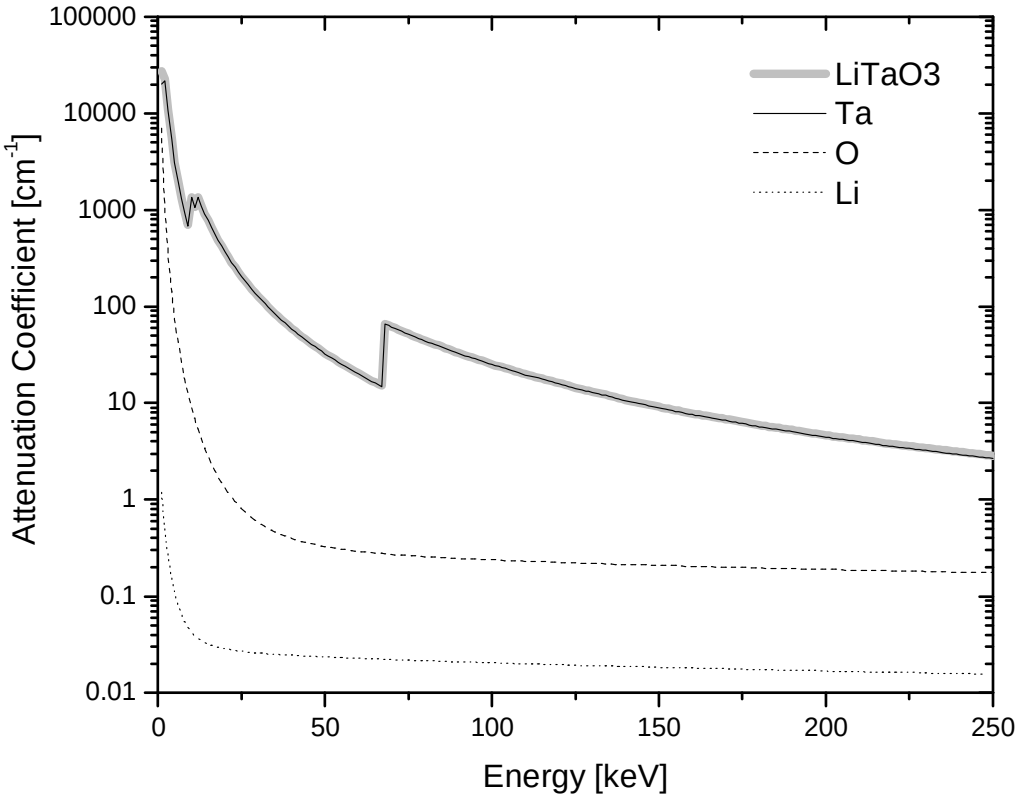

Figure 4.5 - Plot showing the photon attenuation coefficient of lithium tantalate versus each of its constituent atoms. Notice that virtually all of the photon attenuation is due to the presence of tantalum. Photon attenuation data were taken from XMuDat[47].

It will be shown later that a deuterated target can be deposited onto the surface of one of the crystals in neutron production experiments without substantially decreasing the system potential, thereby enabling the paired-crystal technique to be used for producing pyroelectric fusion sources in addition to pyroelectric x-ray sources. Figure 4.3 shows an illustration of the different paired crystal geometries discussed above.

4.3Maximum X-Ray Energy and Parasitic Capacitance

Gil Rosenman showed that the acceleration potential between a pyroelectric crystal and its target can be modeled as a system of two capacitors[29].

Typically, one would find the potential across a charged capacitor by applying the equation

$$V = Q/C \tag{20}$$

The charge produced by the pyroelectric effect can now be substituted for Q:

$$V = \gamma \cdot A \cdot \Delta T / C \tag{21}$$

Finally, the sum of the crystal's capacitance and the capacitance between the crystal and target must be substituted for *C*. The crystal and target are assumed to be of equal area (or semi-infinite). One can then find the acceleration potential:

$$V = \frac{\gamma \cdot A \cdot \Delta T}{\varepsilon_o \varepsilon_{cr} \dfrac{A}{d_{cr}} + \varepsilon_o \dfrac{A}{d_{gap}}} \tag{22}$$

Since the relative permittivity of lithium tantalate in the z-direction[28] is 46, one would expect that the distance between the crystal and target will have a minor effect on the acceleration potential compared to the effect of the crystal thickness. Figure 4.6 shows a plot of the potential change in a pyroelectric accelerator as either the size of the crystal or the size of the gap is changed.

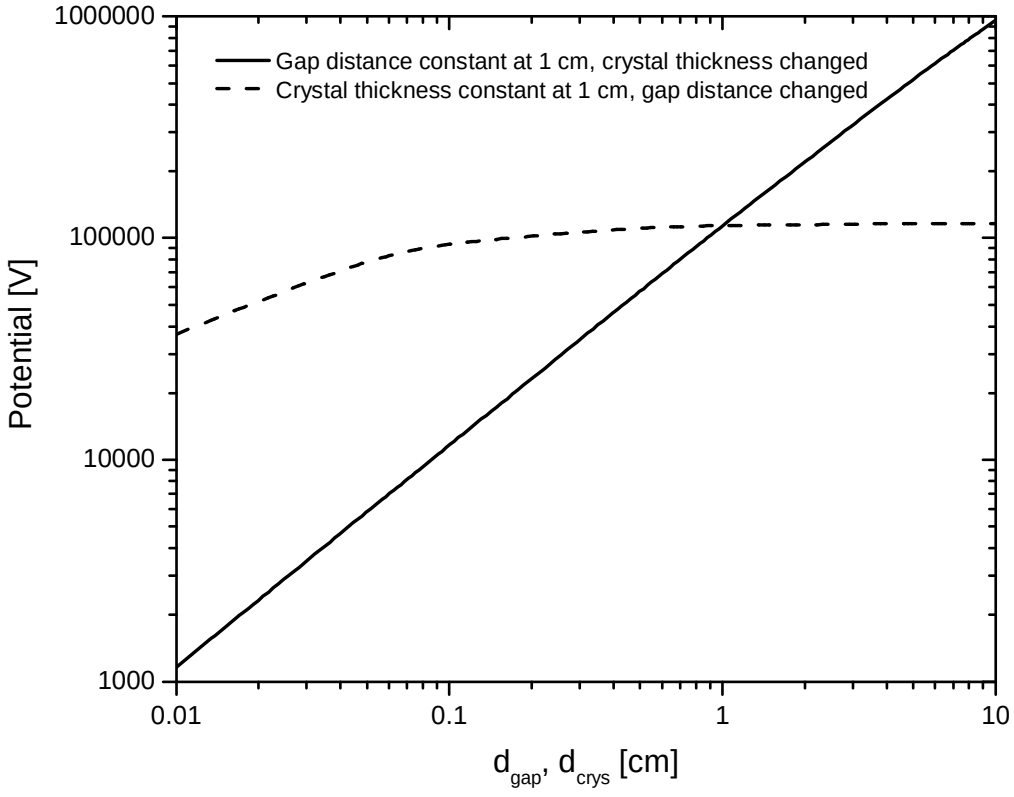

Figure 4.6 - Plot showing the effect of fixing the crystal thickness at 1 cm and varying the gap distance (dashed line) versus fixing the gap distance at 1 cm and varying the crystal thickness (solid line). A $LiTaO_3$ crystal with $\Delta T = 25^oC$ is assumed.

It was found that, for crystals less than 10 mm thick, the maximum x-ray energy increased with crystal thickness in an almost linear manner, as expected from Rosenman's model, as can be seen in Figure 4.7.

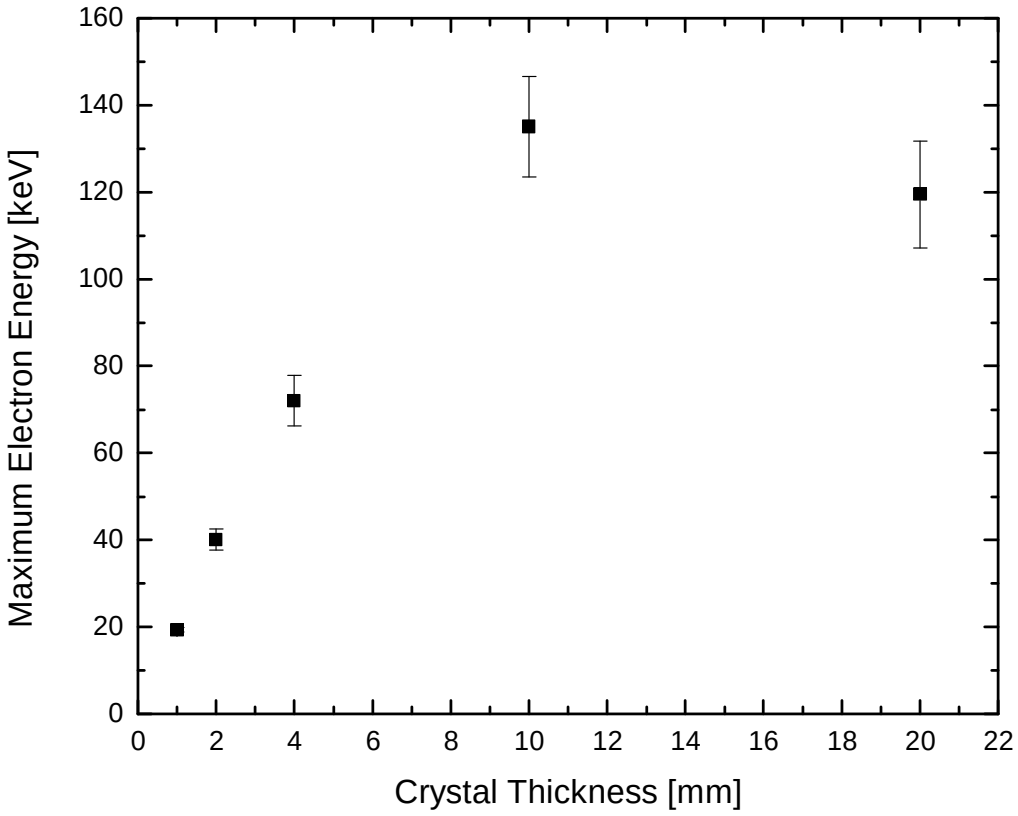

Figure 4.7 - The maximum observed x-ray energy from a pyroelectric source was found to be a linear function of crystal thicknesss for small values of thickness. However, increasing the crystal thickness beyond 1 cm did not improve the electron energy.

At crystal thicknesses of greater than 10 mm, the Rosenman model predicting the linear relationship between the crystal thickness and the maximum x-ray energy seems to break down. In fact, it was observed that the average x-ray energy from 20 mm thick $LiTaO_3$ crystals was less than the average energy from 10 mm thick $LiTaO_3$ crystals. However, Rosenman's model assumes that the only capacitors to be taken into account are the crystal and the gap between the crystal and the target. If a third capacitance is added to account for parasitic capacitance due to the chamber, wires, and so forth, the model agrees much more closely with experiment, as shown in Figure 4.8. In this figure,

the dashed line represents the charged capacitor model without a parasitic capacitance, while the solid line represents the model with a 0.8 pF parasitic capacitance, given by:

$$V = \frac{\gamma \cdot A \cdot \Delta T}{\varepsilon_o \varepsilon_{cr} \frac{A}{d_{cr}} + \varepsilon_o \frac{A}{d_{gap}} + 0.8pF} \tag{23}$$

A pyroelectric coefficient of 190 μC / m^2 °K and temperature change of ΔT = 50°K were assumed, and the crystal area was taken to be 0.25 cm^2, since a 5 mm x 5 mm crystal was used to obtain the experimental data. (The capacitance of a 5 mm x 5 mm x 10 mm thick cylindrical $LiTaO_3$ crystal is 1 pF). However, in order to explain the decrease in energy when crystals of above 1 cm thickness were used, one must return to the problems with thermal conductivity discussed in Section 2.3.

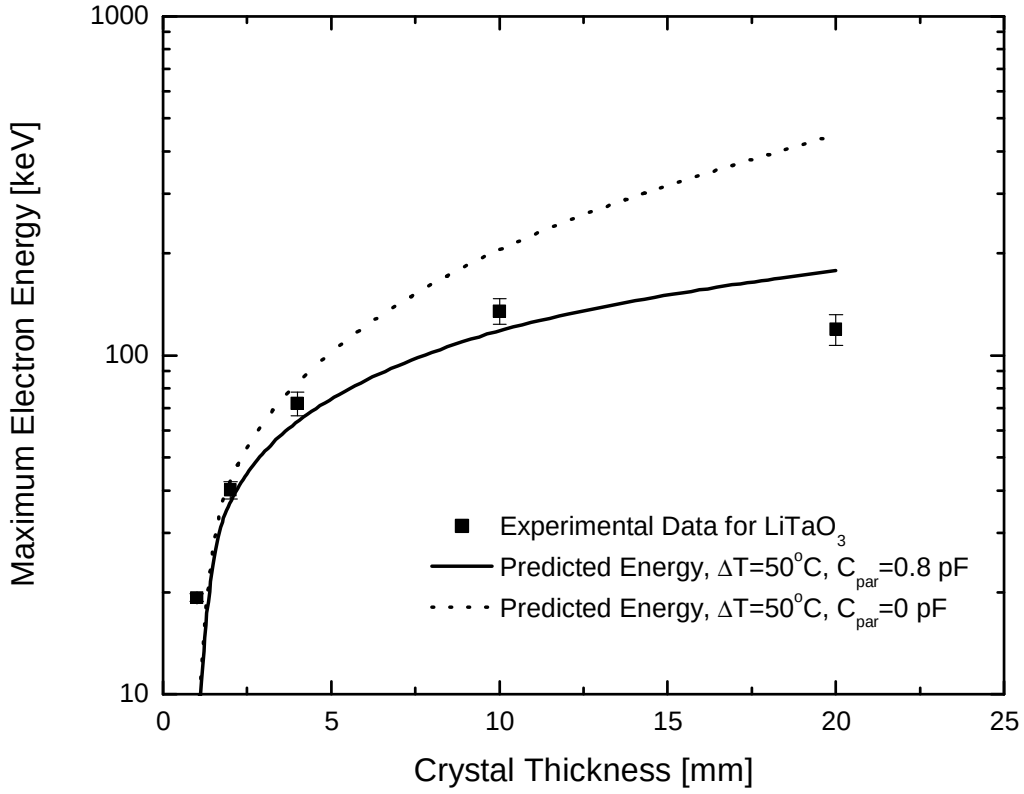

Figure 4.8 - The effect of parasitic capacitance on the relationship between accelerating potential and crystal thickness for a 5 mm x 5 mm rectangular crystal.

4.4 Paired-Crystal Experiments

Due to the principle of superposition, the electric fields from two polarized pyroelectric crystals can be added together if the fields are aligned to provide acceleration in the same direction. If one crystal is polarized such that it repels electrons with a potential of -V, and another crystal attracts electrons with a potential of +V, then the net acceleration potential between the two crystals becomes 2V. Therefore, an accelerator consisting of two simultaneously heated or cooled pyroelectric crystals in opposite polarity was proposed as a method of creating higher-energy x-rays than could be produced with a conventional single-crystal source. (It is fortunate that one of the best pyroelectric materials for x-ray generation, $LiTaO_3$, contains tantalum, which makes it an excellent x-ray target.)

Figure 4.9 shows the geometry of the first experiment designed to test the effect of using paired crystals on the maximum x-ray energy. The x-ray detector was placed perpendicular to the heater, such that it had line of sight to the surfaces of both crystals. It was 7 - 8 cm from the surface of the crystals. The x-ray detector was inside the vacuum chamber, with its signal and power transmitted through the chamber via a 15-pin electrical feed-through. The vacuum chamber was pumped by the mechanical roughing pump. For these experiments, the crystals were heated from room temperature to 90^{o}C over 200 seconds, held at 90^{o}C for 50 seconds, and then cooled back to 20^{o}C. The pressure was 48-53 mTorr. The crystals were both 5 mm x 5 mm x 4 mm $LiTaO_3$ crystals, with the rear surfaces of the crystals both heated and grounded by a copper heating bracket. The bracket was bent to allow x-rays from the crystal surface to be easily measured by the detector. The crystals were attached to the bracket with thermally conductive grease, and were held apart from each other by a triangular piece of circuit board. They were held aloft by pieces of circuit board cut to the proper height with through-holes cut out to hold the crystals. In order to take an x-ray spectrum with only one crystal accelerating the electrons, the target crystal was separated from the copper bracket by a piece of circuit board, which was intended to prevent the bracket from heating the crystal.

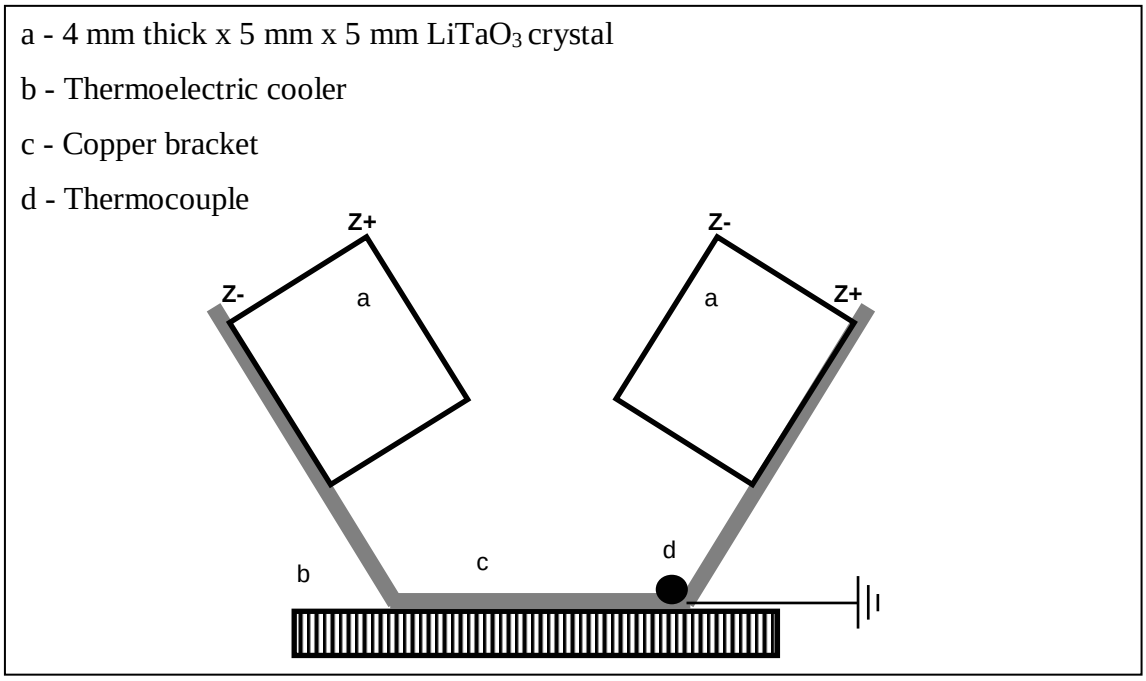

Figure 4.9 - Illustration of an early paired-crystal experiment in which an angled bracket was used to allow improved x-ray measurement.

This experiment yielded the results shown in Figure 4.10. There was a slight improvement when both crystals were heated, but not the doubling of x-ray energy that was expected. The apparent L_α peak shift shown in the figure cannot be due to a shift in detector gain, since the rest of the peaks did not shift. Instead, it may be due to a shift in the yield of tantalum $L_{\alpha 1}$ photons relative to $L_{\alpha 2}$ photons. Since the presence of the spacer in the single-crystal test caused the crystal to be in a slightly different position than it was for the paired-crystal test, the peak shift may also be due to a change in the contribution of copper L-shell x-rays in the peak.

It was thought that the presence of the circuit board between the bracket and the dormant crystal in the single-crystal tests may have caused some unintended heating and cooling of the crystal. It was also thought that the angling of the crystals may have limited the maximum potential when both crystals were cycled by creating a "hot spot" at the closest point. The triangular spacer between the crystals may have had a similar effect, by creating a path for current to leak between the crystals. These considerations were taken into account for the next paired-crystal experiment.

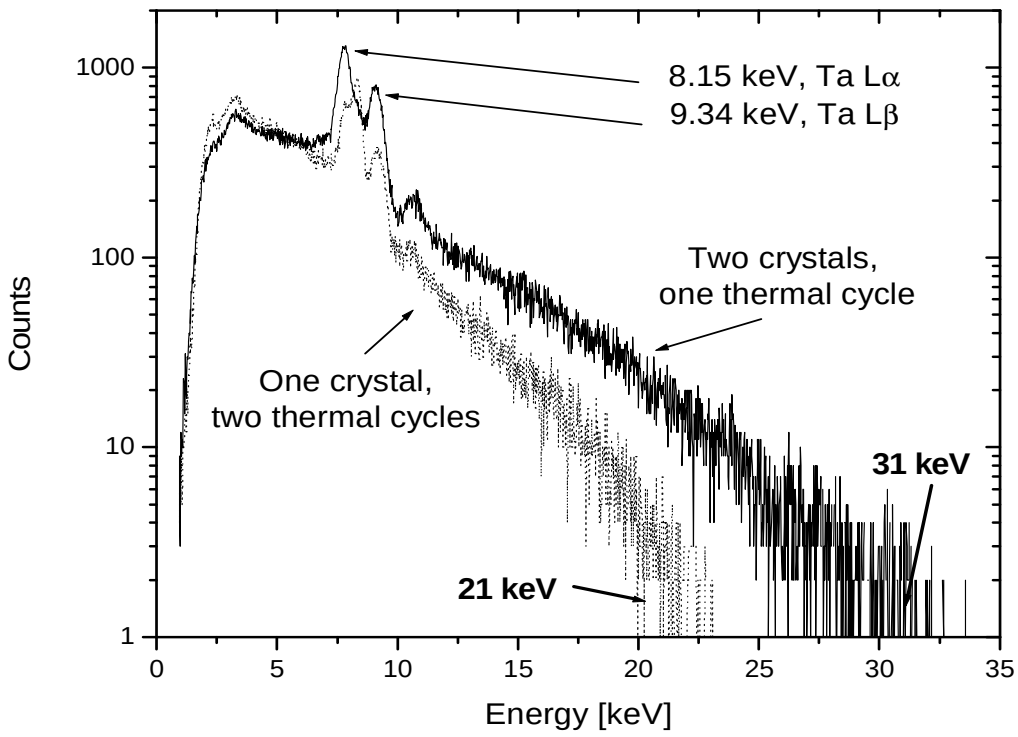

Figure 4.10 - Results from paired-crystal experiment conducted with an angled heating bracket. The energy was increased by using a second crystal, but it was not doubled as expected.

Figure 4.11 shows the experimental geometry used in the next iteration of paired-crystal experiments. Two 4 mm (z) x 5 mm x 5 mm rectangular $LiTaO_3$ crystals were attached to a copper bracket using thermally-conductive grease. The thermocouple wire was bent into a spring to keep it in contact with the copper heating bracket. Once again, the crystals were supported using brackets made out of perforated circuit board. The copper bracket was grounded, and was attached to a thermoelectric cooler using thermally-conductive grease. For the one-crystal system data, the crystal was removed from the heating bracket by ~1 mm, and was held aloft only by the bracket made from perforated board. In this way, the heating cycle for the emitting crystal remained the same as for the two-crystal tests, while leaving the target crystal dormant. Since there was no spacer between the crystal and the bracket, the crystal could not be heated via conduction as in previous experiments. Also, there was no spacer between the crystals, and there was no close point to create a "hot spot," such that most of the problems with the geometry shown in Figure 4.9 were eliminated.

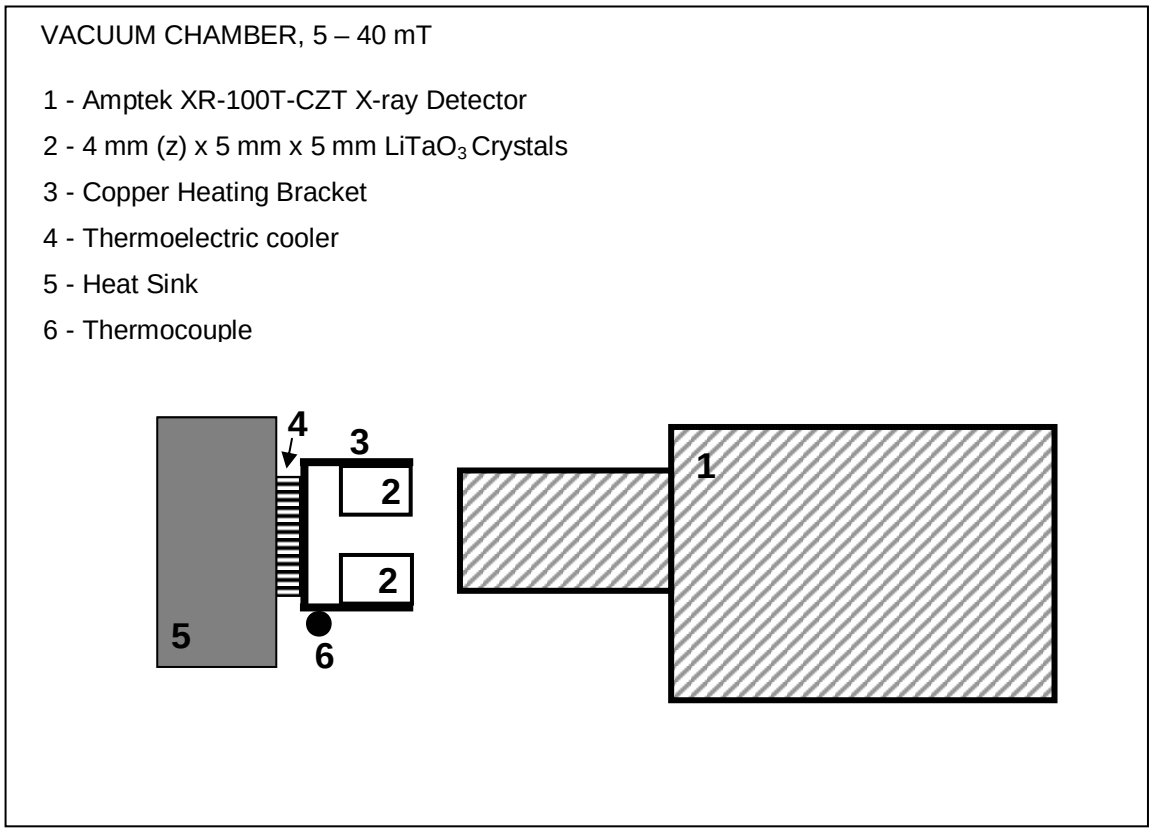

Figure 4.11 - Experimental geometry for early paired-crystal x-ray generation experiments.

Figure 4.12 shows a comparison of the x-ray spectra from the one- and two-crystal system. As the figure shows, the energy from the paired crystal system was roughly double that of the single-crystal system. Additionally, the x-ray yield doubled, due to the increase in bremsstrahlung efficiency resulting from the higher incident electron energy. The doubling of the bremsstrahlung yield is not coincidental. The total bremsstrahlung yield from an incident electron of energy E_o as it slows down in a target is given by[48]:

$$Y(E_o) = \frac{13}{16} kZE_o \qquad (24)$$

where Z is the atomic number and *k* is a constant. Therefore, the doubling of the electric field strength by pairing pyroelectric crystals should double the energy of the emitted electrons, and therefore double the bremsstrahlung yield. The pressure for these experiments was typically 40 mTorr, with the same temperature profile (room temperature to 90°C) as the experiments with the angled bracket.

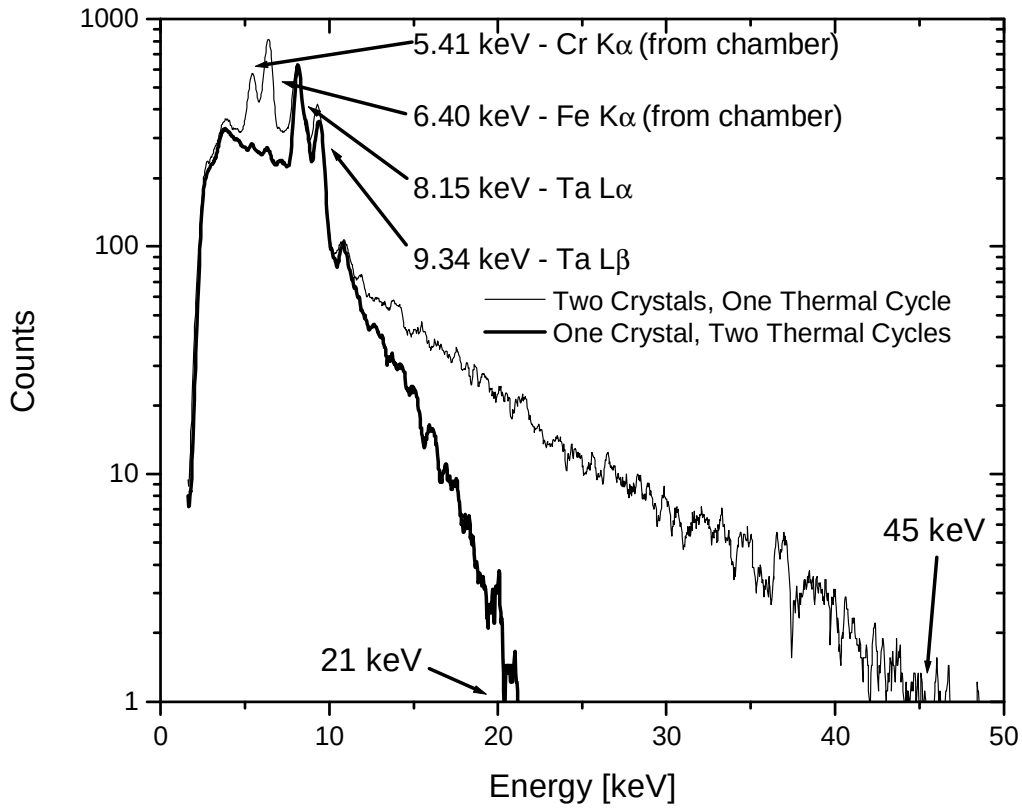

Figure 4.12 - X-ray spectra from a single- vs. paired-crystal system, using rectangular 4 mm x 5 mm x 5 mm $LiTaO_3$ crystals in an early experiment.

For the third iteration of paired crystal x-ray production experiments, several improvements to the x-ray production experiments greatly increased the yield and energy from both the single- and paired-crystal systems. First, the crystals were heated with resistors instead of a heating bracket, with electrical ground provided by an electrode connected to the back of the crystal. (Non-conductive epoxy was used to attach the crystal and electrode to the heating resistor). The leads of the heating resistor were screwed into a terminal strip on an aluminum block, and the crystals were positioned by bending the leads. All thermally-conductive grease was eliminated from the vacuum system, as were the brackets fabricated from perforated board which held the crystals in place in previous experiments. The perforated board brackets were removed because they were thought to increase the parasitic capacitance of the system, and provide an easier path to ground for sparks originating at the crystal surface. Finally, the 4 mm thick crystals were replaced with 10 mm thick crystals to decrease the system capaci-

tance and thereby increase the maximum potential. The crystals were heated from room temperature to 150°C over six minutes and were then allowed to cool naturally back to room temperature. The chamber pressure for these experiments was typically 0.6 - 1.0 mTorr.

The increase in x-ray energy achieved through these modifications allowed the x-ray detector to be moved to the outside of the vacuum chamber. At this time, the x-ray detector was also changed from the Amptek XR-100T-CZT to an Amptek XR-100T-CdTe, although as Figure 4.13 shows, the CZT detector has a slightly higher efficiency at high energy (E > 100 keV).

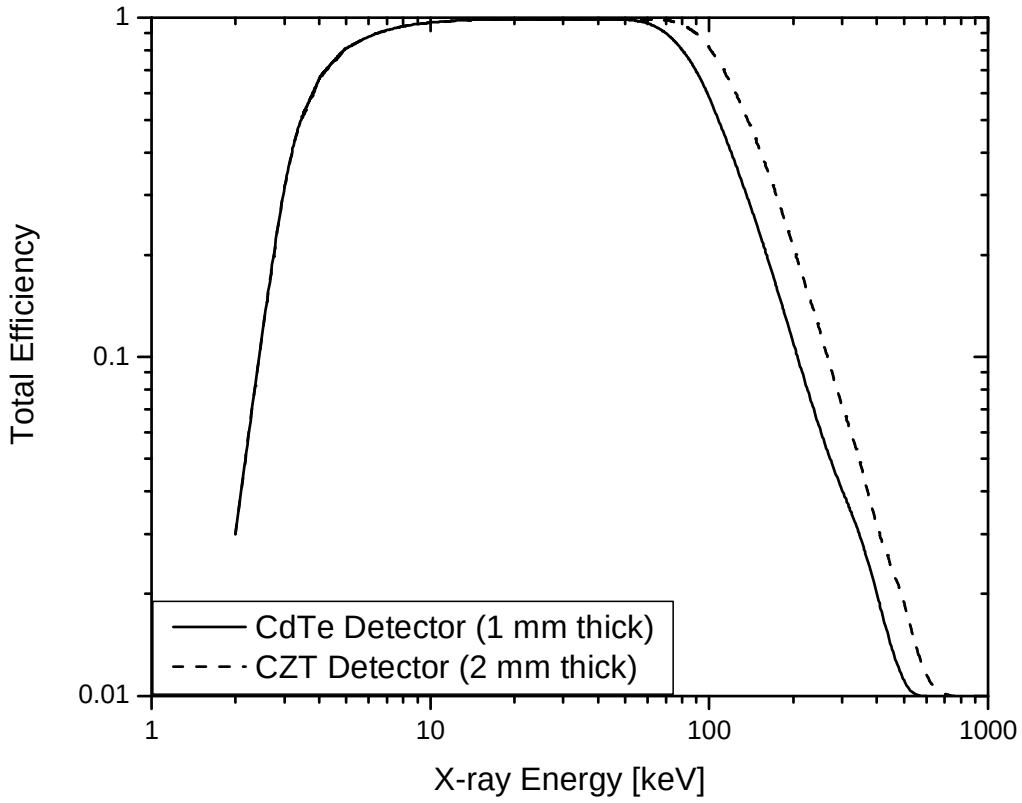

Figure 4.13 - Efficiency of Amptek x-ray detectors used in paired-crystal experiments[49].

These changes had an immediate and positive effect on the x-ray yield and energy from the single- and paired-crystal systems. The maximum energy from a single crystal source increased to above 100 keV, and that of a paired-crystal source increased to more than 200 keV. Figure 4.14 shows a comparison of a paired-crystal source with a single-crystal source using the new experimental geometry. In this experiment, the paired

crystal x-ray spectrum did not reach 200 keV, but the maximum x-ray energy was still much higher than in the single-crystal experiment. For the single-crystal spectra, the power to the heating resistor attached to the target crystal was cut at a switch outside of the vacuum chamber. In this way, the experimental parameters were kept the same, except that one crystal was not heated or cooled. In a separate experiment, the maximum energy from a paired-crystal source was shown to be about 200 keV. (See Figure 4.15). It is of note that the published detector efficiency[49] at 200 keV is 11%, and at 250 keV it is only 6%. Therefore, it is possible that the endpoint energy would have appeared higher with improved detection efficiency at high energy. Nevertheless, the plot shown in Figure 4.15 is the highest-energy spectrum ever published from a pyroelectric x-ray source, and serves as a highlight to the advantages of paired-crystal technology[50].

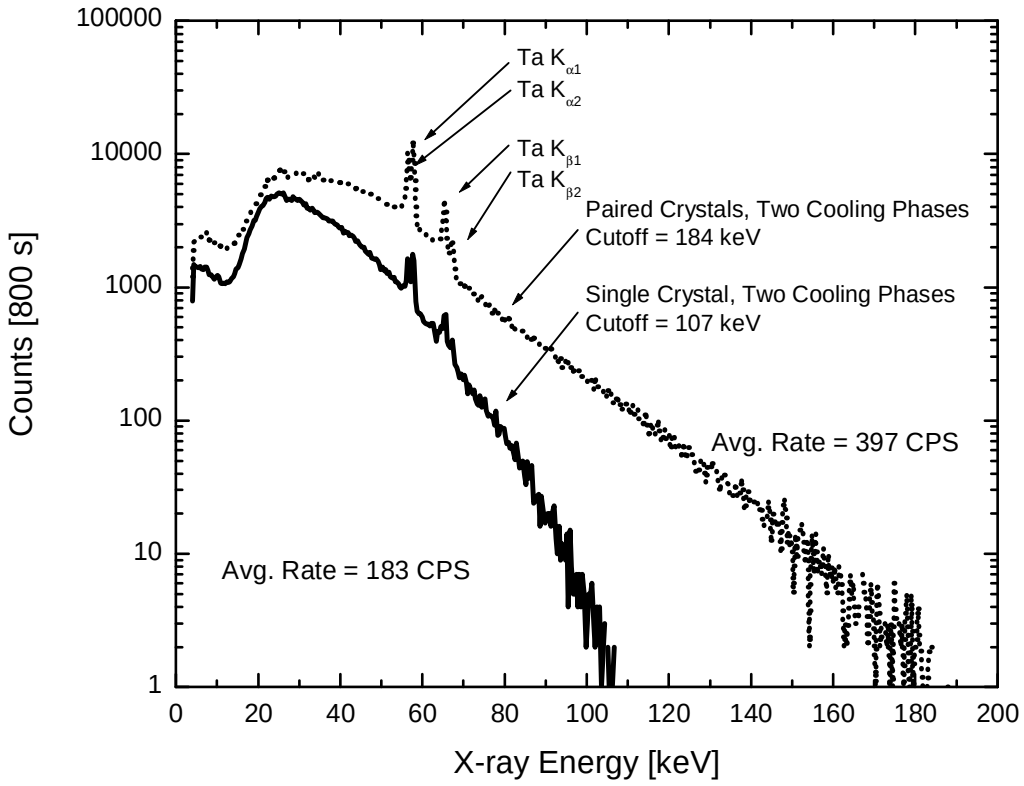

Figure 4.14 - X-ray spectra from single- and paired-crystal sources, using heating resistors and 10 mm (z) x 5 mm x 5 mm rectangular $LiTaO_3$ crystals. Two summed cooling phases for each system are shown.

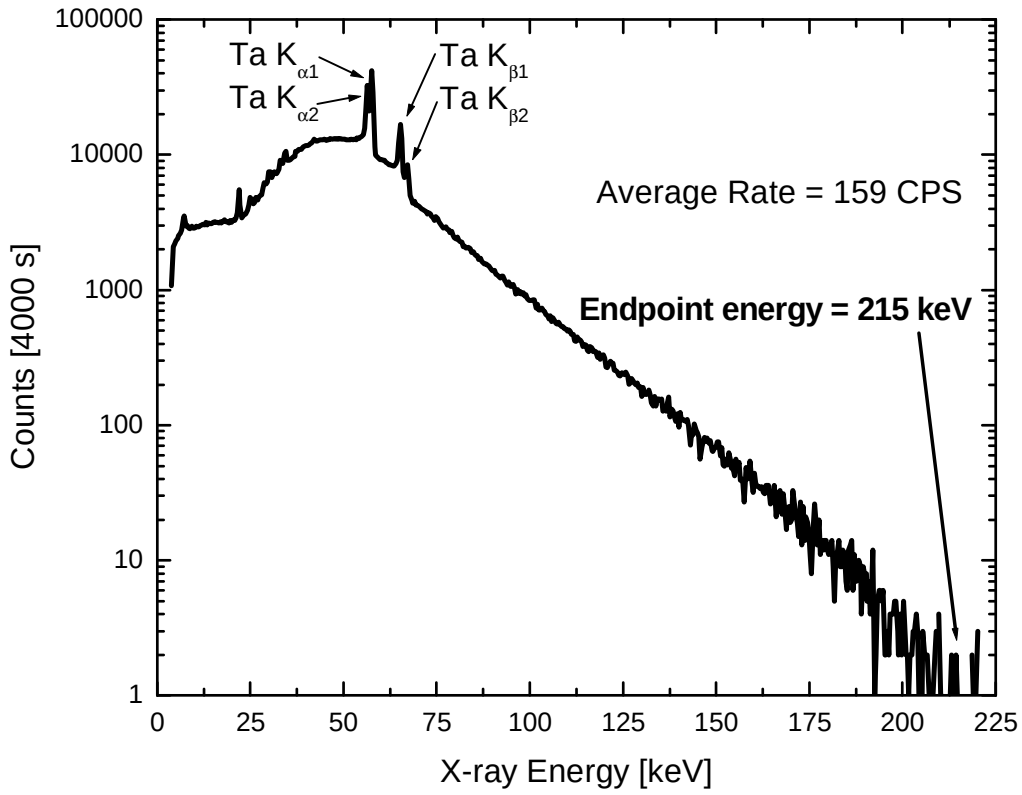

Figure 4.15 - Sum of five spectra taken during cooling from a paired-crystal pyroelectric source.

4.5 X-ray Fluorescence

One objective in the development of pyroelectric crystal x-ray generators was to demonstrate and extend the usefulness of pyroelectric sources for x-ray fluorescence [XRF]. XRF occurs when an electron bound to a target atom is excited by incident x-ray or electron radiation. The incident radiation causes the orbital electron to jump to a higher energy level. When an outer electron jumps down in energy to fill the empty shell, radiation is emitted in the form of x-rays. Since every element has a characteristic set of electron energy levels, the x-rays emitted as the electrons move between levels is specific to the target atom. Therefore, XRF can be used to determine the relative abundances of different elements in a mix of metals, such as steel or bronze. Figure 4.16 shows an illustration of x-ray fluorescence. A competing phenomenon, Auger electron emission, takes place when the excitation energy an atom receives from incident radiation is transferred to an orbital electron, which is then ejected from the atom, leaving a vacancy[66]. Characteristic x-ray energy is emitted when the vacancy is filled.

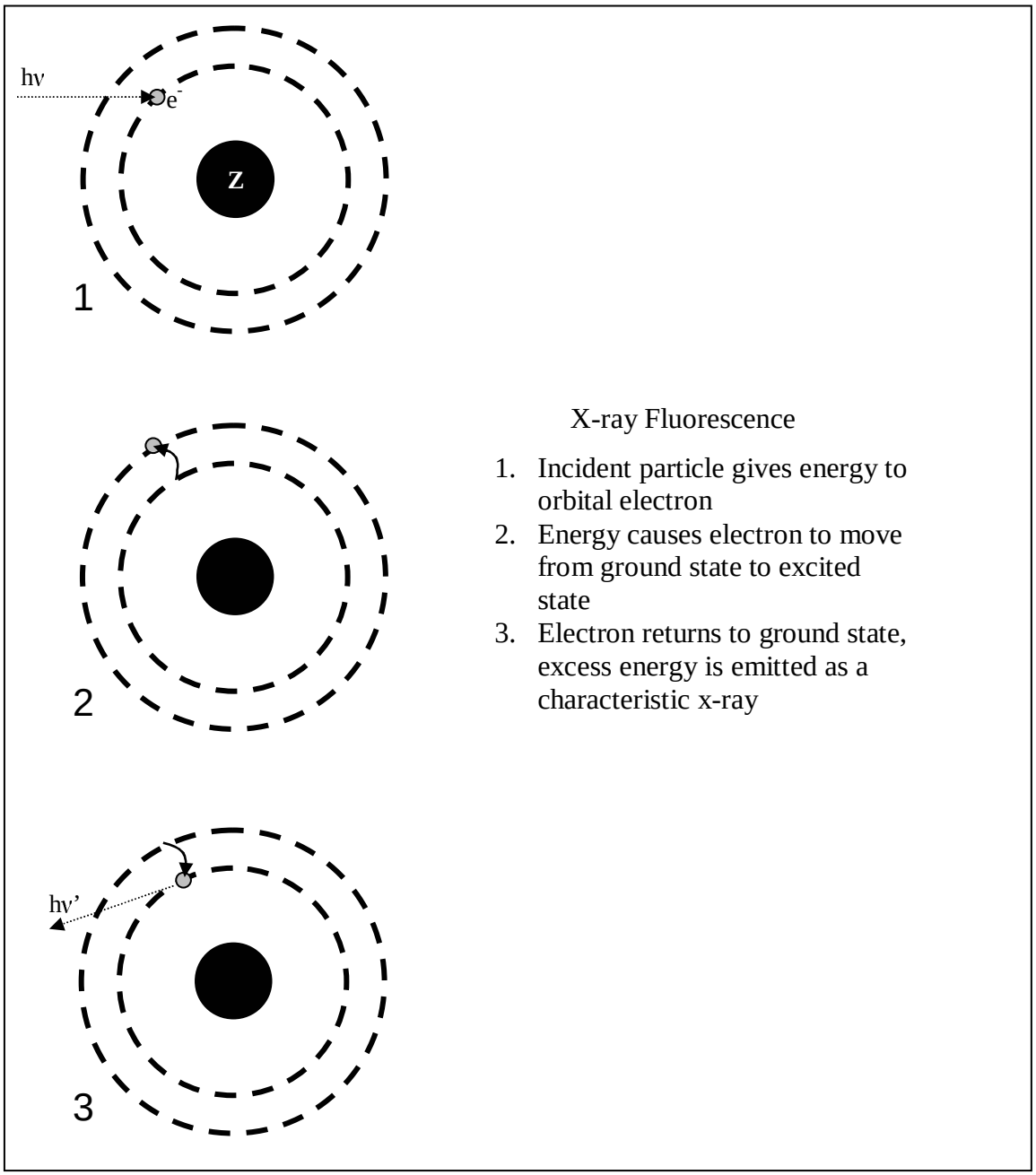

Figure 4.16 - Illustration of x-ray fluorescence

Figure 4.17 depicts the experimental setup for the fluorescence of thorium. Thorium was selected as a target because of its high atomic number (Z = 90). Since the minimum energy for the fluorescence of a given electron orbital increases with atomic number, the ability of pyroelectric crystals to fluoresce thorium would guarantee their ability to fluoresce any element with a lower atomic number. A 0.18 mm thick thorium target was

placed outside of the 0.5 cm glass window on a vacuum chamber flange. Two 10 mm x 5 mm x 5 mm $LiTaO_3$ crystals were placed 1 cm apart, with the center of the crystals being 2 cm from the thorium foil. The CdTe detector was placed behind the foil to observe transmitted x-rays. In order to properly account for the natural radioactivity of thorium, a background measurement was performed prior to the experiment. The background was then subtracted from the gross counts to yield the net counts due to fluorescence from the pyroelectric source.

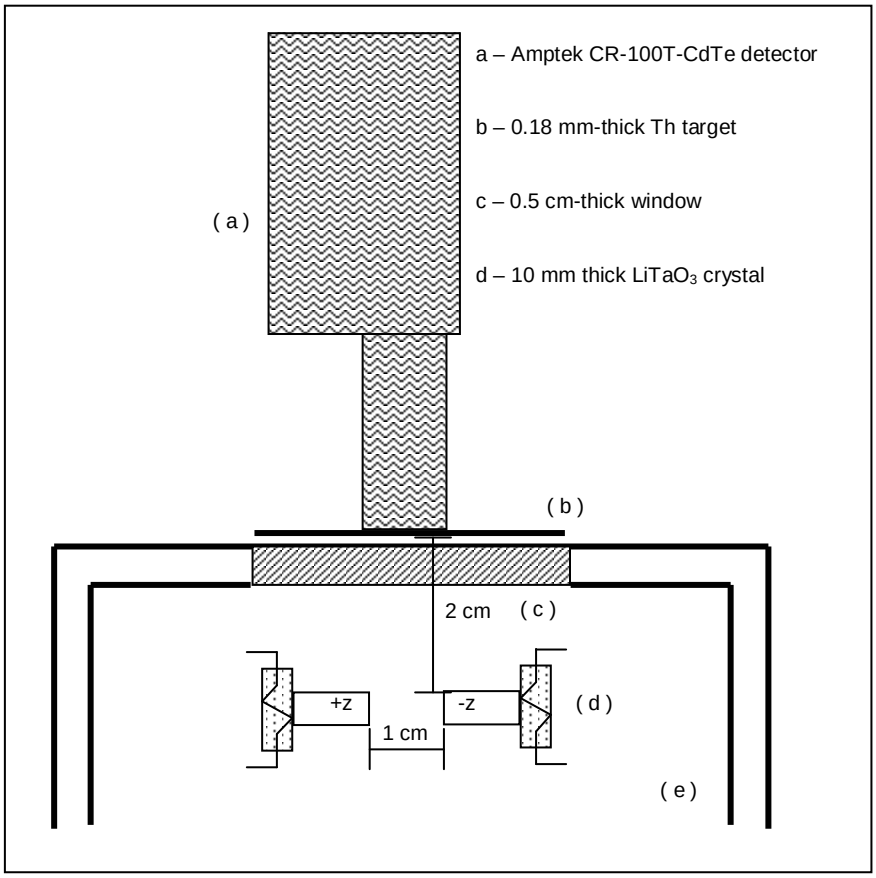

Figure 4.17 - Experimental setup for thorium fluorescence.

Figure 4.18 shows the gross counts from the pyroelectric XRF experiment, as well as the background from the thorium target for the same collection time (1800 seconds). The tantalum characteristic x-ray lines and bremsstrahlung continuum are from the tantalum in the target crystal, and were transmitted through the thin thorium target to the detector.

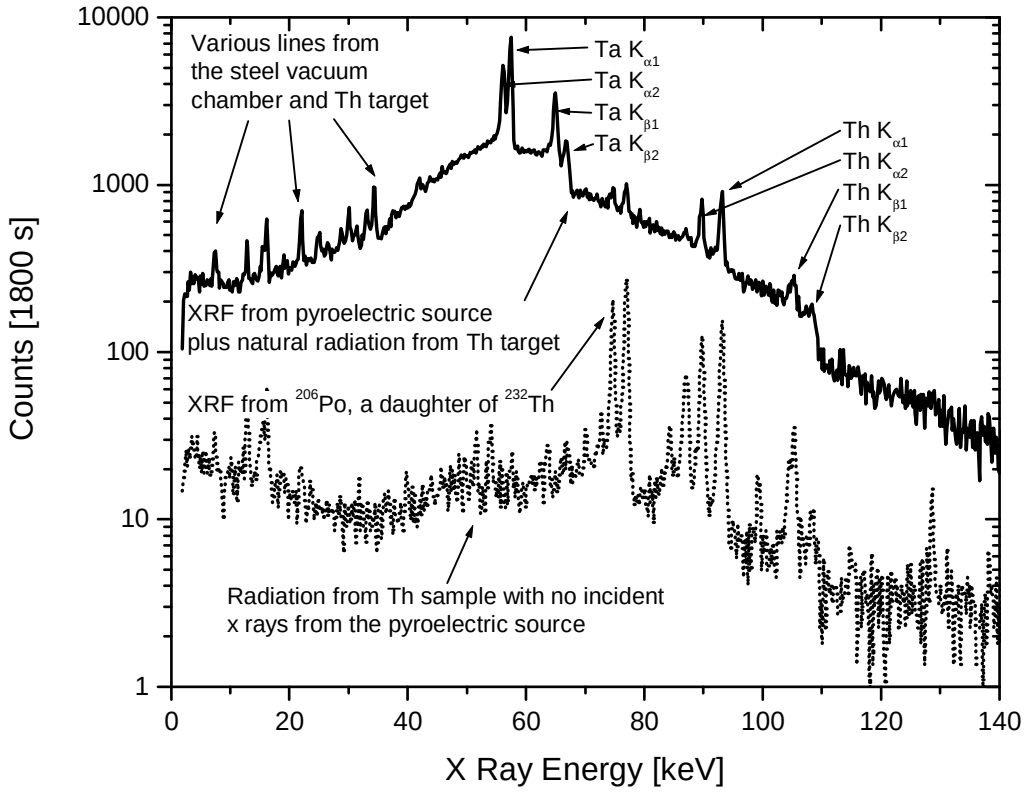

Figure 4.18 - Thorium fluorescence spectrum due to pyroelectric source (gross counts) and background measurement.

Figure 4.18 shows the net counts from x-ray fluorescence, after subtracting the background due to the natural radioactivity of thorium and its daughter isotopes. As Figure 4.18 shows, all four K-shell x-ray lines of thorium can be seen. This suggests that a paired-crystal pyroelectric source can be used to fluoresce any metal with $Z \leq 90$.

Therefore, pyroelectric x-ray generators are useful tools for materials analysis. Due to the low power requirements, the construction of a portable 200 keV pyroelectric x-ray source would be a trivial matter. Coupled with a portable MCA and laptop, this would provide a field researcher with a powerful tool for analyzing the elemental composition of metals in bridges, minerals, airplanes, and so forth.

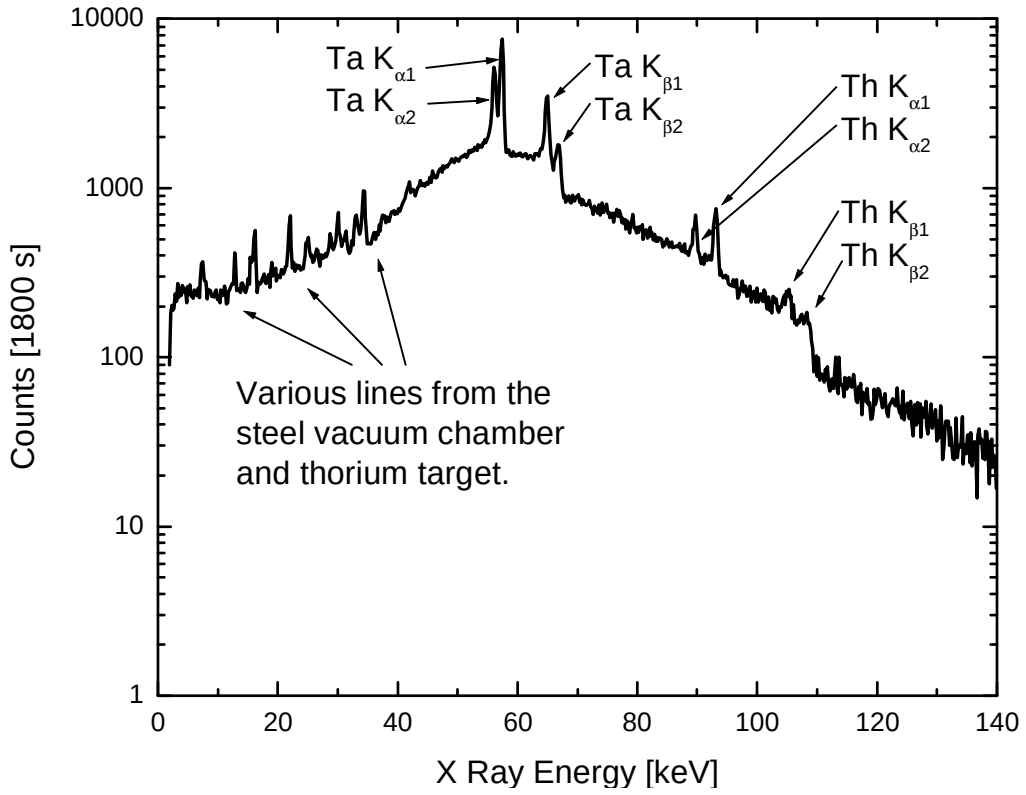

Figure 4.19 - Net counts from the fluorescence of thorium using a pyroelectric source.

X-ray fluorescence experiments were also conducted using a natural uranium target. The target was too thick to use the transmission geometry depicted in Figure 4.17. Instead, the target was placed at an angle to the detector and source, to allow XRF radiation to be "reflected" into the detector, as seen in Figure 4.20. The detector was shielded with lead to eliminate incident x-rays from the pyroelectric crystals. As with the thorium fluorescence experiments, it was necessary to collect a background spectrum, since the sample had some natural radioactivity. The background was subtracted from the gross counts to yield the net counts due to the pyroelectric source.

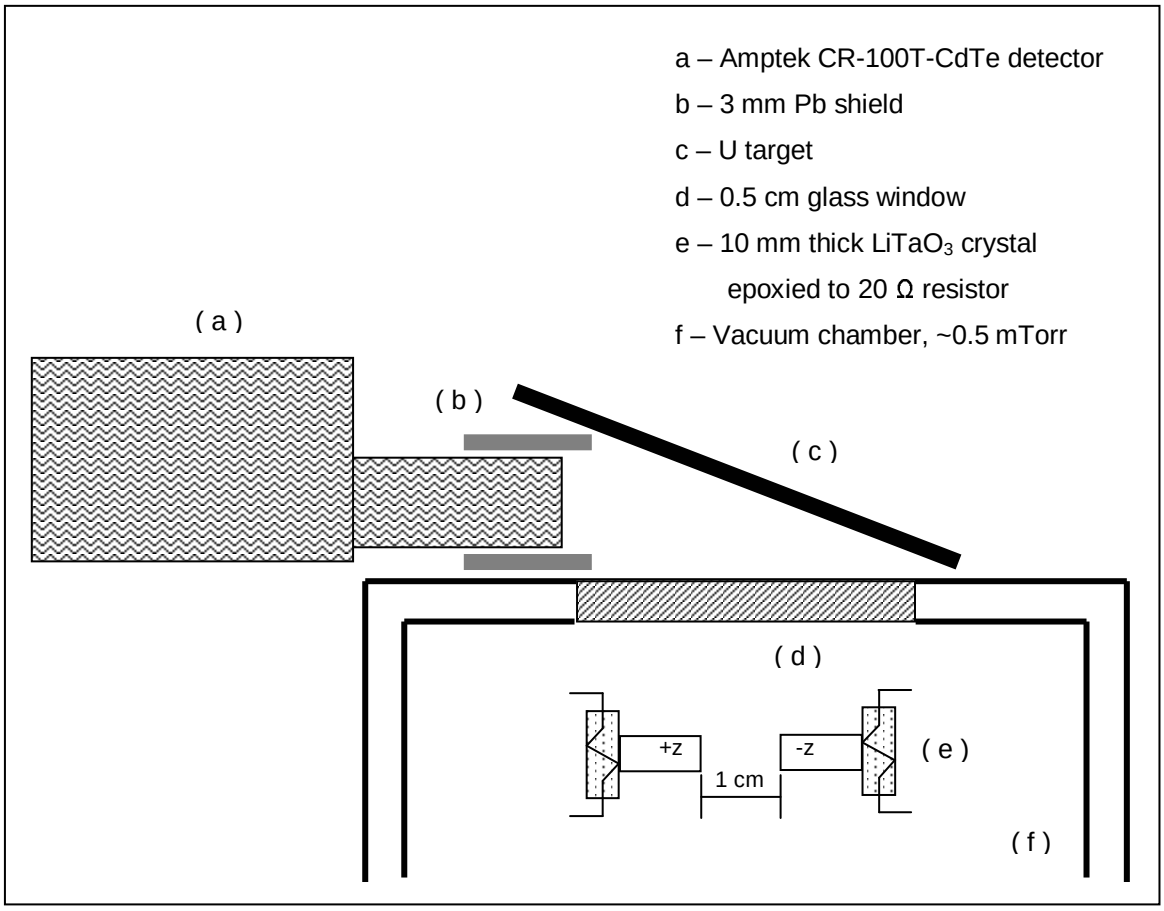

Figure 4.20 - Experimental setup for fluorescence of a natural uranium target using paired 10 mm $LiTaO_3$ crystals.

In these experiments, not all of the k-shell x-rays of the target could be clearly seen, as some bremsstrahlung from the crystals penetrated the lead shielding and added background to the spectra, and due to the relatively low count rate at high energy compared to the thorium fluorescence experiments. However, most of the k_β lines could be clearly seen. This is due to the lower x-ray yield at high energy for this experiment versus experiments performed with a thorium target. (The x-ray energy is sufficient to fluoresce the k_β lines of uranium). A plot of the net counts for three summed 800 second spectra after background was subtracted can be seen in Figure 4.21.

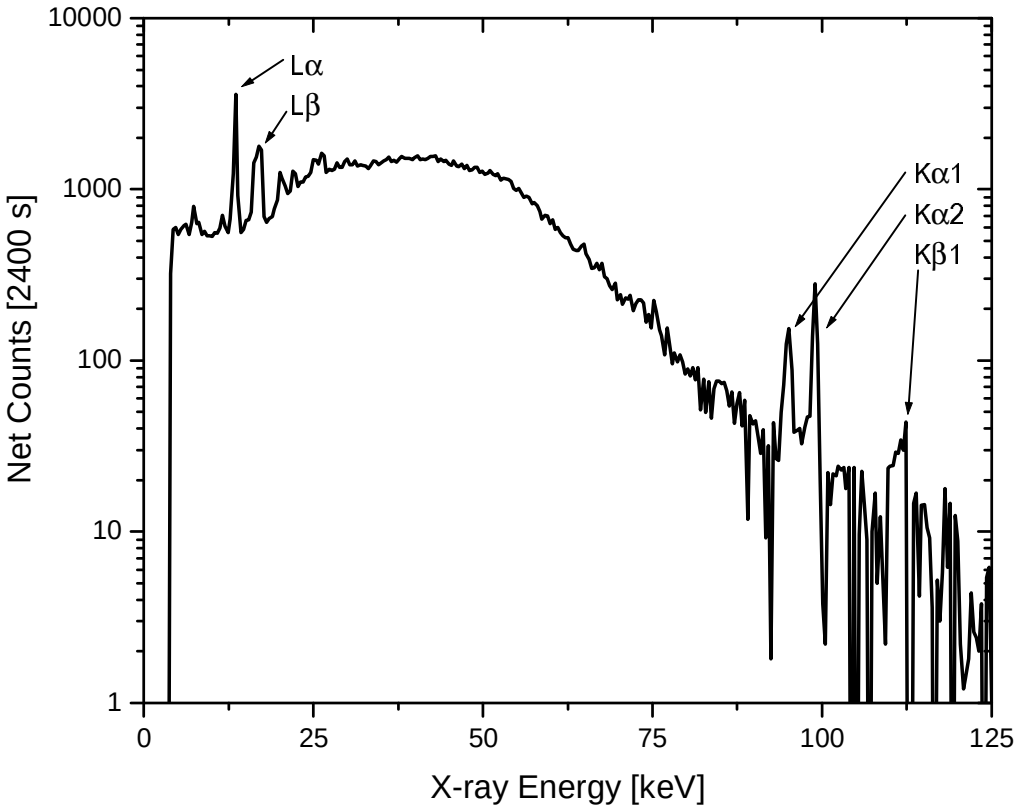

Figure 4.21 - Net x-ray counts from fluorescence of uranium using paired pyroelectric crystals. Three summed spectra are shown after background subtraction, total collection time = 2400 s.

5 Charge Focusing Phenomenon

5.1 Introduction

James Brownridge[13] observed that the electrons emitted by pyroelectric crystals are not emitted in purely divergent beams, as would be expected from a uniformly distributed surface source, but rather are focused. Kukhtarev[31] showed that the focal length was that which would be observed due to the distribution of charge in a ring along the crystal edge. In this section it will be demonstrated that the charge focusing does indeed follow a ring-charge model.

5.2 Photographs of Electron Emission

The charge focusing phenomenon was experimentally verified in a collaboration with Kamron Fazel, who performed the work as an undergraduate research project. A 20 mm x 10 mm lithium tantalate crystal was mounted to a 2 W heating resistor and aimed at a zinc sulfide fluorescent screen. A weak permanent magnet was mounted to the mounting plate holding the resistor, and a second weak magnet was placed outside the chamber to provide the ability to move the crystal back and forth relative to the screen without opening the chamber. The gas pressure was kept below 7.5×10^{-5} for these experiments.

Figure 5.1 shows photographs of the electrons striking the screen, taken with a web-cam. The first photograph shows that at a distance of 0.3 cm, the emission could be seen to come from the outer edge of the crystal. At 0.5 cm, it had focused to a spot. At 1 cm, it was still somewhat focused, and then began to diverge at 2 cm.

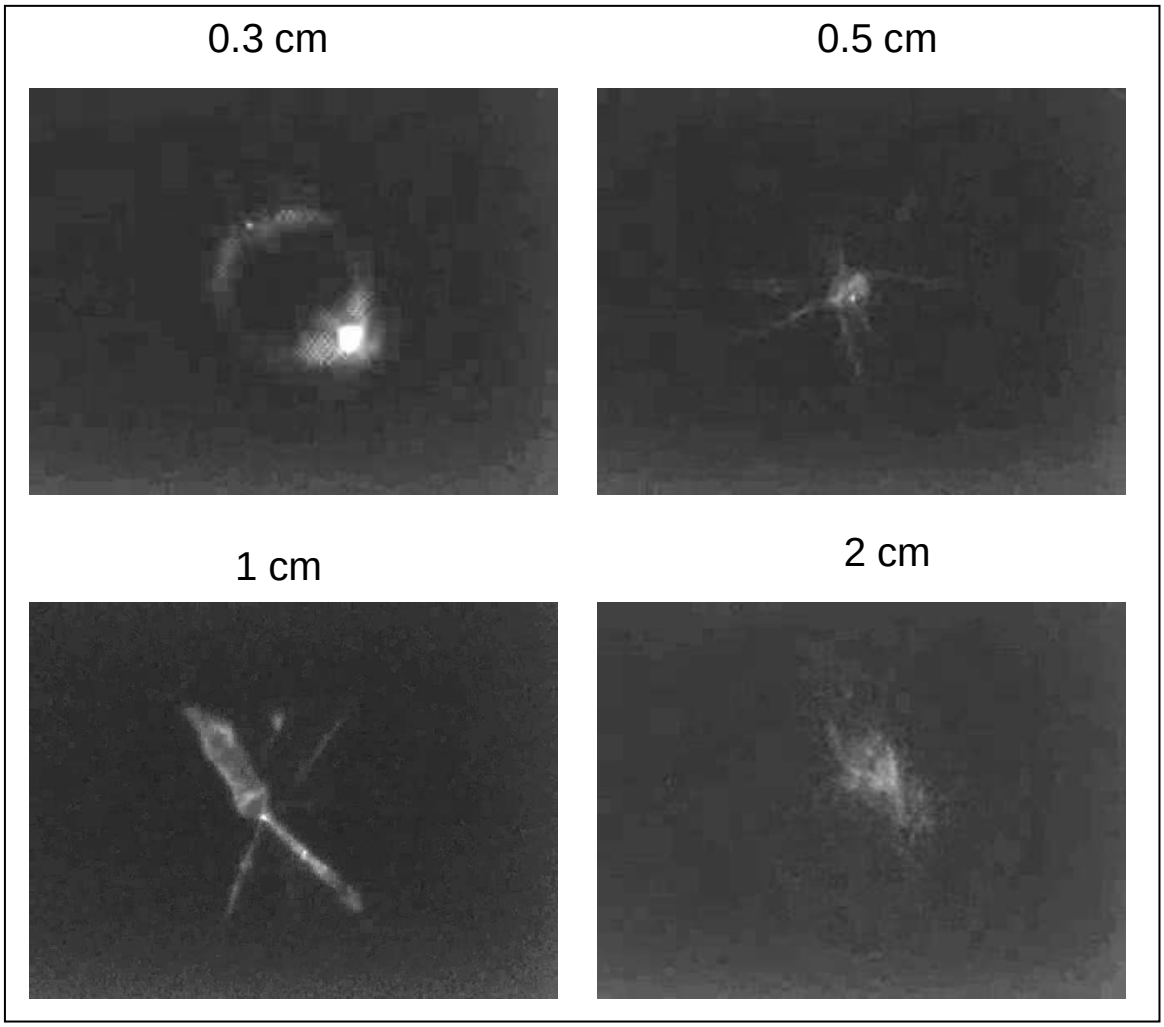

Figure 5.1 - Photographs of fluorescent screen at varying distance from a 20 mm diameter $LiTaO_3$ crystal during electron emission. (Taken by Kamron Fazel).

5.3 Finite Element Modeling of a Ring Charge on a Crystal Surface

By modeling the crystal in a finite element software package [COMSOL Multiphysics 3.2], it was found that a ring charge along the edge of the crystal would create a focusing phenomenon similar to that which was observed experimentally: Emitted charge would be seen as ring very close to the crystal, would appear to be a concentrated dot at intermediate distances, and would diverge at large distances. Referring back to Figure 5.1, it is apparent that the majority of the emitted charge must have followed field lines angled inward. This does not mean that the model in Figure 5.2, which shows many field lines diverging away from the focal point, is incorrect, but rather constrains

the emission location to be on the inner part of the flat crystal surface. The focal point given by the two-dimensional model in Figure 5.2 gives a focal distance of 0.75 cm.

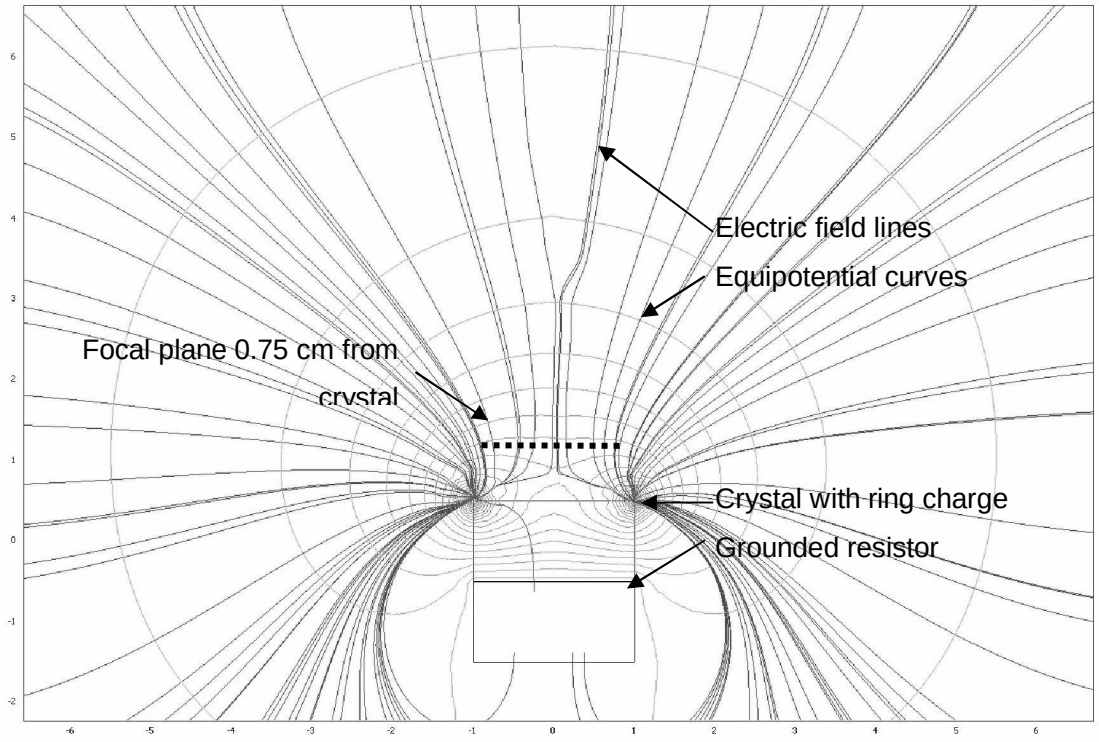

Figure 5.2 - 2D axially-symmetric finite element model of a 20 mm diameter x 10 mm thick lithium tantalate crystal connected to a grounded resistor. The electric field lines shown in this model exhibit charge focusing. [Units on the axes are in cm].

Figure 5.3, included for the sake of comparison, shows that charge focusing cannot occur if the charge on the crystal surface occurs as a uniformly-distributed surface charge. Since the pyroelectric effect results in a polarization of the crystal, one would expect that the charge would indeed be a uniform surface charge unless the charge can migrate. While the surface charge on a polarized dielectric is typically expected to be bound charge, the observation of charge focusing demands that some charge mobility must occur, or that a separate effect, such as the piezoelectric properties of the crystals, causes a radial polarization due to stresses from heating and cooling.

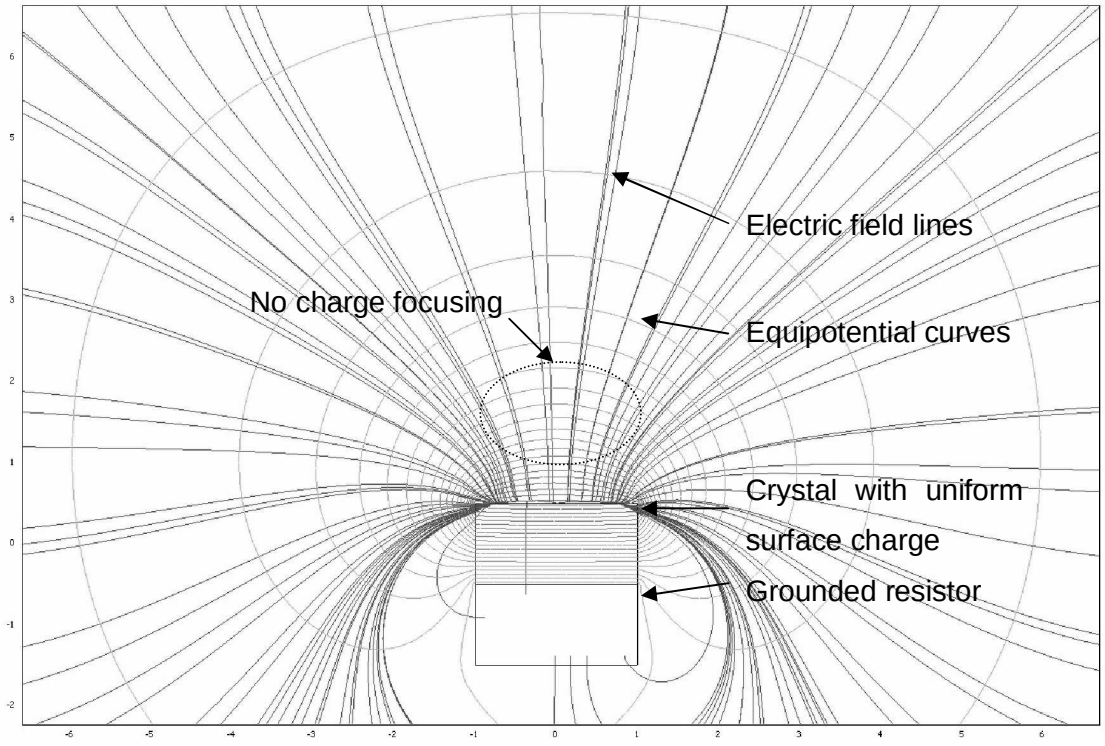

Figure 5.3 - 2D axially-symmetric FEM model of a crystal and resistor showing that charge focusing does not occur if the charge is uniformly distributed along the crystal surface. [Units on the axes are in cm].

Figure 5.4 shows a three-dimensional model in which the charge has been restricted to the edge of the crystal, similar to the two-dimensional model presented in Figure 5.2. This figure shows good agreement with experimental results, as the electric field lines converge (i.e., are focused) at a distance of between 0.5 cm and 1 cm. The exact focal point for this model is shown in Figure 5.5, a plot of the electric field strength along a line extruded upward from the crystal surface at the perpendicular. The maximum field strength corresponds to maximum field line density, and therefore gives the focal length of the crystal. In this case, the focal length is shown to be 0.8 cm.

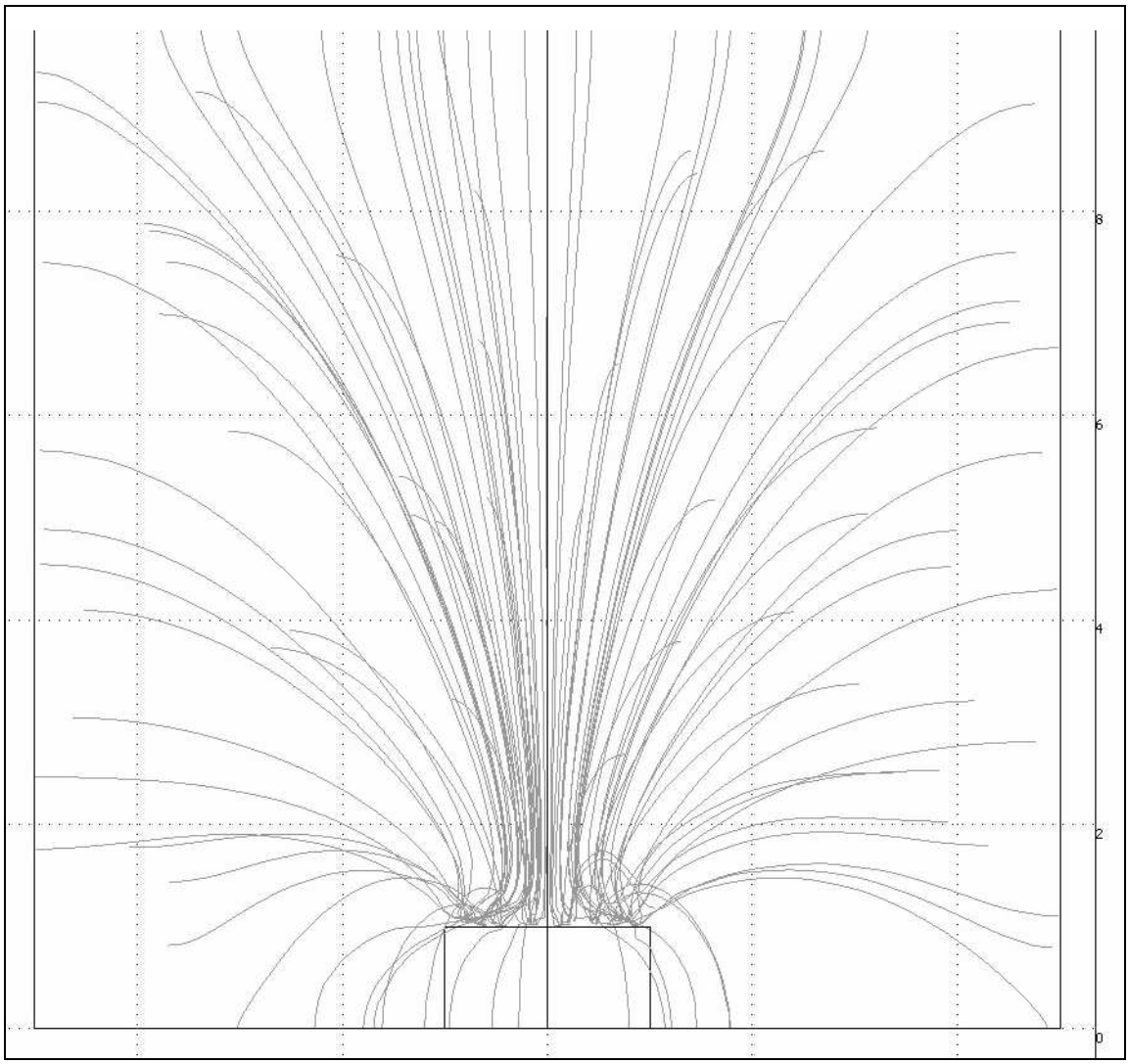

Figure 5.4 - Output of a 3-D FEM model with charge located along the edges of a pyroelectric crystal. The electric field lines are seen to converge in the region from ~0.5 - 1 cm from the crystal surface. The convergence of the field lines is associated with the focal length of the emitted charge. [Units on the axes are in cm].

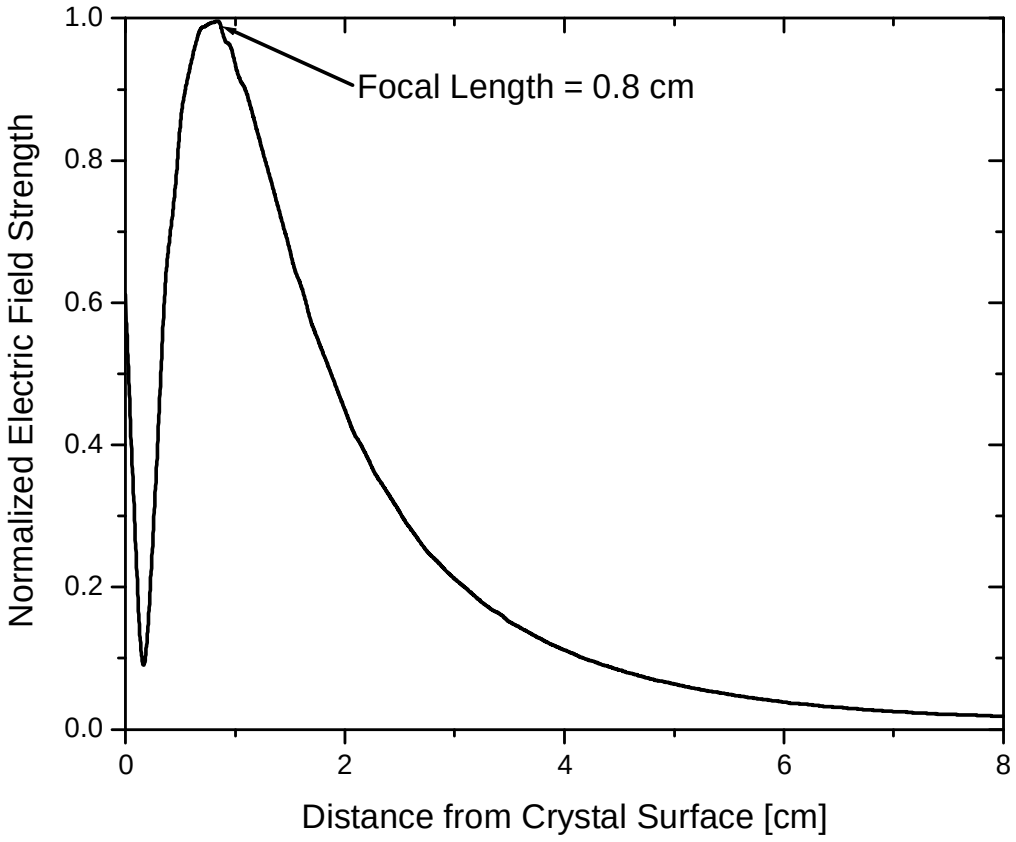

Figure 5.5 - Plot of the electric field length along the crystal axis, from the crystal surface to d = 8 cm. The focal length is at 0.8 cm.

5.4 Prediction of Crystal Focal Length

The assumption of a ring charge distribution on the crystal surface allows the prediction of the focal length with a good degree of accuracy. To first order, the crystal can be disregarded, and the ring charge can be assumed to be floating in space. The ring charge will be assumed to be perpendicular to the *z*-axis, at *z=0*, with a radius of r_0.

The electric field due to a uniform line charge density λ is given by[62]:

$$\vec{E}(\vec{r}) = \frac{1}{4\pi\varepsilon_0}\int \frac{\lambda}{r^2}\hat{r}dl' \qquad (25)$$

An illustration of a ring charge is shown in Figure 5.6.

In cylindrical coordinates, if a circular ring charge of radius r_o is assumed, the path integral of the line charge density λ about the perimeter becomes:

$$\int \frac{\lambda}{r^2}\hat{r}dl' = \int_0^{2\pi} \frac{\lambda}{r^2}\hat{r}\cdot r_o d\theta \tag{26}$$

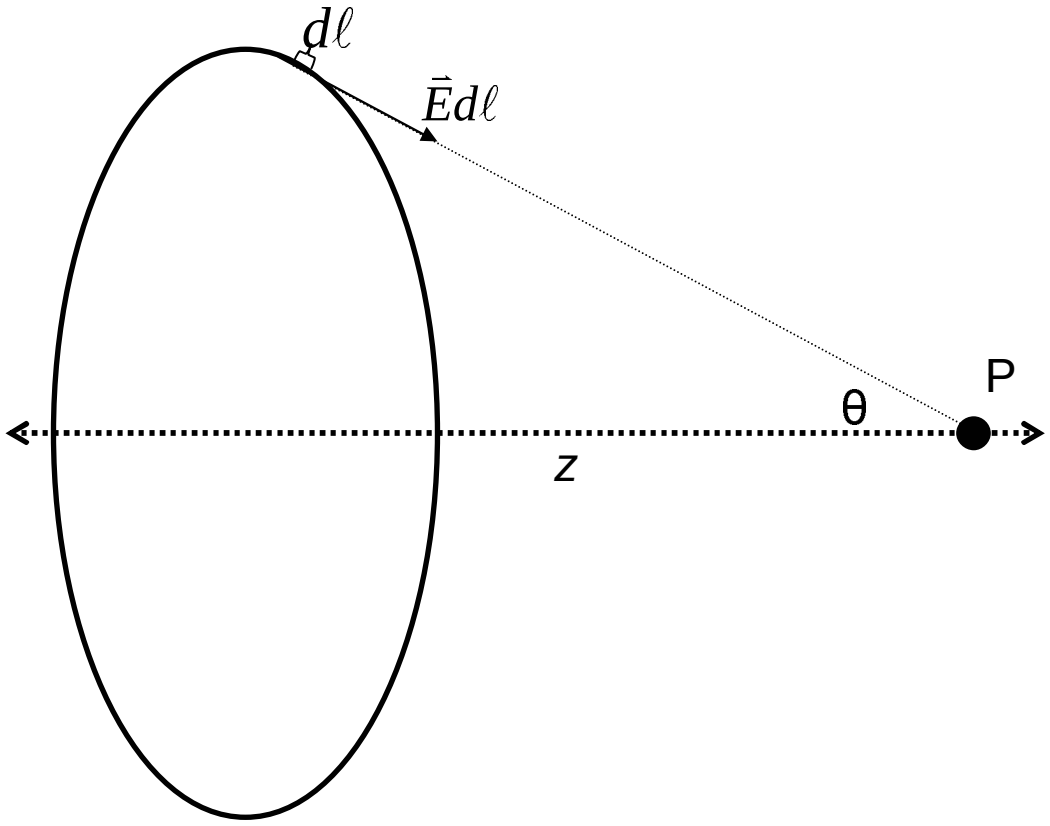

Figure 5.6 - Diagram showing the electric field due to a differential segment of a ring charge, as observed at an observation point P.

At the focal point, the electric field lines at $r = 0$ are perpendicular to the ring charge axis (z-axis). For this reason, the calculation can be simplified by finding the point along the axis where the z-component of the field is at a maximum. To consider only the z - component of the electric field along the ring charge axis, the integrand must be multiplied by the cosine of the angle θ between the vector $\hat{r}$ and the ring charge axis. In cylindrical coordinates, the cosine of θ is equal to z / r and the integral then becomes:

$$\vec{E}_z(z, r=0) = \frac{1}{4\pi\varepsilon_0}\int_0^{2\pi} \frac{z\lambda}{r^3} r_0 \hat{z} d\theta \tag{27}$$

$$\vec{E}_z(z,\vec{r}=0)=\frac{1}{4\pi\varepsilon_0}\int_0^{2\pi}\frac{z\lambda}{((z-z_0)^2+(r-r_0)^2)^{3/2}}r_0\hat{z}d\theta \tag{28}$$

$$\left|\vec{E}_z(r=0,z)\right|=\frac{1}{4\pi\varepsilon_0}\int_0^{2\pi}\left(\frac{z\lambda}{\left(z^2+r_0{}^2\right)^{3/2}}\right)\cdot r_0 d\theta \tag{29}$$

$$\left|\vec{E}_z(r=0,z)\right|=\frac{r_0\cdot\lambda}{2\cdot\varepsilon_0}\left(\frac{z\cdot r_0}{\left(z^2+r_0{}^2\right)^{3/2}}\right) \tag{30}$$

The maximum value of this function will determine the point along the z-axis at which the greatest electric field strength occurs. One can see that the result will be insensitive to the scaling factor $\frac{r_0\cdot\lambda}{2\cdot\varepsilon_0}$, and the maximum field density can be determined using the bracketed term only. The maximum value of the bracketed term can be found by finding the root of its derivative:

$$0=\frac{d}{dz}\left(\left(\frac{z\cdot r_0}{\left(z^2+r_0{}^2\right)^{3/2}}\right)\right) \tag{31}$$

$$0=\left(\frac{r_0}{\left(z^2+r_0^2\right)^{3/2}}\right)-\left(\frac{3r_0z^2}{\left(z^2+r_0^2\right)^{5/2}}\right) \tag{32}$$

Multiplying both sides by $\frac{\left(z^2+r_0^2\right)^{5/2}}{r_0}$:

$$0=z^2+r_0^2-3\cdot z^2 \tag{33}$$

or

$$r_0^2=2z^2 \tag{34}$$

Therefore, there are two focal points, at $z=\pm\frac{r_0}{\sqrt{2}}$. Based on this simple model, the focal length of a pyroelectric crystal should scale with radius, as one would expect. Figure 5.7 shows a plot the field strength along the z-axis (r = 0) for a ring charge with a 1 cm radius, with a maximum value at 7.1 mm. By comparing Figure 5.5 and Figure 5.7, the field strength result taken from a finite elements program, is seems that the analytical isolated ring charge model gives a very accurate prediction of the focal length.

The finite element method result and the isolated ring charge model both seem to agree well with the experiment shown in Figure 5.1.

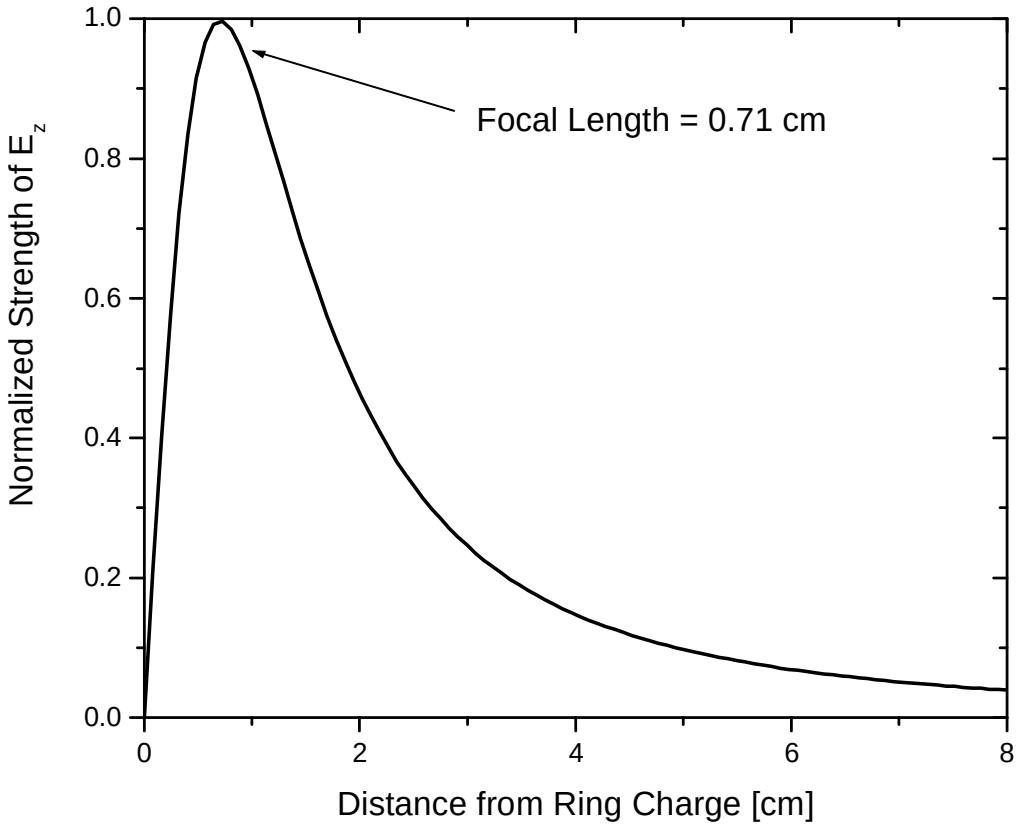

Figure 5.7 - Electric field strength along the axis of an isolated ring charge with a radius of 1 cm. Two foci exist, and are located at z = ± 0.707 cm.

This analysis shows that the charge focusing from a pyroelectric crystal is better explained by a ring charge, formed by charge migration to the edges of the crystal, than by a uniform bound polarization charge. However, the ring charge model cannot explain the asymmetry in the charge emission as shown in Figure 5.1. Therefore, while the ring charge model explains the overall behavior of the electron emission, a complete model would need to include some other effect to describe the asymmetry. More work needs to be done to find a physical explanation for the formation of the ring charge, and to verify that the migration of charge to the edges of the crystal accurately predicts the focal length for crystals with different sizes and shapes. Experiments with crystals of different radii would also help to verify the accuracy of this model.

6 Magnetic Deflection of Electrons and Ions

6.1 Motivation

Upon deciding to pursue neutron production via pyroelectric fusion, it was decided to take a systematic, step-by-step approach to fusion. At that point, the ability of pyroelectric crystals to produce a high acceleration potential[50] had been verified, and ion and electron spectroscopy experiments had been performed [34]. However, the ability of the crystal to ionize a fill gas was of crucial importance to the prospect of pyroelectric fusion. Therefore, the next step toward fusion was to further confirm this ability to ionize by verifying that the charged particles detected during the ion spectroscopy experiments were much more massive than electrons. This task was accomplished by magnetically deflecting the emitted charge, in what was essentially an accelerator mass spectrometry experiment[51].

6.2 Theory

The Lorentz force $\vec{F}$ acting on a charged particle contains a component which is parallel to the electric field $\vec{E}$, and a component which is parallel to the cross product of the particle's velocity vector $\vec{v}$ and the magnetic field $\vec{B}$:

$$\vec{F} = q\left(\vec{E} + \vec{v} \times \vec{B}\right) \tag{35}$$

This means that a magnetic field transverse to the direction of particle travel will cause the particle to deflect by some displacement perpendicular to its initial velocity vector as it travels through the field. The trajectory traced by the particle would be a circle, assuming that the magnetic field was large enough to contain the entire circle. The radius of the circle is inversely proportional to the magnetic field strength, and proportional to the square root of the mass. It is possible, therefore, to select a field size and strength that is sufficient to deflect a light particle (such as an electron), while allowing much more massive particles (such as ions) to continue on their original trajectory without being noticeably deflected.

6.2.1 Geometrical Determination of Deflection Distance

The simplest way to determine the expected angles of deflection for accelerated electrons and ions is to use trigonometry. In a uniform magnetic field, a charged particle traveling perpendicular to the field lines will have a uniform radius of gyration in the plane perpendicular to the field. If the radius of gyration is larger than the size of the magnetic field, then the particle will leave at some angle, and, assuming that the field drops to zero very quickly, will travel along a straight path until it is blocked.

Therefore, one can use the radius of gyration and the size of the field region to determine the angle at which the particle leaves the magnetic field. Then the total deflection distance as measured on a fluorescent screen could easily be predicted based on the distance to the screen and the angle of deflection.

The radius of gyration of a charged particle in a uniform magnetic field is found by balancing the centripetal and centrifugal forces acting on the particle[52]. For a particle with a charge of n e.s.u. (corresponding to n electrons being stripped from an ion), the kinetic energy obtained by passing through the acceleration potential V is:

$$neV = \frac{1}{2}mv^2 \tag{36}$$

where e is the unit of elementary charge, m is the particle mass, and v is the particle velocity. It will be assumed that $v << c$, and that relativistic effects can be neglected. Rearranging Equation 36 to yield the particle velocity, it becomes:

$$v = \left(\frac{2neV}{m}\right)^{1/2} \tag{37}$$

The centrifugal force on the particle is simply:

$$\vec{F}_{centrifugal} = \frac{mv^2}{\rho}\hat{r} \tag{38}$$

where $\vec{r}$ is the radial unit vector in the plane of curvature and ρ is the radius of the particle's trajectory. The centripetal force[52] is then found from the Lorentz force equation[53] for a purely magnetic field (i.e., no electric field component),

$$\vec{F} = ne\left(\vec{E} + \vec{v} \times \vec{B}\right) = ne\vec{v} \times \vec{B} \tag{39}$$

which reduces to:

$$F_{centripetal} = neBv \cdot \hat{r} \tag{40}$$

One can then write a force balance equation:

$$\frac{mv^2}{\rho} \cdot \hat{r} = neBv \cdot \hat{r} \tag{41}$$

which gives the radius of the circular trajectory (henceforth referred to as either the radius of gyration or radius of deflection, ρ_d) as:

$$\rho_d = \frac{mv}{neB} = \frac{1}{B}\left(\frac{2mV}{ne}\right)^{1/2} \tag{42}$$

Harnwell[54] gives the radius of gyration in units of centimeters and Gauss:

$$\rho_d = \left(\frac{144.5}{B}\right) \cdot \left(\frac{M}{n}\right)^{1/2} V^{1/2} \tag{43}$$

where B is the magnetic field strength in Gauss, M is the mass of the particle in atomic mass units, n is the charge of the particle in e.s.u., and V is acceleration potential in Volts. This radius is the radius at which a particle will gyrate in a uniform magnetic field. In the case of a uniform magnetic field that is smaller than the radius of gyration, this equation describes the radius of the particle trajectory as it passes through the field, as illustrated in Figure 6.1.

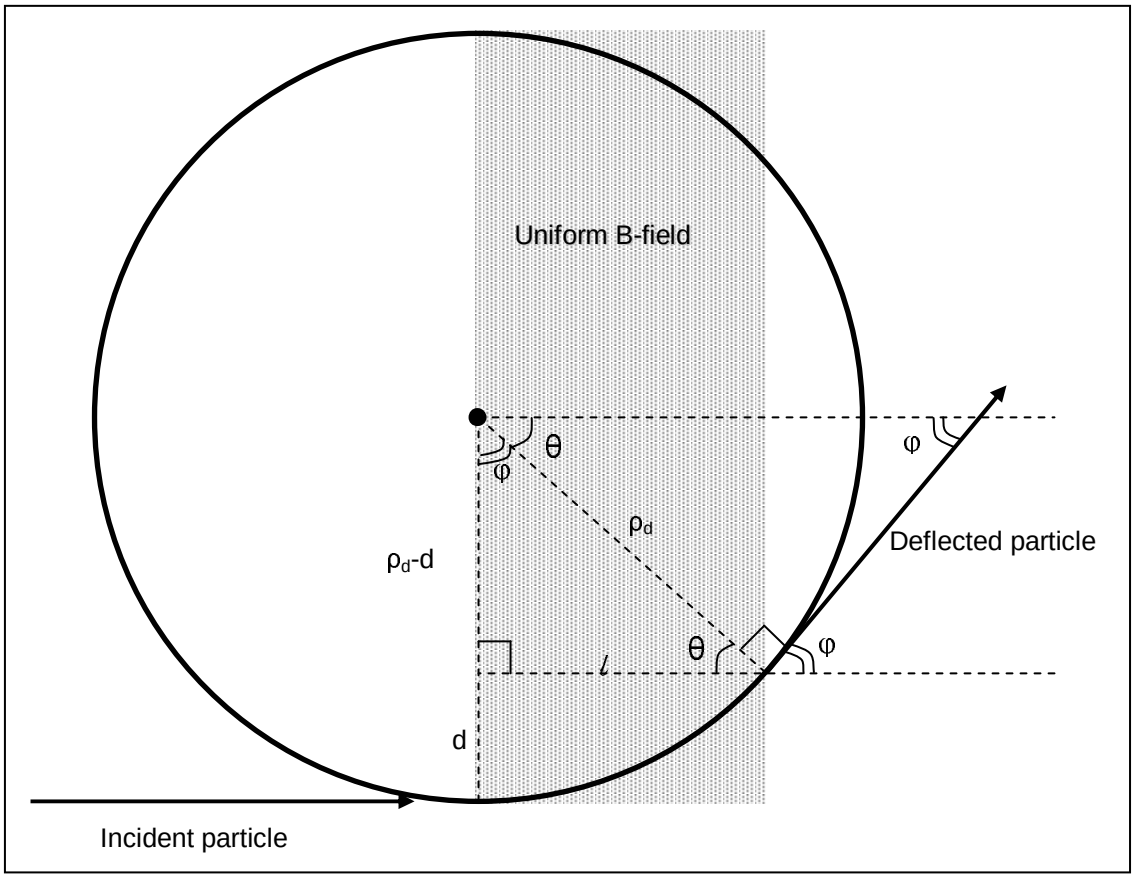

Figure 6.1 - Geometrical description of the deflection of a charged particle incident on a uniform magnetic field (perpendicular to page).

The final deflection distance, as would be measured experimentally on a fluorescent screen, would include a term for the deflection inside the magnetic field (*d* in Figure 6.1), as well as a deflection distance traveled after leaving the magnetic field, which shall be called *D*. If the angle at which the tangent of the deflected particle with the circular trajectory intersects the horizontal is called φ, then the deflection distance inside the magnetic field is given by:

$$d = \rho_d - \rho_d \cos\varphi = \rho_d (1 - \cos\varphi) \tag{44}$$

If one can assume that the deflection distance inside the field is much smaller than the deflection radius, then the deflection inside the field can also be found using the length of the magnetic field region, *l*[55]:

$$d = \frac{l^2}{2\rho_d} \tag{45}$$

(However, this assumption is not appropriate for the experimental geometry used in this research). If the distance between the end of the magnetic field region and the fluorescent screen is called *L*, then the deflection outside the field is given by:

$$D = L \cdot \tan\varphi \tag{46}$$

Finally, the total deflection distance is found to be:

$$D_{tot} = d + D = \rho_d (1 - \cos\varphi) + L \cdot \tan\varphi \tag{47}$$

Due to the dependence of the deflection radius on particle mass, and because a singly-ionized gas molecule or atom has the same magnitude of electric charge as an electron, the radius of curvature is drastically different for ions and electrons. Therefore, it is simple to design a magnetic deflection experiment in which electrons are deflected by a great distance, while ions are deflected very little. Figure 6.2 shows the radii of curvature for different charged particles in an 800 G field, like the one used the experiment to be described later in this section.

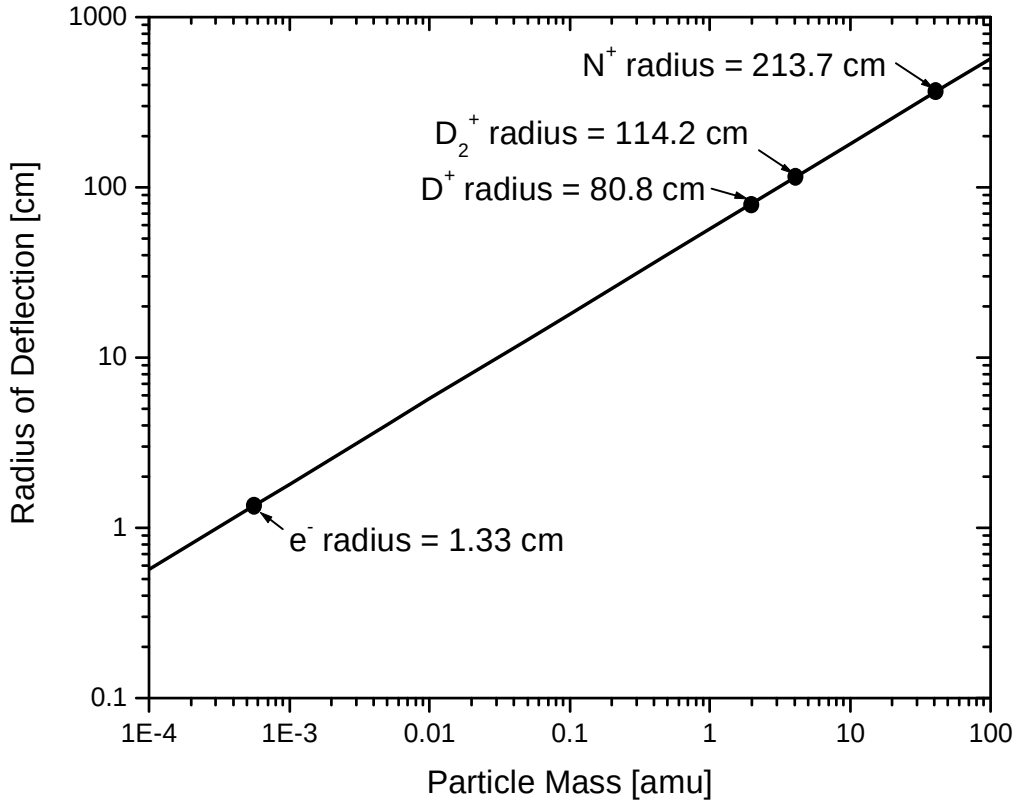

Figure 6.2 - Radii of deflection for various species of singly-ionized gases at 100 keV as compared with electrons in an 800 G uniform magnetic field.

6.2.2 Experimental Verification of Ion Production

In order to verify that the pyroelectric crystals were capable of generating ions, a 5 mm diameter x 10 mm thick $LiTaO_3$ crystal was oriented such that the z^- surface faced a ZnS:Ag fluorescent screen. A collimator with a 4 mm hole was placed 0.7 cm away from the crystal. Two permanent magnets with a diameter of 1.2 cm were held behind the collimator, such that the maximum magnetic field strength was 800 G, perpendicular to the axis of the crystal. The distance between the screen and the end of the magnetic field region was L = 1.2 cm.

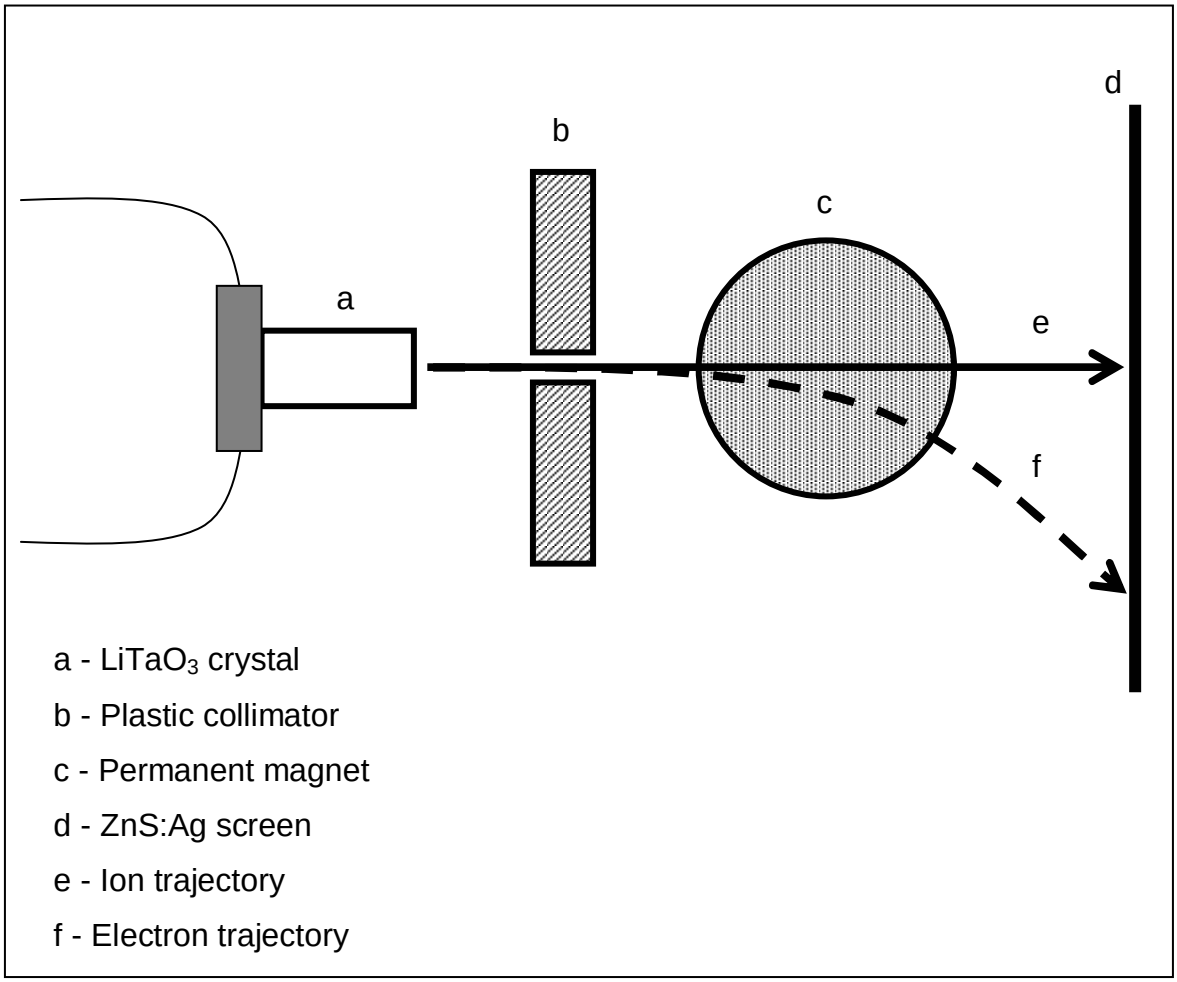

Figure 6.3 - Side view of experiment used to verify ion production via magnetic deflection. Not to scale.

The pressure in the vacuum chamber was 5 x 10^{-5} Torr - 6.5 x 10^{-5} Torr. The crystals were heated with a heating resistor, which supplied 2.5 W of heating power to the z^+

surface of the crystal. A digital camera was held in a ring stand such that it could see the zinc sulfide screen through a window on a vacuum chamber flange. The camera was set to take 2-3.2 second exposures for photographing electron emission, and 5-8 second exposures for photographing ion emission. For the purpose of calculating the deflection distance, the magnetic field was assumed to have a constant effective strength inside the magnetic field region, which immediately dropped to zero outside of this region. Based on Equation 47, and assuming that the effective average field strength was 600 G, one can expect a 100 keV electron to be deflected by -1.56 cm, and a singly-ionized N^+ ion to be deflected by +.008 cm. The effective field strength was taken to be somewhat less than the measured maximum field strength of 800 Gauss to account for the variation of the field strength within the magnetic field region.

Figure 6.4 shows enhanced photographs of the spots created by electron and ion emission from the crystal after passing through the magnetic field. It can be readily seen that the ions were not deflected at all, while the electrons deflected by 1 cm. This proves that the positively charged particles emitted by the z^- surface during the heating phase are ions.

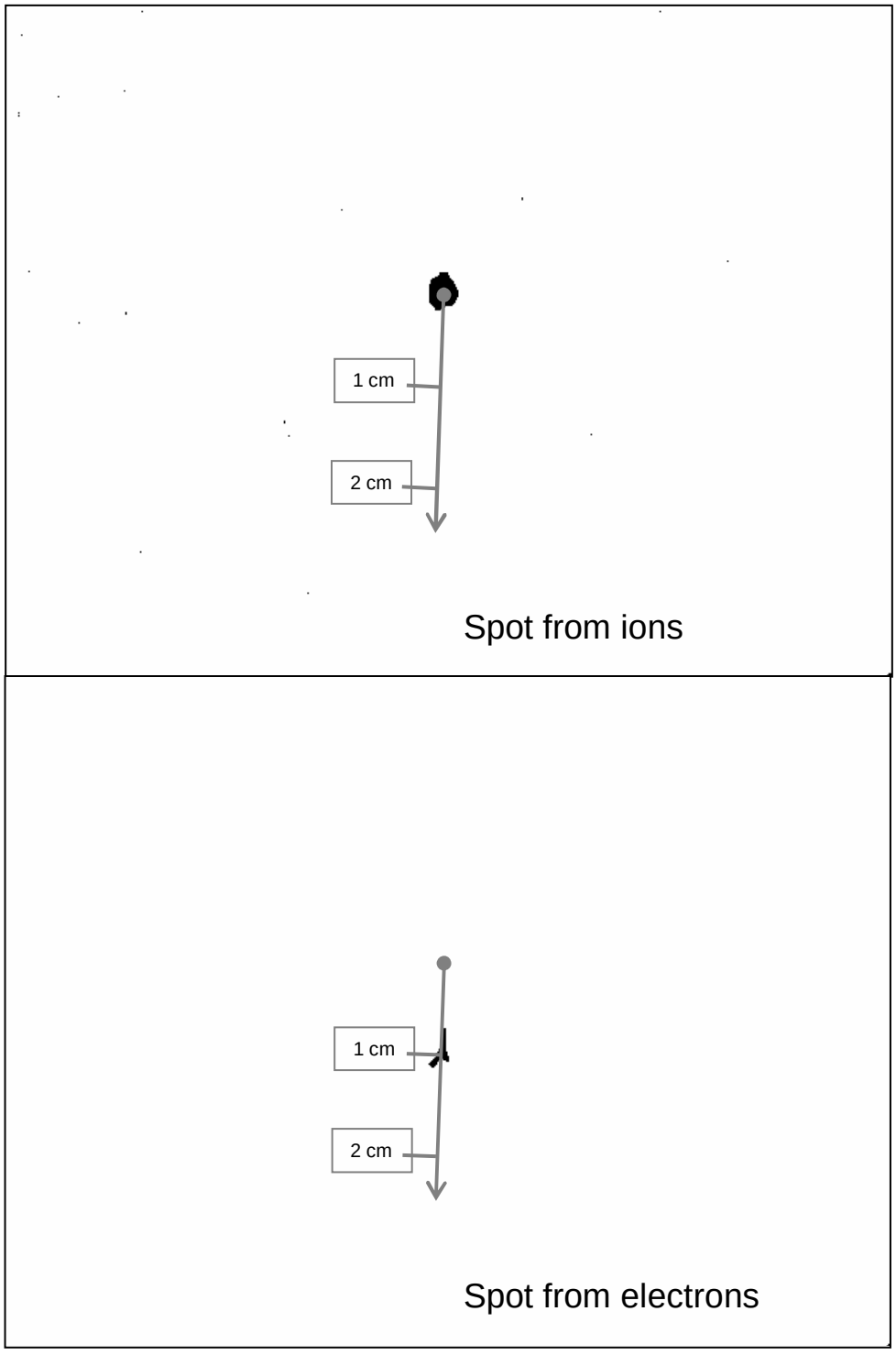

Figure 6.4 - Photographs of the spots produced by deflected electrons and ions hitting the ZnS:Ag screen. Notice that only the electrons, and not the ions, are deflected.

7 Direct Measurement of Ionization Current

7.1 Introduction

The neutron yield from a pyroelectric neutron generator is dependent on the ability of the crystals to create and maintain a strong acceleration field, while emitting some charge in the form of deuterons in order to cause fusion reactions. It is important, therefore, to balance the ionization current with the acceleration potential, since the reduction of charge on the crystal surface due to ion emission causes a decrease in acceleration potential, and thus decreases the maximum deuteron energy and cross section for fusion.

In this series of experiments, various different ionizing cathodes were mounted to the surface of a pyroelectric crystal, and simultaneously measured the x-ray energy and ion current. A figure of merit for neutron production was then formulated. The figure of merit was based on the integrated cross section of deuterons of a given initial energy slowing down in a deuterated plastic target, and used this figure of merit to evaluate the cathode designs and select several that were promising for fusion.

7.2 Experimental Setup

A metal plate was connected to an HP3458A digital multimeter. The multimeter was controlled and read using a version of the program shown in Appendix III. The plate was held 23 mm behind a grounded grid. The grid was 20 mm above the emitting surface of a 20 mm diameter x 10 mm thick $LiTaO_3$ crystal. Different cathodes were mounted to 16 mm diameter copper discs, which were then attached to the z^+ surface of the crystal with conductive silver paint. The following cathode materials were used:

- 4 mm long, 70 nm radius catwhisker tungsten tip;
- 4 mm long, 600 nm radius tungsten tip;
- 4 mm long, 600 nm radius tungsten tip coated with tungsten nanorods (hence-forth referred to as a “nanotree”);
- 12 mm x 12 mm patch of 1 mm long carbon nanotubes, each 30 nm in diameter and spaced apart by about 200 nm;
- 16 mm diameter copper disc coated with tungsten nanorods;

- A small piece (~2 mm x 2 mm) of doped silicon coated with carbon nanorods.

The carbon nanorods were ~200 nm long, and the tungsten nanorods were ~500 nm long. The crystal was heated for 425 seconds to a maximum temperature of ~140^{o}C. It was then allowed to cool naturally back to room temperature. The fill gas was either air (at 0.01 mT, 3 mT, or 6 mT) or deuterium (at 4 mT or 8 mT). While most cathodes were tested in both air and deuterium gas, the tungsten nanorods and carbon nanotubes were only tested in air, and not in deuterium.

During cooling, when the crystal was emitting ions toward the metal plate, the current was collected by the LabView program and then integrated to yield the total ion charge incident on the plate. This value was then corrected for the 56% transparency of the grid to yield the total charge incident on the grid. A CdTe x-ray detector was placed outside the vacuum chamber to measure the x-ray spectrum from the crystal during ion emission. The endpoint energy of these spectra was used to estimate the acceleration potential of the ions.

7.3 Calculating a Figure of Merit for Neutron Production

Since the neutron yield from a pyroelectric accelerator depends on both the ion current and the acceleration potential, a figure of merit for neutron production was developed based on the measured total emission charge and the endpoint energy of the x-ray spectra. This figure of merit was based on a second-order fit of the integrated D-D fusion cross section as an ion slows down in a deuterated polyethylene target as a function of energy. A detailed discussion of the integrated cross section is given later, in Section 8.3. The figure of merit for fusion is given by:

$$FOM = \frac{q}{3.05\times10^{-5}} \cdot \left(-1.02\times10^{-2} E_{EP}{}^{2} + 4.21\times10^{-1} E_{EP} - 4.28\right) \qquad (48)$$

where q is the total ion charge measured per cooling phase in Coulombs and E_{EP} is the measured endpoint energy of the x-ray spectrum in keV. The factor of 3.05 x 10^{-5} was used to normalize the FOM values (by setting the highest measured FOM to 1.00). This figure of merit is proportional to the number of neutrons which would be created if the total measured ion charge was incident on a deuterated target with an acceleration

potential equal to the endpoint energy of the x-ray spectrum. The fit used to obtain the figure of merit is shown in Figure 7.1.

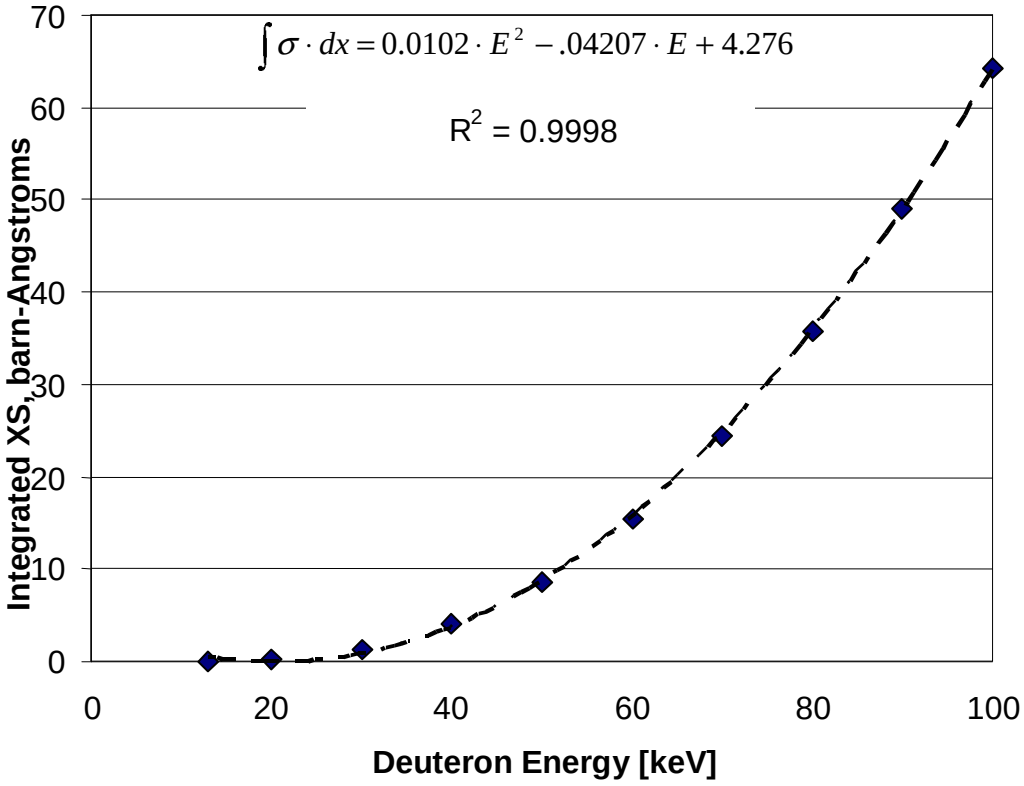

Figure 7.1 - Data used to determine the figure of merit for neutron production based on ion energy and current. The diamonds represent the individual data points of integrated cross section versus energy, while the dashed line represents the fitted quadratic function.

7.4 Results

Figure 7.2 and Figure 7.3 show the results from this experiment. Figure 7.2 shows the charge emitted in the form of deuterons at two different D_2 gas pressures. The two best cathodes for ionizing deuterium were the 70 nm catwhisker tip and two paired 70 nm catwhisker tips. The bare crystal did not yield measurable ion emission, while the 600 nm tip, carbon nanorod sample, and "nanotree" all yielded a measurable but small ion charge.

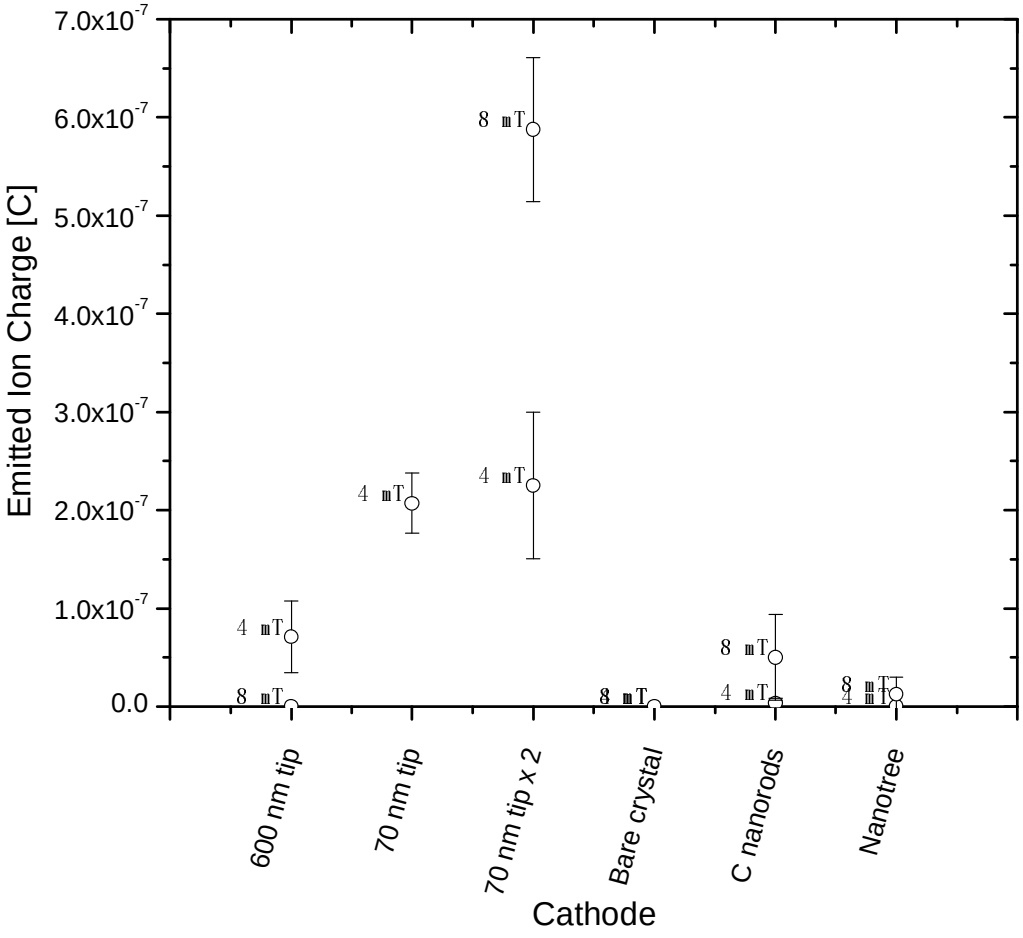

Figure 7.2 - Ion charge emitted by different cathodes in 4 mT or 8 mT D_2 fill gas. The charge was found by integrating the measured current over the length of the cooling phase. The single 70 nm tip was not tested at 8 mT.

Figure 7.3 shows the maximum x-ray energy observed during gas ionization. This figure shows that the paired tip cathode produced a lower acceleration potential than the single 70 nm tip. The poor ionization ability of the 600 nm tip was offset somewhat by the higher acceleration potential.

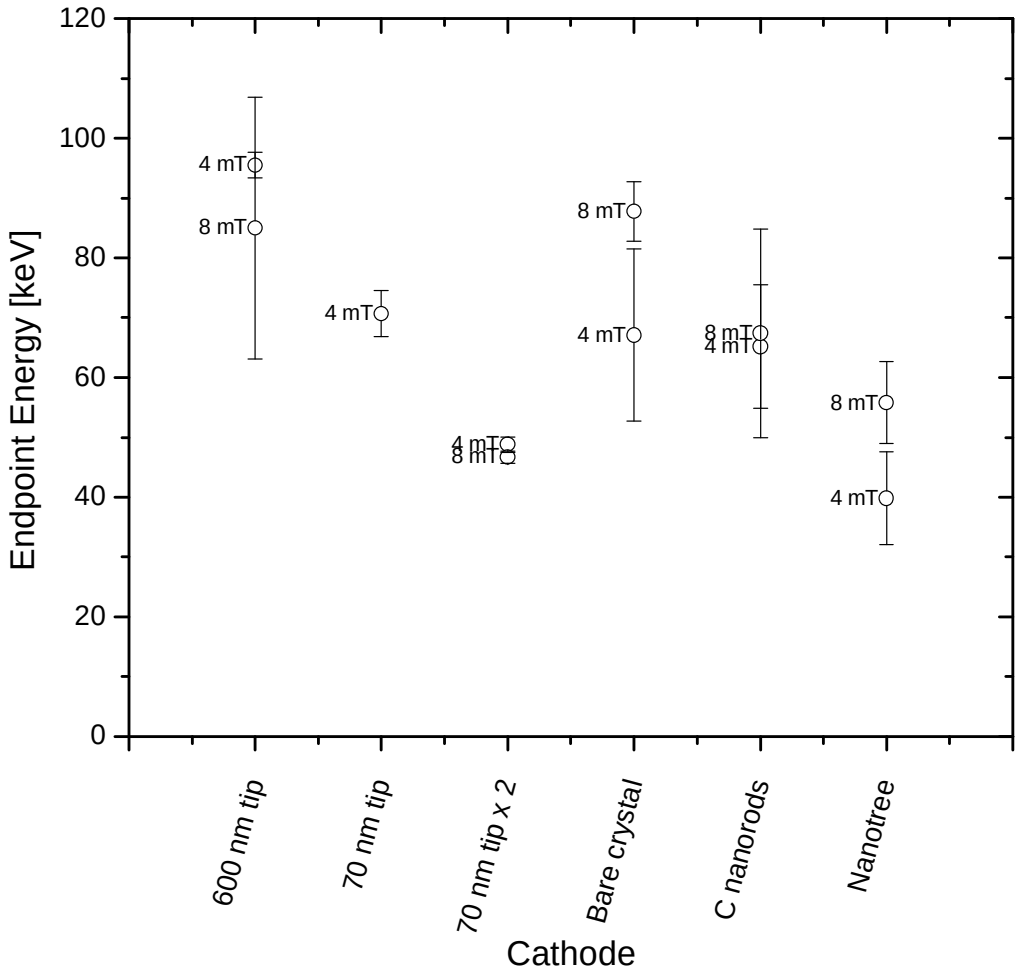

Figure 7.3 - Maximum x-ray energy during D_2 gas ionization for several cathodes.

Finally, Figure 7.5 shows the figure of merit for the cathode designs tested in deuterium gas. The highest figure of merit was for paired 70 nm tips in 8 mT of deuterium, although the single 70 nm tip was not tested at this pressure, and outperformed the paired tips at 4 mT. The bare crystal and nanotree both performed poorly, while the carbon nanorod cathode (at 8 mT) and the 600 nm tip (at 4 mT) seemed to have some promise, but they were both outperformed by the single and paired 70 nm tips. These results seem to mirror the neutron production experiments, in which neutrons were observed when using a 70 nm tip to ionize deuterium, but not when using a bare crystal or 600 nm tip.

Data was also taken for the ability of these cathodes to ionize air. This data was not presented in this section, since it is not important in the development of improved

pyroelectric neutron sources. However, for the sake of reference, a table of all relevant data from the experiments conducted in both air and deuterium is included in Appendix IV.

The results from this experiment suggest that the nanorod cathodes do not offer an advantage over metallic tips in terms of ionization current. While a large array of nanorods would seem to be favorable in this regard to a single tip, the electric field around an individual nanorod is masked by the fields of the surrounding rods, such that the surface behaves more like a flat surface than an array of tips (see Figure 7.4).

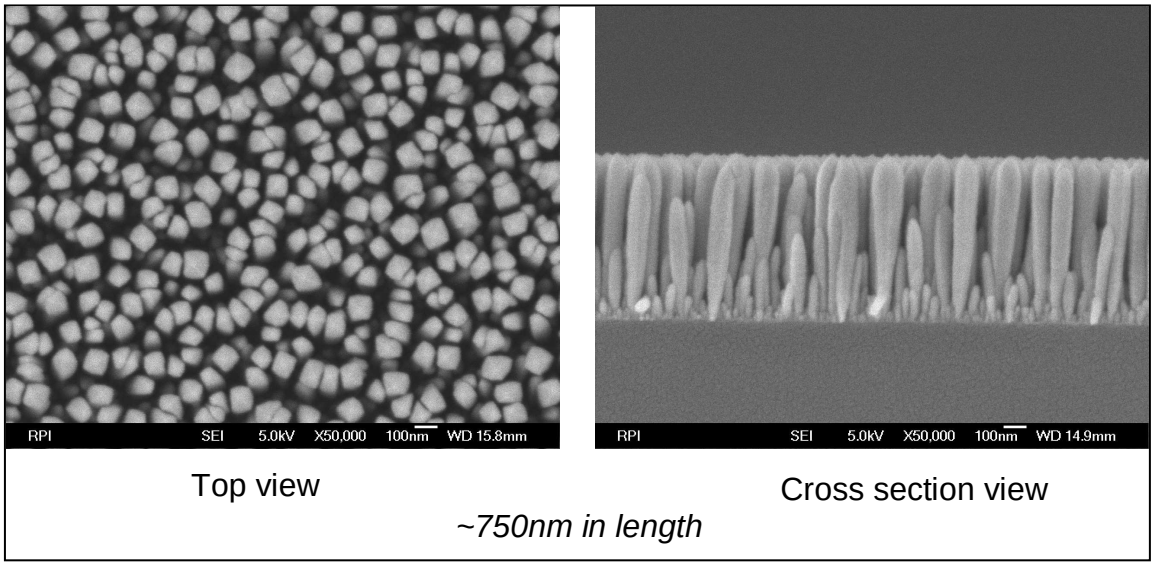

Figure 7.4 - Microscope images of tungsten nanorods deposited on a silicon substrate. This sample was slightly different from the nanorods used in the experiments presented in this section, but is being shown as an illustration of the tight packing of the nanorod arrays.

The use of multiple metallic tips, such as the paired 70 nm tips used in this experiment, has promise, and may offer an advantage over single tips. Fusion experiments have not yet been conducted to test arrays of several metallic tips for advantages in neutron production.

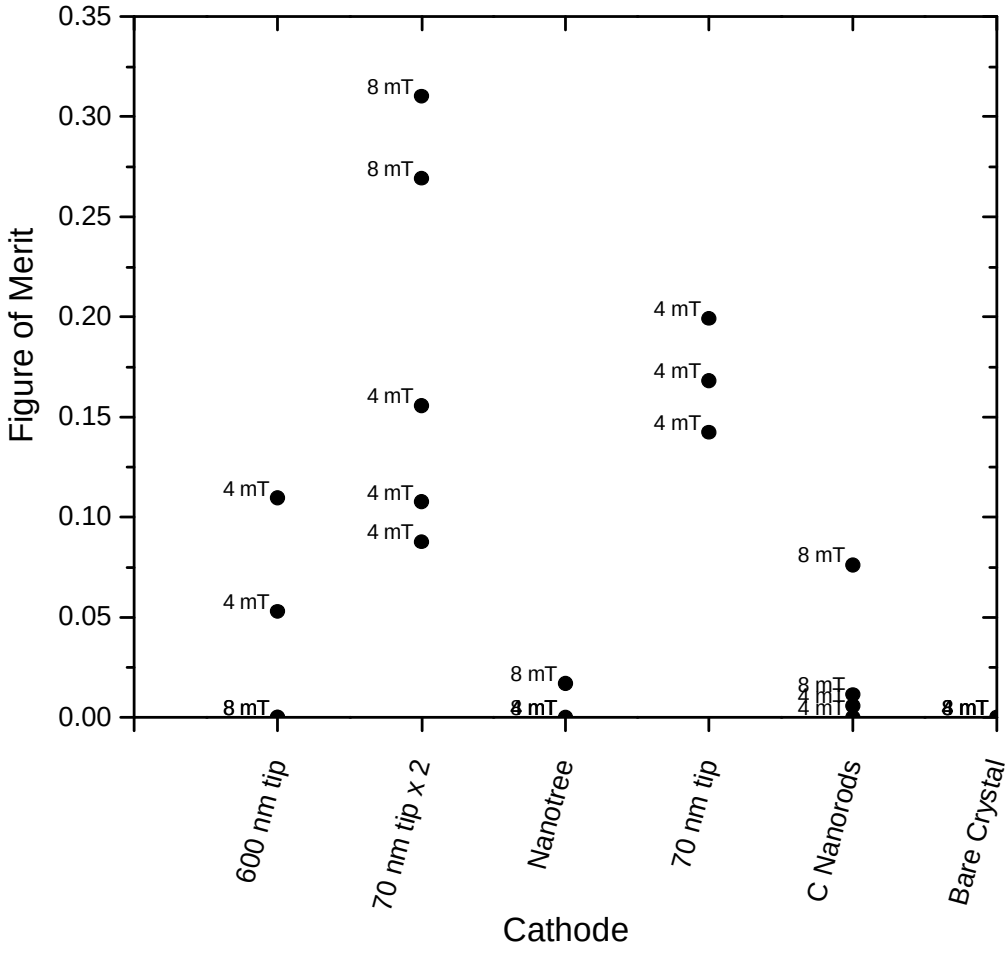

Figure 7.5 - Figure of merit for several cathode designs. The figure of merit was based on the ability to efficiently ionize a fill gas while also allowing a large acceleration potential.

8 Neutron Production Using Pyroelectric Crystals

8.1 Introduction

The successful development of improved pyroelectric x-ray and electron sources led to a search for other uses of pyroelectric crystals in radiation production. Pyroelectric crystals have been shown to generate electric potentials in excess of 200 kV in vacuum, and the ability of pyroelectric crystals to ionize gas and accelerate the ions to high energy has been proven. Therefore, it seems possible to create a neutron source in which the crystals can be used to ionize deuterium gas and then accelerate the deuterons to sufficient energy to create nuclear fusion. In this chapter, the achievement of nuclear fusion through the use of paired pyroelectric crystals will be demonstrated.

8.2 Motivation for Pyroelectric Fusion

The reason for pursuing the goal of pyroelectric fusion was to create a new source of high-energy neutrons for use in applications where portability was very important. Specifically, pyroelectric neutron sources may become very useful in homeland security and mine detection, due to their small size. (The volume of the entire source is expected to be approximately 1500 cubic centimeters). While pyroelectric fusion sources are expected to have low yield relative to conventional portable neutron generators, linear accelerator-driven sources, and reactors, they have several considerable advantages.

8.2.1 Advantages over Portable Neutron Generators [PNGs]

While only a few watts of power (~10-20 W) are required for the operation of a pyroelectric neutron source, this cannot be said to be a real advantage over pulsed PNGs. While PNG power consumption is higher than that of pyroelectric sources, it is still typically only 30-200 W[56], which is not difficult to provide. However, conventional PNGs require high voltage power supplies to provide the ~110 kV acceleration potential for the deuterium and tritium gas ions used in the fusion reaction. Therefore, even "compact" pulsed portable neutron generators tend to be quite large compared with pyroelectric sources. Table III shows a comparison of the length and weight of various portable neutron generators. Included is the size and weight of a prototype portable

pyroelectric neutron source, currently under construction at RPI. While the weight of the sources manufactured by VNIAA was not available, many of their sources (and many ThermoElectron sources) require an external power supply. The ThermoElectron[57] API 120 has an attached power supply, and had a published weight which included both the tube and supply.

Table III - Size and length of various compact neutron generators. (N/A = not available).

Neutron Source	Length, cm	Weight, kg
ThermoElectron[57] API 120	85.1	15
ThermoElectron[58] MP 320	57.2	11.3
VNIIA[56] ING-06	130	N/A
VNIIA[56] ING-07	44	N/A
VNIIA[56] ING-08	190	N/A
VNIIA[56] ING-17	24	N/A
Prototype pyroelectric source**	27	3

Another important advantage of pyroelectric sources over PNGs is that they are comparatively very inexpensive. The RPI prototype pyroelectric neutron source will have a total cost of less than $3000, and much of that cost results from the uniqueness of the source††. For example, the housing chamber of the source cost $600 to fabricate because it was made from custom metal-seal vacuum components, but any sealed metal cylinder would work in its stead. By comparison, the typical cost for a PNG is approximately $100,000.

It is also important to note that while PNGs can be used to generate 10^7 - 10^{10} n / s, certain homeland security applications such as luggage scanning require limiting the neutron yield to 10^6 - 10^7 n / s due to personnel safety concerns[56]. Therefore, in some

** Excludes weight and diameter of flanges on prototype, since a manufactured source would not required flanges. Includes 15 cm extra length for cooling fins and 1 kg extra weight for the low-voltage power supply.

†† This figure does not include the cost of the pumping system, detection electronics, or other laboratory equipment used to design and fill the source.

respects, the lower neutron yield from a pyroelectric source can be an advantage instead of a limitation.

8.2.2 Advantages over Radioisotope Sources

In addition to pulsed neutron generators, another common neutron source for field applications is radioisotopes. Radioisotopes can be manufactured cheaply, and can have a variety of energy spectra and decay constants. The source strength can chosen exactly by selecting an isotope with the proper mass and decay constant. However, there are several severe logistical problems associated with radioisotopes.

First, while isotopic sources can be small, they need to be shielded, due to the fact that they cannot be turned off. Also, if a source is chosen with a large half life (to allow its long-term use and decrease the change in neutron yield over its time of use), it creates a disposal problem.

Pyroelectric sources (and PNGs) are free from both of these problems. They can be turned on and off, thereby eliminating the need for shielding during transport. Pyroelectric D-D fusion sources are also completely safe to dispose of, aside from a small amount of neutron activation of the source itself. The disposal of tritium in a D-T pyroelectric source poses an additional concern, although tritium is among the least dangerous beta emitters due to its low maximum energy, β_{max} = 18.6 keV.

8.2.3 Advantages over Reactors and Linear Accelerators

Nuclear reactors and linear particle accelerators are both powerful means for generating large amounts of neutrons. In the case of a reactor, the neutron spectrum is white, but the flux can be very large, and many samples can be irradiated simultaneously at ports. Linear accelerators are useful for cross section measurements, since time-of-flight [TOF] method can be applied to determine the neutron energy interacting with the sample versus time.

The advantage of a pyroelectric particle accelerator over these techniques of neutron production is quite simple: Pyroelectric neutron sources are much smaller and cheaper, and can be made portable.

8.3 Calculation of Expected Yield

The expected yield from a pyroelectric D-D fusion source can be calculated by treating the deuteron beam as a monoenergetic beam slowing down in the deuterated plastic target. As the incident deuterons lose energy, the cross section for fusion is reduced. By integrating the cross section over the entire depth of penetration and multiplying by the number density of deuterons in the target, one can find the total probability per incident deuteron that fusion will occur.

The neutron yield from a pyroelectric source is a function of the incident deuteron energy, the number density of deuterons in the target, and the number of deuterons produced by the source:

$$S(t, E_0) = N_D \cdot \int_0^{d_{\max}(E_0)} \phi(x,t)\sigma(E(x))dx \qquad (49)$$

where d_{max} is the penetration depth, N_D is the number density of deuterons in the target, σ is the microscopic cross section for the neutron-producing fusion reaction, and ϕ is the total ion flux incident on the target. It is important to distinguish between the total D-D fusion cross section and the cross section for neutron production, since there are two branches of the D-D fusion reaction[59], and only one results in neutron production[60]:

$$D + D \rightarrow {}^3He + {}^1n + Q\ (3.27\ MeV)$$
$$D + D \rightarrow {}^3T + {}^1H + Q\ (4.03\ MeV)$$

It is a very good approximation to assume that half of the total D-D fusion reactions produce neutrons[60].

To first order, absorption of incident ions can be neglected, and Equation 49 can be simplified by assuming that the ion flux is not a function of penetration depth. In this simplification, the ions penetrate to same depth in the target, and simply lose energy as they penetrate. It is also reasonable to assume a monoenergetic ion flux. This assumption is valid because the neutron production usually occurs during one to two minutes of the cooling phase, during which time the field strength does not change rapidly. By applying these assumptions, Equation 49 becomes:

$$S(t) = A \cdot N_D \cdot \phi(t) \int_0^{d_{\max}(E_0)} \sigma(E(x))dx \qquad (50)$$

$$S_{total} = A \cdot N_D \cdot \int_0^t \phi(t)dt \cdot \int_0^{d_{\max}(E_0)} \sigma(E(x))dx \qquad (51)$$

The beam area can now be multiplied by the integrated current to find the total incident ion charge, q. By dividing the ion charge by the charge per ion (1.6×10^{-19} C), we can find the total number of ions incident on the target. Equation 51 then becomes:

$$S_{total} = \frac{q}{1.6 \times 10^{-19}} \cdot N_D \cdot \int_0^{d_{\max}(E_0)} \sigma(x)dx \qquad (52)$$

The slowing down of the incident deuterons in the target was calculated using[61] SRIM 2003. The target was assumed to be deuterated polyethylene, with a density of 0.9 g / cm^3. An error in the density estimate is unimportant, since changes to the density estimate would cause changes in both the stopping power and number density, which would offset each other in the fusion rate calculation. The energy loss per unit length was input into Mathcad for a range of data points between 10 and 300 keV, and a linear interpolation was applied to estimate the value between these points. Figure 8.1 shows a plot of the slowing down of 100 keV incident deuterons in a deuterated polyethylene target.

If the deuterons are assumed to have a constant linear energy loss (i.e., the linear energy loss for the incident deuteron energy is applied to the entire penetration depth), a slight error would be introduced in the neutron yield calculation. This error tends to lead to lower the estimate of neutron yield, since the calculated range of the incident particles is lowered. However, since most neutron production occurs at high energy, the effect of this simplification on the calculation of energy loss is small. For 100 keV D^+ ions, the assumption of constant linear energy loss leads to an estimate of 407 neutrons per nano-Coulomb of incident charge, versus an estimate of 428 neutrons per nC if SRIM is used to calculate the energy loss. Figure 8.2 shows a plot of linear energy loss versus depth in the target for deuterons with 100 keV incident energy, as calculated using SRIM.

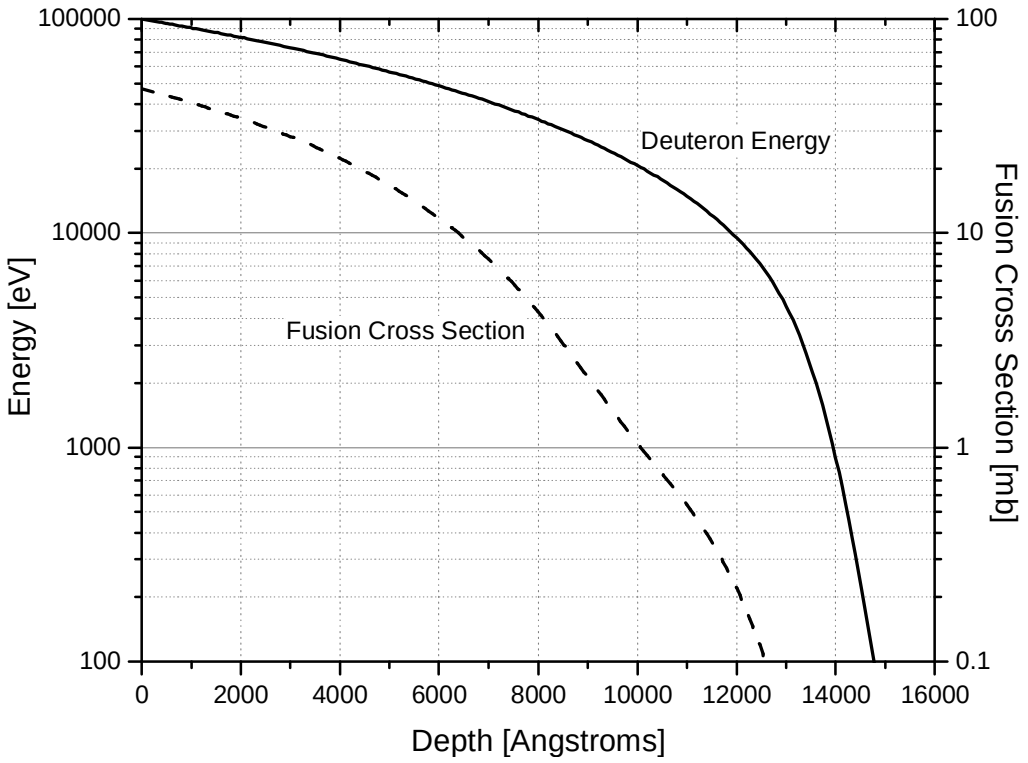

Figure 8.1 - Slowing down of 100 keV incident D^+ ions in 0.9 g / cm^3 DPE. Most of the neutrons are produced in a thin layer at the surface of the target. After the ions penetrate 1 μm (10000 Angstroms) into the target, the cross section for fusion is reduced to below 1 mb.

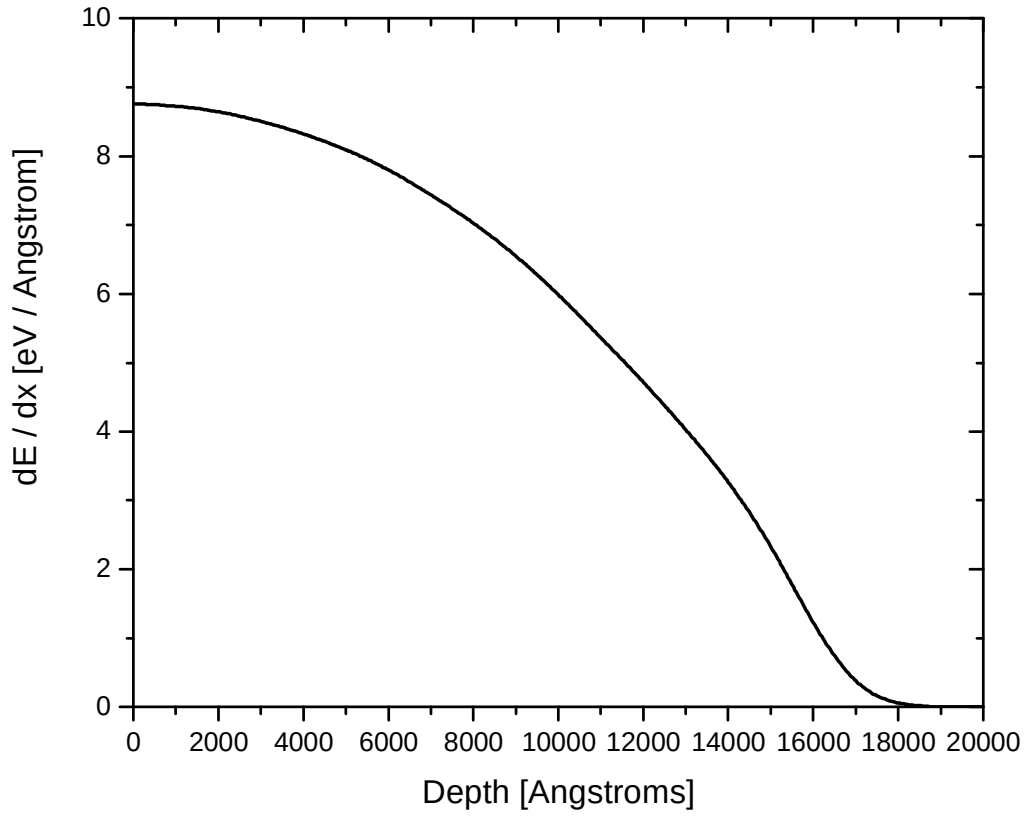

Figure 8.2 - Linear energy loss vs. depth for 100 keV incident D^+ ions penetrating a DPE target. Calculated using SRIM 2003.

The energy at a depth *x* in the target for a given initial energy E_0 was found by subtracting the integrated energy loss per unit length from the initial energy:

$$E(x) = E_0 - \int_0^x \left(\frac{dE}{dx}\right)_{E_0}(x)dx \tag{53}$$

The cross section integrated over the entire depth of penetration could then be found by integrating with respect to depth:

$$\sigma_{\text{int}} = \int_0^{d_{\max}(E_0)} \sigma(x)dx \tag{54}$$

The maximum penetration depth, $d_{max}(E_0)$, corresponds to the depth in the target at which the energy of the deuterons reaches zero.

One can then find P_{fusion}, the probability of producing fusion per incident ion, by multiplying the integrated cross section by the number density of the target deuterons, N_D:

$$P_{fusion} = N_D\left[\mathrm{cm}^{-3}\right]\int_0^{d_{\max}(E_0)}\sigma(x)\left[\mathrm{cm}^2\right]dx[\mathrm{cm}] \tag{55}$$

The deuterium number density is found by multiplying the C_2D_4 target density, 0.9 g / cm^3, by the atom fraction of deuterons in the deuterated polyethylene target and then dividing by the molar mass:

$$N_D = 0.9\frac{\mathrm{g}}{\mathrm{cm}^3}\cdot 4\frac{\mathrm{D}}{\mathrm{molecule}}\cdot 6.02\times 10^{23}\frac{\mathrm{molecules}}{\mathrm{mol}}\cdot 1\frac{\mathrm{mol}}{32\,\mathrm{g}} \tag{56}$$

$$N_D = 6.77\times 10^{-10}\frac{\text{deuterium atoms}}{\text{barn}\cdot\text{Angstrom}} \tag{57}$$

As an estimate of the theoretical limit for the neutron yield from a pyroelectric source, one can assume that all of the charge produced by the pyroelectric effect during a typical experiment (ΔT = 120 °C) is converted to D^+ ions, which are all accelerated at 180 keV. This is typically the maximum acceleration potential observed when operating with a deuterium fill gas.

The total ion production would then be:

$$\phi_D = \gamma\cdot\Delta T\cdot A \tag{58}$$

$$\phi_D = 190\times 10^{-10}\frac{\mathrm{C}}{\mathrm{cm}^2\,^{\circ}\mathrm{K}}\cdot 120^{\circ}\mathrm{K}\cdot 3.14\,\mathrm{cm}^2 \tag{59}$$

$$\phi_D = 7.16\,\mu\mathrm{C} = 4.47\times 10^{13}\ \text{deuterons} \tag{60}$$

The penetration depth of 180 keV deuterons in DPE is calculated to be 29000 Å. By integrating the cross section over this depth, the total integral cross section for the neutron-producing branch of the D-D fusion reaction is found to be σ_{int} = 418 bÅ [barn-Angstroms]. Given the target deuteron density of 6.77 x 10^{-10} / (barn Å), the total fusion neutron production S is:

$$S = 4.47\times 10^{13}\,\text{deuterons}\cdot 6.77\times 10^{-10}\,\mathrm{b}^{-1}\mathrm{Angstrom}^{-1}\cdot 418\,\mathrm{b\ Angstrom} \tag{61}$$

$$S = 1.26\times 10^{7}\ \text{neutrons per heating cycle} \tag{62}$$

It is unrealistic to expect to obtain this yield from a D-D fusion source driven by 20 mm diameter $LiTaO_3$ crystals, for several reasons. First, not all of the charge generated by the crystal is converted into D^+ ions: Since the target crystal is negatively charged during the phase in which fusion occurs, much of the positive charge on the ion-emitting crystal will be neutralized by incident electrons from the opposing crystal. Second, it cannot be guaranteed that the deuterium molecule will be separated during the ionization process. If some of the charge is emitted as D_2^+ instead of D^+, then the energy per deuteron will be reduced by a factor of two, and the cross section for fusion will be greatly diminished. Finally, the assumption that every ion is emitted at the typical maximum energy of 180 keV was based on the fact that, as the field strength increases, so does the ionization probability, such that most ions will be accelerated to a value close the maximum acceleration potential. It is more realistic to assume that, while most ions will be accelerated to the maximum potential due to the increased ionization probability at high field strengths, many ions will still be emitted at lower field strengths, and will therefore not have such a high acceleration potential.

8.3.1 The Question of Power Production

A common question regarding pyroelectric fusion is this: Is it possible to generate a net positive power output using pyroelectric crystals? In order to answer this question, an ideal paired-crystal system will be assumed, in which all of the charge produced by the positively-charged crystal is assumed to be converted to tritium ion current at 250 keV. The probability of fusion per incident 250 keV triton in a deuterated polyethylene target is found by numerically calculating the solution to Equation 55. This gives $P_f = 1.26 \times 10^{-4}$ for 250 keV tritons.

The crystals are assumed to be lithium tantalate, $\gamma = 190\ \mu C / m^2\ °K$. Therefore, if the crystals were heated by $\Delta T = 100\ °K$, they would generate a surface charge density of $\sigma = 19\ mC / m^2\ °K$. The crystals are taken to be 1 cm (0.01 m) thick, in accord with the neutron production experiments performed at RPI and UCLA. The area of the crystals is taken to be 1 cm^2. If all of this charge is converted to ions, and 1.26×10^{-4} fusion events occur for every incident ion, then the total number of fusion events due to the heating of the crystals would be:

$$S = (\text{pyroelectric coefficient} \cdot \text{area} \cdot \Delta T) \times (1.26 \times 10^{-4} \text{ fusion events per ion}) \quad (63)$$

$$S = 1.90 \times 10^{-2} \frac{\text{C}}{\text{m}^2} \cdot \frac{1\,\text{m}^2}{10000\,\text{cm}^2} \cdot \frac{1.26 \times 10^{-4} \text{ fusion events}}{1.602 \times 10^{-19}\ \text{C}} \quad (64)$$

$$S = 1.49 \times 10^{9} \text{ fusion events} \quad (65)$$

The energy release can be found by multiplying the number of fusion events by the energy released per event, which, for a D-T reaction[59], is 17.6 MeV. If it is assumed that all of the energy released per fusion can be recovered as heat, then the expected energy output would be:

$$E = 1.49 \times 10^{9} \frac{\text{fusion events}}{\text{cm}^2} \cdot 17.6 \frac{\text{MeV}}{\text{fusion event}} \cdot 1.602 \times 10^{-13} \frac{\text{J}}{\text{MeV}} \quad (66)$$

$$E = 4.2 \frac{m\text{J}}{\text{cm}^2} \quad (67)$$

Since the crystals were assumed to be 1 cm thick, and there are two crystals in the system, this corresponds to an energy output of 2.1 mJ / cm^3.

Therefore, in order to generate a positive power output from heating this system, one would need to be able to heat the crystals with less than 2.1 mJ / cm^3 of energy. Glass[20] found that the specific heat of $LiTaO_3$ varied with temperature, going from c_p = 24 ± 2 cal / mol °K at 298 °K (room temperature) to a value of c_p = 28 cal / mol °K at 433 °K. Therefore, an average value of 26 cal / mol °K shall be used for this calculation. Assuming no losses due to heat transfer to the surrounding environment and experimental components, the heat required to raise the crystal by 100 °K is:

$$H = N \cdot c_p \cdot \Delta T \quad (68)$$

where N is the number of moles in the sample. In this case, the crystal was assume to have a volume of 1 cm^3. Therefore, if n is the molecular mass, V is the sample volume, and ρ is the density of lithium tantalate (7.46 g / cm^3), then:

$$N = \frac{V \cdot \rho}{n} = 1\,\text{cm}^3 \cdot 7.46 \frac{\text{g}}{\text{cm}^3} \cdot \frac{1\,\text{mol}}{236\,\text{g}} \quad (69)$$

$$N = 0.032\,\text{mol} / \text{cm}^3 \quad (70)$$

Plugging this back into Equation 68:

$$H = 26 \frac{\text{cal}}{\text{mol}\ ^{\text{o}}\text{K}} \cdot 4.18 \frac{\text{J}}{\text{cal}} \cdot 0.032\,\text{mol} \cdot 100^{\text{o}}\,\text{K} \quad (71)$$

$$H = 347\ \mathrm{J/cm^3} \tag{72}$$

Therefore, 2.1 mJ / cm^3 of energy could be recovered from fusion, but even with ideal heating, 347 J / cm^3 would be needed to heat the crystals. The fusion yield could be increased by using a crystal with larger area, since the pyroelectric coefficient (which dictates the ion yield) is a linear function of crystal area. However, this would result in a greater crystal volume, which also scales linearly with area. Using a thinner crystal to reduce the required heat would result in a decrease in the acceleration potential, as shown in Figure 4.8. Pyroelectric crystals cannot therefore be used to generate fusion power, unless a crystal is found which can create a much higher potential for a given amount of heating energy than a lithium tantalate crystal of equivalent thickness. This seems unlikely, since the energy output found in this optimistic calculation was ~2 x 10^5 times less than the energy input.

8.4 Experimental Setup

8.4.1 Effect of Target Thickness on Acceleration Potential

When it was first proposed that a plastic target be introduced between the crystals, concern was raised that the target would lower the acceleration potential available to accelerate the ions, since the ions would stop before being accelerated all the way to the charged face on the target crystal. However, it can easily be shown that this effect can be disregarded.

First, assume that the crystals are two infinite parallel plates, separated by 2 cm of vacuum ($\varepsilon = \varepsilon_0$). Next assume that the target is a uniform layer between the crystals, with a thickness of 45 μm. (This is the measured thickness of a layer of deuterated polystyrene similar to those used in the neutron production experiments presented in this chapter. The measured target was noticeably thicker than the targets used in most experiments). The dielectric constant of polyethylene and polystyrene is approximately[28] 2.5 ε_0. From Gauss' Law[62], the electric field due an infinite uniform surface charge is:

$$\left|\vec{E}\right| = \frac{\sigma}{2\varepsilon_0} \tag{73}$$

Therefore, the potential between the crystals would be equal to:

$$V = -2 \cdot \left(\int_0^{45\,\mu\text{m}} \frac{\sigma}{2 \cdot 2.5\varepsilon_0} dz + \int_{45\,\mu\text{m}}^{2\,\text{cm}} \frac{\sigma}{2 \cdot \varepsilon_0} dz \right) \tag{74}$$

$$V = -\left(\int_0^{45\,\mu\text{m}} \frac{\sigma}{2.5\varepsilon_0} dz + \int_{45\,\mu\text{m}}^{2\,\text{cm}} \frac{\sigma}{\varepsilon_0} dz \right) \tag{75}$$

where σ is the surface charge density, and the factor of two by which the term in parenthesis is multiplied is due to the superposition of the electric fields from two crystals. For a given surface charge, this calculation shows that the potential between the crystals, after this 45 μm-thick plastic target is added, is still 0.9964 times its value without the plastic. This shows that a thin plastic layer can safely be used as a target between the crystals without drastically reducing the acceleration potential.

8.4.2 Choice of Fill Gas

The cross section for nuclear fusion in a deuterated target is greatly dependent on the choice of fill gas. There are four important nuclear reactions to consider:

$$D + D \rightarrow {}^3He + {}^1n$$

$$D + D \rightarrow {}^3T + {}^1H$$

$$D + T \rightarrow {}^4He + {}^1n$$

$$D + {}^3He \rightarrow {}^4He + {}^1H$$

Of these reactions, D-T fusion has by far the highest cross section in the energy range attainable with pyroelectric crystals. However, tritium is radioactive, emitting a beta particle[63] with a half-life of $\tau_{1/2}$ = 12.32 years and a maximum energy of 18.6 keV. Therefore, it is not convenient to conduct laboratory experiments with a D-T source. (In the future, D-T will provide the most viable option for a high-yield commercial source, since a commercial source would not have to be vented and re-filled, thus containing the tritium inside the reaction chamber). At high energy (E > 120 keV), the D-^{3}He fusion has a greater cross section than D-D fusion. The product of D-^{3}He fusion is not a neutron, however, but a proton. Therefore, while ^{3}He may be an interesting fill gas in the production of a compact proton source, it is not a useful gas for the manufacture of a neutron source.

Figure 8.3 shows the cross section for three fusion reactions. These cross sections were calculated using a fit based on the five Duane coefficients for each reaction[64]:

$$\sigma_T(E) = \frac{A_5 + \left[(A_4 - A_3 E)^2 + 1\right]^{-1} A_2}{E\left[\exp(A_1 E^{-1/2}) - 1\right]} \qquad (76)$$

Here the energy is given in units of keV and the cross section is given in barns. The Duane coefficients for the plots shown in Figure 8.3 are listed in Table IV.

Table IV - Duane coefficients[64] for selected fusion reactions.

	$D(d,t)^1H$	$D(d,n)^3He$	$D(t,n)^4He$	$D(^3He,^4He)^1H$
A_1	46.097	47.88	45.95	89.27
A_2	372	482	50200	25900
A_3	4.36×10^{-4}	3.08×10^{-4}	1.368×10^{-2}	3.98×10^{-3}
A_4	1.220	1.177	1.076	1.297
A_5	0	0	409	647

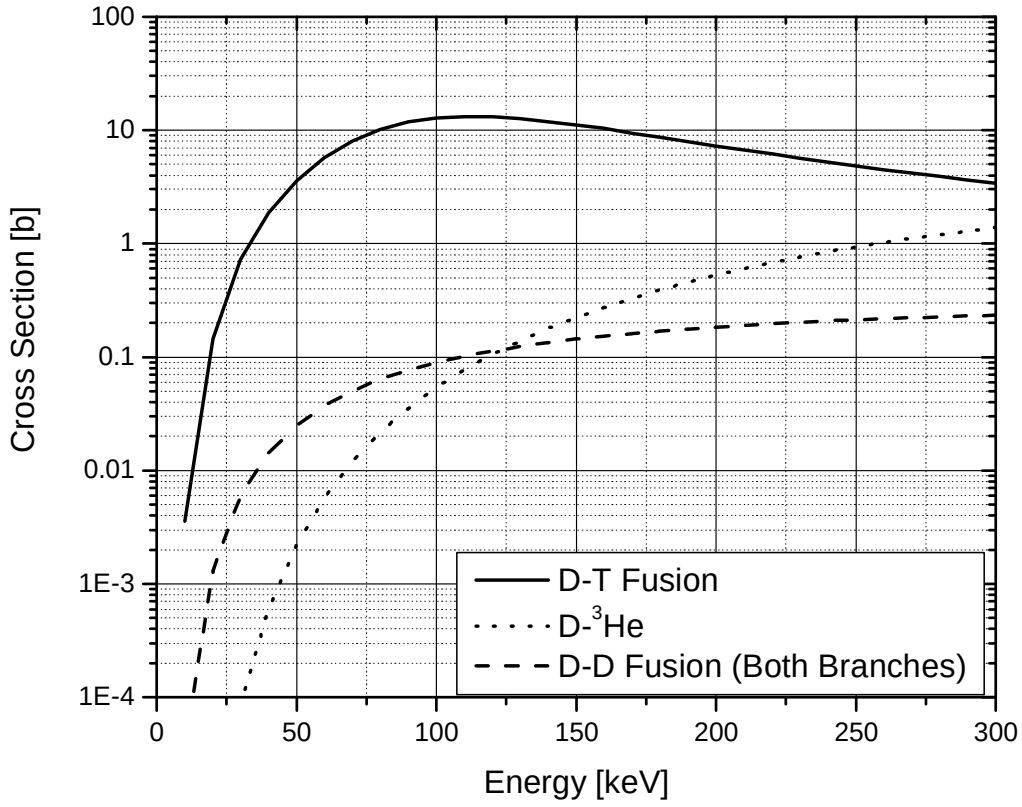

Figure 8.3 - Cross sections for three fusion reactions, calculated using Equation 76.

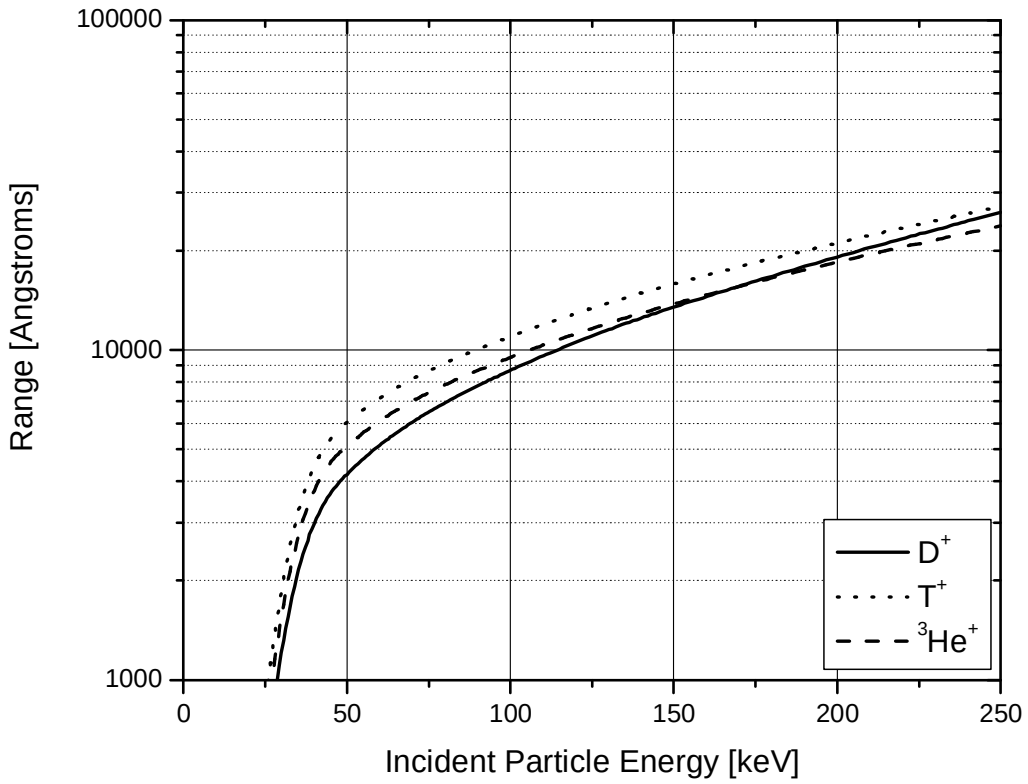

Figure 8.4 - Range for three incident ions in 0.9 g / cm^3 deuterated polyethylene. Range data[61] was found with a SRIM 2003 Monte Carlo calculation.

This leaves D-D fusion as the most convenient choice for laboratory experiments with pyroelectric crystals. In the experiments presented in this chapter, a deuterium fill gas was ionized near a metallic tip mounted to a crystal, which then accelerated the ions into a deuterated plastic target layer on an opposing crystal. Deuterium is stable, and is also inexpensive ($200 for 50 L). It is important to reiterate, however, that only one of the two possible D-D fusion reactions produces neutrons. Since the reactions occur with almost equal probability, only one neutron will be produced for every two D-D fusion events.

In the case of pyroelectric fusion, since the incident ions slow down as they penetrate the target, the number of fusion events must be calculated by integrating the cross section over the penetration depth of the ion in the target. The total expected fusion events per nano-Coulomb of incident ions is plotted in Figure 8.5, although only fusion events from the neutron-producing branch of the D-D reaction are included. It is interesting that, while the D-^{3}He reaction has a higher cross section than D-D fusion at high

energy, the integration of the cross section curve for the whole range of particle energy due to slowing-down in the target negates this advantage, and the result is that the neutron-producing D-D reaction and D-^{3}He have nearly the same yield for the entire energy range between 100 keV and 250 keV.

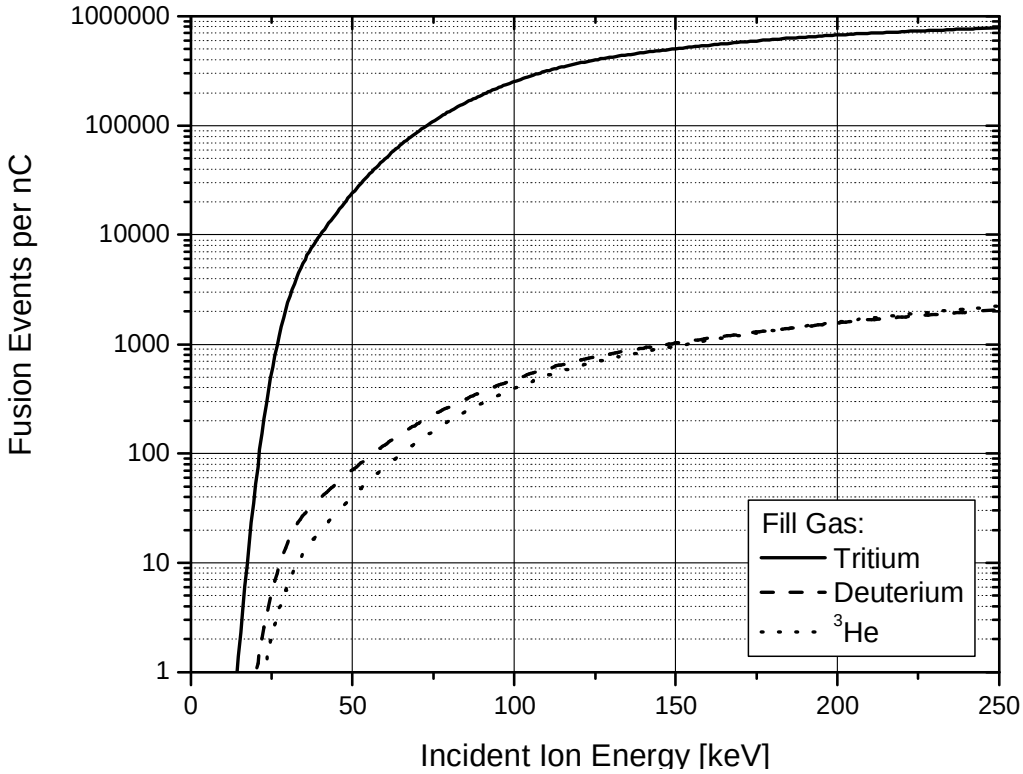

Figure 8.5 - Fusion events per nC incident D^+ ions for three different fill gases. A deuterated polyethylene target is assumed. Only the neutron-producing D-D reaction is included.

8.4.3 Gas Ionization

8.4.3.1 Calculation of Ion Yield from Impact Ionization Events

Effective deuterium gas ionization is essential to the production of neutrons with a pyroelectric crystal. Successful neutron production experiments[65] showed that some deuterium gas ionization must have occurred in experiments using paired 10 mm-thick lithium tantalate crystals. In the first of these experiments, a copper disc holding an ionizing 70 nm catwhisker tip was mounted to the crystal surface using conductive epoxy. The results were later repeated in a similar experiment using a 200 nm-radius tip

mounted with conductive epoxy. (Later, both experiments were repeated with non-conductive epoxy).

It is important to consider the contribution, if any, of impact ionization by electrons traveling through the fill gas. From the ideal gas law, one can estimate the concentration of gas molecules *n* based on the gas pressure *P*, the gas temperature *T*, and the universal gas constant, $R = 82.05$ (L atm) / (kmol °K):

$$\frac{n}{V} = \frac{P}{RT} \tag{77}$$

For a gas at 4 mTorr (5.26×10^{-6} atm) at 273°K, this yields:

$$\frac{n}{V} = \frac{5.26\times10^{-6}}{82.05\cdot 273}\frac{\text{kmol}}{\text{L}} = 2.35\times10^{-7}\,\frac{\text{mol}}{\text{L}} \tag{78}$$

The gas density is therefore 4.7×10^{-10} g / cm^3. ESTAR[46] gives the stopping power of deuterium for 100 keV electrons as 8.74 MeV cm^2 g^{-1}. Therefore, the energy deposited per unit length in a 4 mTorr D_2 gas is:

$$8.74\,\frac{\text{MeV cm}^2}{\text{g}}\cdot 4.7\times10^{-10}\,\frac{\text{g}}{\text{cm}^3} = 0.0041\frac{\text{eV}}{\text{cm}} \tag{79}$$

The W-value, or average energy loss per ion pair created, is 36.5 eV for H_2 gas[66]. This value is higher than the ionization potential for H_2 because ionization is not the only mode by which charged particles can lose energy in a fill gas. On average, therefore, an electron would need to travel $36.5\,\text{eV} \div .0041\,\text{eV/cm} = 89$ meters to deposit enough energy to ionize a singly H_2 (or D_2) molecule.

Table V - Ionization potential of different gas species[28,67]. "N/A" = not applicable.

Gas Species	First Ionization Potential, V	Second Ionization Potential, V
H_2	15.426	*N/A*
H	13.598	*N/A*
He	24.587	54.418
C	11.260	24.383
N	14.534	29.601
N_2	15.581	27.12
O	13.618	35.117

O_2	12.071	*N/A*
CO_2	13.773 ± .002	*N/A*
H_2O	12.612	*N/A*

However, it was seen in Section 3.2 that a 20 mm diameter crystal (such as those used in the fusion experiments discussed in this chapter) emitted -368 nC of electrons during a heating phase, corresponding to 2.3 x 10^{12} electrons. If all of the charge is assumed to be emitted as electrons at 100 keV, the total energy deposited in the fill gas per unit length is found to be:

$$0.0041\frac{\text{eV}}{\text{electron cm}}\cdot 2.3\times10^{12}\,\text{electrons} = 9.43\frac{\text{GeV}}{\text{cm}} \qquad (80)$$

Since 36.5 eV is required to ionize a hydrogen molecule, and assuming a similar ionization potential is required for deuterium, one would expect $9.43\,\text{GeV/cm} \div 36.5\,\text{eV/ion pair}$ = 2.58 x 10^8 ion pairs per cm, or approximately one impact ionization event for every 10^4 electrons emitted at 100 keV in 4 mT of D_2. However, since many of these ions will be created far from the crystal, they will not all accelerate to the full energy available due to the potential between the crystals. Instead, the ions would form a continuum of energy, as represented by the peak tails in Figure 3.2. The counts in the tail can be controlled, therefore, by changing the D_2 fill gas pressure.

8.4.3.2 Surface Barrier Detector Measurement of Ion Current from a Tipped Crystal

The ionizing tip causes an increase in current due to field ionization. In an effort to determine how to improve the neutron yield, measurements of the ion energy from tipped crystals were performed using a Canberra PIPS A-300-19-AM surface barrier detector.

In the first such experiment, the ion source was a 70 nm catwhisker tip mounted to a 16 mm diameter copper disc. The disc was attached to a 10 mm thick, 20 mm diameter lithium tantalate crystal using either conductive silver paint or non-conductive JB weld epoxy. The collimator aperture area was approximately 1/50 mm^2. The crystal was heated from room temperature to ~130^{o}C over 600 seconds, and was then allowed to

cool to room temperature naturally. The distance from the crystal to the collimator was 4 cm.

Figure 8.6 shows typical results from this experiment. The tip mounted to the crystal with a conductive interface never produced an observable ion peak. The entire spectrum was composed of bremsstrahlung x-rays, which usually had a maximum energy of around 80 keV. (The maximum x-ray energy was difficult to measure, since high count rates often resulted in pulse pileup and dead times of >50%.) When the tip was mounted to the crystal with non-conductive epoxy, a clearly-visible ion peak was observed on top of the bremsstrahlung continuum. The dead time for the non-conductive epoxy spectrum shown in Figure 8.6 was 6%. The dead time for the experiment with conductive paint was 20%. The maximum ion peak energy observed for a 70 nm tip mounted with non-conductive epoxy was 74 keV.

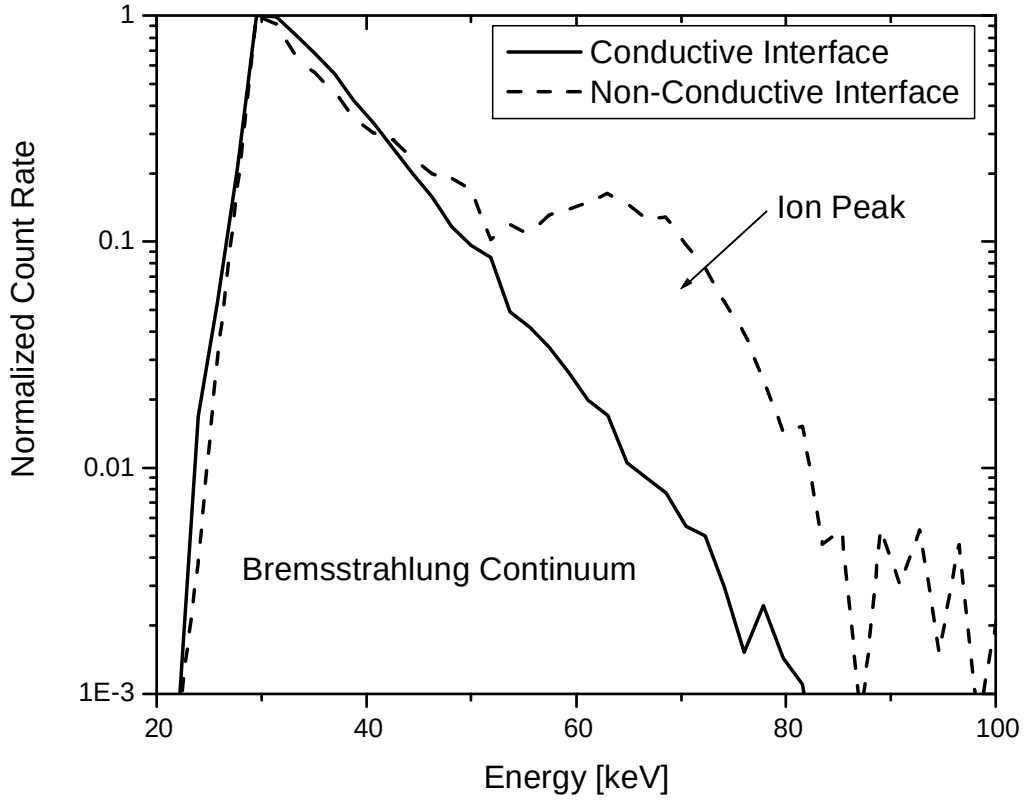

Figure 8.6 - Ion emission spectra measured by a collimated PIPS detector for deuterons ionized by 70 nm tips mounted to a 10 mm thick, 20 mm diamter $LiTaO_3$ crystal. The use of a non-conductive interface between the tip and crystal resulted in a visible ion peak.

When the 70 nm tip was replaced with a 200 nm tip, the results changed somewhat. The tip mounted with conductive paint yielded ion peaks, but they were low in energy (<55 keV) and unclear relative to the peaks observed with non-conductive epoxy. The tip mounted with non-conductive epoxy yielded peaks with up to 79 keV energy, which is similar to the 70 nm tip results explained earlier. Figure 8.7 shows the results from typical experiments. The dead time for the non-conductive epoxy plot was 10%. For the conductive epoxy plot, the dead time was 30%. (The collimator aperture for the experiments with the 200 nm tip was ~1/15 mm^2.)

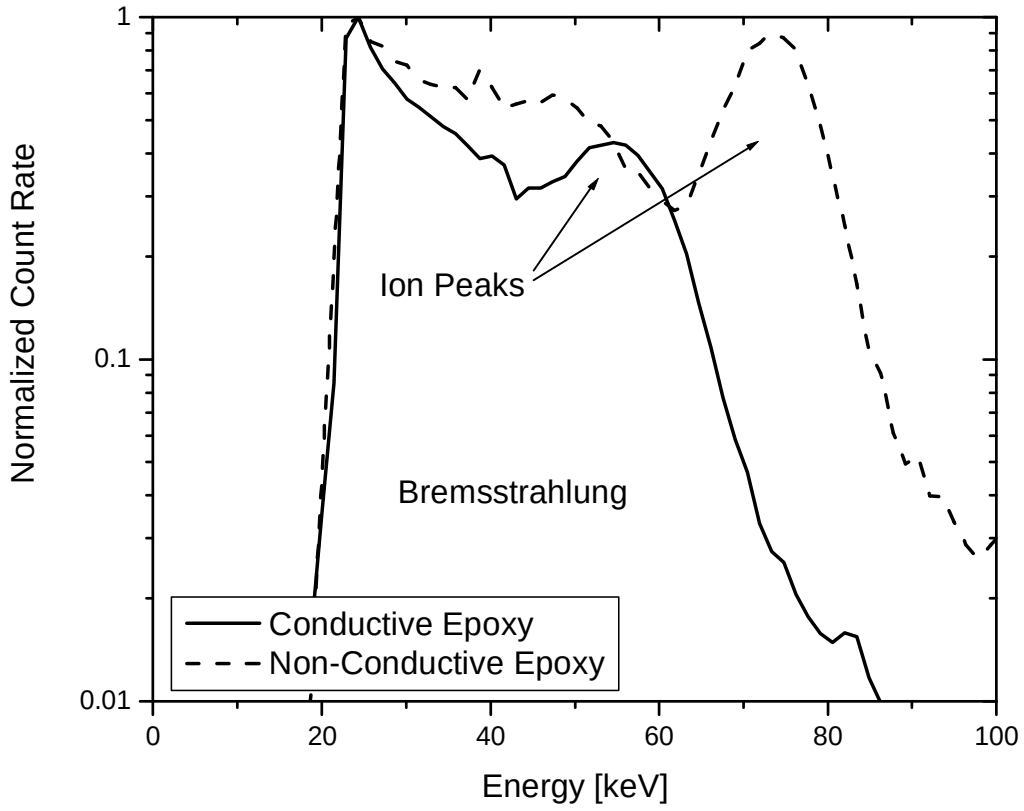

Figure 8.7 - Ion emission spectra for 200 nm-radius ionizing tip mounted to a 10 mm thick, 20 mm lithium tantalate crystal. Ions were seen for both a conductive- and non-conductive interface.

Both of these experiments suggest that the ion energy is improved when a non-conductive interface material is used to mount the tips to the crystals. In the case of the 70 nm tip mounted with conductive paint, the ion peak was not even visible, suggesting that it was either below the discriminator level of the detector (25 keV) or that ions were not produced. It is thought that the ionization efficiency was too high to allow a high

acceleration potential to build up, and that the reduction of ionization efficiency by switching to non-conductive epoxy remedied this problem. This is evidence that the 200 nm tip is less efficient in ionizing gas than the 70 nm tip, since it yielded a visible ion peak even when conductive paint was used in place of non-conductive epoxy, suggesting that the crystal was able to reach a higher potential before ionizing the gas.

8.4.4 Target Preparation

Two types of deuterated targets were used in these experiments. In the first successful fusion experiments conducted at RPI[65], the target was deuterated polystyrene, -$(C_8D_8)_n$-, in a ~45 μm layer[‡‡] on the surface of the target crystal. To prepare the target, about a hundred milligrams of deuterated polystyrene [DPS] were placed in a jar containing roughly 75 mL of xylene. The jar was placed on a hot plate in a fume hood, and was heated to around 120°C, just below the boiling point of xylene[68], which is 135-145°C. After a short period of time, the chunks of DPS could be seen to distort and expand. Within about an hour, the DPS was completely dissolved. At this point, the xylene was brought to its boiling point, and was gently boiled to thicken the solution. A pipette was then used to transfer some of the solution to the surface of the target crystal. The surface tension of the solution was usually enough to keep the solution from running down the sides of the crystal. In the event that some of the solution did flow down the side of the crystal, it could be wiped off with an acetone-soaked cotton swab once dry.

It is important to mention that the flash point of xylene[68] is only 27 - 32°C, which is far below the temperature to which it was heated during target preparation. For this reason, it is important to avoid sparks and not to carry cellular phones near the fume hood where the target is being prepared, since the vapors from xylene can ignite due to a spark once it is heated past the flash point.

Deuterated polystyrene was easy to work with, and created even target layers on the crystal. However, in terms of usefulness in neutron production experiments, it is surpassed by deuterated polyethylene [DPE]. Deuterated polyethylene -$(C_2D_4)_n$- was

[‡‡] The thickness of the layer was estimated by depositing an equivalent amount of deuterated polystyrene / xylene solution on a piece of metal as was deposited on the crystal. The thickness of the layer on the metal was then measured with a DeFelsko 6000-series Eddy current thickness gauge.

eventually chosen over DPS due to its improved deuterium density. However, it was much more difficult to dissolve polyethylene in the hot xylene. The method of making a solution was kept the same, except that the solution had to be kept on the hot plate below the boiling point for about four to six hours before most of the DPE was dissolved. If the solution was used prematurely, when the DPE was soft and transparent but not completely dissolved, then the target would appear white and flaky once the xylene had evaporated. However, by keeping the mixture hot for four to six hours before boiling, a smooth, transparent target could be made. Due to the thinness of the solutions, the surface tension of the DPE target was usually not sufficient to hold it on the surface of the crystal while it was deposited and dried. Instead, a razor or cotton swab was used to remove the excess from the sides of the crystal after the target was dry.

A third target option would have been to use a metal implanted with deuterium, such as erbium deuteride (ErD_3). This was the method used in the UCLA pyroelectric fusion experiments[17]. However, deuterated polystyrene is superior to erbium deuteride in terms of the total fusion cross section for a deuteron slowing down to below the threshold energy for fusion in the target. [See Figure 8.8].

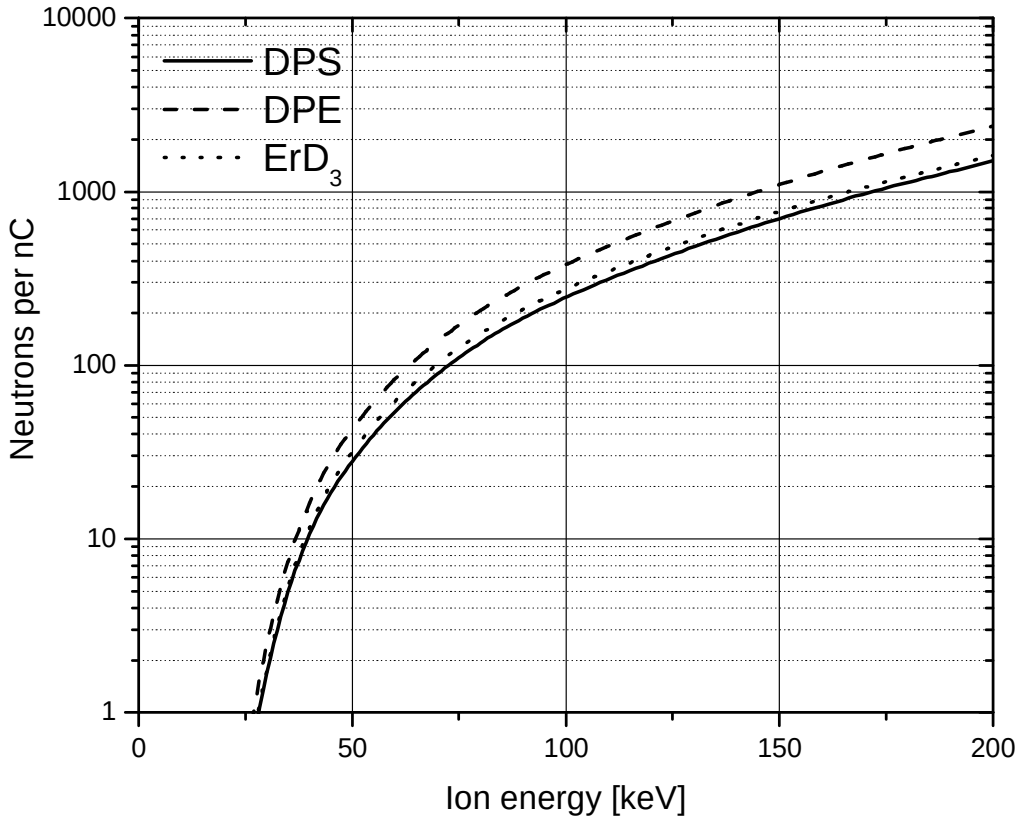

Figure 8.8 - Number of fusion neutrons produced per nano-Coulomb of incident deuterons for three viable target options.

8.4.5 Mounting the Crystal

The neutron production experiments presented in this chapter used two lithium tantalate crystals mounted such that the z+ face of one crystal was opposite to the z- face of the other crystal. Both crystals were cylindrical, with a thickness (along the polarization axis) of 10 mm and a diameter of 20 mm.

Each crystal was attached to a thermoelectric heater, which was typically a Melcor HT-series device such as the HT3-12-30-T2, with a maximum temperature of 225°C and a maximum power input of 30 W. The crystal was attached to the heater with GC Electronics #19-2092 electrically-conductive epoxy. The crystal was worked back and forth to spread the epoxy layer to entire interfacial area between the crystal and heater. The electrically conductive epoxy was found to help prevent crystals from cracking during heating or cooling, which appears to be caused by electrical sparking through the

crystal. A 5 mm wide strip of conductive metal such as copper was placed between the crystal and the thermoelectric heater to provide ground.

Once the crystals were mounted to the thermoelectric devices, a thermocouple was epoxied with JB Weld to the corner of one thermoelectric cooler to provide temperature indication. At this time, the target crystal was coated with the deuterated plastic target. A 70 nm-apex catwhisker tungsten tip with a shank diameter of 0.5 mm and a length of 3-4 mm was soldered to a copper disc with a diameter of 16 mm. The disc was polished with a wire brush on a Dremel tool to remove burrs and ridges along the outside edge. A hole was drilled through the center of the disc to allow the shank of the tip to be fixed in place prior to soldering. After the tip was soldered in place, the excess shank protruding from the back of the disc was cut off with pliers and sanded smooth.

JB Weld non-conductive epoxy was deposited onto the surface of the ion-emitting crystal, with 2 mm along the edge of the crystal left bare. The copper disc was then pressed into the epoxy. The practice of leaving a ring of bare crystal on the outside of the disc was found to inhibit spark discharge, which occurred in great frequency when the epoxy was deposited all the way out to the edge of the crystal. It is also important to not leave a gap underneath the crystal, since this can create a region of high electric field strength, which can also lead to enhanced probability of discharge.

Once the epoxy and target were dry, the thermoelectric coolers were mounted with nylon screws to a copper heat sink. The heat sink consisted of two 20 mm x 50 mm x 50 mm rectangular uprights mounted onto a base. The base was 100 mm x 100 mm x 38 mm, with a removable 100 mm x 32 mm x 24 mm cold finger in the bottom, through which a U-tube could carry cooling liquid. The edges of the entire copper assembly were chamfered to avoid creating regions of locally high electric field which would help cause discharge. CAD drawings of the assembled experiment are shown in Figure 8.9 and Figure 8.10.

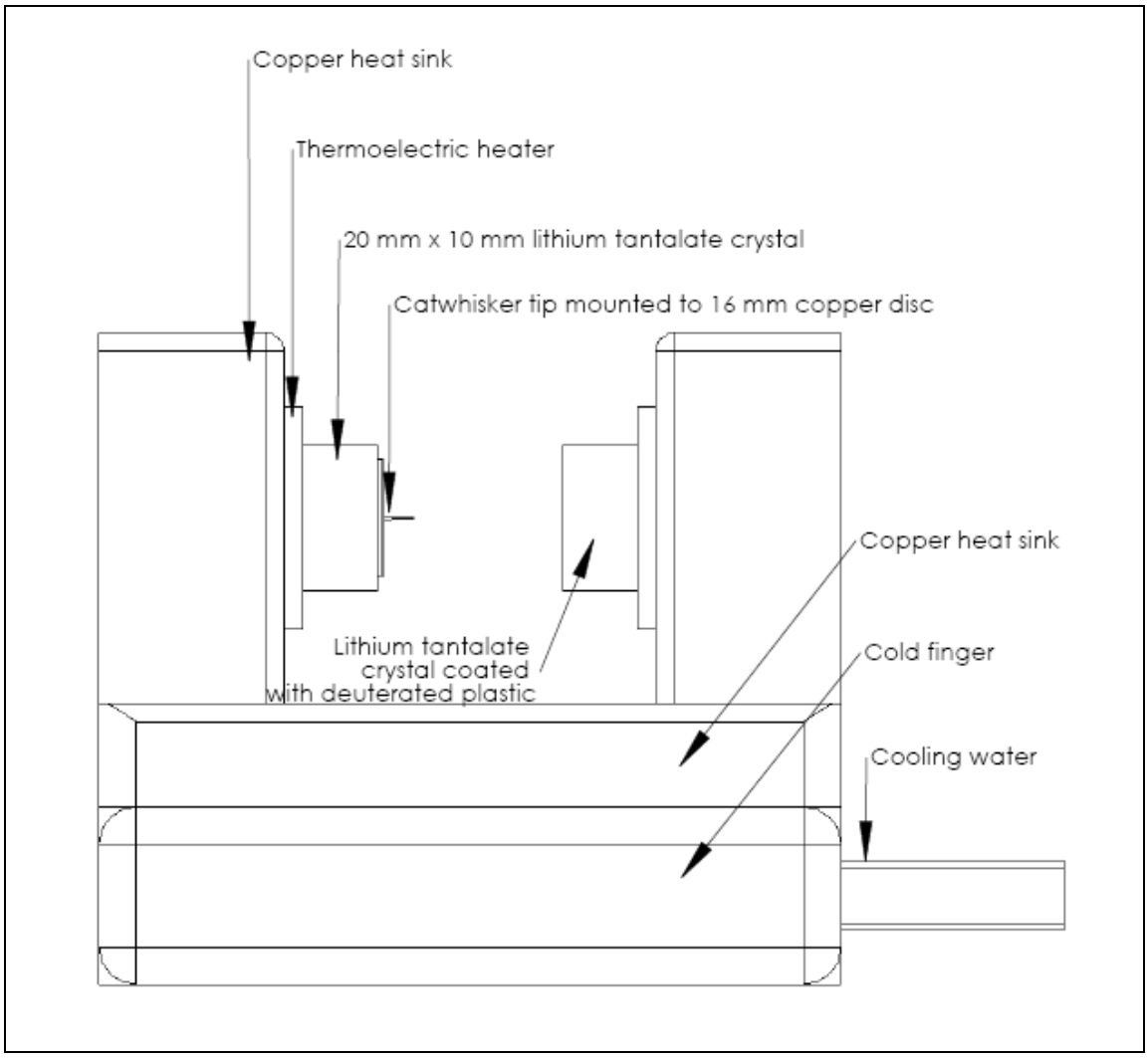

Figure 8.9 - Cross-section view of experimental apparatus for fusion neutron production.

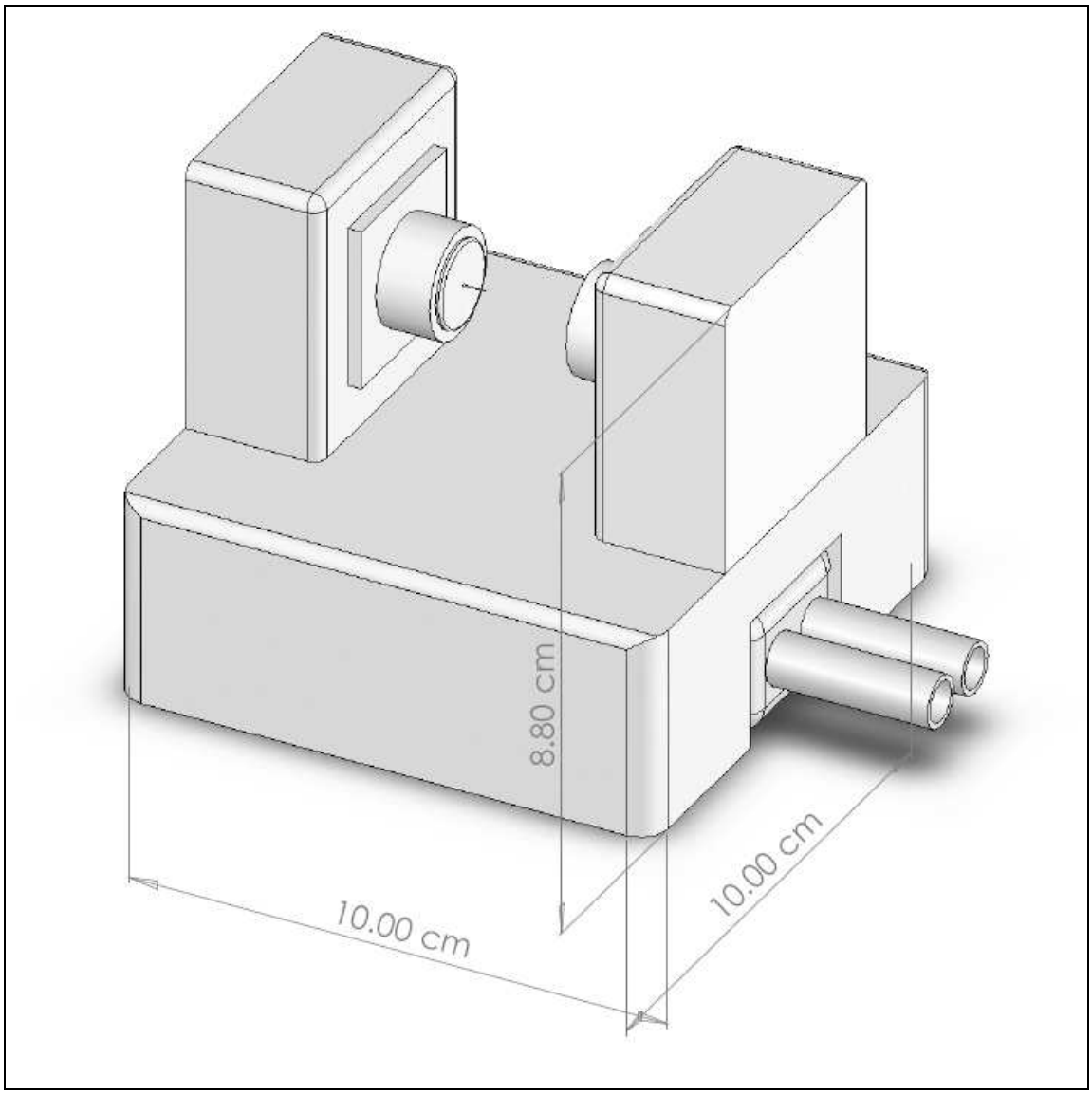

Figure 8.10 - Trimetric projection of experiment model showing major dimensions.

8.5 Experimental Results

8.5.1 Neutron Production Experiments with Conductive Epoxy Interface

In early neutron production experiments[65], the interface between the crystal and the copper disc was conductive epoxy. It was believed that the conductivity of the interface would allow for better charge flow to the tip, thereby creating a higher ion current. It was later found that the use of a non-conductive epoxy at the interface improved the neutron yield. Nevertheless, the results in this section were obtained using the conductive epoxy. Another difference between these experiments and those conducted

afterward is that in the early experiments, deuterated polystyrene was used as a target instead of deuterated polyethylene, which reduced the cross section for fusion.

The crystals were separated by 15 mm (from the tip to the target). The tip was 3 mm long, and was a catwhisker tungsten tip with a 70 nm apex radius. The crystals were heated to 130 °C over 350 seconds using a low-voltage power supply, and then allowed to cool naturally via conduction through the thermoelectric heater and copper heat sink. Cooling water at room temperature was pumped through a copper cold finger in the base of the heat sink in order to help remove heat.

The chamber was pumped down to a base pressure of around 10^{-6} torr, and then filled with deuterium gas to a pressure of 10^{-5} to 10^{-1} torr. (Fusion was observed over a wide range of pressures, from 1×10^{-4} torr to 3×10^{-2} torr).

Neutrons were detected with a 3" x 3" Eljen EJ-301 proton recoil detector shielded by 1.7 mm of lead on the front of the detector, and 25 mm of lead on all sides. Lead has a photon attenuation coefficient[28] of μ = 5.55 cm^2 / g at 100 keV, and μ = 0.999 cm^2 / g at 200 keV, and a density of 11.3 g / cm^3. Due to the high photon attenuation coefficient, the transmission of x-rays through the 1.7 mm shield at 100 keV was only .0018%, and 200 keV it was only 14%. Therefore, in addition to the discrimination against x-rays afforded by the amplifier discriminator setting and pulse shape discrimination, the detector was also well shielded against x-rays of the energies expected in the experiment. Thus, the probability of x-ray pulse pileup (which may give an observed pulse amplitude above the ~200 keV discriminator setting) was greatly reduced.

8.5.2 Effect of Ionizing Tip Radius

In an effort to increase the number of deuterons available for fusion, several experiments were conducted using ionizing tips which had 200 nm and 600 nm radii. The reason for the belief that an increase in tip radius would have a positive effect came from a simple model for the electric field in the vicinity of a tip.

First, the tips were modeled as a small sphere mounted to an infinitely small post, such that the solution for the electric field around an equipotential sphere could be used for the field around the tip. This model is a gross approximation, but the enhancement of the electric field near a tip is due to the curvature of the tip, or, to put it simply, its

"sphereness." Therefore, it was thought that even this gross approximation would provide a useful model for field behavior.

The electric field outside of a sphere of uniform potential is given by the inverse square law:

$$\vec{E}(r) = \frac{A}{r^2}\hat{r} \tag{81}$$

where *A* is a constant. *A* can be found using the definition of the electric potential at the surface of the sphere[62], $r = r_o$:

$$V(\vec{r}) = -\int_{\infty}^{\vec{r}} \vec{E}(\vec{r}) \cdot d\vec{\ell} \tag{82}$$

Due to symmetry the electric field is only a function of the radius. The electric field vector is parallel to the radial unit vector, such that the dot product is always equal to one:

$$V(\vec{r}) = V(r) = -\int_{\infty}^{r} \left|\vec{E}(r)\right| dr \tag{83}$$

$$V(r_o) = -\int_{\infty}^{r_o} \frac{A}{r^2} dr = \frac{A}{r_o} \tag{84}$$

Therefore, $A = rV(r_o)$, and the equation for the electric field around a conducting sphere at potential $V(r_o)$ is completely defined:

$$\vec{E}(r) = \frac{r_o V(r_o)}{r^2}\hat{r} \tag{85}$$

The electric field described by Equation 85 has a magnitude that increases with *decreasing* tip radius, but the field decays more slowly with *increasing* tip radius. One can estimate the critical ionization radius for a tip charged to a certain potential $V(r_o)$ by assuming that all gas molecules inside a radius in which $E(r)$ is greater than the ionization potential divided by the atomic radius will be ionized, and all atoms outside this radius will remain neutral. First assume that deuterium has the same ionization potential as hydrogen, which, for the H_2 molecule, [28] is 15.6 V. The atomic radius can be estimated using the Bohr model of the hydrogen atom[69], with the electron in the first quantum state. This gives:

$$r_D = 0.0529\ \text{nm} = a_o \tag{86}$$

where a_0 is the Bohr radius. Therefore, one can estimate that the gas will become ionized when it is in a region where:

$$E(r) \geq \frac{15.6\,\text{V}}{a_o} = 2.95\times10^{11}\ \text{V/m} \tag{87}$$

Figure 8.11 shows the electric field strength outside of a 150 kV charged sphere versus distance from the center for spheres of various radii.

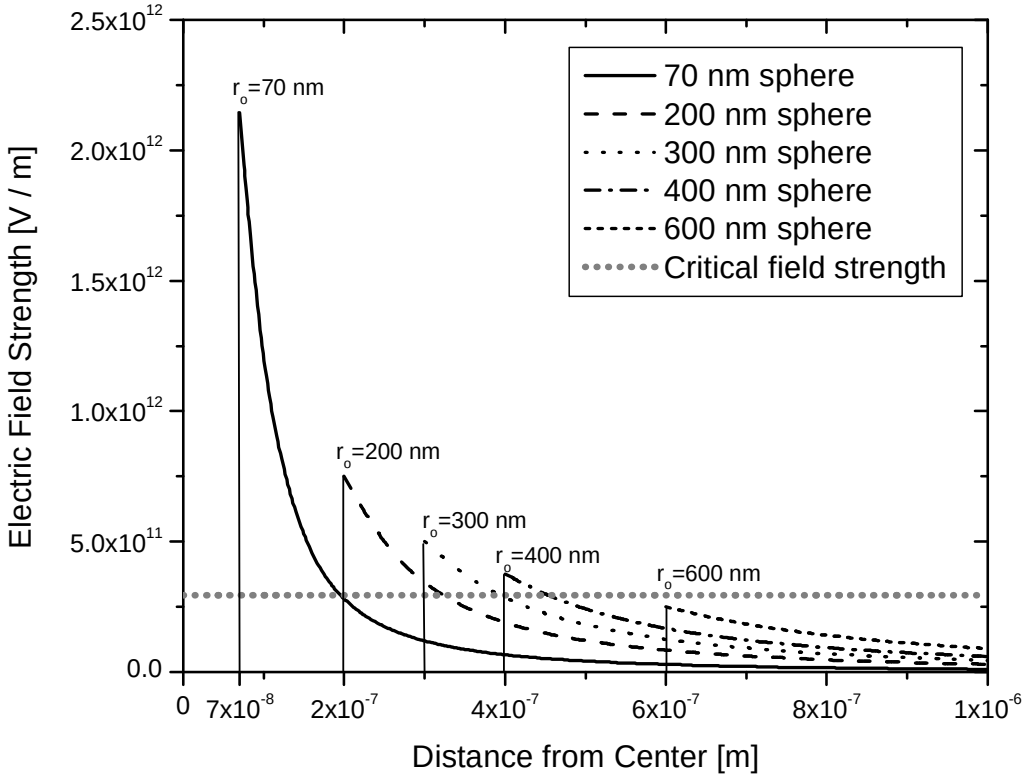

Figure 8.11 - Electric field strength outside of a 150 kV sphere as compared to the critical field strength for the ionization of D_2.

To optimize the tip size based on this model, one must maximize the volume of the region inside the critical radius of ionization, exclusive of the volume of the conducting sphere:

$$V_{crit} = \frac{4\pi}{3}\left(r_{crit}^3 - r_{sphere}^3\right) \tag{88}$$

This optimization calculation ignores some possible benefits of the high electric field near small tips, such as a possible improvement in D^+ versus D_2^+ ionization. As Figure 8.12 shows, this model predicts that, for a 150 kV potential, the sphere radius most

effective at ionizing deuterium gas would be approximately 300 nm. Furthermore, the 70 nm sphere, corresponding to the 70 nm catwhisker tip used in most neutron pyroelectric production experiments, would seem to be far from the optimum based on this model.

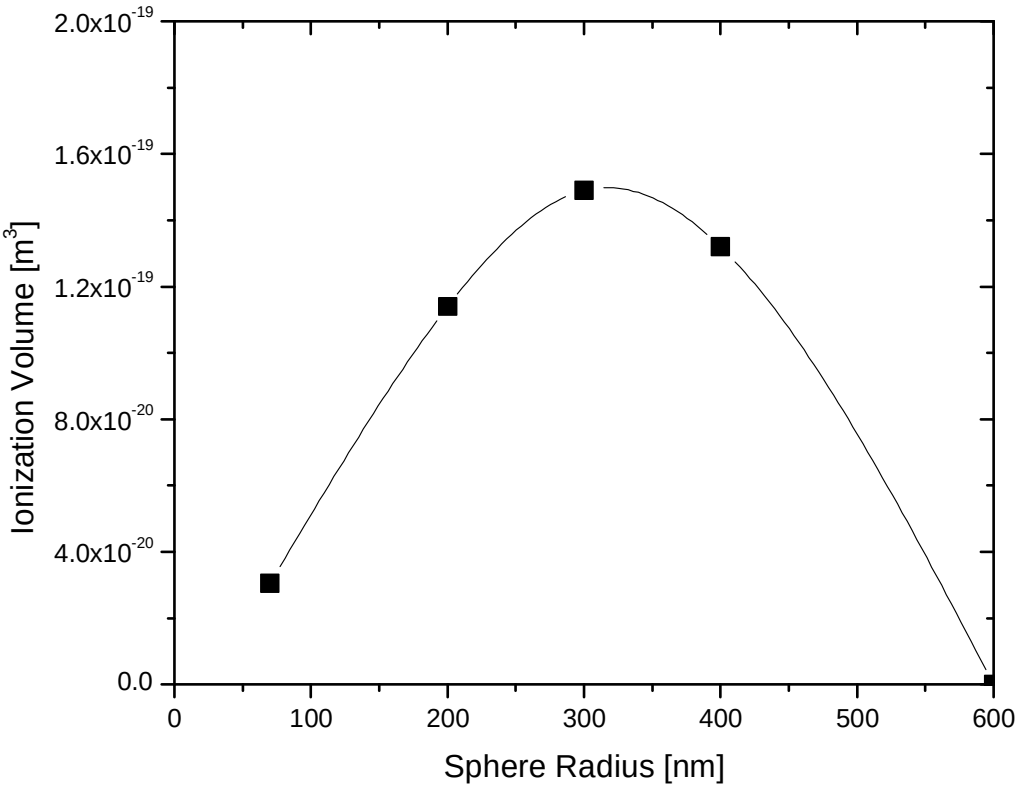

Figure 8.12 - Plot showing the volume of ionization versus sphere radius for deuterium gas in the vicinity of a sphere charged to 150 kV.

This model was tested by comparing the neutron yield from pyroelectric neutron experiments using 200 nm tips with similar experiments using 70 nm tips. It was found that, with conductive epoxy, the 200 nm tips yielded a slight improvement over the 70 nm tips (14000 ± 500 neutrons / cooling phase versus 10600 ± 500 neutrons per cooling phase).

However, when non-conductive epoxy was used to mount the tip and copper disc to the crystal, the 200 nm tips were far inferior to the 70 nm tips. Figure 8.13 is an MCS plot from the most successful neutron production experiment using a 200 nm tip. Aside from the "plasma peak" at t = 150 s, there is essentially no above-background emission. (The occurrence of spurious neutron count rate peaks, such as the one shown in Figure

8.13, might be due to the formation of a plasma in the tip vicinity. This phenomenon is discussed in detail in Section 8.5.5). The total observed yield for this experiment (i.e., not corrected for intrinsic or geometrical detector efficiency) was 211 observed neutrons, versus over 3000 observed neutrons for the most successful experiment in the same configuration with a 70 nm tip.

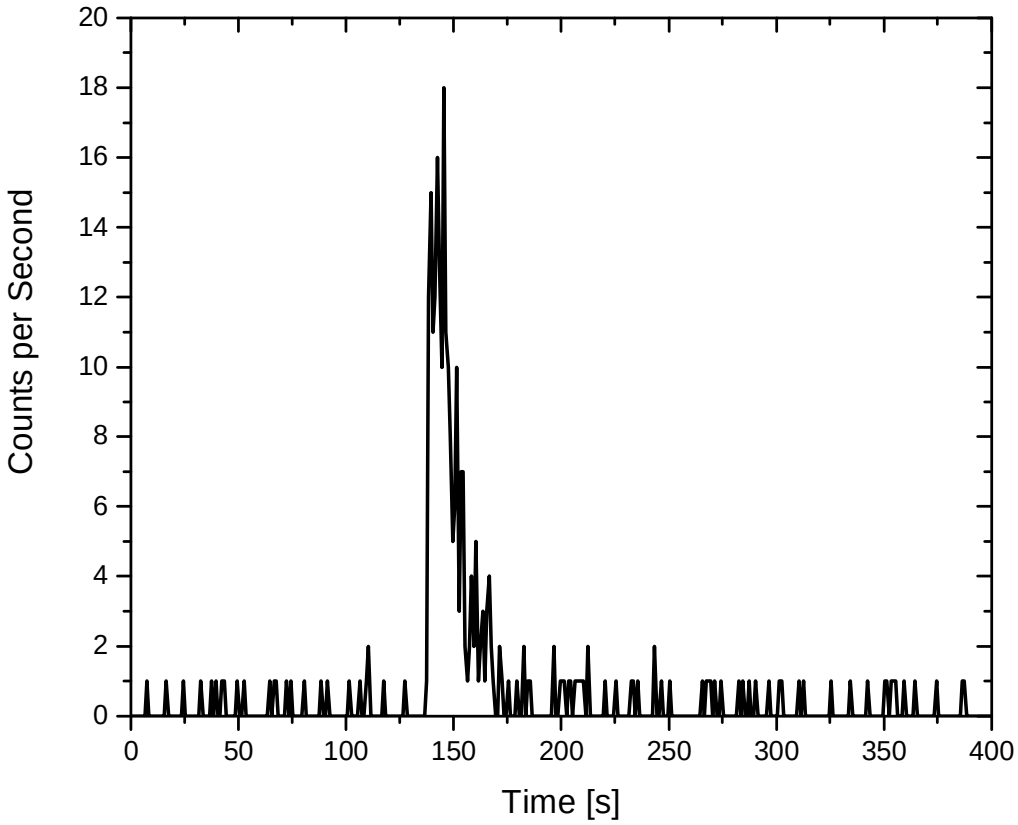

Figure 8.13 - Neutron count rate versus time for an experiment with a 200 nm tip and a non-conductive interface between the tip mount and the crystal.

Why did the 200 nm tip not give the expected benefit in neutron yield? There are several possible answers. First, Figure 8.12 shows the volume of ionization for a sphere charged to 150 kV. If the same analysis is performed for a sphere charged to a lower potential, say 100 kV, the result is very different. Figure 8.14 shows that when the sphere is only given a potential of 100 kV, instead of 150 kV as before, the radius with the maximum ionization volume shifts to a lower value (~200 nm instead of ~300 nm). Still, even at 100 kV, the charged sphere model shows that a 200 nm tip should be favorable to a 70 nm tip.

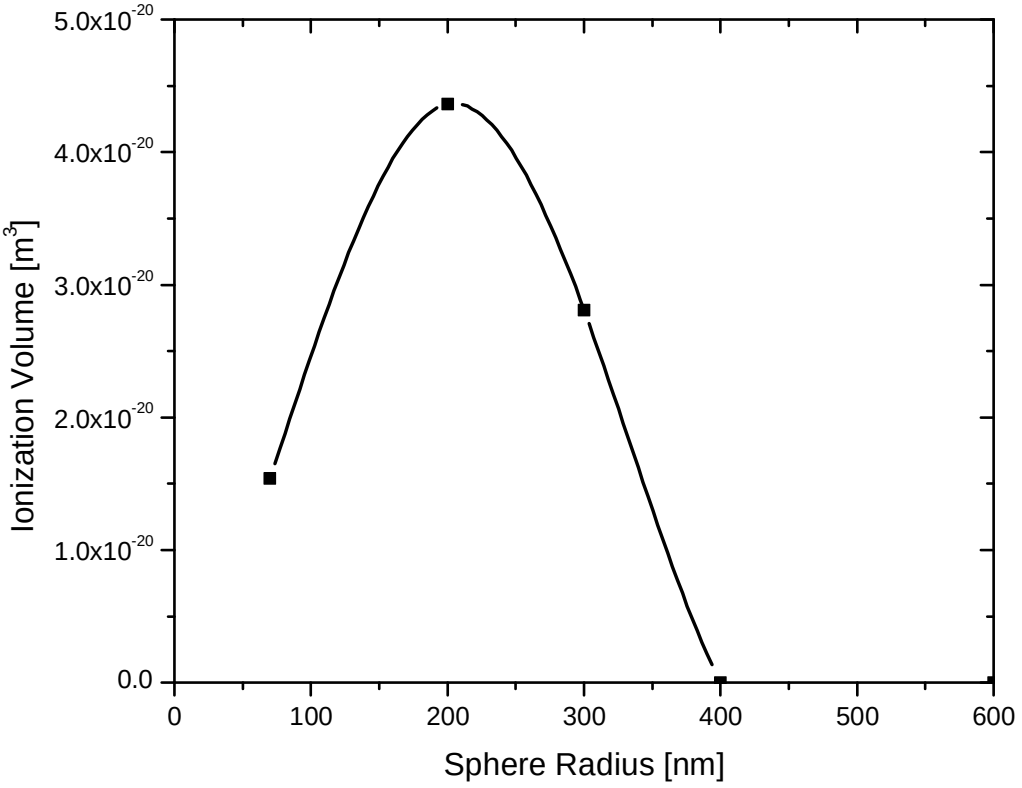

Figure 8.14 - Volume of deuterium gas ionization in the vicinity of a 200 nm tip at 100 kV.

Finite element modeling of a sphere and tip give another clue. Figure 8.15 shows a 2D model run in COMSOL Multiphysics. In the model, a 0.1 mm-radius sphere was set at 1000 V potential and placed in a grounded 2 cm x 2 cm box. In the adjacent box, a 0.1 mm-radius hemisphere on a 0.1 mm-radius cylindrical post was set to 1000 V and placed in an identical grounded box.

Figure 8.16 shows the strength of the electric field on a line drawn along the horizontal through the center of both boxes. This plot shows that the inclusion of the post, in what is a more accurate representation of a real tip than a sphere in free space, causes the maximum electric field strength to decrease, but to fall off more slowly at increasing distance from the center. In comparison to the sphere model, the post essentially makes the hemisphere behave like a sphere of a slightly larger radius. This may explain why there wasn't an advantage in using the 200 nm tip instead of a 70 nm tip.

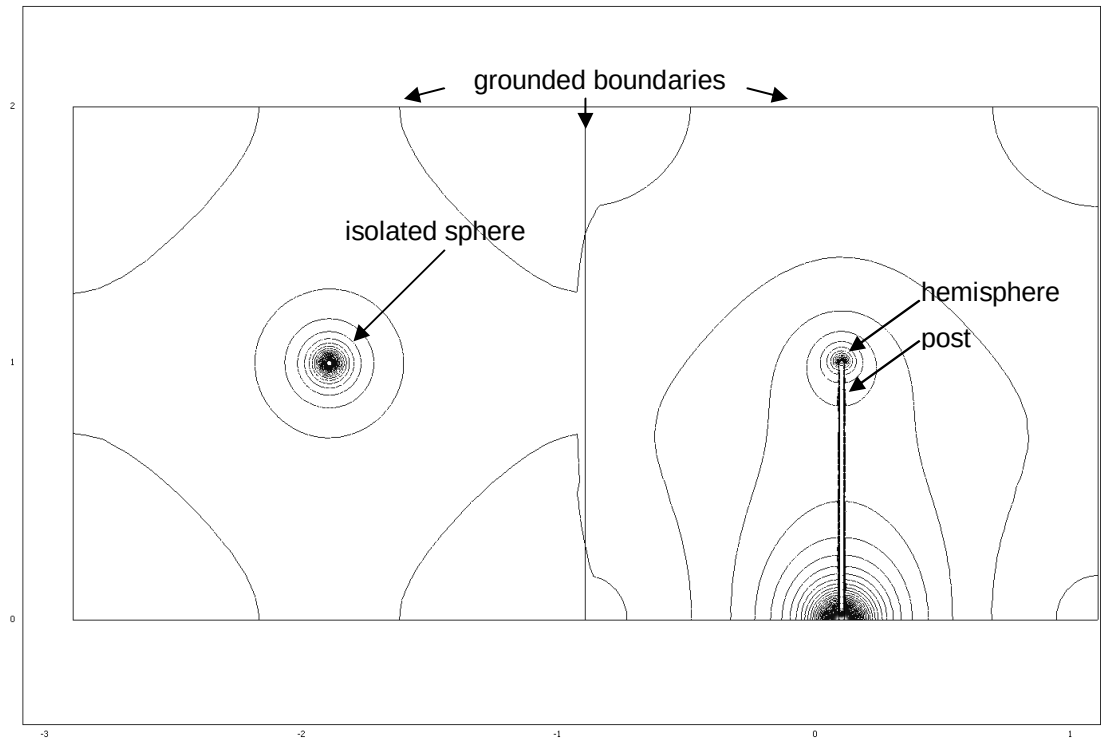

Figure 8.15 - COMSOL finite element analysis plot of electric potential contours in the vicinity of a charged sphere and a hemisphere on a conducting post. Both objects had radii of 0.1 mm and were in 2 cm square grounded containers.

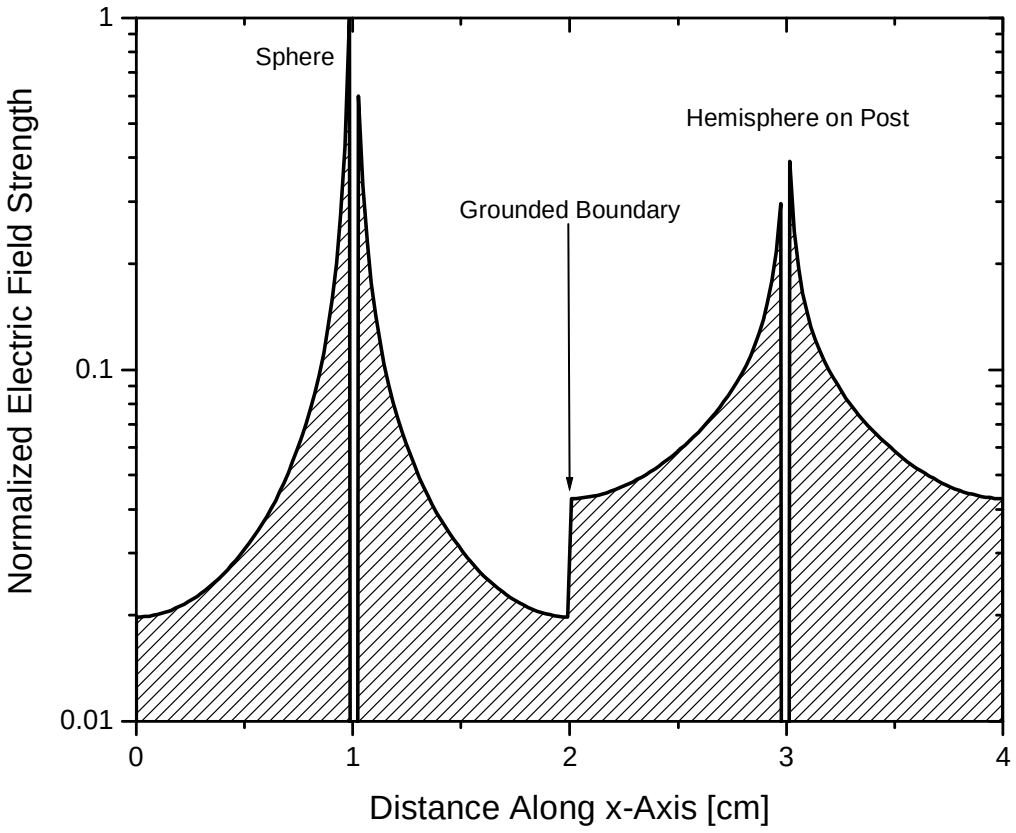

Figure 8.16 - Field strength along a horizontal line drawn through a sphere [left] and hemisphere on a post [right], both at 1000 V. Grounded barriers exist at 0, 2, and 4 cm.

8.5.3 Neutron Production Experiments with Non-Conductive Epoxy Interface

After successfully producing neutrons with a paired-crystal pyroelectric source, the next step was to attempt to improve the neutron yield to move closer to a practical source for field and industrial applications. The experimental setup remained the same throughout this chapter (see Figure 8.10). The only changes were to the target, ionizing tip, and the interfacial layer of epoxy holding the copper disc (to which the ionizing tip was mounted) to the crystal surface. The most successful method of increasing neutron yield was to replace the conductive epoxy interface used in Section 8.5.2 with non-conductive epoxy .

At this point, the analog electronics used to perform pulse-shape discrimination were replaced with an Acqiris PCI analyzer board. A detailed description of this system is given in Appendix I.

The use of non-conductive epoxy was shown earlier (see Figure 8.6) to have a benefit in terms of producing high-energy positive ions, presumably because the field and acceleration potential can build to a high value before charge is removed at an appreciable rate via field ionization. This advantage resulted in a dramatic increase in neutron yield when non-conductive epoxy was used in place of conductive epoxy when attaching the ionizing tip to the crystal surface. Figure 8.17 shows a single neutron spectrum from an experiment utilizing a tip mounted with non-conductive epoxy compared to three summed spectra from an experiment utilizing conductive epoxy. The bins are somewhat wider for the non-conductive epoxy data, and the detection efficiency was better due to the use of a larger detector (5.1% instead of 1.3%).

The experimental data plotted in Figure 8.17 represent the most successful experiment run with non-conductive epoxy. This run resulted in the detection of 3039 fusion neutrons with pulse heights above 150 keV_e. The intrinsic detector efficiency with a discriminator level of 150 keV_e was calculated in SCINFUL and found to be $\eta_{int} = 0.48$. The distance to the detector from the center of the target crystal was $d = 8.1$ cm. Since the detector had a radius of $a = 6.35$ cm, the solid angle for detection Ω, assuming that the crystal behaves in a similar manner to a point source, is:

$$\Omega = 2\pi\left(1 - \frac{d}{\sqrt{d^2 + a^2}}\right) \tag{89}$$

$$\Omega = 2\pi\left(1 - \frac{8.1}{\sqrt{8.1^2 + 6.35^2}}\right) = 1.338 \tag{90}$$

The total detection efficiency η_{tot} is then given by:

$$\eta_{tot} = \frac{\Omega \cdot \eta_{\text{int}}}{4\pi} \tag{91}$$

$$\eta_{tot} = \frac{1.338 \cdot 0.48}{4\pi} = 0.051 \tag{92}$$

Thus, in the run where 3023 ± 55 neutrons were observed, 59000 ± 1000 neutrons were generated by the pyroelectric source.

Therefore, the total neutron yield improved from 10600 ± 500 neutrons per cooling phase (the best observed yield from a 70 nm tip mounted with conductive epoxy) to

59000 ± 1000 neutrons per cooling phase. The error in the calculated neutron yield is due to counting statistics only. Additional error due to the detector efficiency calculation is not included.

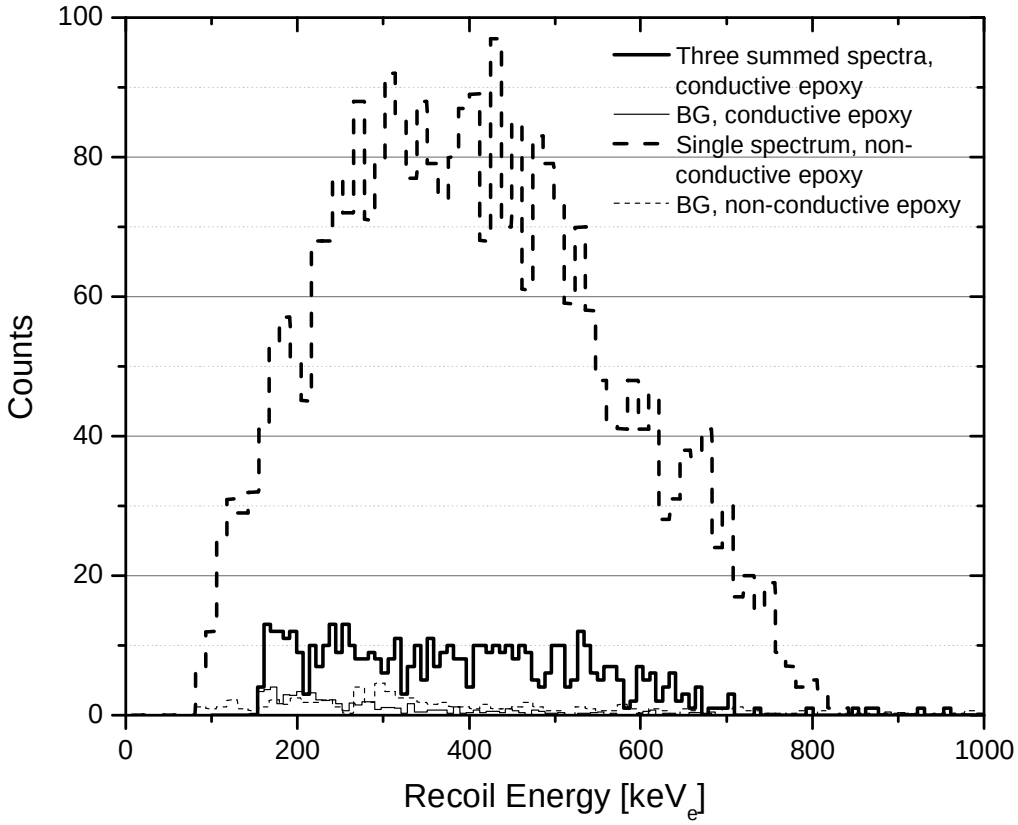

Figure 8.17 - A single neutron spectrum from a system with non-conductive epoxy connecting the ionizing tip to the crystal compared to three summed spectra from a system using conductive epoxy.

Figure 8.18 shows that the neutron spectra from our neutron experiments are consistent with measurements using the same neutron detector in a time-of-flight experiment (with 2.5 ± 0.1 MeV neutrons) and a SCINFUL[70] simulation of the detector with 2.5 MeV neutrons. The apparent difference in endpoint energy for the pulse height spectra shown in Figure 8.17 can be attributed to poor statistics at this energy.

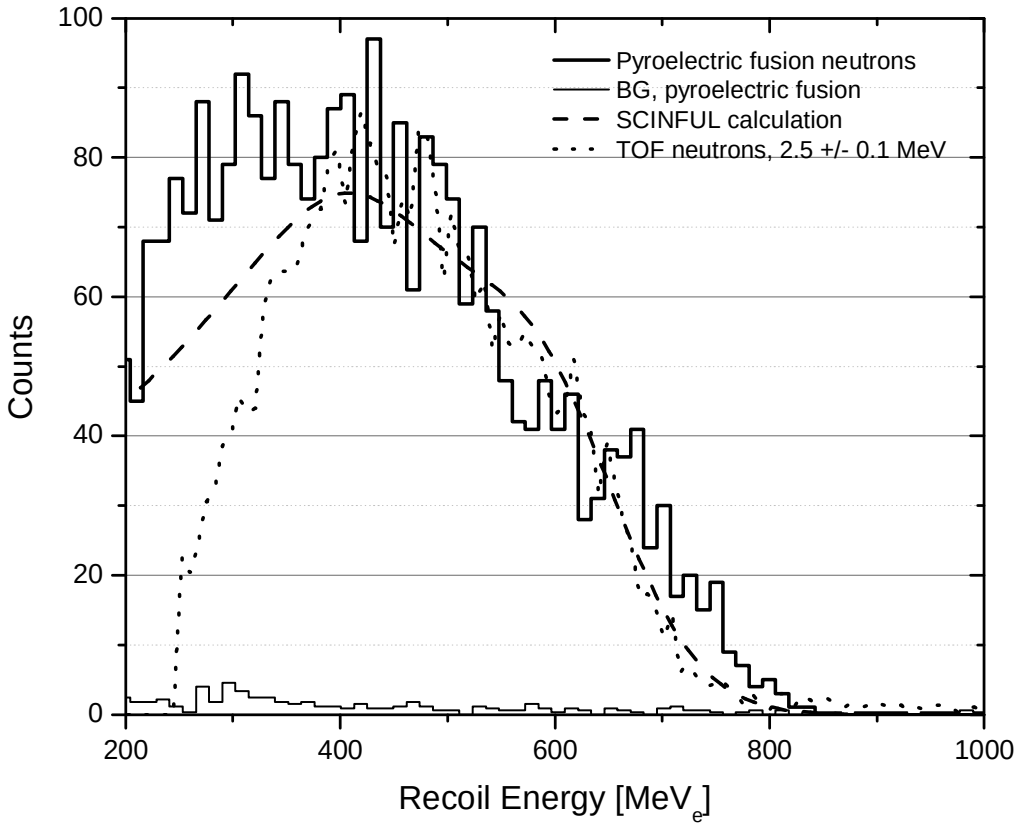

Figure 8.18 - Comparison of neutron spectra from experiments using non-conductive epoxy with pulse height spectrum from a time of flight experiment (dashed line) and a spectrum calculated with a SCINFUL simulation of the detector (dotted line).

It is important to consider the difference in neutron detector location when comparing the experiments conducted with non-conductive epoxy with the earlier experiments using conductive epoxy. This is because the neutron emission angle from D-D fusion is highly anisotropic. In the experiments using conductive epoxy[65], the detector was at an angle of $5\pi/4$ relative to the axis of the incident ions in lab coordinates. For 100 keV incident deuterons, the anisotropy of the emitted neutrons[71] results in the under-prediction of neutron yield by 4% if the yield is calculated by assuming isotropic emission. The detector used in the experiments with non-conductive epoxy that resulted in the increase in neutron yield shown in Figure 8.17 was positioned at an angle of $\pi/2$ in lab coordinates. This is a less favorable angle for neutron emission, and the neutron

yield calculated using assuming isotropic emission under-predicts the source strength by 26.7% for 100 keV incident deuterons. The calculation of the differential cross section for anisotropic neutron emission from D-D fusion is discussed in detail in Appendix V.

8.5.4 "Plasma" Peaks

It is observed that, during the neutron emission phase of the heating cycle, there may be one or more instances in which the x-ray and neutron count rates simultaneously increase by more than an order of magnitude. One hypothesis is that this phenomenon is due to the formation of a plasma near the ionizing tip. If there is a high enough population of electron / ion pairs near the tip, then Debye shielding will prevent the potential of the tip from affecting the ions and electrons, and a state of quasi-neutrality is achieved. At this point, a plasma is formed, and the number of ions (for neutron production) and electrons (for x-ray production) are both increased. As ions and electrons leave the plasma region, they are no longer shielded from the external potential, and are accelerated into their respective target crystals. As the population of the plasma region is reduced, the increase in the count rate decays back to the non-plasma value. At this point, the appearance of the count rate peaks cannot be controlled, but rather occurs randomly. However, it is clear that the ability to control the occurrence of these peaks would greatly improve the neutron yield from a pyroelectric source.

Figure 8.19 shows a count-rate peak which was observed during a neutron production experiment conducted with a non-conductive interface between tip and crystal. In this experiment, a total of 2337 neutrons were counted. 1326 of these were counted during the peak (57 ± 3% of the total). The increase in the count rate in the photon window was due to an abundance of high-energy x-rays (over the discriminator level) produced by the secondary electron pairs.

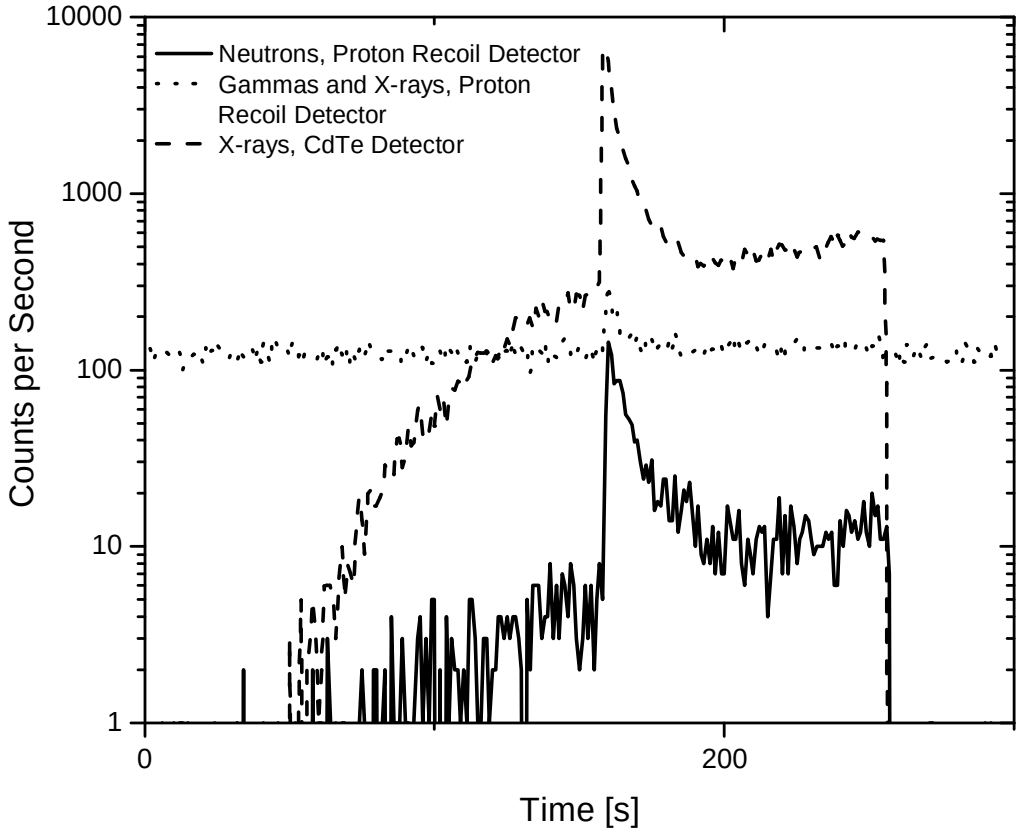

Figure 8.19 - Plot of neutron and photon count rate vs. time for a neutron production experiment in which a count rate peak was observed.

Contamination of the neutron spectrum with gammas and x-rays can be discounted, since the increase in counts in the photon window was constrained to pulse heights of less than 105 keV_e, which corresponds to the Compton edge of a 225 keV x-ray, as shown in Figure 8.22. The discriminator setting for the neutron window was set to ~150 keV_e.

However, similar peaks have been observed when operating at base pressure in air, 10^{-6} - 10^{-5} Torr. These experiments were conducted with the same geometry used for neutron production experiments, and the crystals were heated and cooled with the same temperature profile. The only difference is the lack of a fill gas. The position of the x-ray detector changed between experiments, but the neutron detector was in the same position, with the same amount of lead shielding. No neutrons are observed without a deuterium fill gas, but the x-ray MCS spectra show peaks. This gives some reason to doubt that the cause of the peaks is plasma formation, since the gas population is two to

three orders of magnitude less when at base pressure than it is during neutron production experiments. Figure 8.20 shows the x-ray MCS spectrum from one such experiment.

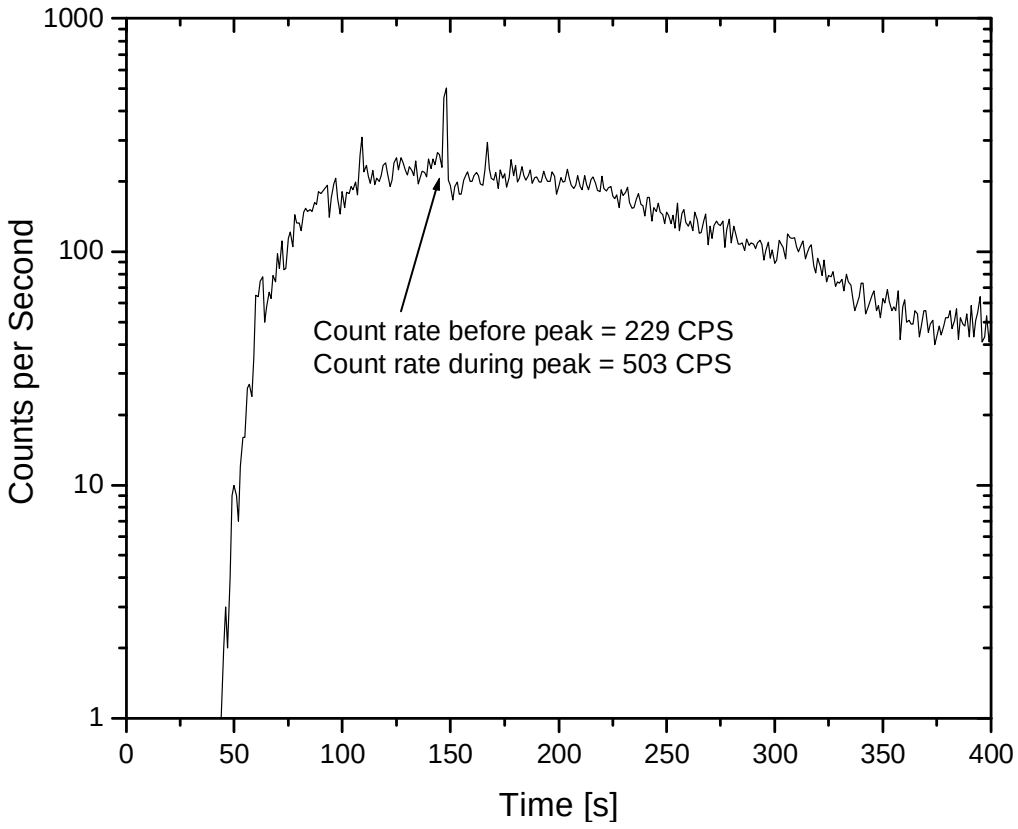

Figure 8.20 - "Plasma" peak from an experiment at base pressure.

Figure 8.21 shows that the neutron count rate does not increase due to the observation of a “plasma” peak when no deuterium fill gas is present. This is evidence that the increased neutron yield observed in Figure 8.19 is not due to x-ray count pileup.

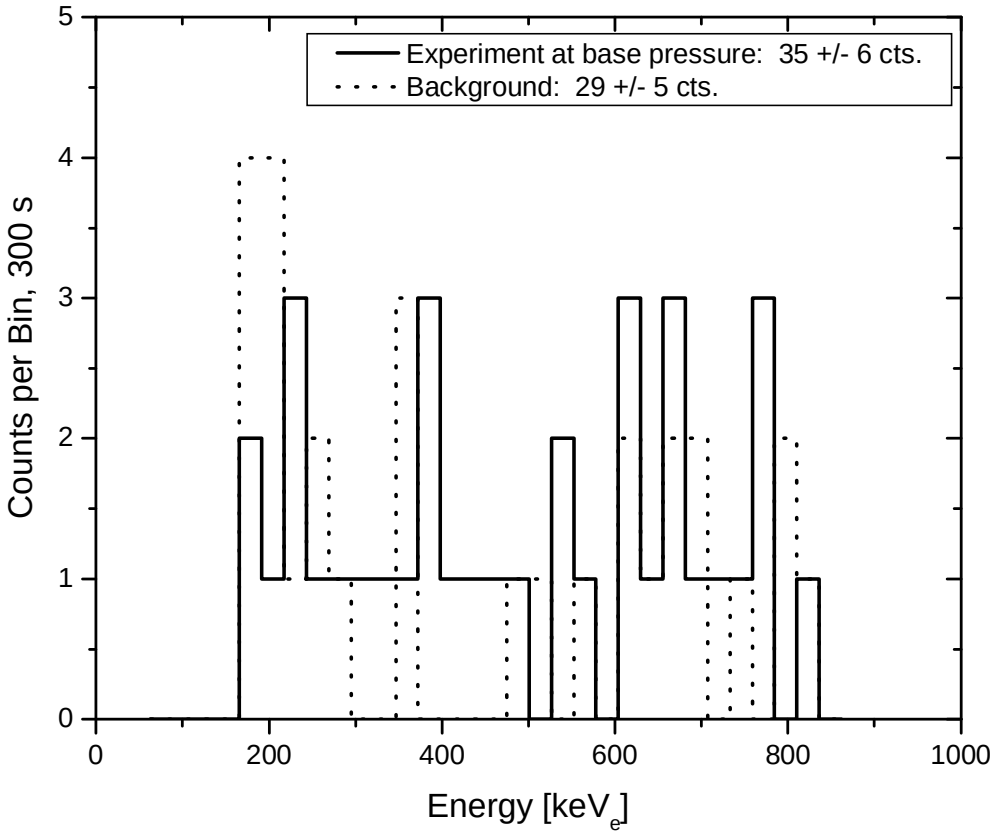

Figure 8.21 - Neutron window counts from an experiment in which a count rate was observed in absence of a fill gas. The counts observed were not significantly above background. The x-ray endpoint energy was >150 keV.

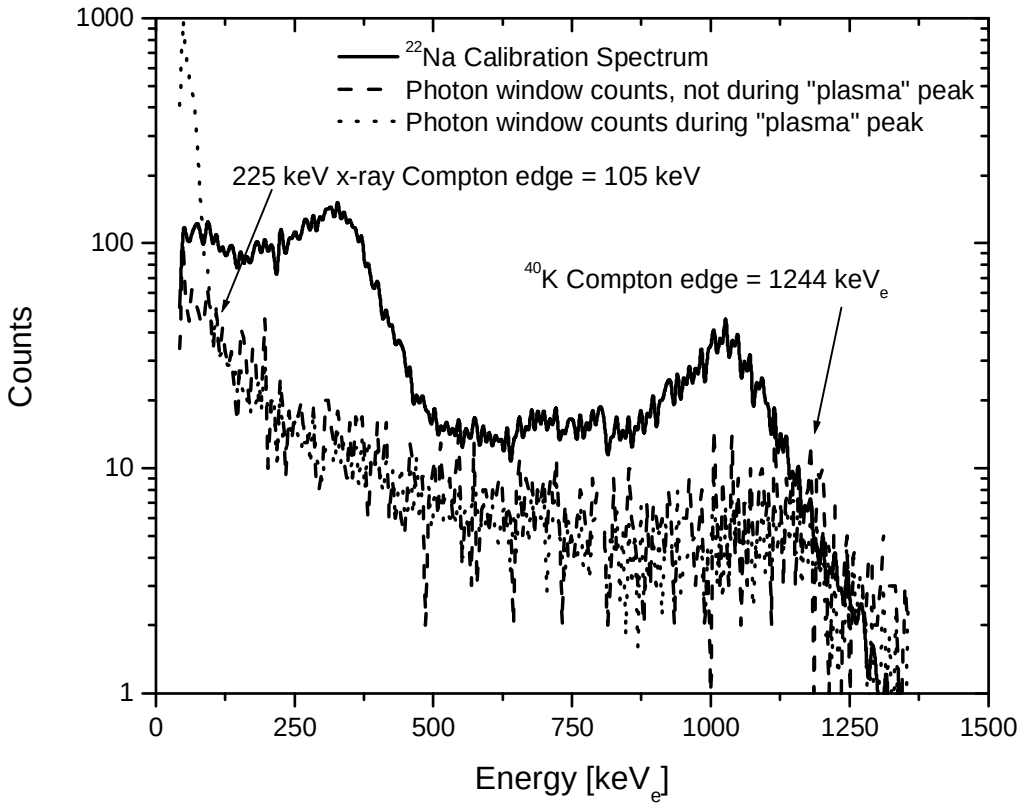

Figure 8.22 - Plot showing the counts in the photon window during a "plasma" peak versus the counts during normal operation. The increase in counts is due entirely to pyroelectric x-rays. The spectra were normalized to appear equal over the high-energy regime.

It is important to verify that the increase in yield is indeed due to the formation of a plasma. This can be done by examining the three conditions for plasma formation[72]. These conditions are:

1. The Debye length must be much smaller than the dimensions of the experiment:

$$\lambda_D < L \tag{93}$$

$$\lambda_D = \left(\frac{\varepsilon_o K T_e}{n e^2} \right)^{1/2} \tag{94}$$

where λ_D is the Debye length, L is the size of the experiment, KT_e is the kinetic temperature of the plasma, n is the particle density far from the external potential, and e is the elementary unit of charge. For temperature in units of °K, this reduces to[72]:

$$\lambda_D = 6900 \cdot \left(\frac{T}{n} \right)^{1/2} \text{ centimeters} \tag{95}$$

In a plasma, charges can redistribute themselves to compensate for any large external potentials. The Debye length is a gauge of the thickness of this shielding layer (it is the characteristic exponential decay length of a shielded external potential). If the size of the experiment is larger the Debye length, then a stable region of plasma can exist in a volume free of the effect of external electrostatic potential.

2. The number of particles in the Debye sphere, N_D, must be large enough to validate the concept of Debye shielding. (The Debye sphere describes the volume of the shielded region.) This is quantified by the inequality:

$$N_D >> 1 \tag{96}$$

where

$$N_D = \frac{4}{3} n \pi \lambda_D{}^3 \tag{97}$$

3. The plasma must be governed by electromagnetic forces, instead of hydrodynamic forces. In a magnetic confinement fusion device, this condition is met when the product of the plasma oscillation frequency ω_p and the mean time between random collisions of the atoms is $\tau_{p.}$

$$\varpi_p \tau_p > 1 \tag{98}$$

In a pyroelectric source however, the hypothetical plasma would not oscillate, since there is no magnetic confinement field. Therefore, only the first two of these criteria will be considered.

To see if the first of the plasma conditions is satisfied, one must find the Debye length for the plasma. If the pressure in the system is 4 mTorr, the number density n of deuterium per unit volume V can be found using the ideal gas law:

$$\frac{n}{V} = \frac{P}{RT} \tag{99}$$

Equation 99 yields a number density of 5.44 x 10^{-12} mol / cm^3, or 1.32 x 10^{20} atoms / m^3 for a room temperature gas. If it could be assumed that the plasma was at thermal

equilibrium, one could consider a room temperature plasma (T = 293°K), with a kinetic temperature KT of 2.52 x 10^{-2} eV. For this condition, the Debye length of the plasma is 3.51 x 10^{-5} cm, which is much smaller than the scale of the experiment (i.e., several centimeters). Figure 8.23 shows the Debye length as a function of temperature for a 4 mTorr deuterium fill gas.

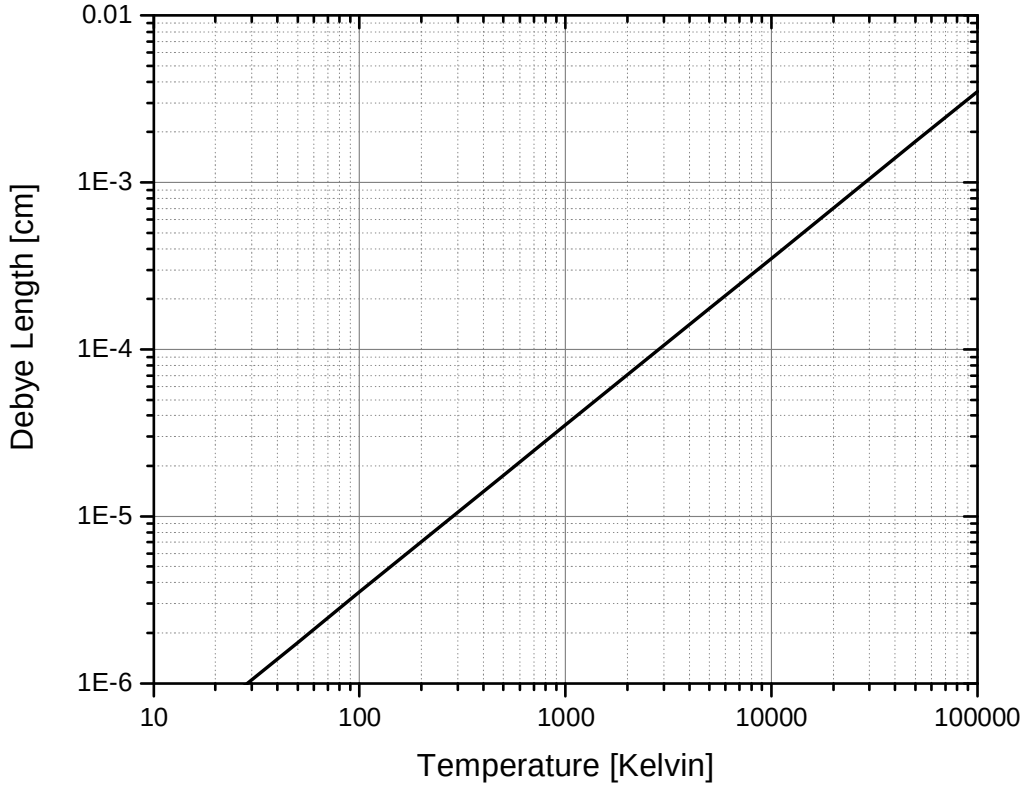

Figure 8.23 - Debye length for a 4 mTorr deuterium gas as a function of temperature.

However, the ions in a pyroelectric accelerator are not in thermodynamic equilibrium, but instead are being accelerated away from the charged tip. By calculating the Debye length based on the energy of the deuterons as they accelerate away from the tip, one can see that the first condition for plasma formation is only satisfied for a very short distance around the tip. Figure 8.24 shows that for a spherical tip charged to 100 kV, the Debye length would be greater than 1 cm by the time the particles traveled 25 nm from the tip for any gas pressure up to 10 mTorr.

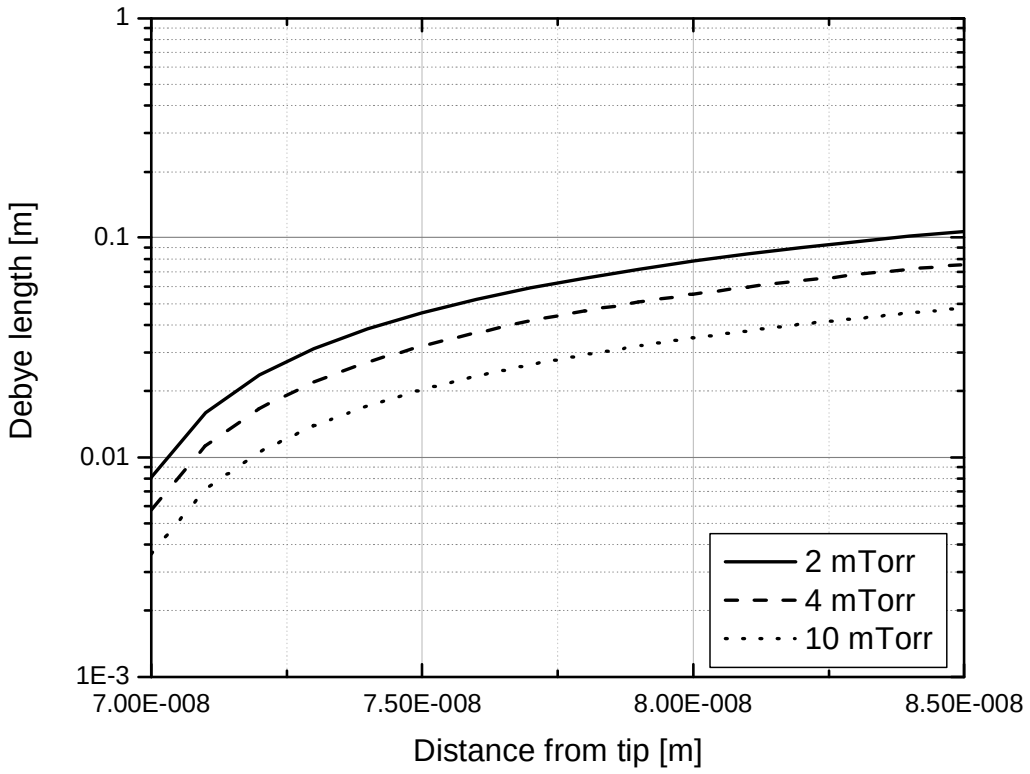

Figure 8.24 - Debye length for a deuteron plasma as a function of radius as the ions accelerate away from a 70 nm radius sphere charged to 100 kV.

Therefore, from the first plasma criterion, it seems doubtful that the formation of plasma can explain the spurious count rate peaks. However, the second condition for plasma formation is that the number of particles inside the Debye sphere must be large, such that the concept of Debye shielding is valid. Figure 8.14, shows that the ionization volume is on the order of 10^{-20} - 10^{-19} m^3. The ideal gas law revealed that the gas density at room temperature in the experiment is on the order of 10^{-20} particles per cubic meter. Therefore, the population of the ionization region is on the order of one particle. This suggests that the calculated Debye shielding length is invalid in determining whether a plasma exists around the tips used in pyroelectric neutron production experiments. However, since the particle density inside the ionization volume is so low, one can also see that the population of this region will vary greatly. This is especially true since the velocity of D_2 gas particles at room temperature is ~1100 m / s, which is great compared to the width of the ionization region (tens to hundreds of nanometers). The average population of the ionization region, which was said to be about one particle, will be

comprised of many particles rapidly passing in and out of the volume, at a rate of about 10^{10} events per second (for a critical radius of 200 nm). The statistical variation in the gas population around the tip may explain the random nature of the "plasma" peak formation. For example, if the gas population fluctuated above a certain value, the Debye shielding criteria would suddenly be satisfied, and the formation of plasma would be the expected result.

The phenomenon of spurious count rate peaks may be due to a phenomenon other than plasma formation, and more work is required before the cause of these peaks can be determined with certainty. However, the understanding and control of these peaks is clearly an important means of increasing the neutron yield from pyroelectric neutron sources, and warrants further study. In future experiments, a low-light astronomy camera will be used to attempt to photograph characteristic light from the plasma in order to verify whether plasma production is the cause of the count rate peaks.

9 Discussion and Conclusions

9.1 Introduction

The work constituting this thesis represented several important steps forward in the field of pyroelectric radiation generation. The following chapter summarizes those achievements and outlines future research goals which can further advance the science of producing useful radiation with pyroelectric crystals.

9.2 Electron and Ion Emission Experiments

This research confirmed that the charge emitted by pyroelectric crystals is focused, and that the focal length was accurately predicted for a 1 cm-radius crystal by assuming that all of the charge was located at the crystal edge. A model based on the Fowler-Nordheim equation for field electron emission from conductors in strong electric fields was modified to allow the calculation of the time dependence of electron emission for a given geometry. An electron beam was extracted from a beryllium window on the vacuum chamber and measured with a Faraday cup in an experiment that showed the possibility of creating an industrial or medical pyroelectric electron source by allowing the transport of the beam to the outside of the vacuum chamber.

Both electrons and ions were measured with a collimated surface barrier detector to quantify their energy spectra. The ion energy and current produced by different cathodes mounted to pyroelectric crystals in deuterium gas were used to assign a figure of merit for each cathode as a means of maximizing the neutron yield from pyroelectric fusion. The maximum electron energy measured from a bare crystal was 143 keV. The maximum ion energy from a bare crystal was measured to be 98 keV. The maximum measured ion energy with a crystal connected to an ionizing tip (with non-conductive epoxy) was 79 keV.

9.3 X-ray Production Experiments

This work represented the first independent verification of the generation of x-rays using pyroelectric crystals, first observed by Brownridge[5]. The modeling of the crystals and target as a system of capacitors[10] was used to predict an improvement in the accel-

eration potential as a function of crystal thickness. This model was verified experimentally, and experiments showed that it was difficult to improve the acceleration potential in a lithium tantalate system by increasing the crystal thickness past 1 cm, due to parasitic capacitance and difficulty in heating. The use of paired pyroelectric crystals was shown to be a viable technique for generating x-rays with a maximum energy of over 200 keV. The energy and yield achieved during the course of this work is still the greatest reported for a pyroelectric x-ray generator. By using the advantage in x-ray energy afforded by the paired lithium tantalate crystals, it was shown that the characteristic k-shell x-rays of any element up to thorium (z = 90) and uranium[§§] (z = 92) could be fluoresced. This is clear evidence that pyroelectric x-ray generators have a wide range of research and industrial applications, and can effectively replace x-ray tubes and radioisotopes in x-ray fluorescence applications.

9.4 Neutron Production Experiments

The neutron production experiments discussed in Chapter 8 were the first confirmation of the possibility of pyroelectric fusion published the previous year[17]. Unlike the previous work, the crystals were cycled between room temeperature and ~140°C, and could therefore be heated using low-wattage thermoelectric coolers instead of cryogenic cooling. The source developed at RPI also used paired crystals, which are expected to eventually allow a substantial improvement in neutron yield versus single crystal systems due to the energy dependence of the fusion cross section and target penetration depth. Finally, methods of improving neutron yield, such as optimizing the ionizing tip diameter and better understanding the phenomenon of "plasma peaks," were identified, and preliminary research on these methods was conducted. The pyroelectric fusion work conducted as part of this thesis has been recognized as having potential for homeland security applications, and it will be continued under a grant from the Department of Homeland Security. With continued improvement in neutron yield, a commercial pyroelectric fusion source is inevitable, and will likely be the smallest and least expensive neutron source on the market.

[§§] Poor statistics at high energy prevented clear discernment of the $k_{\beta 2}$ peak.

9.5 Future Work

9.5.1 X-ray Generation and Pyroelectric X-ray Imaging

Pyroelectric x-ray generation is already a commercially viable technology, but there are still several areas in which further research would be beneficial. First of all, it may be possible to raise the upper limit on x-ray energy by finding new pyroelectric crystals which are more thermally conductive than lithium tantalate (to allow thicker crystals to be used), or which have a higher pyroelectric coefficient or lower relative permittivity, in order to create a higher potential for a given crystal size and ΔT.

There is a possibility that pyroelectric x-rays can be used to produce low-power portable x-ray imaging systems. Experiments were conducted at RPI using a Photonic Science XRGEMSTAR CCD x-ray camera, with an x-ray source comprised of a 30 mm diameter by 10 mm thick lithium tantalate crystal and molybdenum target, in which the x-rays from the target were used to image electronics equipment and bait fish.

Figure 9.1 shows an image of a PC BIOS chip taken using this system. These experiments were somewhat successful, but more work needs to be conducted before pyroelectric x-ray imaging becomes a useful technology.

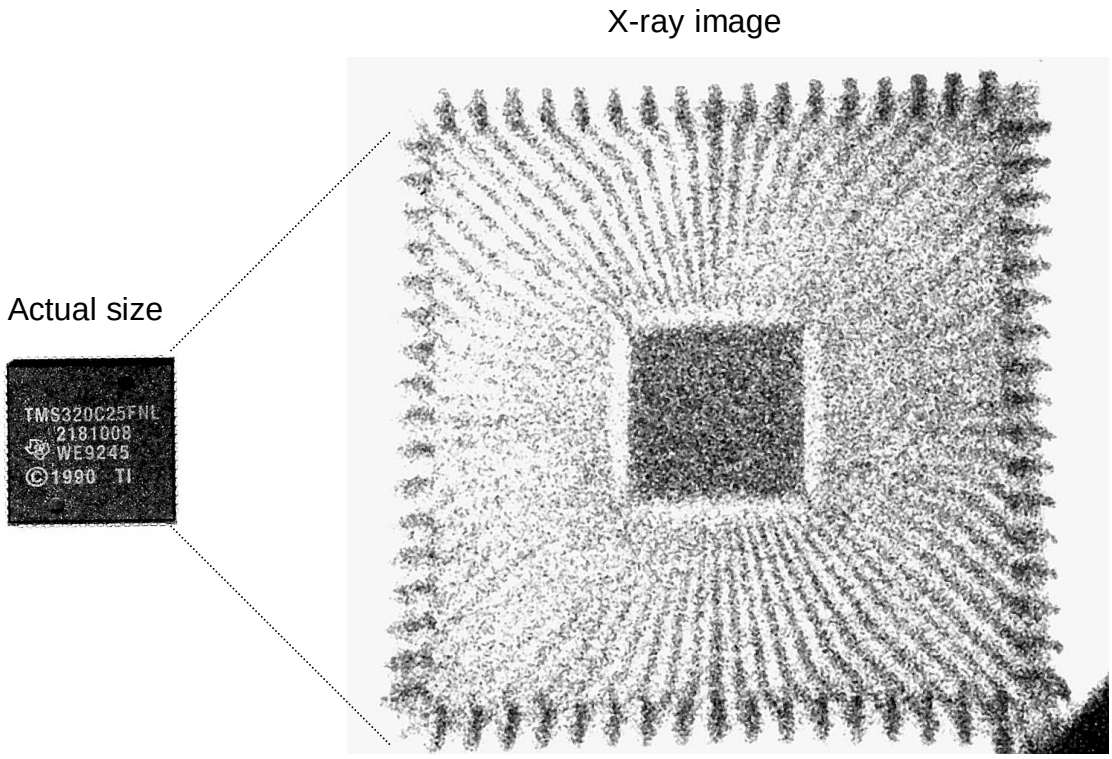

Figure 9.1 - Image of the internal circuitry of a Texas Instruments TMS320C25FNL digital signal processor. Exposure time = 30 seconds. Actual width = 24 mm.

9.5.2 Physical Model for Charge Focusing

Experiments have shown that the electron emission from a pyroelectric crystal is focused, and that the focal length is predicted well by the assumption that all of the crystal charge moves to the edge, forming a ring (See Chapter 5). However, this behavior cannot be predicted based on a bound-charge model of a polarized crystal, and is also not predicted by a model assuming free charges on the crystal surface. Therefore, a more sophisticated model needs to be developed to explain the formation of the ring charge and the asymmetry of the charge emission observed in Figure 5.5.

9.5.3 Experimental Design

This is a rather broad and apparent topic, but it is certainly of import for the future of pyroelectric x-ray and neutron generation. It has been demonstrated in this thesis that the acceleration potential for a pyroelectric radiation source is inversely proportional to its capacitance. The model of acceleration potential presented in Section 4.3 was limited to semi-infinite planar surfaces in the interest of simplicity. One might seek, therefore, to improve performance by considering crystal and target geometries which would reduce capacitance relative to the current planar crystal surfaces and targets. There will also always be a need for the reduction of electrostatic discharge by polishing the crystals and maximizing the distance between the crystals and surrounding surfaces. Finally, the experimental geometry can be improved to maximize the number of field lines (i.e., the number of emitted particles) which reach the target, instead of being lost to surrounding surfaces.

9.5.4 Design of and Testing of New Crystals

Lithium tantalate and lithium niobate are popular materials for pyroelectric x-ray and neutron generation due to their convenient Curie temperature, low cost, and good ratio of pyroelectric coefficient to capacitance. However, since pyroelectric radiation generation is a new technology, many crystals desirable for similar favorable properties are not readily available from commercial suppliers. Principle among these are doped species of pyroelectric crystals. (For example, $BaTiO_3$ with trace cobalt doping has a pyroelectric coefficient[18] of 1200 - 3500). Doped crystals also have a distinct disadvantage, however, in that they typically are more electrically conductive than un-doped crystals. One possible advantage is that while doped crystals have increased electrical conductivity, electrical conductivity is typically married to thermal conductivity. Therefore, it may be possible to avoid high relaxation current by using thick crystals, thereby adding low capacitance to the improvement in pyroelectric coefficient. It may also be possible to design new crystal species specifically for their merit (i.e., low capacitance and high pyroelectric coefficient) as pyroelectric radiation sources. It is important, therefore, to test species of crystals other than $LiTaO_3$ and $LiNbO_3$ to see if an improvement can be

made upon the currently available ~250 kV maximum potential in a paired-crystal pyroelectric radiation source.

9.5.5 Neutron Experiments

9.5.5.1 Optimizing Tip Diameter

It has been shown, experimentally and theoretically, that tips which are too great in apex radius cannot ionize deuterium gas. However, in Section 8.5.3 it was shown that the best tip radius for deuterium gas ionization may not be the smallest available radius, since larger tips may ionize a greater volume of gas, as long as the field in the tip vicinity stays above a critical value for a reasonable distance from the tip. The continued study of the effect of tip size on ionization efficiency will therefore aid in the design of neutron sources with long lifetimes and good ionization efficiencies.

9.5.5.2 Optimizing Experimental Materials

It was demonstrated that the neutron yield was greatly improved by switching from conductive epoxy to non-conductive epoxy. One hypothesis is that the reduction in interface conductivity causes the necessity of a higher electric field for a given electron current, thus causing the pyroelectric charge to be depleted in the form of ions at higher energy. However, to this date experiments have only been conducted with two epoxies, and it would be beneficial to test a wide range of epoxies to determine the optimum conductivity. It is also necessary to determine whether some other property of the epoxy is responsible for the change in neutron yield.

9.5.5.3 Studying Changes in Tip Radius and Target Material

The neutron generators discussed in Chapter 8 consisted of 70 nm - 200 nm tips as the ion source, and a thin (~10 micrometer) deuterated plastic layer as the target. It is known that strong fields are present in the vicinity of the tip. It is necessary to study the change, if any, in the shape of the tip due to the strong field and the electron current incident on the tip due to the field ionization reaction. The long-term performance of tips of different diameters must be tested to determine whether the rate at which a tip is destroyed is dependent on the tip radius.

It is important to study the deuterated plastic target to determine the useful lifespan of the target. There are several means by which the target may be ruined. Microscopic surface defects on the target-coated crystal could cause large local electric fields, which could then field ionize the target atoms when that crystal is positively charged. The ion current necessary for the fusion reaction could also destroy the target, by kinetic energy transfer to the outermost target atoms, causing ablation. Finally, the chemistry of the target over a long period of use has not been studied. It is therefore unknown whether the heating and cooling of the target, or the strong electric field, cause it to adsorb impurities, the presence of which would cause a reduction in the target efficiency.

9.5.5.4 Developing New Methods for Gas Ionization

The neutron production experiments performed as research for this thesis were almost all performed with either bare crystals (which yielded no neutrons) or crystals attached to a metallic tip. The purpose of the tip was to enhance the electric field in a small volume, and thereby increase the yield of ions from field ionization.

There are other ways to ionize a fill gas. One method may be to use a hot filament to emit electrons, which would then cause impact ionization with the surrounding gas, as in a Bayard-Alpert gauge. It is also possible to have a field ionization source, but to separate that source from the pyroelectric crystals, such that the ion current and accelerating field strength can be de-coupled. For example, a transformer providing 15 kV of accelerating potential from an input voltage of ± 12 V has been shown to be a sufficient power supply to ionize gas when coupled to a carbon nanotube cathode[73]. A secondary advantage of separating the ion source from the crystals is that both crystals could be covered with deuerated targets, thereby doubling the neutron yield per thermal cycle.

9.5.5.5 Understanding and Controlling Count Rate Peaks

As demonstrated in Section 8.5.5, the random occurrence of peaks in the neutron count rate, currently attributed to the formation of plasma, causes a tremendous increase in the x-ray and neutron yield. However, none of the explanations for the peaks offered in Section 8.5.5 is entirely satisfactory. For example, the classic criteria for plasma formation are not met in the system, but the rate of change in the count rate is more

suggestive of plasma formation than of a surface effect or the change over from D_2^+ production to D^+ production. The study and understanding of the nature of these peaks would be of great benefit, especially if it led to the ability to control their formation.

9.5.5.6 Designing a Portable System

The goal of pyroelectric fusion is to allow the production of low-cost portable neutron sources. However, research on this topic has been conducted with bench-top systems with attached gas supplies and turbomolecular pumps, and with copious amounts of analytical instrumentation. As a proof of concept, it is important to design and build a sealed portable source, filled with either deuterium or tritium, that can be used without the support of an attached pump or gas supply. This source would be of great value in demonstrating the merits of pyroelectric fusion technology.

References

[1] Lang, S. B., "Pyroelectricity: From ancient curiosity to modern imaging tool", *Physics Today*, pp. 31 - 36, August 2005.

[2] Jona, F., and Shirane, G. Ferroelectric Crystals. Pergamon Press, New York, (1962).

[3] Lines, M. E., and Glass, A. M., Principles and Applications of Ferroelectrics and Related Materials. Clarendon Press, Oxford, 1977.

[4] Rosenblum, B., Bräunlich, P., and Carrico, J. P., "Thermally stimulated field emission from pyroelectric LiNbO3," *App. Phys. Lett.* **25**, pp. 17 - 19 (1974).

[5] Brownridge, J. D., "Pyroelectric x-ray generator," *Nature*, **358**, pp. 277-278 (1992).

[6] Kalent'ev, V.A., Kortov, S. V., and Zatespin, A.F., *Sov. Tech. Phys. Lett.* **13** (11), (1987).

[7] Rosenman, G. I., et al., *Sov. Phys. Tech. Phys.* **26** (2) (1981).

[8] Kortov, V. S. et al., *Sov. Phys. Tech. Phys.* **25** (9) (1980).

[9] Minakova, E. V., Tirhomirova, N. A., and Khrustalev, Yu. *A. Phys. Chem. Mech. Surf.* **5** (7), pp. 1861-1864 (1990).

[10] Rosenman, G. I., Pechorskii, V. I., Chepelev, Yu. L., Boikova, E. I., and Issakova, L. E., "Exoemission of pyroelectrics," *Phys. Stat. Solidi*, **120**, pp. 667-670 (1983).

[11] Biedrzycki, K., "Polarization reversal-induced electron emission from tryglycine sulface ceramics," *Ferroelectrics*, **119**, pp. 33-39 (1991).

[12] www.amptek.com/coolx.html

[13] Brownridge, J. D., and Shafroth, S. M., "Self-focused electron beams produced by pyroelectric crystals on heating or cooling in dilute gases," *Appl. Phys. Lett.*, **79**, pp. 3364-3366 (2001).

[14] Brownridge, J. D., and Shafroth, S. M. "Electron beam production by pyroelectric crystals," International Conference on High-Power Electron Beam Technology [EBEAM 2002], Hilton Head, SC, October 27 - 29 (2002).

[15] Danon, Y., NEER Grant #04ID14596, "A Novel Compact Pyroelectric X-ray and Neutron Source," Award date: 7/1/2004.

[16] Geuther, J. A., and Danon, Y., "Magnetic deflection of electrons and ions produced by pyroelectric crystals", Transactions of the ANS National Meeting, San Diego CA, June 5 - 9, (2005).

[17] Naranjo, B., Gimzewski, J., and Putterman, S., "Observation of nuclear fusion driven by a pyroelectric crystal," *Nature*, **434**, pp. 1115-1117 (2005).

[18] Lang, S. Sourcebook of Pyroelectricity, Gordon and Breach, New York (1974).

[19] Arago, C., Marques, M., and Gonzalo, J. A., "Composition dependence of the transition temperature in mixed ferroelectric - ferroelectric systems," *Phys. Rev. B.*, **62**, pp. 8561-8563 (2000).

[20] Glass, A. M., "Dielectric, thermal, and pyroelectric properties of ferroelectric $LiTaO_3$," *Phys. Rev.*, **172**, pp. 564 - 571 (1968).

[21] Johnston, Jr, W. D., and Kaminow, I. P., "Temperature dependence of Raman and Rayleigh scattering in $LiNbO_3$ and $LiTaO_3$," *Phys. Rev.*, **168**, pp. 1045 - 1054 (1968).

[22] Barrow, D. E., Petroff, T. E., Tandon, R. P., and Sayer, M., "Characterization of thick lead zirconate titanate thick films using a new sol gel based process," *J. Appl. Phys.* **81**, pp. 876 - 881 (1997).

[23] Takagi, Y., Kimura, S., and Takeuchi, Y., "Structural phase transition of $CsNO_3$ crystal -- spontaneous polarization," *Ferroelectrics*, **284**, pp. 129-135 (2003).

[24] Sayle, R. and Bissell, A., "RasMol: A program for fast realistic rendering of molecular structures with shadows," *Proceedings of the 10th Eurographics UK '92 Conference*, University of Edinburgh, Scotland (1992).

[25] Boysen, H. and Altorfer, F., "A neutron powder investigation of the high temperature structure and phase transition in $LiNbO_3$," *Acta Cryst. B,* **50**, 405-414 (1994).

[26] Brownridge, J. D., and Shafroth, S. M., "Electron beam production by pyroelectric crystals," http://arxiv.org/ftp/physics/papers/0209/ 0209079.pdf.

[27] www.roditi.com

[28] Lide, D. R. (Ed.), Handbook of Chemistry and Physics, 76th Edition, CRC Press, New York (1996).

[29] Rosenman, G., Shur, D., Krasik, Ya. E., and Dunaevsky, A., "Electron emission from ferroelectrics," *J. Appl. Phys.*, **88**, pp. 6109 - 6161 (2000).

[30] www.almazoptics.com

[31] Kukhtarev, N., Kukhtareva, T., Bayssie, M., Wang, J., and Brownridge, J. D., "Generation of focused electron beam by pyroelectric and photogalvanic crystals," *J. Appl. Phys.*, **96**, pp. 6794 - 6798 (2004).

[32] Cengel, Y., Introduction to Thermodynamics and Heat Transfer, McGraw-Hill, New York, (1999).

[33] Mills, A. F., Heat Transfer, Irwin, Boston, MA, (1992).

[34] Geuther, J. A., and Danon, Y., "Electron and positive ion acceleration with pyroelectric crystals," *J. Appl. Phys.*, **97**, 074109 (2005).

[35] Brownridge, J. D., Shafroth, S. M., Trott, D. W., Stoner, B. R., and Hooke, W. M., "Observation of multiple nearly monoenergetic electron production by pyroelectric crystals in ambient gas," *Appl. Phys. Lett*. **78**, pp. 1158-1159 (2001).

[36] Gomer, R., Field Emission and Field Ionization, Harvard University Press, Cambridge, (1961).

[37] Guth, E., and Mullin, C. J., " Electron emission of metals in electric fields," *Phys. Rev.*, **61**, pp. 339-348, (1942).

[38] Farrall, G. A., "Numerical analyis of field emission and thermally enhanced emission from broad-area electrodes in vacuum," *J. Appl. Phys.*, **41**, pp. 563-571, (1970).

[39] Murphy, E. L., and Good, Jr., R. H., "Thermionic emission, field emission, and the transition region," *Phys. Rev.*, **102**, pp. 1464-1473, (1956).

[40] Jensen, K. L., "On the application of quantum transport theory to electron sources," *Ultramicroscopy*, **95**, pp. 29-48, (2003).

[41] Jensen, K. L., "Electron emission theory and its application: Fowler-Nordheim equation and beyond," *J. Vac. Sci. Technol. B*, **21**, pp. 1528-1544, (2003).

[42] Forbes, R. G., "Field electron and ion emission from charged surfaces: a strategic historical review of the theoretical concepts," *Ultramicroscopy*, **95**, pp. 1-18, (2003).

[43] Fowler, R. H., and Nordheim, L., "Electron emission in intense electric fields," *Proc. Roy. Soc. (London) A*, **119**, 173-181, (1928).

[44] Brownridge, J. D., and Shafroth, S. M., "X-ray fluoresced high-Z (up to Z = 82) K-x-rays produced by $LiNbO_3$ and $LiTaO_3$ pyroelectric crystal electron accelerators," http://arxiv.org/ftp/physics/papers/0311/0311090.pdf

[45] Geuther, J., Danon, Y., Saglime, F., and Sones, B., "Electron acceleration for x-ray production using paired pyroelectric crystals", *Abstracts of the Sixth International Meeting on Nuclear Applications of Accelerator Technology [AccApp'03]*, pp. 591-594, San Diego, CA, June 1-5, (2003).

[46] Berger, M. J., Coursey, J. S., Zucker, M. A., and Chang, J., "NISTIR 4999: Stopping-power and range tables for electrons, protons, and helium ions," http://physics.nist.gov/PhysRefData/Star/Text/contents.html (2005).

[47] Nowotny, R. "XMuDat: photon attenuation data," version 1.0.1., University of Vienna, Austria (1998).

[48] Shultis, J. K., and Faw, R. E., Radiation Shielding, American Nuclear Society, LaGrange Park, IL (2000).

[49] http://www.amptek.com/anczt1.html

[50] Geuther, J. A., Danon, Y., "High-energy x-ray production with pyroelectric crystals," *J. Appl. Phys.*, **97**, 104916 (2005).

[51] Geuther, J. A., Danon, Y., "Magnetic deflection of electrons and ions produced by pyroelectric crystals", ANS Annual Meeting, San Diego, CA, June 5 - 9, (2005).

[52] White, F. A., Mass Spectrometry in Science and Technology, Wiley and Sons, New York (1968).

[53] Jackson, J. D., Classical Electrodynamics, 3rd Ed., Wiley and Sons, USA (1999).

[54] Harnwell, G. P., Principles of Electricity and Electromagnetism, McGraw-Hill, New York (1938).

[55] Jauncey, G. E. M., Modern Physics: A Second Course in College Physics, Van Nostrand, New York (1948).

[56] Aleksandrov, V. D., *et. al*., "Applicatoin of neutron generators for high explosives, toxic agents and fissile material detection," *Appl. Radiat. Isot,* **63**, pp. 537-543 (2005).

[57] Chichester, D. L., Lemchak, M., and Simpson, J. D., "The API 120: A portable neutron generator for the associated particle technique," *Nucl. Instrum. Methods Phys. Res. ,Sect.. B*, **241**, pp. 753-758 (2005).

[58] http://www.thermo.com/eThermo/CMA/PDFs/Product/productPDF_24487.pdf

[59] Glasstone, S., and Lovberg, R. H., Controlled Thermonuclear Reactions: an Introduction to Theory and Experiment, Van Nostrand, Princeton, NJ (1960).

[60] Arnold, W. R., Phillips, J. A., Sawyer, G. A., Stovall, E. J., and Tuck, J. L., "Cross sections for the reactions D(*d*,*p*)T, D(*d*,*n*)He^3, T(*d*,*n*)He^4, and He^3(*d*,*p*)He^4 below 120 keV," *Phys. Rev.*, **93** (3), pp. 483 - 497 (1954).

[61] Ziegler, J. F., and Biersack, J. P., SRIM 2003.26 Code, IBM Company.

[62] Griffiths, D. J., Introduction to Electrodynamics, 3rd Ed., Prentice Hall, Upper Saddle River, NJ (1999).

[63] Baum, E. M., Knox, H. D., and Miller, T. R. (Editors), Chart of the Nuclides, Knolls Atomic Power Laboratory, Schenectady, NY (2002).

[64] Huba, J. D., NRL Plasma Formulary, 2002 Revision, Naval Research Laboratory, Washington, D.C. (2002).

[65] Geuther, J., Danon, Y., and Saglime, F., "Nuclear reactions induced by a pyroelectric accelerator," *Phys. Rev. Lett*. **96**, 054803 (2006).

[66] Knoll, G. F., Radiation Detection and Measurement, Wiley and Sons, New York (2000).

[67] Guo, C., Li., M., Nibarger, J. P., and Gibson, G. N., "Single and double ionization of diatomic molecules in strong laser fields," *Phys. Rev. A.*, **58** (6), pp. 4721 - 4724 (1998).

[68] http://www.osha.gov/SLTC/healthguidelines/xylene/recognition.html

[69] Krane, K. S., Modern Physics, Wiley and Sons, New York (1996).

[70] Dickens, J. K., computer code SCINFUL, ORNL-6462, 1988; NEA Data Bank Program No. PSR-0267, (1994).

[71] Brown, R. E., and Jarmie, N., "Differential cross sections at low energies for $^{2}H(d,p)^{3}H$ and $^{2}H(d,n)^{3}He$," *Phys. Rev. C*, **41** (4), pp. 1391 - 1400 (1990).

[72] Chen, F. F., Introduction to Plasma Physics and Controlled Nuclear Fusion, Plenum Press, New York (1984).

[73] Xu, X. G., *et al.*, "Measurements of X-rays from Nanotubes and Nanorods," ANS National Meeting, Boston, MA, June 24 - 28, (2007).

[74] http://www.apace-science.com/eljen/ej-301.htm

[75] http://www.eljentechnology.com/datasheets/EJ301%20data%20sheet.pdf

[76] Dushman, S., Scientific Foundations of Vacuum Technique, Wiley and Sons, New York, (1962).

[77] Shie, J.-S., Chou, B. C. S., and Chen, Y.-M. "High-performance Pirani vacuum gauge," *J. Vac. Sci. Technol. A.*, **13**, pp. 2972 - 2979 (1995).

[78] Stanford Research Systems, IGC100 Ion Gauge Controller Operating Manual and Reference, Sunnyvale, CA (2001).

[79] Cohen, E. R., Lide, D. R., and Trigg, G. L. (Eds.), AIP Physics Desk Reference, 3rd Edition, Springer-Verlag, New York (2003).

Appendix I - Neutron Detection Electronics

The neutron emission presented in Chapter 8 was detected using a proton recoil detector. This detector relies on the scattering of incoming neutrons with hydrogen atoms in the scintillating medium. Since hydrogen nuclei (protons) are identical in mass to neutrons, it is possible for a neutron to lose all of its momentum (i.e., impart all of its energy) to a proton in a collision. The energy imparted in a collision corresponds to the pulse height of the detector signal. For neutron collisions with hydrogen, any pulse height, from 0 eV to the incident neutron energy, is equally probable. Due to detector resolution, carbon scattering effects, and detector nonlinearity[66], the observed response function to a source of monoenergetic neutrons for a 5" x 3" EJ-301 scintillator looks instead like the spectrum shown in Figure I.1.

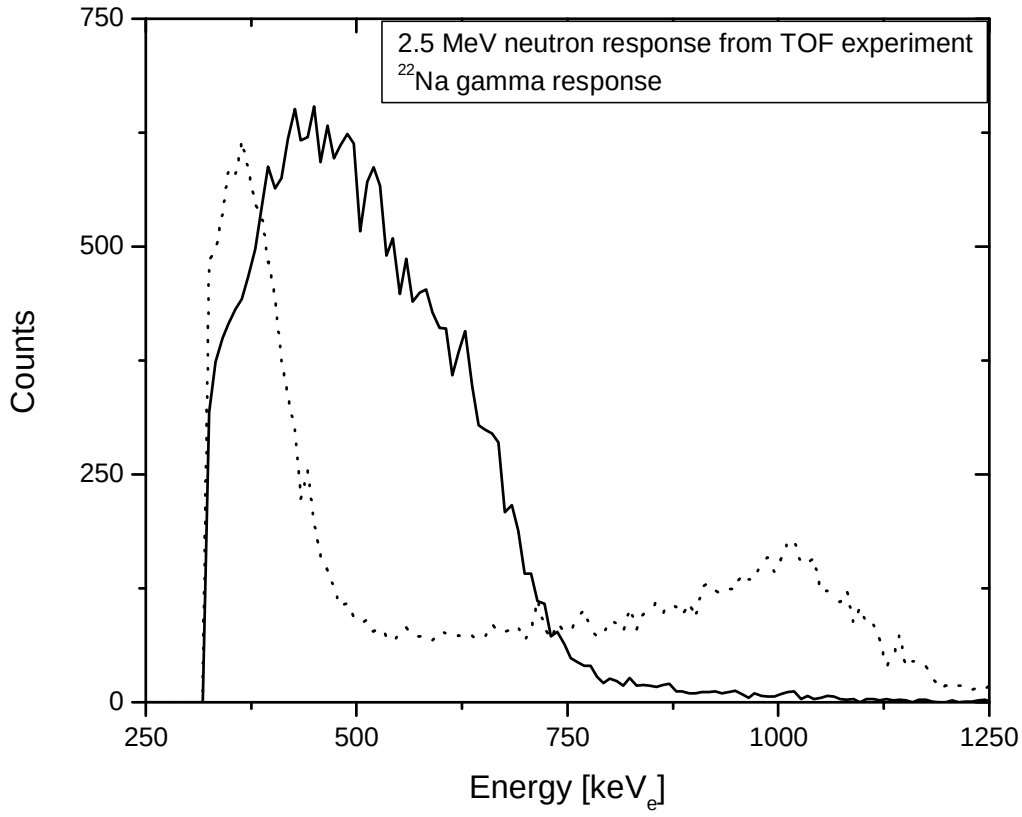

Figure I. 1 - Measured neutron and gamma response in an EJ-301 scintillator.

Figure I.1 shows that the light output from incident gammas, which usually Compton scatter with the atomic electrons in the scintillator instead of scattering off the nucleus, is higher than the proton recoil light output for incident neutrons of the same energy. The

x-axis of the pulse height distribution is therefore calibrated in units of MeV_e (MeV-electron), which corresponds to the detector's response to gammas. The neutron energy is then determined by finding the energy of the edge in terms of MeV_e, and then converting to MeV_p (MeV-proton) using a calibration curve such as the one shown in Figure I.2. This curve was prepared by plotting the light output for neutrons of different energy produced in a time-of-flight [TOF] experiment, and plotting that output against a calibrated MeV_e scale. Data from a published calibration curve[66] are included for comparison.

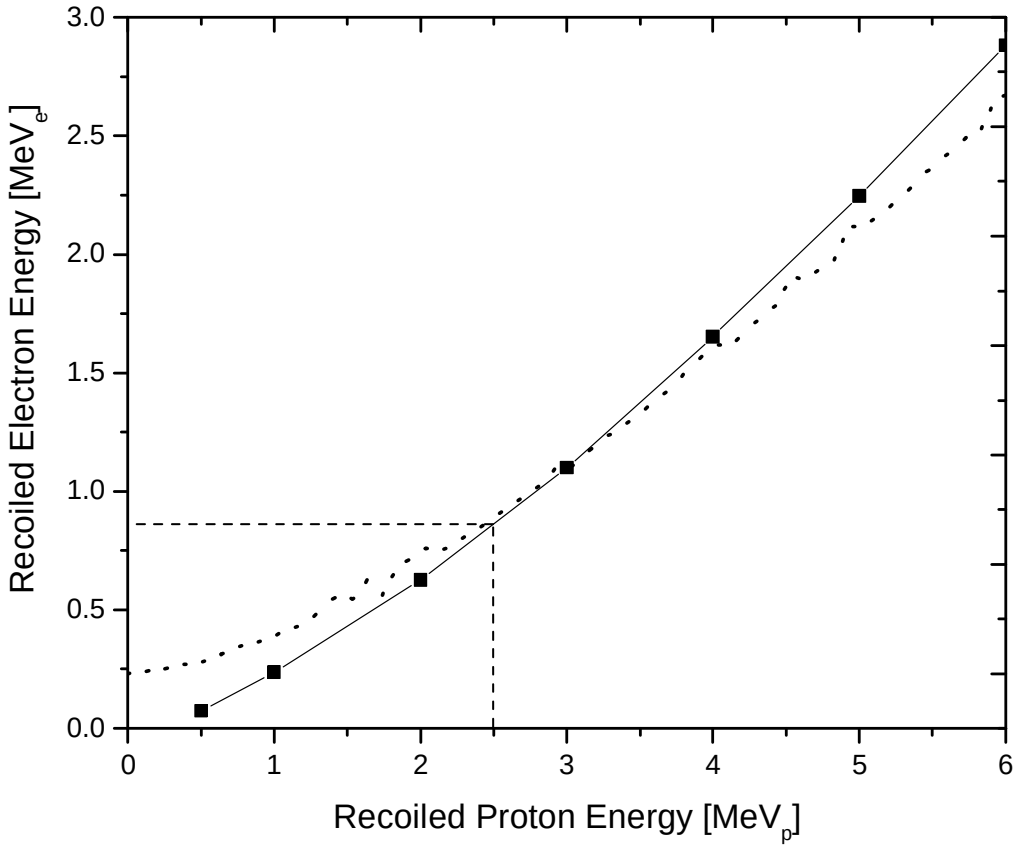

Figure I. 2 - Proton recoil energy versus electron recoil energy. The six points shown as black squares were using TOF method and is used to calibrate the neutron energy scale of the detector. The data represented by the dotted line was taken from Knoll[66]. The dashed line shows that a pulse height spectrum from 2.5 MeV neutrons would have an endpoint of ~750 keVe.

The neutron detector used in this work was a 5" diameter x 3" Eljen 510-50X30-5/301 proton-recoil detector. The liquid scintillator was coupled to a Photonis XP4572B photomultiplier tube and a Photonis VD105K/01 base (not terminated). The scintillating

material[74] was EJ-301, which is composed[75] of 55% hydrogen and 45% carbon (by atomic fraction)[***], and has identical behavior to NE-213.

The detection system discriminates against gammas via pulse shape discrimination. Since gamma pulses have a much shorter fall-time than neutrons, gamma counts can be eliminated by electronically selecting long pulses and rejecting short pulses. In early experiments, the signal from the detector anode was analyzed with analog electronics. In these experiments, the detector power supply was set to -1100 V. The signal from the anode was sent to a preamp, and was then divided between two legs. The first leg was delayed in a delay amplifier and then amplified by a spectroscopy amplifier, and finally sent to the linear input of a linear gate. The second leg was amplified and conditioned by a delay line amplifier, and then sent to a PSA / SCA. This module provided start and stop signals to a TAC based on the pulse time. The TAC then discriminated against short pulses (i.e., gamma pulses) while providing a control signal to the linear gate upon receiving long pulses (i.e., neutron pulses). In this case, the linear gate would allow the signal from the anode output to be sent to the multi-channel analyzer. See Figure I.3.

[***] The composition of EJ-301 is 3.98 x 10^{22} atoms per cm^3 carbon, and 4.82 x 10^{22} atoms per cm^3 hydrogen.

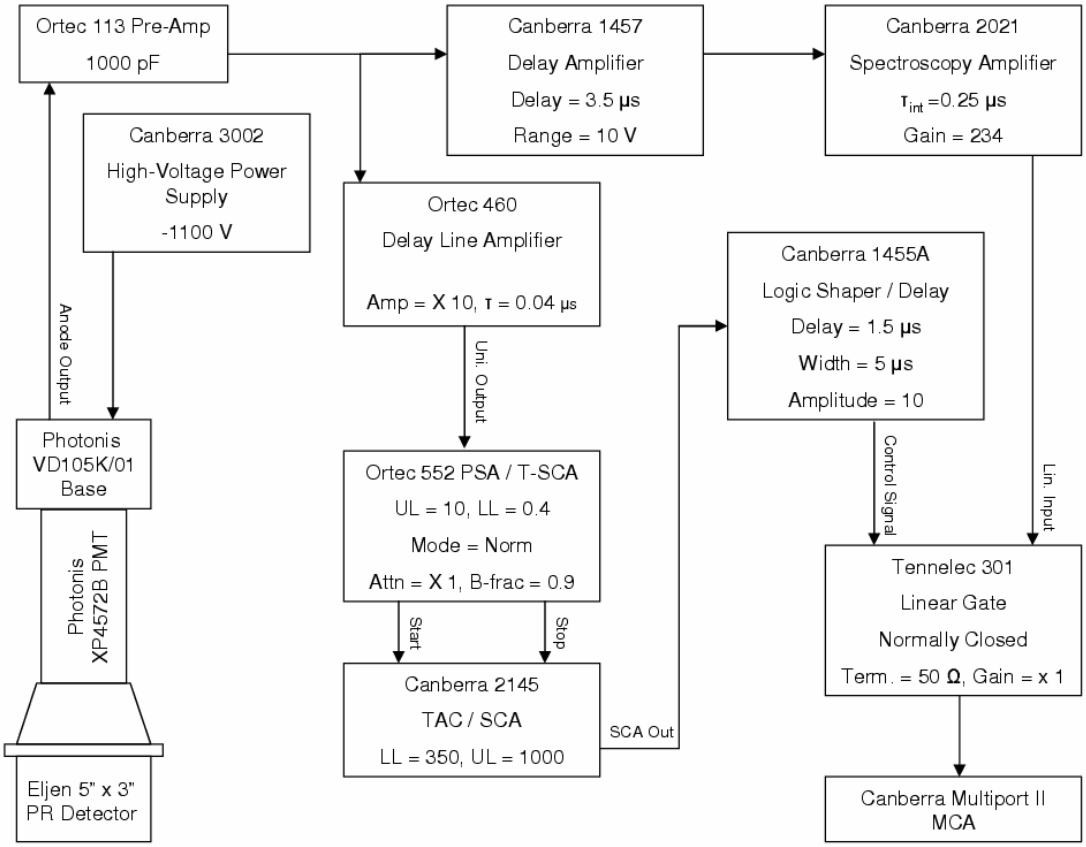

Figure I. 3 - NIM electronics used to detect neutrons and discriminate against photons.

In later experiments, the NIM electronics were replaced with an Acqiris AP240 data acquisition board. In addition to the simplicity of requiring only a high-voltage power supply instead of a NIM bin full of electronics, this system offered enhanced capabilities over the original NIM-based system. Specifically, each pulse could be recorded individually, along with the time at which it was recorded, allowing an entire experiment to be "re-played" on the computer. It was then also possible to look at neutron *and* gamma pulses in a fall-time scatter plot, in real time, while viewing gamma or neutron pulse height spectra. When using the Acqiris board to collect data, the high power supply was set to -1400 V instead of -1100 V to increase the pulse amplitude.

The Acqiris board had 8 bit resolution and sampled at 1-2 gigasamples per second. The signal from the anode of the proton recoil detector was digitized by the board. Each pulse from the detector was sampled at many points, and the points from each pulse could either be compared to find the maximum pulse height, or integrated versus time to

yield the integral pulse area. The Acqiris board also gave the fall time for each pulse to allow pulse shape discrimination.

The software used to control the board and analyze the data was written by Frank Saglime. In the software, fall-time scatter plots, fall-time histograms, MCA, and MCS spectra could be viewed and saved. By defining polygons based on fall time and pulse height, the pulses could be separated into a neutron window and photon (gamma and x-ray) window. Pulses from neutrons tend to have a higher ratio of slow light component to fast light component than pulses from photons, and the resulting difference in pulse fall-time can be used to distinguish neutrons from photons. Figure I.4 shows a fall time scatter plot from a successful neutron production experiment. The upper group of data points is grouped in the neutron window, and represents the neutrons generated by pyroelectric fusion. The lower group of data points consists of background gammas and x-rays produced by the pyroelectric accelerator. The lower boundary of the neutron window (effectively acting as a pulse height discriminator) corresponds to 93 keV_e. When calculating the total neutron yield, only neutron pulses of above 150 keV_e in pulse height were counted. This provided additional assurance that x-ray pulses were not counted as neutrons.

Figure I. 4 shows that neutron and photon fall time distributions can overlap for low values of pulse height. The neutron window settings were chosen to be conservative at low energy. However, to verify that photons contributed very little to our neutron count, the photon yield from a pyroelectric experiment was simulated using a low-energy gamma source. When a ^{133}Ba calibration source was located in the proximity of the neutron detector to provide the same photon count rate as observed in pyroelectric neutron generation experiments (~500 CPS), it was observed that the leakage of photon counts into the neutron window occurred at a rate of about 0.2 counts per second.

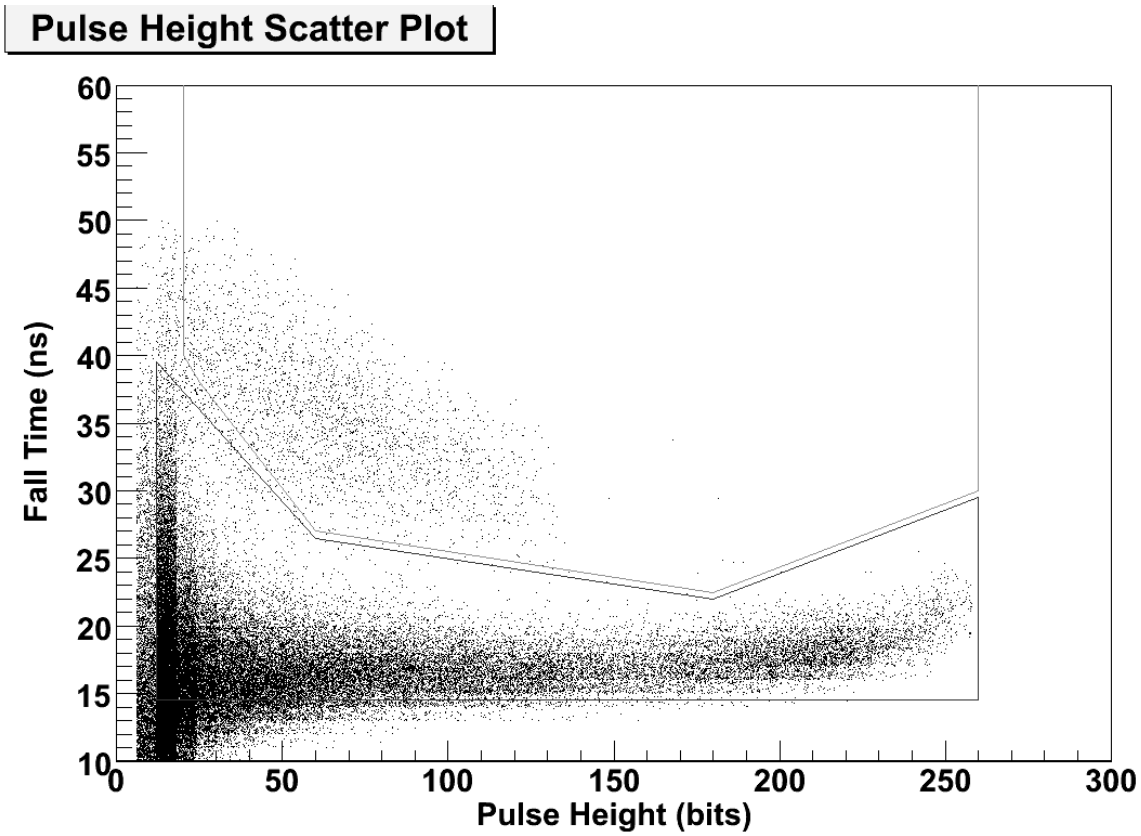

Figure I. 4 - Fall-time scatter plot from a successful neutron production experiment. Upper window collects neutron counts, lower window collects photon counts.

Appendix II - Vacuum System and Instrumentation

II.1 Vacuum Chamber

II.1.1 Elastomer Seal Components

In experiments performed for this thesis, it was necessary to frequently open and close the vacuum chamber to modify the experiment, replace crystals, and so forth. Therefore, it was important to design the experiments with vacuum seals that could be re-used, and flanges that could be easily separated and put back together. For this reason, Quick Flange vacuum components were selected for most of the experimental apparatus. Quick Flange seals consist of a metal centering ring which holds an elastomer (e.g., Buna-N, silicone, or Viton) o-ring. These seals are clamped between smooth surfaces of the two adjoining flanges.

Since Quick Flange seals are elastomer, they can be re-used, and they can be quickly taken apart due to the use of either a single wing-nut collar clamp or several double claw clamps to secure the connection. However, there are several limitations of the Quick Flange design. First, the elastomer seals do not hold vacuum as well as metal seal flanges, and the seals themselves can outgas slightly. Typically, therefore, elastomer seal components are only rated to 10^{-8} Torr. Second, the use of polymer seals limits the temperature to which the system can be heated, from 100^{o}C in the case of Buna-N to 200^{o}C for silicone or Viton. For this reason, the vacuum chamber cannot be baked out at very high temeperatures.

II.1.2 Metal Seal Components

Metal seal, or Con-Flat, vacuum components are far superior to elastomer seal components in terms of vacuum rating (10^{-13} Torr) and maximum temperature (450°C). They are also less expensive than Quick Flange components. Con-Flat flanges function by knife edges on the flange mating surfaces cutting grooves into a copper seal. This seal does not outgas, and leaks less than an elastomer seal. However, copper seals must be discarded after each use, and Con-Flat flanges are sealed with bolts or cap screws, and so they are far less convenient than Quick-Flanges for applications where the system has to be opened and re-sealed frequently. There were some instances in the course of

this thesis where Con-Flat flanges were used. A Con-Flat seal was chosen to attach a beryllium window to the vacuum system, and a portable pyroelectric neutron source, currently under construction, is fabricated entirely with Con-Flat seals (and an all-metal valve).

II.2 Vacuum Pumps

II.2.1 Rotary-Vane Mechanical Pumps

Rotary vane mechanical vacuum pumps are useful for roughing applications (i.e., pumping from atmospheric pressure to ~20 mTorr). They operate via rotating vanes mounted off-axis, such that as the vanes rotates inside the pump, the volume between the vanes and the exhaust port increases for half a turn, and then decreases for half a turn. As the volume decreases, gas is pushed through the exhaust port, and then travels through a reservoir of oil which seals the pump from outside pressure. The early x-ray experiments described in Section 4.2 were pumped by a Welch Duo-Seal Model 1402 rotary vane pump, which had an ultimate pressure of ~25 mTorr.

II.2.2 Diaphragm Pumps

Diaphragm pumps have an operating range of atmospheric pressure to ~1 Torr. In the pumping system used for the neutron production experiments discussed in Chapter 8, a DIVAC 0.8T diaphragm pump was used as the backing pump for the turbomolecular high-vacuum pump. Diaphragm pumps use a piston to drive a diaphragm back and forth in a cavity, with gas being expelled through a check valve.

II.2.3 Oil Vapor Diffusion Pumps

Oil vapor diffusion pumps are used in conjunction with a backing pump (i.e., fore-pump) to reach high vacuum, with an ultimate base pressure of 10^{-9} - 10^{-10} Torr. Diffusion pumps operate by evaporating low vapor pressure oil with an electric heater. The oil vapor then travels vertically through a stack of cones, which direct the oil back to the bottom of the reservoir at a high velocity. Gas molecules which contact the oil vapor can be trapped and transported to the bottom of the diffusion pump, where the oil is re-

condensed and the trapped molecules are removed from the vacuum by the forepump outlet, which is located just above the oil reservoir.

The diffusion pump used in the pumping system for the x-ray experiments discussed in Chapter 4 was an air-cooled Key High Vacuum DFP-3000, with a maximum pumping speed of 285 L / s (for air). The DFP-3000 took 8 minutes to warm up, and has a maximum operating pressure of 100 mTorr. For this reason, it was separated from the vacuum chamber by valves until the chamber was pumped to <100 mTorr by the rotary vane backing pump. While diffusion pumps are cheap and powerful, they are not ideal for experiments which must be altered often, since they must warm up prior to use, and are therefore more favorable for experiments which do not require frequent venting and re-pumping. It is also important to protect the pyroelectric crystals from being coated with stray oil droplets, which can cause excess leakage current along the sides of the crystal. In order to prevent this occurrence, it is necessary to use a liquid nitrogen "cold trap," in which a cold finger causes contaminant vapors (such as oil) to condense.

II.2.4 Turbomolecular Pumps

Turbomolecular pumps operate by compressing gas via a series of rotor and stator stages. The rotors have rapidly moving fan blades which collide with the gas molecules and propel them downward into the next stage, until they reach the last stage and are removed by the backing pump. Due to the high rate of motion of the rotors, turbo-molecular pumps cannot usually pump against full atmospheric pressure. Instead, the gas must first be pumped to low pressure with a backing pump. After a diffusion pump had been used to provide high-vacuum pumping for many of the electron, ion, and x-ray production experiments, it was replaced with a turbomolecular pump due advantages in small size, ease of use, and lack of a warm up / cool down time.

The pumping system used in the neutron production experiments discussed in Chap-ter 8 was a Leybold BMH 70 DRY turbomolecular pumping station. The turbomolecular pump (Leybold TW70H-DN63ISO-K) ran at 1200 Hz (72000 RPM), and was coupled to a diaphragm backing pump (DIVAC 0.8T). The turbopump is rated to pump N_2 at 60 litres per second, or H_2 40 litres per second. The ultimate base pressure was rated at $< 4 \times 10^{-9}$ Torr with the DIVAC backing pump, although this figure is made

under the assumption that the pump is sealed with a blank Con-Flat (i.e., metal seal) flange. The maximum pressure for turbomolecular pump operation was 15 Torr.

II.3 Vacuum Measurement

II.3.1 Pirani Vacuum Gauges

Pirani vacuum gauges[76] operate on the principle that the rate of heat transfer from a hot object to the surrounding gas is a function of the gas pressure. By measuring a temperature-sensitive physical property of a hot filament, a change in heat transfer (and thus change in pressure) can be detected[77].

Convectron gauges were used for all of the experiments in this thesis. Convectron gauges are constant temperature Pirani gauges, in which the voltage across a tungsten filament held at a set temperature is adjusted to keep the temperature constant. The voltage required to maintain the temperature setpoint can then be used to find the rate of heat transfer, and thus the vacuum pressure. These gauges use convection in addition to conduction to increase their operating range to 10^{-4} - 10^{3} Torr.

Since most Pirani gauges are factory-calibrated for measuring N_2, and the heat transfer from the filament is dependent on the gas species, it is necessary to convert the pressure readout on the gauge controller to the pressure corresponding to the gas being measured by using a gas correction curve. For pressures less than 1 Torr, the curve is linear, corresponding to a constant gas correction factor. For the Pirani gauge, the gas correction factor for deuterium at low pressure[78] is 0.79. To find the deuterium pressure, the gauge reading must be multiplied by the gas correction factor. Therefore, a 10 mTorr reading on a gauge calibrated for nitrogen would correspond to 7.9 mT of deuterium.

II.3.2 Bayard-Alpert Gauges

In Bayard-Alpert gauges, also known as ionization gauges, a glass tube encases a filament surrounded by a coil. The filament is heated, causing thermionic electron emission. The electrons then ionize the surrounding gas via impact ionization. The ionization current is used to measure the gas pressure. Bayard-Alpert gauges are useful for measuring gas pressures of less than 1 mTorr. Just as the heat transfer of the fila-

ment in a Pirani gauge is gas-dependent, so is the ionization current in a Bayard-Alpert gauge. The gas correction factor for deuterium is 0.35 for gauges calibrated for N2. In the experiments presented in this thesis, a Bayard-Alpert gauge was used in conjunction with a Pirani gauge to provide temperature indication from atmospheric pressure down to high vacuum.

II.4 Vacuum System Used for X-ray, Ion, and Electron Production Experiments

For the first two and a half years of this project, the vacuum system was comprised of an elastomer-seal chamber centered around a KF 80 tee and a KF 80 4-way cross, with pumping provided by a rotary vane roughing pump coupled to an oil vapor diffusion pump. The modularity of the vacuum chamber components made it easy to run many various experiments without having to buy new vacuum chamber components. However, the system was limited by the poor pumping power of the (salvaged) roughing pump and the long warm-up time for the diffusion pump. The ultimate pressure of the system was ~ 10^{-6} Torr, which was sufficient for all of the experiments composing in this thesis. Photographs of the modular vacuum chamber and the pumping station are shown in II.1 and Figure II.2, respectively.

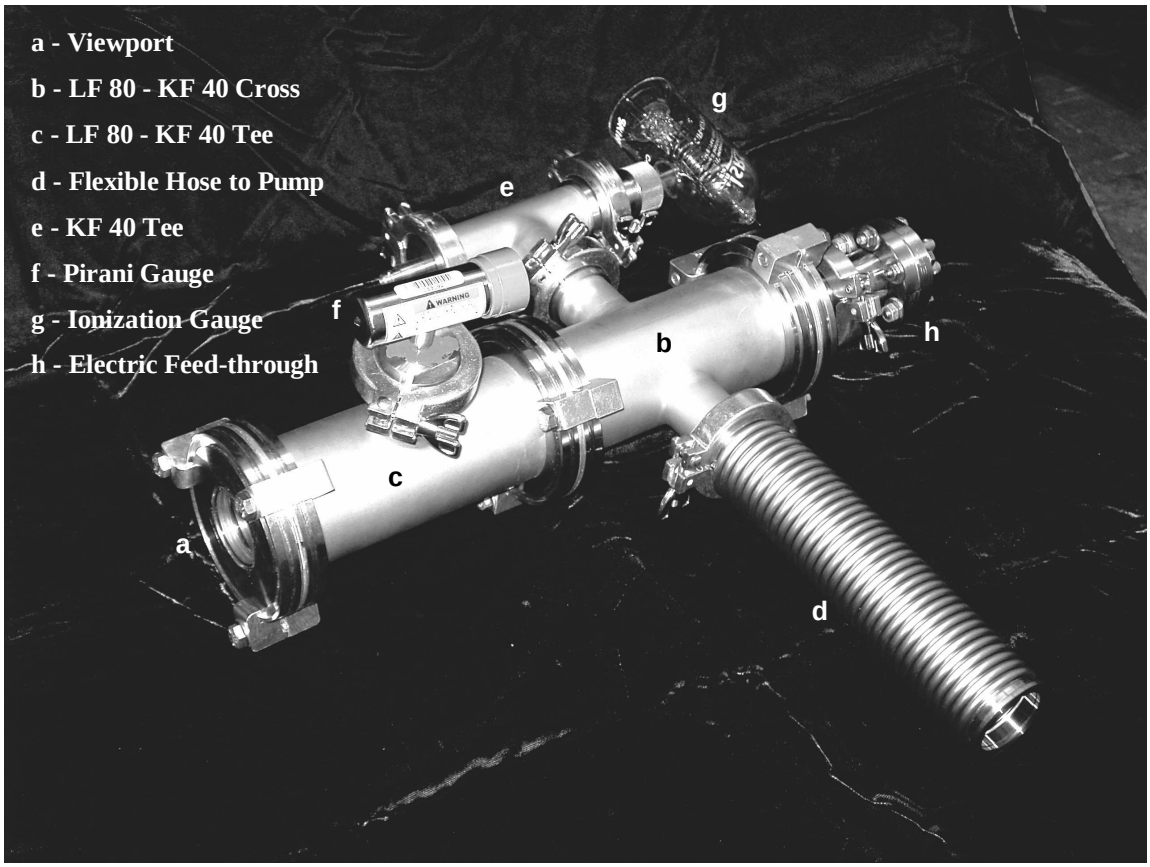

Figure II. 1 - Modular vacuum chamber used in most x-ray, electron, and ion emission experiments.

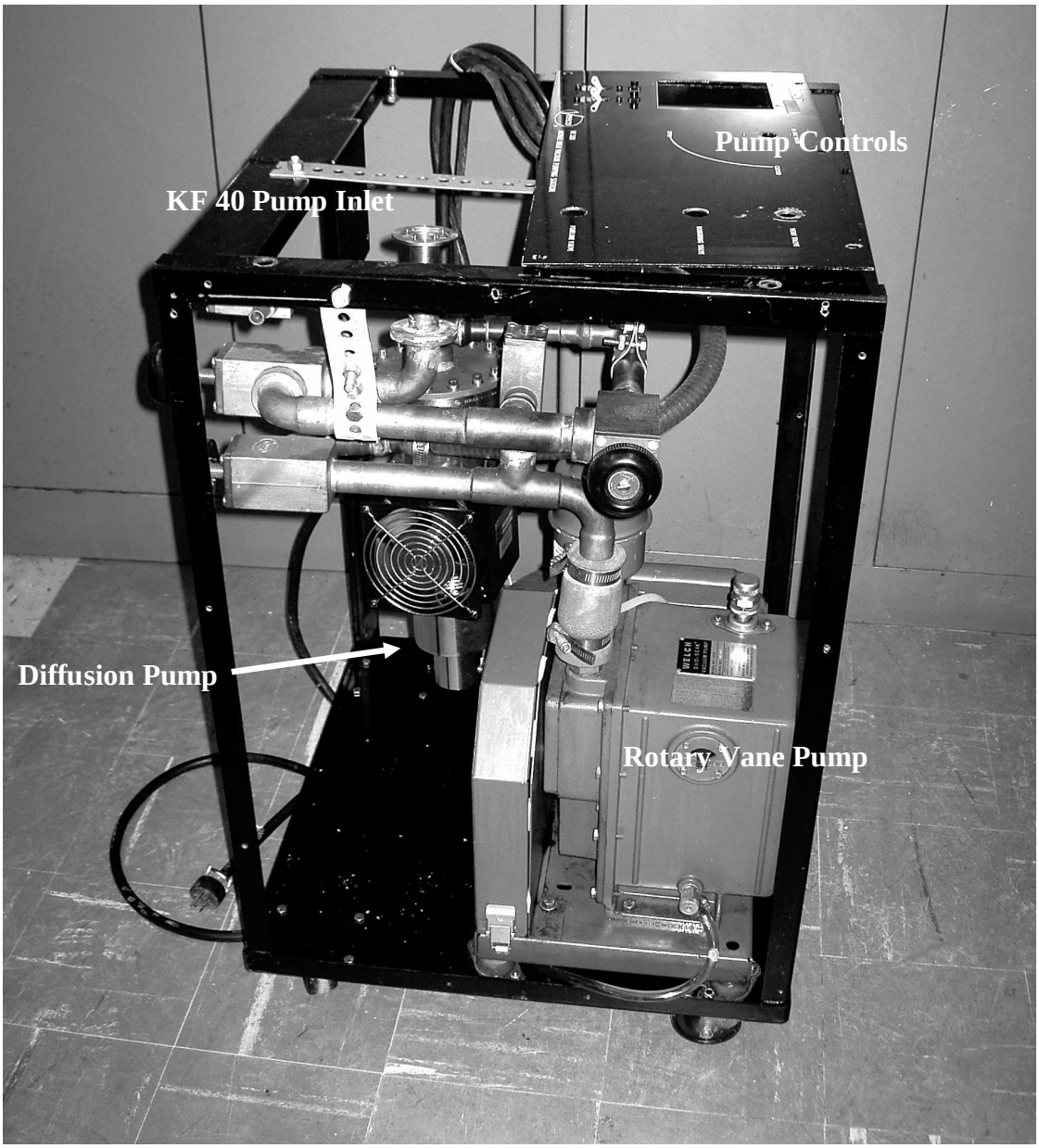

Figure II. 2 - Pumping system used for the x-ray, electron, and ion emission experiments.

II.5 Vacuum System Used for Neutron Production Experiments

The vacuum chamber used in all of the neutron production experiments was a custom-made elastomer-seal chamber from Laco Technologies. This chamber consisted of a stainless steel cylindrical canister with inlet ports halfway up the side. These ports were used to attach vacuum instrumentation, gas feed-throughs, cooling liquid feed-throughs, and electrical feed-throughs to operate the experiment inside the chamber.

Two mounting rails were welded into the chamber to make it versatile to accommodate unforeseen changes to the experiment. The top of the canister was sealed with an LF 160 blank flange, which was made out of aluminum. The aluminum in the center of the flange was bored out such that a 7.6 cm diameter section in the center of the flange had only a 0.6 cm radius, while the rest of the flange had a 1.2 cm radius. This modification was unimportant for the neutron production experiments, but rather was included to allow the chamber to transmit low-energy x-rays for use in x-ray imaging experiments. Table VI gives the dimensions for the vacuum chamber. Photographs of the vacuum chamber and the turbomolecular pump are shown in II.5.

Table VI - Descriptive dimensions for the vacuum chamber used in the neutron production experiments.

Dimension	Value
Chamber Inner Diameter	14.5 cm
Depth of Chamber	15.7 cm
Distance between Mounting Rails	6.4 cm
Distance from Chamber Bottom to Mounting Rails	2.5 cm
Width of Mounting Rails	1.2 cm
Number of KF 16 Ports	2
Number of KF 40 Ports	5

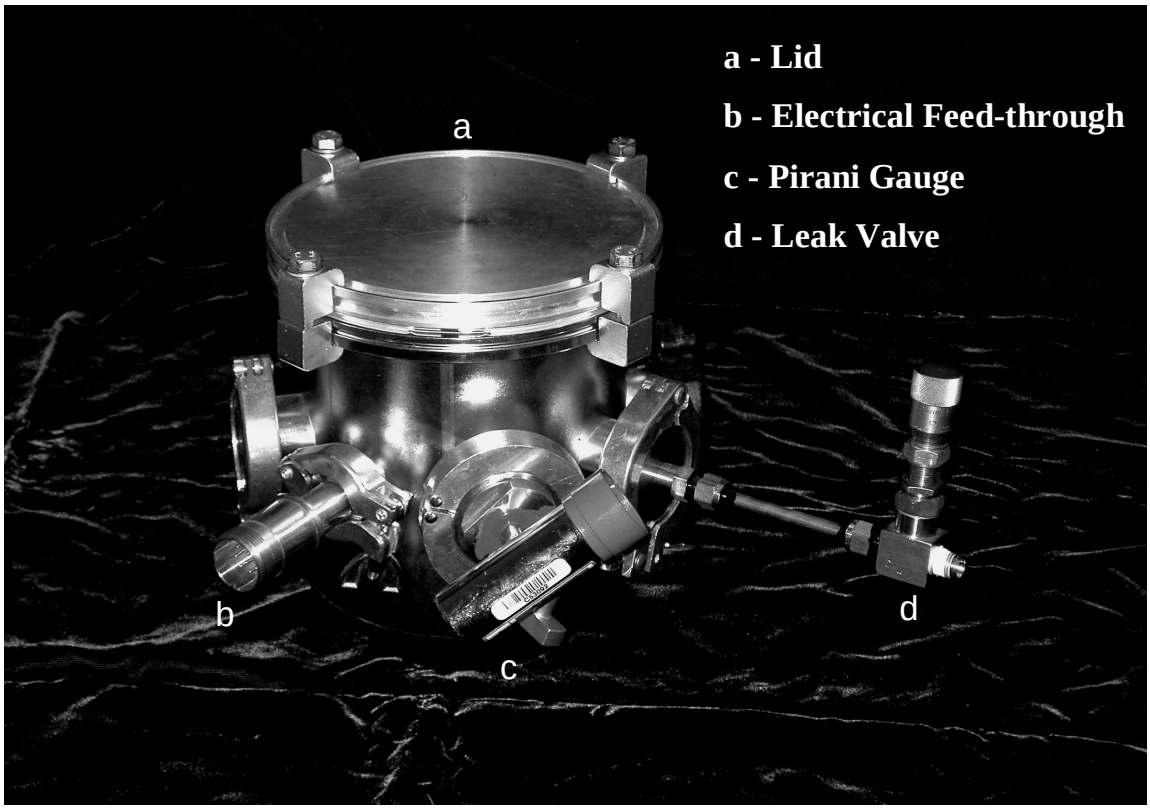

Figure II. 3 - Vaccum chamber used in neutron production experiments, shown with electric feed-through, Pirani gauge, and gas leak valve.

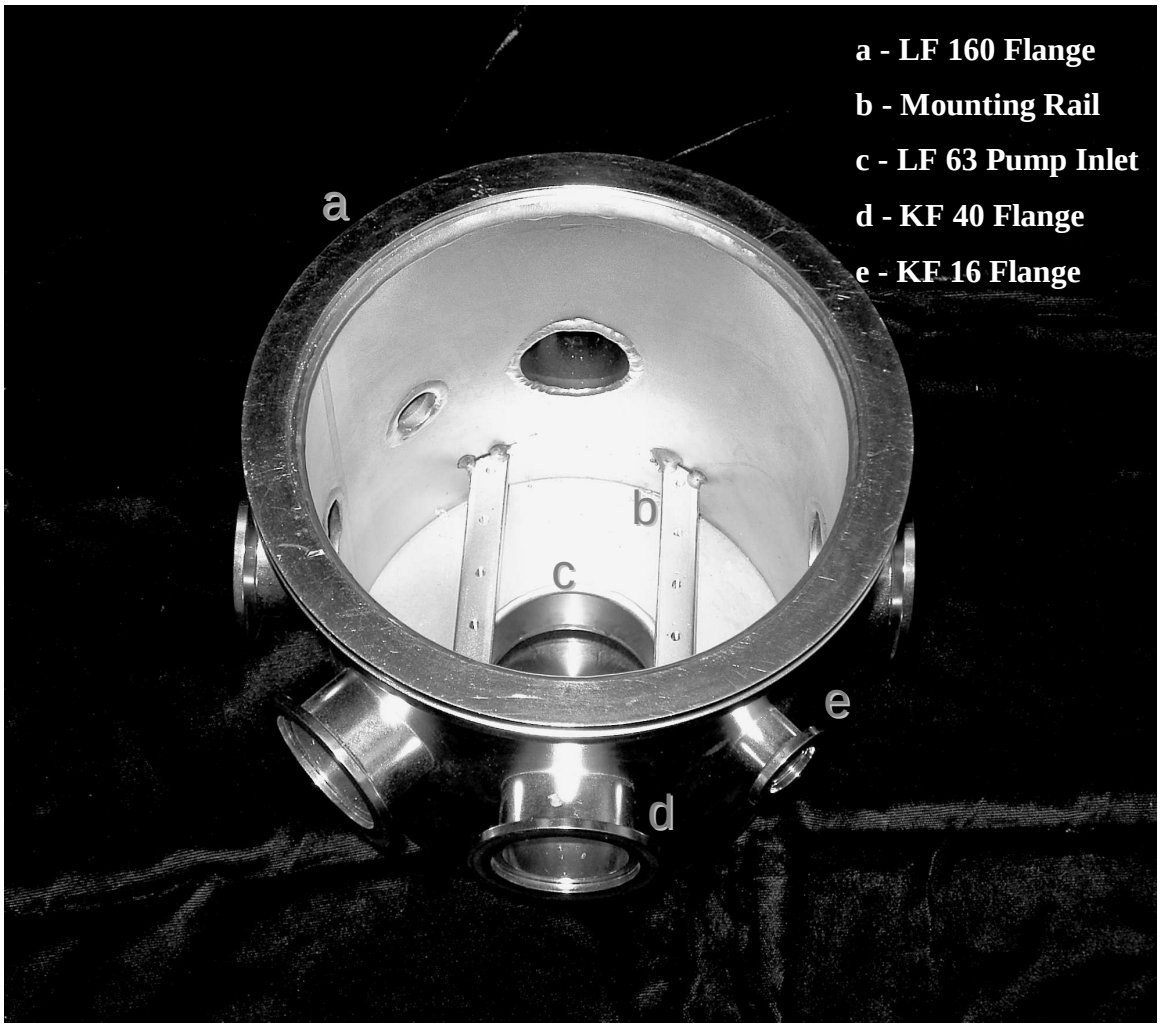

Figure II. 4 - Vacuum chamber used in neutron production experiments, shown open without attached instruments and pump.

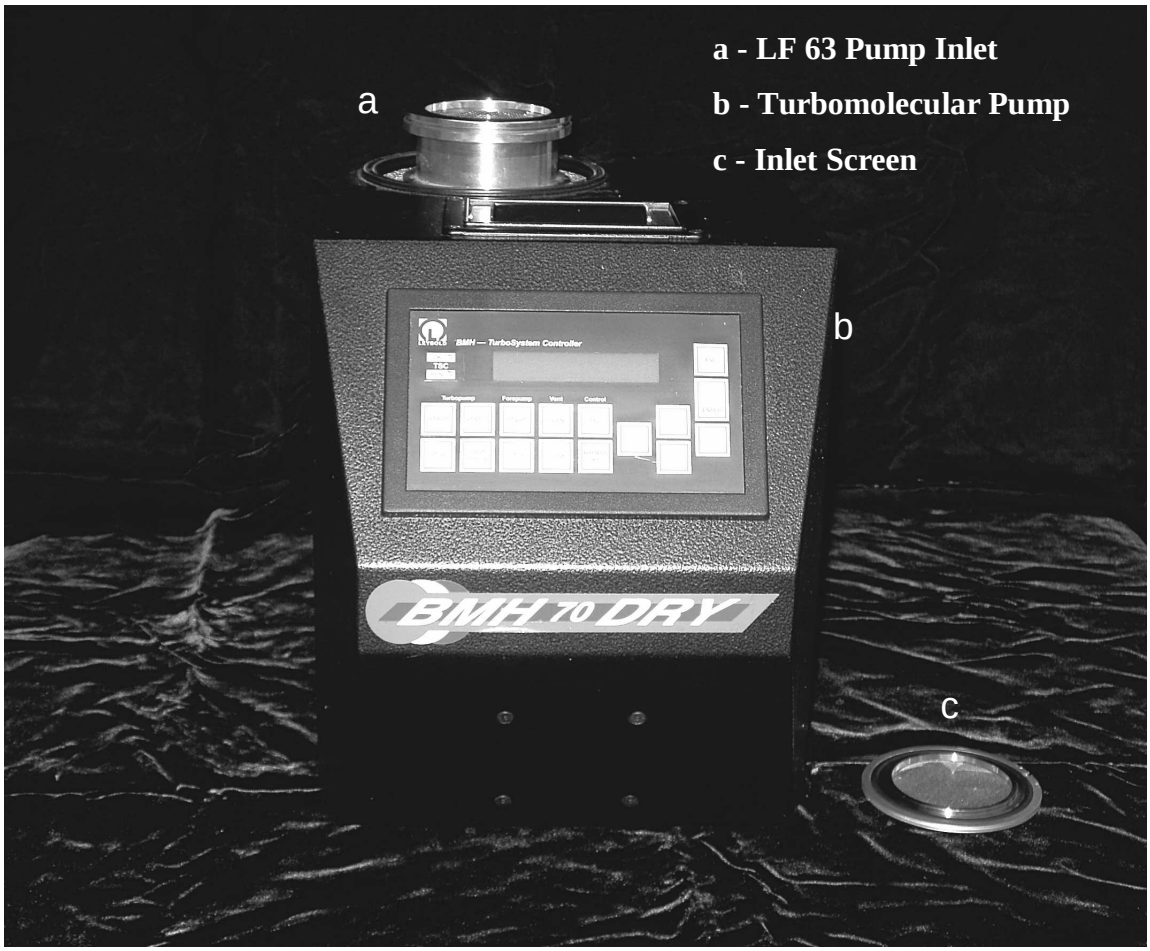

Figure II. 5 - Leybold BMH 70 DRY turbomolecular vacuum pump used in the pyroelectric neutron production experiments. The vacuum chamber was attached to the LF 63 pump inlet.

Appendix III - Electron Detection Program

The following block diagram was for a program written in Labview Express 7.0 in order to collect electron and ion current data. The current was collected from an HP3458A multimeter. The software driver for the multimeter was found on the National Instruments ftp site. Temperature data for the crystal was also collected by this program, using an HP3457 multimeter. The HP3458A driver was found to work for this multimeter as well. The program collected data for a pre-set amount of time, graphed the data on-screen in real time, and wrote the data to an output file at the end of each run. The block diagram has been split into two halves to make it larger and easier to use.

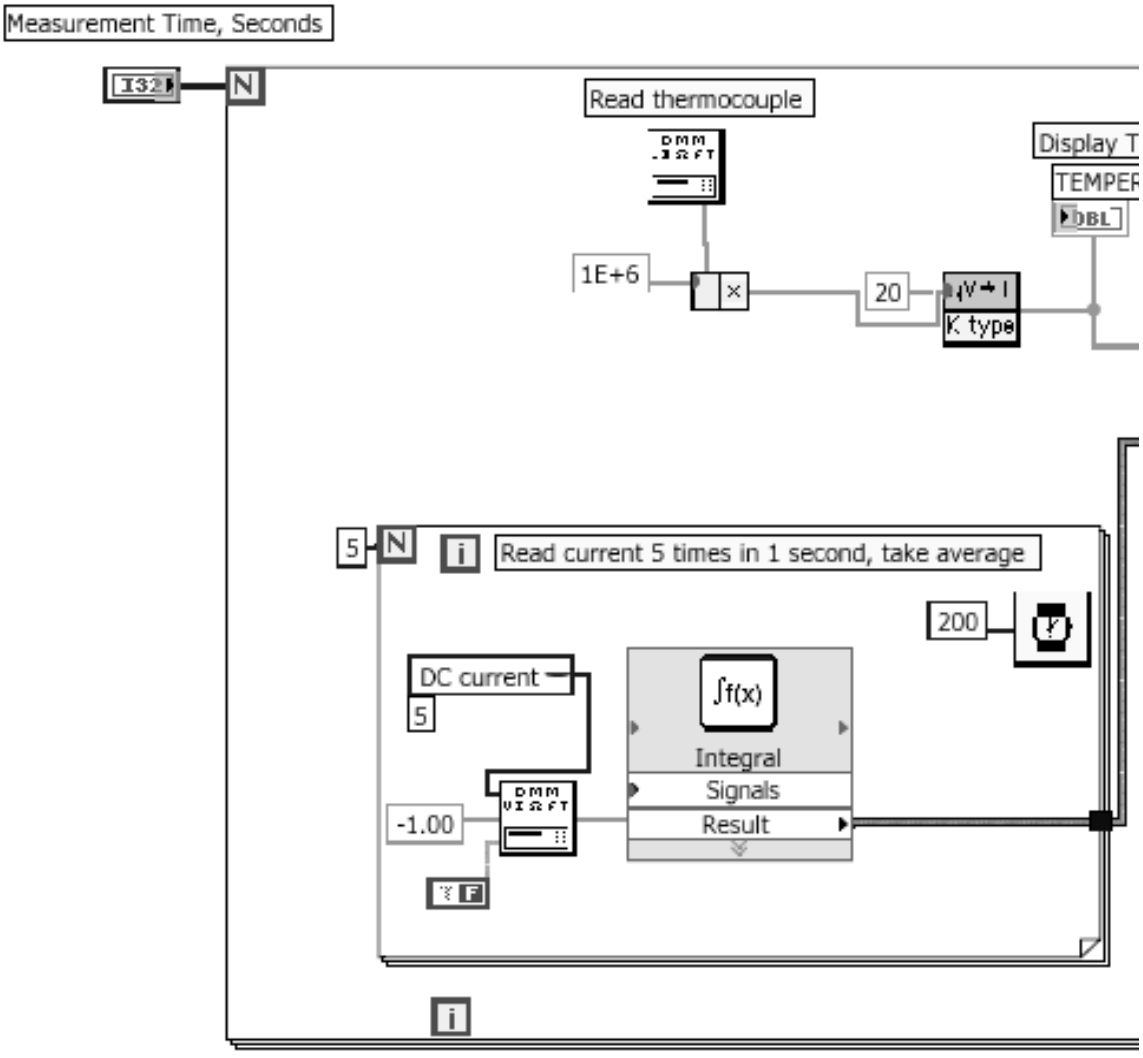

Figure III. 1 - Left hand half of block diagram of Labview program used to collect temperature and current data from pyroelectric ion and electron emission experiments.

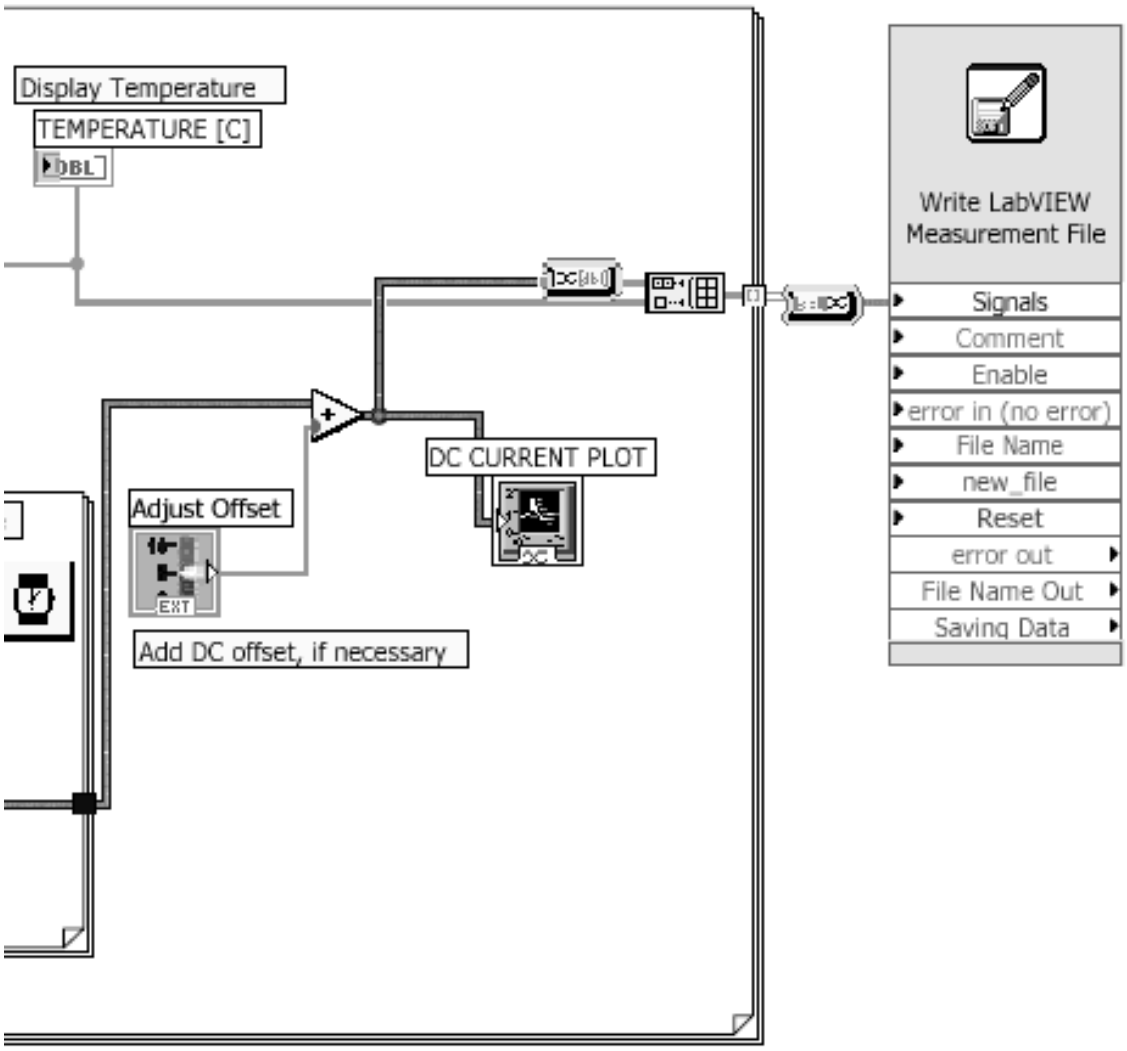

Figure III. 2 - Right hand half of block diagram for the Labview current and temperature data collection program.

Appendix IV - Data from Cathode Tests

The data below is the complete set of results from the experiments discussed in Chapter 7. A figure of merit was calculated for the experiments conducted in air to in comparing the x-ray energy and ionization rate with the deuterium ionization experiments, but is not meant to suggest that neutrons can actually be produced with an air fill gas.

Table VII - X-ray endpoint energy and total emitted ion charge measured for different cathodes mounted to pyroelectric crystals.

Cathode	Gas	Emitted Ion Charge [C]	X-ray Endpoint Energy [keV]	Figure of Merit
600 nm tip	Air 0.01 mT	6.35E-07	59.6	0.42
600 nm tip	Air 0.01 mT	5.86E-07	69.5	0.47
600 nm tip	Air 0.01 mT	8.47E-07	66.8	0.65
600 nm tip	Air 3 mT	1.29E-07	83.5	0.13
600 nm tip	Air 3 mT	5.86E-07	82.7	0.58
600 nm tip	Air 6 mT	2.49E-07	77.9	0.23
600 nm tip	Air 6 mT	3.11E-07	87	0.32
600 nm tip	D_2 4 mT	4.50E-08	97	0.05
600 nm tip	D_2 4 mT	9.65E-08	94	0.11
600 nm tip	D_2 8 mT	0	100.5	0.00
600 nm tip	D_2 8 mT	0	69.5	0.00
W Nanorods	Air 0.01 mT	6.98E-08	97.2	0.08
W Nanorods	Air 0.01 mT	1.13E-07	109.9	0.15
W Nanorods	Air 3 mT	1.60E-08	114.2	0.02
W Nanorods	Air 3 mT	9.44E-08	86.5	0.10
W Nanorods	Air 6 mT	2.38E-08	49.3	0.01
70 nm tip x 2	Air 0.01 mT	0	56.5	0.00
70 nm tip x 2	Air 0.01 mT	5.16E-07	43.3	0.23
70 nm tip x 2	Air 3 mT	5.31E-07	45.2	0.25

70 nm tip x 2	Air 3 mT	1.57E-06	47.9	0.80
70 nm tip x 2	Air 6 mT	1.43E-06	47.1	0.71
70 nm tip x 2	Air 6 mT	1.79E-06	51.4	1.00
70 nm tip x 2	D_2 4 mT	1.66E-07	49.3	0.09
70 nm tip x 2	D_2 4 mT	2.01E-07	49.8	0.11
70 nm tip x 2	D_2 4 mT	3.09E-07	47.4	0.16
70 nm tip x 2	D_2 8 mT	5.36E-07	47.4	0.27
70 nm tip x 2	D_2 8 mT	6.40E-07	46	0.31
C Nanotubes	Air 0.01 mT	4.82E-07	42.3	0.21
C Nanotubes	Air 0.01 mT	6.60E-07	42.1	0.28
C Nanotubes	Air 6 mT	8.28E-07	33.7	0.26
C Nanotubes	Air 6 mT	1.05E-06	33.2	0.33
Nanotree	Air 0.01 mT	3.14E-08	47.7	0.02
Nanotree	Air 0.01 mT	1.19E-07	59	0.08
Nanotree	Air 0.01 mT	2.58E-07	55	0.16
Nanotree	Air 3 mT	0	61.2	0.00
Nanotree	Air 3 mT	0	65.7	0.00
Nanotree	Air 6 mT	1.69E-07	65.5	0.13
Nanotree	Air 6 mT	2.24E-07	62	0.16
Nanotree	D_2 4 mT	0	34.3	0.00
Nanotree	D_2 4 mT	0	45.3	0.00
Nanotree	D_2 8 mT	0	50.9	0.00
Nanotree	D_2 8 mT	2.47E-08	60.6	0.02
70 nm tip	Air 0.01 mT	2.82E-07	52	0.16
70 nm tip	Air 0.01 mT	3.72E-07	57.9	0.24
70 nm tip	Air 0.01 mT	8.14E-07	61.2	0.56
70 nm tip	Air 3 mT	5.75E-07	51.8	0.32
70 nm tip	Air 3 mT	4.88E-07	63.3	0.35
70 nm tip	Air 6 mT	5.37E-07	59.3	0.36
70 nm tip	Air 6 mT	1.08E-06	58.5	0.71

70 nm tip	D_2 4 mT	1.72E-07	71.1	0.14
70 nm tip	D_2 4 mT	2.20E-07	66.6	0.17
70 nm tip	D_2 4 mT	2.29E-07	74.4	0.20
Carbon Nanorods	Air 0.01 mT	0	43.9	0.00
Carbon Nanorods	Air 0.01 mT	5.58E-09	50.4	0.00
Carbon Nanorods	Air 3 mT	0	58.5	0.00
Carbon Nanorods	Air 3 mT	0	51.5	0.00
Carbon Nanorods	Air 6 mT	0	58.2	0.00
Carbon Nanorods	Air 6 mT	0	69.8	0.00
Carbon Nanorods	D_2 4 mT	0	57.9	0.00
Carbon Nanorods	D_2 4 mT	6.74E-09	72.5	0.01
Carbon Nanorods	D_2 8 mT	1.87E-08	55	0.01
Carbon Nanorods	D_2 8 mT	8.07E-08	79.7	0.08
Bare Crystal	Air 0.01 mT	0	75.2	0.00
Bare Crystal	Air 0.01 mT	0	55.2	0.00
Bare Crystal	Air 3 mT	0	71.1	0.00
Bare Crystal	Air 3 mT	0	100.7	0.00
Bare Crystal	Air 6 mT	0	66.3	0.00
Bare Crystal	Air 6 mT	8.49E-08	84.6	0.09
Bare Crystal	D_2 4 mT	0	56.9	0.00
Bare Crystal	D_2 4 mT	0	77.3	0.00
Bare Crystal	D_2 8 mT	0	84.3	0.00
Bare Crystal	D_2 8 mT	0	91.3	0.00

Appendix V - Anisotropy of Neutron Emission from D-D Fusion

The strong P-wave contribution[71] to the angular distribution of D-D fusion reaction products results in anisotropic emission at low incident deuteron energies. This effect is important to consider when calculating the neutron yield based on the observed counts at a detector at some position near the experiment, since the angle of the detector will greatly affect the observed counts for a given source strength.

Brown and Jarmie[71] performed measurements of the angular dependence of the $D(d,n)^3He$ and $D(d,p)^3H$ cross sections at an energy range of 19.9 keV to 116.9 keV. They performed a least-squares fit of the observed ^3H and ^3He angular distribution to a mathematical function for the differential cross section:

$$\sigma(\theta) = a + b \cdot \cos^2(\theta) + c \cdot \cos^4(\theta) \text{ mb / steradian} \qquad (100)$$

The magnitude of the anisotropy increased with increasing energy over the range studied by Brown and Jarmie.

If we take the incident deuterons to be ~100 keV, we can apply the coefficients *a*, *b*, and *c* measured at 100 keV to determine the angular neutron distribution[†††]. Brown and Jarmie give a = 1.018 mb / sr, b = 0.755 mb / sr, and c = 0.20 mb / sr at this energy. The resulting function for $\sigma(\theta)$ is shown in Figure V. 1. This plot shows that the angle at which the neutron detector was located in the experiments with conductive epoxy, $\frac{5\pi}{4}$ [lab system], is more favorable for detecting neutrons than the placement of the detector in the experiments using non-conductive epoxy, in which the detector was located at $\frac{\pi}{2}$ [lab system].

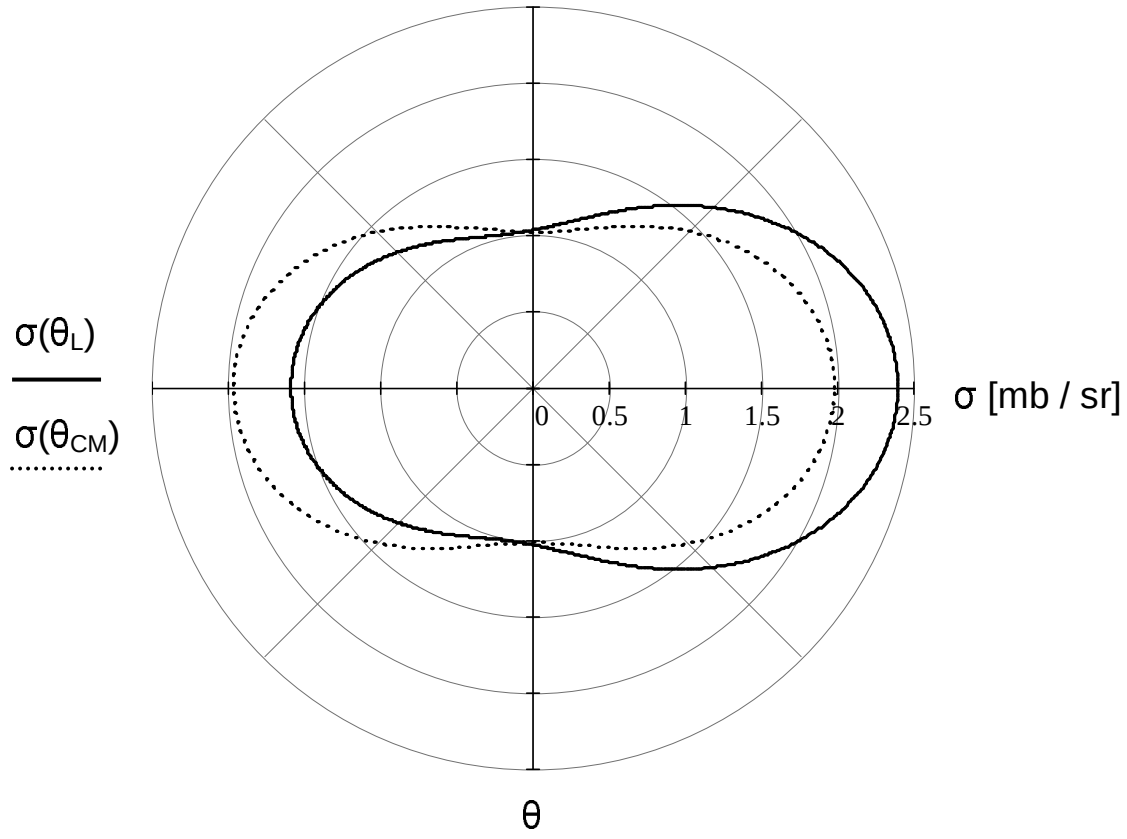

Figure V. 1 - Angular dependence of neutron emission cross section [mb / sr], given in terms of the emitted neutron angle relative to the angle of the incident deuteron. Shown for center-of-mass system (dashed line) and laboratory system (solid line).

The angular cross section was converted from the center-of-mass system to the laboratory system using[79]:

$$\sigma(\theta_L) = \sigma(\theta_{CM}) \frac{\left(1+\gamma^2+2\gamma\cos\theta_{CM}\right)^{3/2}}{1+\gamma\cos\theta_{CM}} \tag{101}$$

$$\gamma = \left[\frac{M_1 M_3}{M_2 M_4} \frac{1}{(Q/K)(1+M_1/M_2)} \right]^{1/2} \tag{102}$$

where M_1 and M_2 are the masses of the reactants, M_3 is the mass of the light product nucleus, M_4 is the mass of the heavy product, Q is the energy released by the reaction, and K is the initial kinetic energy of the projectile nucleus. The resulting angular cross section is in terms of the emission angle of the light product nucleus. Since the function given by Equation 100 gives the angular distribution of the heavy product nucleus, π radians must be added to θ_{CM} to yield the angular distribution of the light product

nucleus before converting the cross sections from the center-of-mass system to the lab system. The resulting differential cross sections for the detector angles used in the pyroelectric neutron production experiments are $\sigma\left(\frac{5\pi}{4}\right) = 1.258\,\frac{\text{mb}}{\text{sr}}$ (conductive epoxy experiments) and $\sigma\left(\frac{\pi}{2}\right) = 1.033\,\frac{\text{mb}}{\text{sr}}$ (non-conductive epoxy experiments).

The neutron yield calculations in Chapter 8 were performed by assuming that the neutron emission was isotropic. The equation used to determine the source yield S_{iso} based on the observed counts N for isotropic emission is[66]:

$$S_{iso} = N\frac{4\pi}{\varepsilon_{\text{int}}\Omega} \tag{103}$$

where ε_{int} is the detector intrinsic efficiency and Ω is the solid angle. This equation is based on a more general equation for determining the observed yield for a given source strength S_{gen}:

$$S_{gen} = \frac{N}{\varepsilon_{\text{int}}\Omega}\frac{\sigma_{total}}{\sigma(\theta)} \tag{104}$$

where σ_{total} is the total cross section, integrated over all angles. The ratio $\sigma(\theta)/\sigma_{total}$ gives the fraction of all emitted neutrons which are intercepted by a detector at angle θ. The neutron yields calculated in Chapter 8 were found by assuming that neutron emission is isotropic. Therefore, to correct for anisotropic emission, the calculated source strength must be corrected by multiplying by the ratio of the calculated general source strength to isotropic source strength:

$$S_{gen} = S_{iso}\cdot\frac{S_{gen}}{S_{iso}} \tag{105}$$

$$S_{gen} = \frac{\left(\frac{N\cdot 4\pi}{\varepsilon_{\text{int}}\Omega}\right)\frac{\sigma_{total}}{\sigma(\theta)}}{4\pi} = S_{iso}\cdot\frac{\sigma_{total}}{4\pi\cdot\sigma(\theta)} \tag{106}$$

The angle integrated cross section is given by[71]:

$$\sigma_{total} = 4\pi\left(a + \frac{b}{3} + \frac{c}{5}\right) \tag{107}$$

At 100 keV, σ_{total} = 16.44 mb, and σ_{total} / 4π = 1.31 mb / sr. Since it was shown earlier that $\sigma\left(\frac{5\pi}{4}\right) = 1.258\,\frac{\text{mb}}{\text{sr}}$ and $\sigma\left(\frac{\pi}{2}\right) = 1.033\,\frac{\text{mb}}{\text{sr}}$ the assumption that emission is isotropic results in an under-prediction of the neutron yield at the detector locations used in the pyroelectric fusion experiment in Chapter 8. If the deuterons in the pyroelectric fusion experiments discussed in Chapter 8 can be assumed to be 100 keV, the correction factor S_{gen} / S_{iso} for including the effect of anisotropic neutron emission in the calculated source strength would be 1.041 at a detector location of $\frac{5\pi}{4}$ radians, and 1.267 at a detector location of $\frac{\pi}{2}$ radians.

The correction factors are based on the assumption that the detectors are geometric points at the specified locations. In reality, the detectors occupy a range of angles centered about the given points. An additional error results from the changing energy of the deuterons, which are believed to start at an energy of more than 100 keV, but lose energy as they penetrate the target. A 30% error is applied to the calculated source strength to account for this assumption and for the unknown energy of the deuterons. Due to the large magnitude of this assumed error relative to the counting error, the counting error is now omitted. The neutron yield from a pyroelectric fusion experiment with conductive epoxy then becomes:

$$S = (10600 \cdot 1.041) \pm 30\% = 11000 \pm 3300 \text{ neutrons per cycle} \tag{108}$$

The yield from the experiments conducted with non-conductive epoxy becomes:

$$S = (59000 \cdot 1.267) \pm 30\% = 75000 \pm 22000 \text{ neutrons per cycle} \tag{109}$$